Master Thesis, Department of Geosciences

The lower crust and upper mantle beneath the western Barents Sea and Svalbard: evidence from combined active source and array seismology

Guri Odden

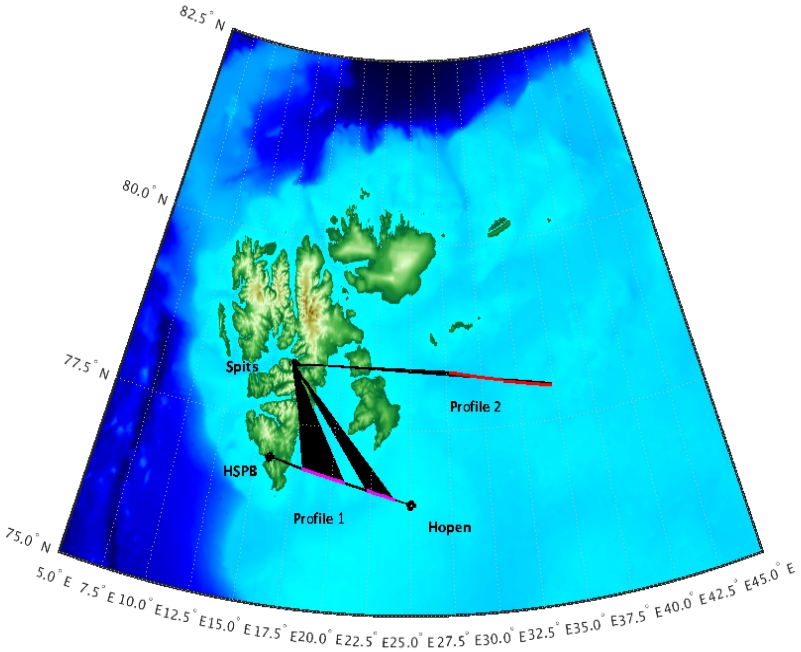

UNIVERSITY OF OSLO

FACULTY OF MATHEMATICS AND NATURAL SCIENCES

The lower crust and upper mantle beneath the western Barents Sea and Svalbard: evidence from combined active source and array seismology

Guri Odden

Master Thesis in Geosciences
Discipline: Geophysics
Department of Geosciences
Faculty of Mathematics and Natural Sciences

University of Oslo

1. June 2015

Supervisors: Dr. Alexander Minakov (UiO), Dr. Johannes Schweitzer (NORSAR) and Prof. Jan Inge Faleide (UiO).

This work is published digitally through DUO – Digitale Utgivelser ved UiO

http://www.duo.uio.no

It is also catalogued in BIBSYS (http://www.bibsys.no/english)

Aknowledgements

First of all I would like to thank my supervisors Dr. Alexander Minakov and Dr. Johannes Schweitzer I am grateful for your guidance, discussions, time and patience, without you there would not have been much of a thesis.

I would also like to give a special thanks to Prof. Jan Inge Faleide for helpful discussions and for critical reading of my master thesis. Thanks to Sergei Medvedev for helping me improve the ray tracing plots.

My fellow students and friends at the Department of Geosciences and CEED are thanked for making long days with studying and writing much more fun. I would also like to give a special thanks to Eva Hauk Fritzell for always answering "stupid" questions regarding LaTeX and Thomas for the support you've given me the last year.

To my mother and father, thank you for your motivation, understanding and financial support.

Abstract

Svalbard is one of few places on Earth where an upwelling mantle flow associated with recently formed divergent plate boundary interacts with continental lithosphere. Seismic tomography studies, elevated heat flow and petrological data from upper mantle xenoliths indicate anomalously hot mantle and thin lithosphere (about 50 km). The Early Cretaceous opening of the Arctic Ocean and formation of the High Arctic Large Igneous Province resulted in abundant dolerite sills in the sedimentary cover and giant-like dike swarms cross-cutting the crystalline basement in the Svalbard region. Despite decent data coverage, velocity models obtained from wide-angle seismic data in the Svalbard region are often characterized by poor resolution in the upper mantle due to limited source-receiver offset.

The datasets in this study originates from two wide-angle refraction surveys conducted in the vicinity of Kong Karl's Land in 2008 and Hopen Island in 2014. Both surveys were shot with air guns with the total volume of about 80 l by the research vessel Håkon Mosby. The seismic line shot in 2008 was recorded with the seismological array on Spitsbergen (SPITS) and sampled crust and upper mantle in east-west direction, while the line shot in 2014 was recorded at SPITS, and the seismic stations at Hornsund (HSPB) and on Hopen Island (HOPEN) leading to sampling of crust and upper mantle in both north-south and east-west directions.

Band-pass filtering, cutting, NEZ-LQT rotation, beamforming both at the source and receiver sides, and tau-p transformations have been performed on the data to enhance the signal-to-noise ratio for certain seismic phases and have resulted in clear mantle refractions at offsets up to 420 km. The travel-time data are inverted for a 1D P-wave velocity model, following Diebold and Stoffa (1981). Other 1D velocity models previously published by different authors will also be discussed. The 3D model Barents50 from Ritzmann et al. (2007) has been evaluated by ray tracing and travel-time modelling, and it has revealed some differences in travel times when compared to the data in this thesis. Full waveform modelling by a frequency-wavenumber integration method (Bouchon, 1981) has been performed in order to study offset dependent amplitude variations and the generation of converted S-waves.

Discrepancies between the modelled travel-times from Barents50, Barents, Barey, Barez and Fennoscandia and the travel-times of the onsets from the data in this thesis was evident. The largest deviations between the previously published data and the data from this thesis was found in the crust. Previous depth and velocity estimates of the upper mantle are similar to the inverted 1D data. Some previous publications in this area supports magmatic underplating, however in this thesis no signs of magmatic underplating in the lower crust is evident and the largest P-wave velocity in the crust is 6.6 km/s.

With this contribution new methodological developments that will allow for better imaging of the uppermost mantle from long-offset refraction data will be discussed.

Contents

1 Introduction **1**

1.1 Objective and outline of thesis . . . 1
1.2 Dataset . . . 2
1.3 Seismic arrays and stations . . . 2
1.3.1 SPITS Array . . . 4
1.3.2 HOPEN Station . . . 5
1.3.3 HSPB Station . . . 5
1.4 Geological background . . . 5
1.4.1 Tectonic evolution . . . 7

2 Data Processing **11**

2.1 Processing . . . 11
2.1.1 Filtering . . . 11
2.1.2 Cutting . . . 12
2.1.3 Coordinate transformations . . . 12
2.1.4 Beamforming . . . 13
2.1.5 Tau-p transform . . . 15
2.2 Seismic data management and processing implementation . . . 16
2.3 Processing results . . . 16
2.3.1 Filtering . . . 19
2.3.2 Cutting . . . 22
2.3.3 Coordinate transformations . . . 23
2.3.4 Beamforming . . . 26
2.3.5 Tau-v_{app} seismograms . . . 30
2.3.6 Reduced seismograms . . . 39
2.3.7 Composite seismograms . . . 43

3 Forward modelling **49**

3.1 Methods . . . 49
3.1.1 Travel-time modelling . . . 49
3.1.2 Amplitude modelling . . . 50
3.2 Implementation . . . 51
3.3 Results . . . 51
3.3.1 Travel-time curves from 1D models . . . 51
3.3.2 Travel-time curves from Barents50 . . . 55
3.3.3 Raypaths in the Barents50 3D model . . . 58
3.3.4 Synthetic seismograms . . . 64

4 1D inversion **67**
4.1 1D inversion method . . . 67
4.2 Implementation . . . 68
4.3 Results . . . 68
4.3.1 1D velocity models . . . 68
4.3.2 Synthetic seismograms . . . 70

5 Discussion **76**
5.1 General velocity structure . . . 76
5.2 The upper mantle . . . 77
5.2.1 Moho depth . . . 78
5.2.2 Travel-time differences . . . 78
5.2.3 Uncertainties related to inversion . . . 80
5.2.4 Magmatic underplating . . . 80
5.2.5 Azimuthal anisotropy . . . 81
5.3 Crustal structure . . . 83
5.4 S-waves . . . 84
5.5 Amplitude variations . . . 84

6 Conclusion **87**
6.1 Further work . . . 87

References **94**

A Appendix **95**
A.1 Data processing . . . 95
A.2 Forward modelling . . . 178
A.2.1 Raypaths in Barents50 . . . 178
A.2.2 Synthetic seismograms . . . 184
A.3 Inversion . . . 186
A.3.1 1D inverted velocity models . . . 186
A.3.2 Synthetic seismograms from inverted data . . . 190

List of Tables

2.1 Stations at SPITS that have data from the two profiles are ticked off . . . 17
2.2 Offset data for all the different profiles. . . . 17
4.1 Pick uncertainity σ in milliseconds . . . 68
4.2 Pick rms for the different profiles . . . 69

A.1 1D velocity model Barents, from Kremenetskaya et al. (2001) 186
A.2 1D velocity model Barey, from Schweitzer and Kennett (2002) 186
A.3 1D velocity model Barez, from Schweitzer and Kennett (2002) 187
A.4 1D velocity model Fennoscandia, from Mykkeltveit and Ringdal (1981). 187
A.5 1D velocity model from inversion for $P2$. 187
A.6 1D velocity model from inversion for $P1_s$. 188
A.7 1D velocity model from inversion for $P1_h$. 189
A.8 1D velocity model from inversion for $P1_{ho}$. 189

1 Introduction

1.1 Objective and outline of thesis

During the last three decades numerous studies and publications considering the crustal structure and crustal properties of the western Barents Sea has been published, Ritzmann et al. (2007), Levshin et al. (2007), Hauser et al. (2011) and Klitzke et al. (2015).

Barents50 is a regional 3D crust and upper mantle velocity and density model for the Barents Sea region (Ritzmann et al., 2007; Levshin et al., 2007). The crustal velocities are derived from seismic refraction experiments and deep seismic reflection data. Lower crustal and upper mantle velocities are determined by comparing observed gravity anomalies and density models of the deep seismic reflection data and surface wave data. Places where there were a good fit between the gravity anomalies and density models the density models were converted back to seismic velocities. The model constrains can be found in Ritzmann et al. (2007).

Hauser et al. (2011) created a probilistic seismic model for the Barents Sea with the Barents50 and several, at that point, unpublished 1D models. Hauser et al. (2011) use a Markov Chain Monte Carlo algorithm to sample an *a priori* distribution and subsequently test them agains previously published data to generate an *a posteriori* distribution.

In addition the regional 1D models: Fennoscandia (Mykkeltveit and Ringdal, 1981), Barents (Kremenetskaya et al., 2001), Barey and Barez (Schweitzer and Kennett, 2002) will be utilized in this thesis. Fennoscanndia are based on reflection and refraction data in Scandinavia, Barents is Fennoscandia adapted to the Barents Sea with seismic events while Barey and Barez are a combination of Barents and Ak135. These 1D models have been used for event location in the Barents Sea region.

The construction of the previous models are based on data from reflection and refraction surveys with active sources to image the crust and Moho boundary and inversion of surface waves of passive seismic events to image the upper mantle. This approach have large uncertainties in the uppermost mantle. Reflection and refraction data are limited by offset and can at their larges offsets only image the Moho boundary, while surface wave tomography have large uncertainties at depths shallower than 70-80 km, i.e., the upper mantle from ~30-70 km is poorly constrained and hence imaging this region will give important information about the physical properties of the upper mantle. The nature of the upper mantle, especially its strain condition is important to understand since it controls much of the plate tectonics.

In this thesis the aim is to establish a method with the main focus of imaging the lower crust and upper mantle, filling the gap between the existing methods to image the upper mantle in this region with active source seismology. The lower crust and upper mantle velocities will be compared to previously published papers from this region, in addition any possible

elastic anisotropy created by the Caledonian Orgeny and the more recent Eocene compression will be discussed.

This thesis comprises six chapters; an introduction, three main chapters, a discussion and a conclusion. In the introduction a presentation of the dataset, seismic stations, arrays and a geological background can be found. Subsequently in chapters 2-4; processing, forward modelling and inversion are presented. Each of these chapters consists of three sections; theoretical background, implementation and results.

1.2 Dataset

The datasets in this thesis originates from two wide-angle refraction experiments conducted in the vicinity of Kong Karl's Land in 2008 and Hopen Island in 2014. They were recorded by the seismological stations HSPB and HOPEN and the seismological array SPITS, see **Figure 1.1**. Not all stations detected both refraction experiments, and the measurements of the different experiments at the different stations are named accordingly:

- $P1_s$: the refraction line from 2014 recorded at SPITS array.
- $P1_h$: the refraction line from 2014 recorded at HSPB station.
- $P1_{ho}$: the refraction line from 2014 recorded at HOPEN station.
- $P2$: the refraction line from 2008 recorded at SPITS array.

Profile 1 was shot along an east-west line and due to Tusenøyane (Thousand Islands) the line is not continuous, while Profile 2 was shot along a west-east line, see **Figure 1.1**.

Both wide-angle refraction experiments originates from seismic acqusitions performed by the research vessel Håkon Mosby. The air gun sources had a total volume of 80 l, and in both acqusitions Ocean Bottom Seismometers (OBS) were used. Processed and interpreted OBS - data from the 2008 acqusition can be found in Minakov et al. (2011), while OBS data from 2014 are under processing.

1.3 Seismic arrays and stations

During the last three decades a lot has happened to the way seismological data are measured, processed and stored. From 1D analog measurements in the early 1900's to digital three-component broadband stations and arrays utilized today. The standard directions three-component stations measure are the vertical, east and north component.

Seismic signals are measured by either inertial- or strain-seismometers. Inertial seismometers measure ground motion relative to an inertial reference while strainmeters measure the relative motion of one point on the ground to another (Haskov and Alguacil, 2004). The ground motion relative to an inertial reference is in most cases larger than the relative motion

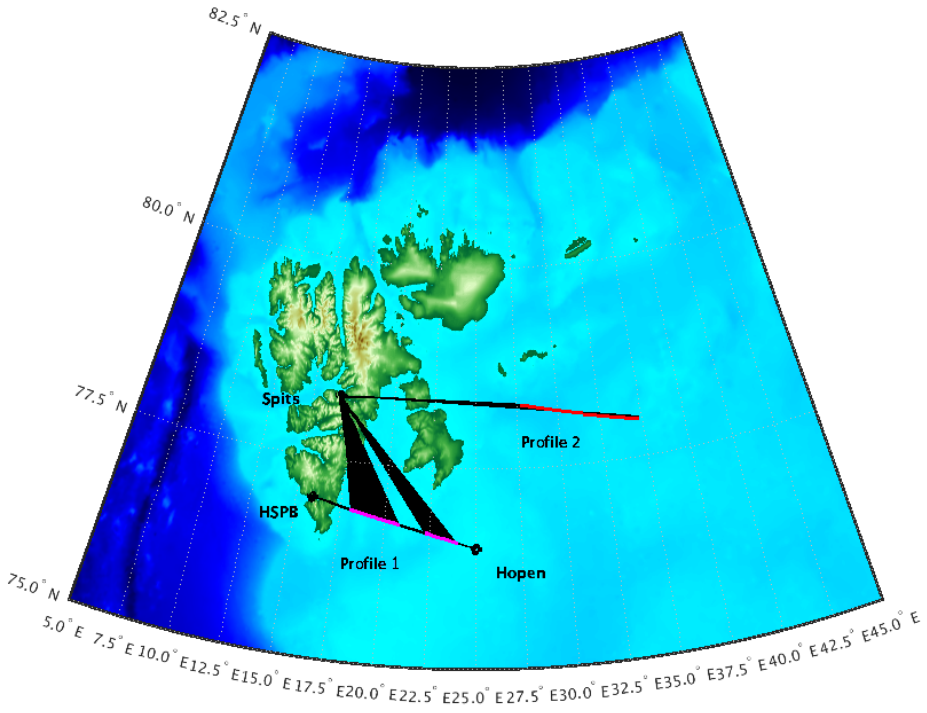

Figure 1.1: Study area, acqusition lines and seismological stations. The red line represents the acqusition line from 2008, while magneta represents the acqusition line from 2014. Black circles represents the seismological array on Spitsbergen (SPITS), the seismological station at Hornsund (HSPB) and the seismological station on Hopen Island (HOPEN). Black lines represents the main area of which the seismological stations receive energy from.

between two points and hence an inertial seismometer is more sensitive to earthquakes. But for low frequency signals maintaining the inertial reference become more difficult. To be able to digitize and record the measurements, recorders and digitizers are fit together with the seismometer to be able to record and send the measuremts as digitized files. This will not be further explained here, but for more information about seismic stations see Haskov and Alguacil (2004)

The frequency range of seismometers is designed to fit the type of measurements that the station is designed for. Common sensors are: broadband sensors, short-period sensors and strong motion sensors/accelerometers. Short-period sensors cover higher frequency ranges, e.g. above 1 Hz. Strong motion sensors measure large amplitude high frequency events and the frequency ranges are often from 0.1 Hz and up to 100 Hz. Broadband sensors have a wider frequency range and do often cover the classical short-period and long-period bands, typical frequency range of broadband sensors can be from 10mHz to 50 Hz e.g., (Haskov and Alguacil, 2004).

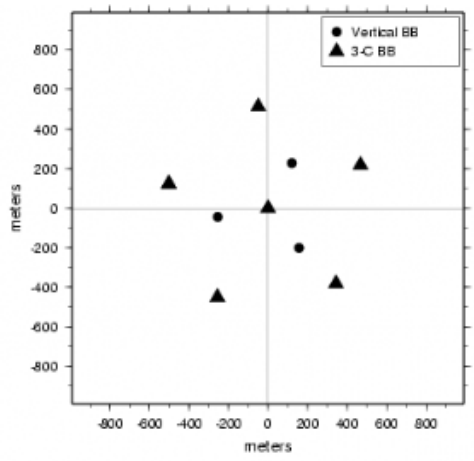

Figure 1.2: SPITS array configuration, the filled black circles are vertical stations while the black triangles are 3-component broadband stations, figure from NORSAR (2015).

A seismic array is an array of seismic stations deployed in a way that makes it possible to infer characteristics of the seismic wavefield at any point between stations or close to stations in the array by studying the waveforms recorded at the stations (Schweitzer et al., 2012). Arrays are designed to monitor seismicity on local, regional and world-wide scale. A single seismic station can measure the ground movement, but compared to an array the ability to locate seismic events and detect low-magnitude events is lower. The size of an array can be defined by its aperture. Aperture is the largest possible distance between two seismic stations in the array (Schweitzer et al., 2012). Arrays with large aperture, ~100 km, are used to record and locate teleseismic events (Rost and Thomas, 2002). While smaller aperture arrays can detect and study P- and S-waves at regional distances due to similar waveforms.

1.3.1 SPITS Array

The SPITS seismological array was installed in November 1992 and is operated by NORSAR. The array is located in Adventdalen, Spitsbergen (78.1777°N/16.3700°E). SPITS is a type-9-element-array (Schweitzer et al., 2012) with a central station SPA0 and two rings with three and five stations, respectively, see **Figure 1.2**. With an aperture of ~1 km Rost and Thomas (2002) defines it as a small/very small aperture array.

The array was installed with nine short-period vertical seismometers with a sampling frequency of 40 Hertz (Hz) but updated in 1994 and in 2004 (Gibbons et al., 2011). Today, the array consists of three-component broadband sensors at six of the nine stations with a sampling frecuency of 80 Hz. The array has kept the original array geometry.

1.3.2 HOPEN Station

The HOPEN seismological station is located on the 47 km² large Island of Hopen south-east of Spitsbergen (76.50840°N/25.01090°E). The station was installed in October 2007 with a three component broadband sensor (Schweitzer et al., 2009) and it is operated by the University of Bergen. The data from HOPEN used in this thesis has a sampling frequency of 100 Hz.

Due to short distance from the open sea to the seismological station the main source of seismic noise comes from swell (ocean waves) and wind.

1.3.3 HSPB Station

The HSPB broadband seismological station is operated by the Polish Polar Station in Hornsund, southern Spitsbergen (77.00188°N/15.53318°E). It was installed by NORSAR and the Polish Academy of Sciences in September 2007 with a three-component Streckeisen STS-2 seismometer and a Güralp CMG-DM24 data logger (Wilde-Piorko et al., 2009). The instrument was installed on a concrete plinth, where the casing protects against tilt, air pressure and temperature changes. The station is only a couple of hundred meters from the open sea and the main source of seismic noise comes from swell and wind.

Data from this station are sampled at 1, 0.1 and 0.001 seconds, or 1, 10 and 100 Hz, respectively (Wilde-Piorko et al., 2009). The data from HSPB used in this thesis has a sampling frequency of 100 Hz.

1.4 Geological background

The Barents Sea, named after the Dutch navigator and explorer Wilhelm Barents, is an epicontinental sea situated in the north-western corner of the Eurasian continental shelf e.g., north of Norway and Russia (Smelror et al., 2009). It is bounded by the Norwegian - Greenland Sea in the west, Franz Josef Land in the north and Novaya Zemlya in the east. The Barents Sea itself covers an area of 1.3 million square kilometers and is considered as a part of the Arctic Ocean (Worsley, 2008).

As an area at the corner of the Eurasian continent the Barents Sea has been affected by continent collisions, major periods of rifting and subsequent formation of the Arctic Ocean and the Norwegian-Greenland Sea. Post-Caledonian rifting periods led to development of passive margins in the west and north, while eastern areas were more prone to complex tectonic events that eventually formed Novaya Zemlya and the Timan-Pechora Basin (Faleide et al., 2008; Roberts and Sidlecka, 2002). Three orogenic phases have been described by Gudlaugsson et al. (1998) and Marello et al. (2013): the Timanian-, the Caledonian- and the Uralian orogeny. In addition numerous periods of rifting took place and induced the complex intracratonic setting found in the region today, see **Figure 1.3**.

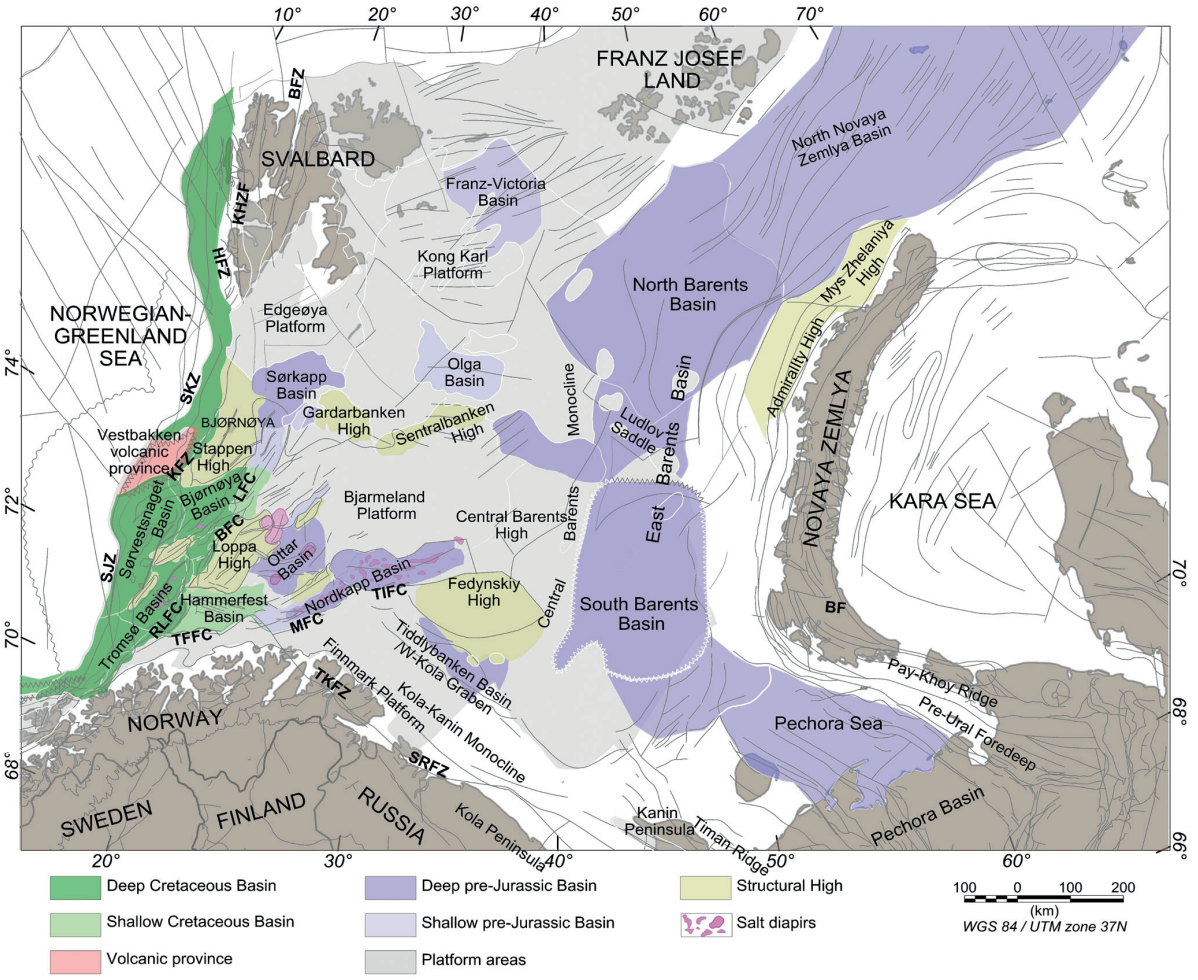

Figure 1.3: Structural setting, basins and physiographic domains in the Barents Sea from Marello et al. (2013). The abbreviations denote the major fault structures: BF, Baidsratsky Fault Zone; BFC, Bjørnøyrenna Fault Complex; BFZ, Billefjorden Fault Zone; HFZ, Hornsund Fault Zone; KFZ, Knølegga Fault Zone; KHFZ, Kongsfjorden–Hansbreen Fault Zone; LFC, Leirdjupet Fault Complex; MFC, Maasøy Fault Complex; RLFC, Ringvassøy–Loppa Fault Complex; SJZ, Senja Fracture Zone; SKZ, Sørkapp Fault Zone; SRFZ, Sredni–Rybachi Fault Zone; TIFC, Thor Iversen Fault Complex; TFFC, Troms–Finnmark Fault Complex; TKFZ, Trollfjorden–Komagelva Fault Zone.

1.4.1 Tectonic evolution

Timanian Orogeny

During Neoproterozoic the megacontinent Rodinia experienced a major period of rifting and subsequent plate separation, which formed the continents Baltica, Laurentia, Siberia and Avalonia (Shipilov and Vernikovsky, 2010). Baltica was surronded by oceans, the Iapetus Ocean between Baltica and Laurentia, the Æris Sea between Baltica and Siberia and the Tornquist Sea between Baltica and Avalonia (Torsvik et al., 1996). In Mid-Late Riphean the N-E margin of Baltica experienced crustal extension which led to the initiation of a rifted passive margin (Roberts and Sidlecka, 2002; Olovyanishnikov et al., 2000). During Vendian the tectonic regime changed from an extensional to a compressive phase initiating the Timanian Orogeny (Olovyanishnikov et al., 2000). In Late Precambrian to early Cambrian the Riphean to early Vendian ocean floor, island arc rocks, sedimentary rocks, plutons and crystalline basement were involved in a contraction collision leading to the formation of complex terranes against the northeastern margin of Baltica (Roberts and Sidlecka, 2002). The Timanian terranes extend from Northwest Russia and all the way to the northeastern part of the Varanger Peninsula in Finnmark. Although their extent is poorly understood, the terranes are also found under the Timanian-Pechora basin and in parts of the Barents shelf (Olovyanishnikov et al., 2000; Roberts and Sidlecka, 2002).

Caledonian Orogeny

A complex sequence of southeast directed convergent movements culminated into the closure of the Iapetus Ocean and the subsequent continent collision between Laurentia and Baltica and the formation of Laurussia in late Silurian to early Devonian (Johansen et al., 1994; McKerrow et al., 2000; Ritzmann and Faleide, 2007). During the collision the Baltic plate subducted beneath the Laurentian plate, and the interaction between the two plates resulted in the formation of the Caledonian mountain chain, which extends from east North-America over the Bristish Isles and Scandinavia and Greenland and up to Svalbard (Torsvik et al., 1996). The main phase of the orogeny in Scandinavia is the Scandian event, 420-400 Ma (Spengler et al., 2009). In the western Barents Sea the basement was consolidated during the Caledonian orogeny, and the structural grains from the orogeny are believed to have influenced later structural developement, with a general N-S Caledonian fold and thrust belt (Gudlaugsson et al., 1998; Ritzmann and Faleide, 2007).

At this time, the western Barents Sea was situated on a major tectonic junction with one Caledonian branch striking northeastly, probably a continution of the Scandinavian-Greenland arm and a second Caledonian branch striking towards the Svalbard Archipelago and north-east Greenland (Gudlaugsson et al., 1998; Ritzmann and Faleide, 2007). Gud-

laugsson et al. (1998) speculated whether these two brances could have led to an independent microcontinent called Barentsia. However recent models from high-resolution areomagnetic data have suggested a tectonic scenario, where arc-shaped Caledonian nappes close to the Varanger Peninsula have a NE-SW orientation, while the nappes reorientate to a NNW-SSE/NW-SE trend across the Nordkapp Basin and the Bjarmeland Platform (Gernigon and Brönner, 2012).

Uralian Orogeny

Following the Caledonian Orogeny another orogenic period was initiated in Early Carboniferous. Transpressional reactivation of existing faults in the eastern part of the Barents Sea initiated a tectonic shift and resulted in the closure of the Uralian Ocean by eastward subduction beneath the Siberian craton (Cocks and Torsvik, 2006). The collision between Laurussia and the western Siberian plate resulted in the supercontinent Laurasia. Subsequently an active margin propagated northwards and reached the eastern Barents Sea in Late Carboniferous - Early Permian (Johansen et al., 1994).

Late Palaeozoic and Mesozoic rifting

From late Palaeozoic throughout Mesozoic extensional tectonics dominated in the Barents Sea. It is believed that the structural grains from earlier collision events have had a cumulatice effect on the location, orientation and geometry of the sedimentary basins formed in Late Palaeozoic to Mesozoic (Gudlaugsson et al., 1998; Faleide et al., 1993). There is counsensus about two main extensional phases in this period; Early-Mid Devonian to Early-Mid Carboniferous and Permian to Early Triassic (Gabrielsen et al., 1990).

Extension and formation of large basins occured after the Caledonian orogeny in Devonian time (Gudlaugsson et al., 1998). A gravitational collapse with both back-sliding and low angle ductile detachments occured. Post-Caledonian extensional collapse in the western Barents sea was proposed by Gudlaugsson et al. (1998), and Johansen et al. (1994) argue for graben formation in the southwestern Barents Sea. Onshore Devonian grabens on Svalbard have been interpreted as post-orogenic basins by several authors (Larsen et al., 2005; Gabrielsen et al., 1990). Both onshore and offshore observations of the stratgraphic record reflect a regional extensional regime in this period (Gabrielsen et al., 1990; Johansen et al., 1994). Large interior sag basins developed as the response of regional subsidence and have been interpreted as the first stage in the rift system development of the southwestern Barents Sea. Gudlaugsson et al. (1998) proposed that this rift system inherited the fan-shaped structural grains from the Caledonides.

In Early Permian a large shallow-marine carbonate platform had evolved in the Barents and Kara Sea region, eustatic sea-level changes occurred and during sea-level high the entire

shelf was flooded and carbonates were deposited. During Permian several transgressions of the shelf occured and by the end of Permian an extensive marine shelf covered the entire Barents and Kara Sea region (Worsley, 2008). In the western Barents Sea subsidence and salt tectonics dominated throughout the Triassic (Gabrielsen et al., 1990). The thickness of the Triassic sediments found on Svalbard is 250-1200 meters and 2000-3000 meters thick in the platform areas in the western Barents Sea (Mørk et al., 1982)

In the western Barents Sea rifting and block tilting occured in Mid-Jurrassic and increased throughout the Jurassic and into the early Cretaceous (Johansen et al., 1994). Some local erosion on structural highs occured removing Jurassic and locally upper Triassic strata, well defined depocenters in adjacent basins were created as a response to the rifting and block tilting (Faleide et al., 1993). In Late Jurassic - Early Cretaceous the rifting commenced and induced NE-SW trending structures in the Northeast Atlantic, such as the Bjørnøya Basin (Worsley, 2008). Cretaceous subsidence and rifting were more moderate in the eastern Barents Sea (Johansen et al., 1994). The Cretaceous rifting in the western Barents Sea led to complex structures and Gabrielsen et al. (1990) found indications of local early Cretaceous inversion.

Rifting prevailed into the Early Cretaceous and opening of the Amerasian Basin in the Arctic Ocean caused uplift and tilting in the northern parts of the Barents and Kara Sea region (Johansen et al., 1992). At this time the Barents Sea was an open shelf only with structural highs and platforms separating the basins (Smelror et al., 2009). Unlike the southwestern Barents Sea the platform areas in the northern Barents Sea did not experience that much late Mesozoic tectonism (Breivik et al., 2005). In Early Cretaceous the small tectonic movements in the north were accompanied by volcanic activity (Grogan et al., 1998). This volcanic activity has been considered as part of the High Arctic Large Igenous Province (HALIP). The HALIP linked Greenland, Svalbard Franz Josef Land and adjacent shelf areas together before continental breakup and ocean basin formation (Maher, 2001). The Early Cretaceous HALIP may have created underplating in the crust and upper mantle. In case of relatively thick lithosphere ultramafic primary magmas would solidify below the Moho. If the lithosphere had been significantly eroded we may expect mafic magma to be emplaced and solidify withing the lower crust (Dörr et al., 2013).

Cenozoic

The development of the western Barents Sea margin occured in the Cenozoic as a response to the main continental break-up in earlies Eocene time and subsequent seafloor spreading (Johansen et al., 1992). In western Spitsbergen a fold and thrust belt developed as a response to the opening of the Norwegian-Greenland Sea in Paleogene. The origin of this fold and thrust belt has been related to the evolution of a dextral transform fault system between Greenland

and Spitsbergen Blinova et al. (2012, and references therein).

In Late Cenozoic the westernmost part of the Barents Shelf was uplifted and ~ 1 kilometers of sediments were removed (Worsley, 2008). The uplift of the western Barents Shelf and opening of the Fram strait has been related to mantle upwelling and thermal erosion of the lithosphere beneath the Svalbard Archipelago (Dörr et al., 2013).

2 Data Processing

Seismological networks monitor seismicity on a local, regional and world wide scale, this means that hundreds of events are recorded on the seismological stations in this study. Automatic routines are set up at NORSAR Data Processing Center (NDPC) to detect and process events (Ringdal, 1999). The routines at NDPC do some initial processing of detected events, but for further analysis more processing should be performed on the data.

2.1 Processing

2.1.1 Filtering

Data from a seismic station are the sum of ground motion generated from a natural or man-made source including the effect of the propagation path, recording instrumentation and noise. Noise is considered the unwanted part of the ground movements, e.g. the definition of noise depends on the available data, aim of the study and method of analysis (Aki and Richards, 2002).

Measured data can be expressed as a linear system, where the input data is the seismic source and the output data is the source combined with the effects of propagation path and noise. Fourier analysis is a natural tool to study linear systems since it has the same linear properties. A linear system is defined by its response to a delta function in time, a delta function, $\delta(t)$, is the limit of a sequence of continuous functions with a corresponding impulse response $f(t)$. In the frequency domain the delta function give rise to the transform of the impulse response $F(\omega)$, also called transfer function. The derivation below follows Pujol (2003) and Stein and Wysession (2013). An arbitrary signal, $x(t)$ has a transfer function given by:

$$Y(\omega) = X(\omega)F(\omega) \tag{2.1}$$

Where $X(\omega)$ is the transform of $x(t)$ and $F(\omega)$ is the transform of $f(t)$. The time domain equivalent can be found by inverting **Equation 2.1**:

$$y(t) = \frac{1}{2\pi} \int_{-\infty}^{\infty} X(\omega)F(\omega)e^{i\omega t}\, d\omega \tag{2.2}$$

To see the relation between the input function, transfer function and output function in the time domain, one can express $X(\omega)$ and $F(\omega)$ in the time domain and insert it into **Equation 2.2**.

$$y(t) = \frac{1}{2\pi} \int_{-\infty}^{\infty} \left[\int_{-\infty}^{\infty} x(\tau)e^{-i\omega\tau}\, d\tau \right] \left[\int_{-\infty}^{\infty} f(\tau')e^{-i\omega\tau'}\, d\tau' \right] e^{i\omega t}\, d\omega \tag{2.3}$$

Rearranging the terms and using the inverse transform of the delta function and eliminating

the frequency integral yields:

$$y(t) = \int_{-\infty}^{\infty} \left[\int_{-\infty}^{\infty} f(\tau')\delta(t - \tau' - \tau)\, d\tau' \right] d\tau \tag{2.4}$$

Integrating the inner integral in **Equation 2.4** and employing the sifting property of the delta function yields:

$$y(t) = \int_{-\infty}^{\infty} x(\tau) f(t - \tau)\, d\tau \tag{2.5}$$

This integral, **Equation 2.5** can in the time domain be expressed as the convolution of $x(t)$ and $f(t)$.

$$y(t) = x(t) * f(t) \tag{2.6}$$

The relation between operations in the time domain and the frequancy domain for linear systems are seen from **Equation 2.1** and **2.6**. Multiplication in the frequency domain corresponds to convolution in time domain and reverse. The response of a system for an input signal is defined by the impulse response in either the time or the frequency domain. This can be quite convenient in signal filtering, where it is possible to define bandpass filters and simply multiply the fourier transform of the signal with the filter and subsequently transform the spectrum back to the time domain. It is also possible to filter the signal in thee time domain, but filters are often easier to define in the frequency domain and transformation and inverse transformation are computational fast (Stein and Wysession, 2013).

2.1.2 Cutting

Some of the noise recorded on seismological stations cannot be removed by filtering itself, and cutting has to be performed. Careful removal of abnormal measurements is crucial to optimize the signal-to-noise ratio (SNR).

2.1.3 Coordinate transformations

The three component data ZEN are not aligned towards the source and various types of wave phases will be found on the components. Aligning the coordinate system towards the source will result in different types of wave phases on each of the components (Stein and Wysession, 2013). Both 2D and 3D rotation is possible. 2D rotation alignes the east-west and north-south components in transverse and radial direction. While a 3D rotation alignes the coordinate system in the direction of P-, SV-, and SH-wave propagation. Rotating ZEN to ZRT with an appropriate azimuth (Θ) yields:

$$\begin{bmatrix} Z \\ R \\ T \end{bmatrix} = M_{ZRT} \begin{bmatrix} Z \\ E \\ N \end{bmatrix} \tag{2.7}$$

Where M_{ZRT} represents the rotation matrix:

$$M_{ZRT} = \begin{bmatrix} 0 & 0 & 1 \\ \cos\Theta & \sin\Theta & 0 \\ -\sin\Theta & \cos\Theta & 0 \end{bmatrix} \tag{2.8}$$

Rotation to align the coordinate system with the three wave phases P, SV and SH can be done by rotating ZEN to LQT. L is aligned in the P-wave phase movement, Q is aligned in the SV-wave phase movement and T is aligned in the SH-wave phase movement. This means that the majority of the P-, SV- and SH- energy are measured on L, Q and T, respectively. Rotating ZEN to LQT with its appropriate incidence angles i, and backazimuth Φ transforms the 3-component ZNE station to an optimized 3-component LQT station and it can be written as:

$$\begin{bmatrix} L \\ Q \\ T \end{bmatrix} = M_{LQT} \begin{bmatrix} Z \\ E \\ N \end{bmatrix} \tag{2.9}$$

Where M_{LQT} represents the rotation matrix:

$$M_{LQT} = \begin{bmatrix} \cos i & -\sin i \sin\Phi & \sin i \cos\Phi \\ \sin i & \cos i \sin\Phi & \cos i \cos\Phi \\ 0 & -\cos\Phi & \sin\Phi \end{bmatrix} \tag{2.10}$$

The incidence angle is rather difficult to determine since the incoming energy depends on the local velocities just beneath the seismic station. Areas of local heterogeneity can occur and this will make it difficult to determine the incidence angle, in addition the incidence angle is frequency dependent.

2.1.4 Beamforming

The idea behind beamforming is quite simple, summing coherent parts of a signal will increase the SNR, while incoherent part of the is suppressed. Beamforming is often only performed for a seismic array but in cases where the source parameters are known and the waveforms are assumed simple it is possible to utilize events as source beams (Krüger et al., 1993). E.g., it is possible to create three kind of beams: source-, receiver- and double-beam. The optimal beam is the double-beam, where individual traces from both source and receiver domain are stacked together after applying a travel-time correction.

To correct for differences in the travel-time between the different stations these parameters have to be known:

- Position vector: $\mathbf{r}_j = f(x, y, z)$.

- Backazimuth Φ, is the angle which the wavefront approaches the array with measured between geographical north and the epicenter in [°], and azimuth(Θ) is given by: $\Theta = \Phi \pm 180$[°].
- Crustal velocity immediately below the array v_c measured in [km/s].
- Angle of incidence i measured in [°].
- Absolute value of the apparent velocity vector, v_{app} for a plane wave crossing the array [km/s].
- Slowness vector s, $s = 1/v_{app}$, [s/km].
- Elevation of station sites, z [km].

Summing traces together without any kind of travel-time correction will result in destructive interference for the event. It is neccesary to correct for differences in travel-time due to offset changes, station position and elevation. For an active source setup the travel-times changes with offset and the delay in travel-time, $\Delta(t)$ can be found by taking the change in offset and divide by the apparent velocity, v_{app}. Number of traces that should be stacked together depend on the survey, but the difference in travel-time should not be larger than $1/4$ of a wavelength (Rost and Thomas, 2002). On the receiver site traces with the same component from all stations are summed up at a reference station.

The time delay depend on the relative station position with respect to the reference station. Time delay for stations in the same horizontal plane depend on the wavefront parameters (Φ, v_{app}). The derivation below follows Schweitzer et al. (2012). The time delay is expressed as:

$$\tau_j = \frac{-x_j \cdot \sin\Phi - y_j \cdot \cos\Phi}{v_{app}} \tag{2.11}$$

Or it can be vectorized as:

$$\tau_j = \boldsymbol{r}_j \cdot \boldsymbol{s} \tag{2.12}$$

Including station elevation the time delay is defined as:

$$\tau_j = \frac{-x_j \cdot \sin\Phi - y_j \cdot \cos\Phi}{v_{app}} + \frac{z_j \cdot \cos i}{v_c} \tag{2.13}$$

The time delay correction for stations with elevation differences depend on the crustal velocities v_c in addition to (Φ, v_{app}). It can either be negative or positive, positive time delay corresponds to an advance of the signal while a negative time delay correspons to a delay (Schweitzer et al., 2012). Travel-time correction is a crucial step in beamforming since the traces will be corrected and summed togeter, if the travel-time correction is incorrect signal onsets will destructively interfere and the SNR decreases. In **Figure 2.1** filtered data, source-beam and the corresponding double-beam have been plotted, note how the SNR increase and how the max amplitude decrease.

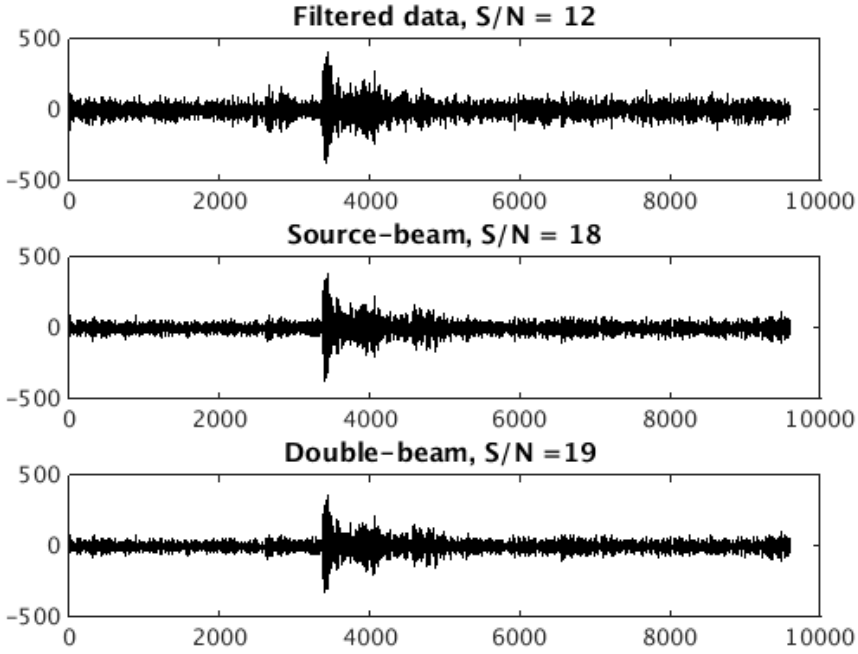

Figure 2.1: Filtered data, source-beam and double-beam, the signal-to-noise ratio increase with beamforming while the maximum trace amplitude decrease. Four traces were summed together at the source-beam and three stations were summed togheter to create the double-beam.

To create a beam the different recordings at all stations should be summed at the reference station applying their corresponding time delay, **Equation 2.11** or **2.13**. The beam of an entire array can thus be expressed as:

$$b(t) = \frac{1}{M}\sum_{j=1}^{M} w_j(t + \boldsymbol{r}_j \cdot s) = \frac{1}{M}\sum_{j=1}^{M} w_j(t + \boldsymbol{\tau}_j) \tag{2.14}$$

Where $w_j(\boldsymbol{r}_j, t)$ represents the data of the seismogram from site j at time t and M are the number of stations. **Equation 2.14** represents the operation of summing the recordings with proper time delays and are called beamforming.

2.1.5 Tau-p transform

Mapping data in the $\tau - p$ domain is a convenient way of transforming and displaying seismic data since $\tau(p)$ describes each point on the traveltime curve $T(x)$. Hence $t - x$ data can easily be represented in the $\tau - p$ domain. Slant-stack is a linear transformation that transforms the entire wavefield in $t - x$ to the $\tau - p$ domian. The transform can be expressed as:

$$S(\tau, p) = \int_{-\infty}^{\infty} P(\tau + px, x)dx \tag{2.15}$$

Where P represents the sampled wavefield and S the transformed wavefield. The slant stack, **Equation 2.15** can be performed in the frequency domain, applying the Fourier central slice

theorem:

$$S(\omega, p) = P(\omega, -2\omega p) \tag{2.16}$$

Representing data in the $\tau - p$ can be convenient since different arrivals are located differently in the $\tau - p$ domain. In addition offset hyperbolas will appear as ellipses in the $\tau - p$ plane. In order to minimize artifacts on the slant-stack and produce reasonable images Clayton and McMechan (1981) mention two important factors; dense sampling of the offset and coherency of source signature in case of multiple shots.

2.2 Seismic data management and processing implementation

Raw-data from SPITS, HOPEN and HSPB were retrieved from the NORSAR database by Johannes Schweitzer. He created *.gse* files from the data and the corresponding UKOOA files from the surveys. From here on, the description "raw-data" will be used for the data retrieved from the NORSAR database. Each trace in the *.gse* files has an overlap with the neighbouring traces of ~10 seconds.

The data files were then converted and imported into MATLAB R2014b and processing routines were set up. The tau-p extrapolated wavefields were calculated by the slant-stack. The slant-stack code are written by Shauna Oppert and Marco Perez but is originally a modified version of XinXiang Li's code from 1996 (Oppert and Perez, 2001). The slant-stack transformation is performed as a linear transform in the Fourier domain. During the transformation the sampling rate is changed to 4 ms.

2.3 Processing results

The SPITS array has 6 3-component broadband sensors and 3 vertical broadband sensors. Downtime on the stations occur and data recieved from NORSAR for the stations for $P1_s$ and $P2$ can be seen in table 2.1.

$P1_s$, $P1_h$ and $P1_{ho}$ had 585 traces before processing, and $P2$ had 827. A complete collection of the different offset-ranges can be found in table 2.2. Due to the source-receiver geometry $P1_s$ and $P1_h$ are sampled with decreasing offset, while $P2$ and $P1_{ho}$ are sampled with increasing offset. Nevertheless time-offset plots in this thesis are plotted with increasing offset.

SPITS P2

The raw-data for SPA1 BZ $P2$ can be seen in **Figure 2.2**. Raw-data from all components are dominated by noise and occational large-amplitude traces. The very large-amplitude noise at an offset of 265 kilometers (km) is present on all components and on all stations, i.e., it is another seismic event.

Table 2.1: Stations at SPITS that have data from the two profiles are ticked off. 3-C BB are 3-component broadband stations, V BB are vertical broadband stations.

Stations	$P1_s$	$P2$
SPA0, 3-C BB	✓	
SPA1, V BB	✓	✓
SPA2, V BB		✓
SPA3, V BB	✓	
SPB1, 3-C BB	✓	
SPB2, 3-C BB	✓	✓
SPB3, 3-C BB	✓	✓
SPB4, 3-C BB	✓	
SPB5, 3-C BB	✓	✓

Table 2.2: Offset data for all the different profiles.

Profile	Station	Offset (km)	
$P1_s$	SPA0	160.01 - 197.55	224.61 - 261.11
$P1_s$	SPA1	160.32 - 197.75	224.76 - 261.21
$P1_s$	SPA3	160.04 - 197.72	224.82 - 261.36
$P1_s$	SPB1	160.17 - 197.43	224.38 - 260.79
$P1_s$	SPB2	159.25 - 196.71	223.76 - 260.26
$P1_s$	SPB3	159.40 - 197.16	224.32 - 260.92
$P1_s$	SPB4	160.58 - 198.32	225.43 - 261.97
$P1_s$	SPB5	160.86 - 198.30	225.30 - 261.74
$P1_h$	HSPB	57.05 - 127.09	164.78 - 210.78
$P1_{ho}$	HOPEN	40.47 - 72.73	106.89 - 174.51
$P2$	SPA1	252.67 - 416.96	
$P2$	SPA2	252.70 - 416.97	
$P2$	SPB2	252.43 - 417.70	
$P2$	SPB3	253.42 - 417.69	
$P2$	SPB5	252.89 - 417.20	

The vertical component has coherence of amplitudes in the offset-range 270-417 km and time-range ~40-60 seconds (s). This coherency appear on all the vertical $P2$ components.

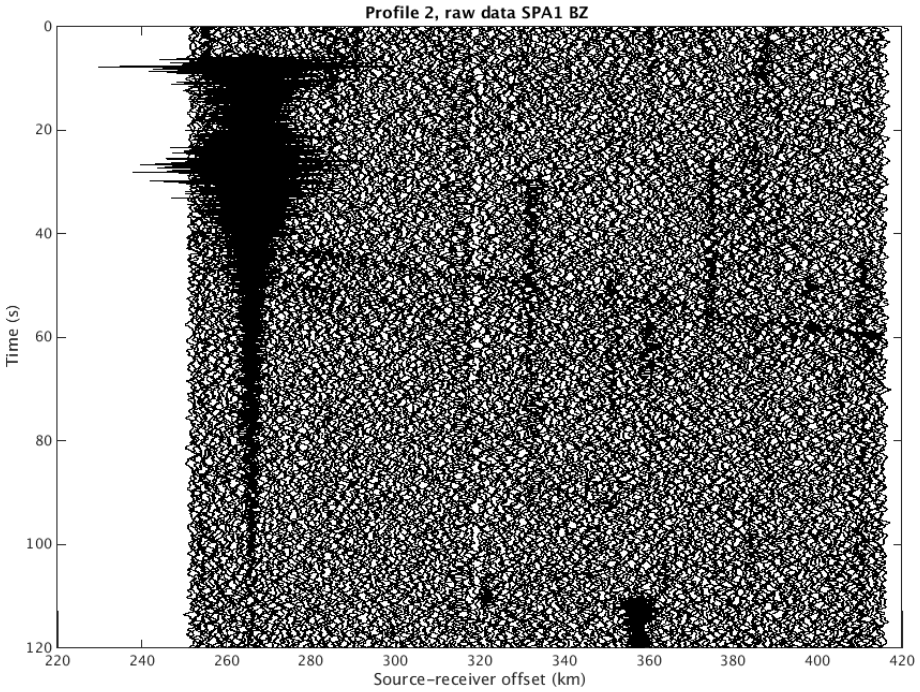

Figure 2.2: Raw data of $P2$ SPA1 BZ, scaled by a factor of 0.001 and plotted every 3rd trace.

SPITS P1

On all the vertical components at $P1_s$ coherency of amplitudes occur in the offset-range of 165-196 km and time-range 30-36 s, see **Figure 2.3**. On SPB1 and SPB4 the coherency is not seen in the offset-range 160-175 km due to large amplitude traces. Large amplitude traces occur at 180 km on all components and all stations. The east-west and north-south components of SPA0, SPB1, SPB3 and SPB5 have the same amplitude throughout the entire line, and the only high amplitude traces can be found at an offset of 180 km. All three components of SPB2 have high amplitude traces at 248-250 km offset, while all three components of SPB4 have high amplitude traces in the ranges: 160-180, 239-249 and 257-261 km.

At an offset of ~195 km there were two traces of 0 data, see **Figure 2.3**.

HSPB

The vertical component of HSPB has similar amplitudes in the first part of the line (57-127 km), only three large amplitude events stands out at 90, 98 and 110 km offset. The second part of the line has no high amplitude events, here the amplitudes are similar throughout the line, but higher than the first part, see **Figure 2.4**. On the horizontal components, HE and HN, the amplitude vary more throughout the lines, see **Figure A.1** and **A.2**. Here oscillations within the waves occur at all offsets and through all traces. In the small offset part of HN

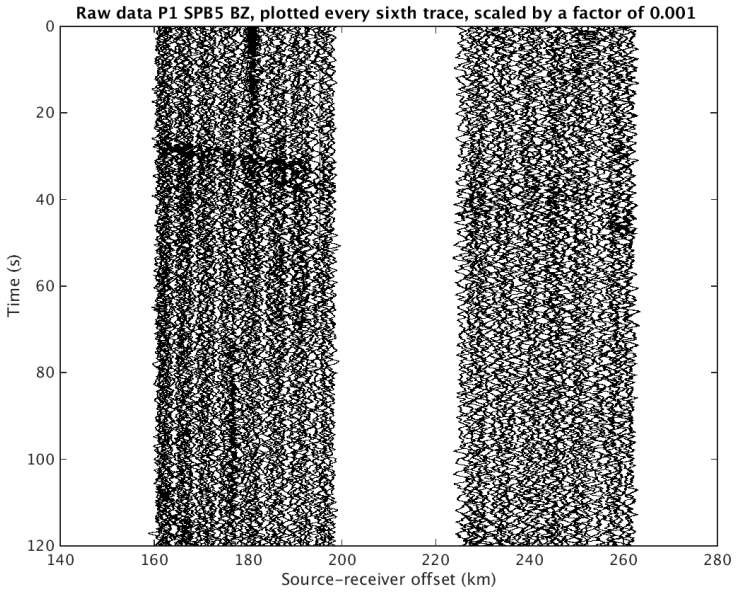

Figure 2.3: Raw data of Spits P1 SPB5 BZ, scaled by a factor of 0.001 and plotted every 6th trace.

traces with long periods occur, the small oscillations are still present but the period of the wave seemed to have become very large. This phenomenon also occurs on the large offset part of HE.

HOPEN

Raw data from HOPEN can be seen in **Figure A.4**, **A.3**, **2.5**. All three components have no cohereny throughout the lines. The vertical (HZ) and east-west (HE) components are similar, on the small offset part of the line the amplitudes are higher than on the large offset part and there are no high or very-high amplitude noise present. The amplitudes on HE are generally higher than on HZ. The north-south component (HN) has a lot of high and very-high amplitude noise. **Figure A.4** has been scaled by a factor of 0.0001, ten times more than HZ and HE.

2.3.1 Filtering

A Butterworth bandpass filter was applied to the data, the frequency range was determined by testing different ranges and $P1_s$ and $P2$ ended up with a frequency range of $5-15$ Hz and filter order $N = 5$. HSPB and HOPEN were filtered with a 3-6 Hz Butterworth bandpass filter, HSPB had a filter order of $N = 5$, while the filter order for HOPEN were $N = 3$. Coherency of amplitudes are from here on described as arrivals or onsets, P_n is a P-wave refracted in the upper mantle, P_g is used for all P-waves in the crust and S is used for all S-waves.

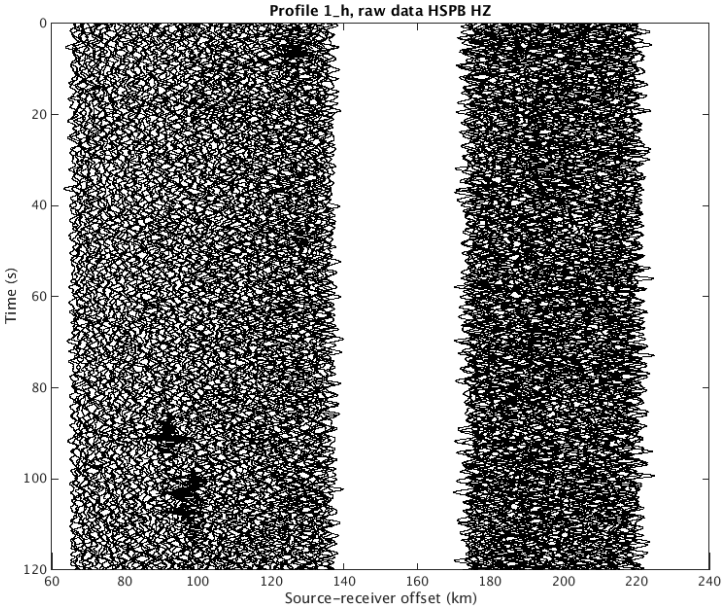

Figure 2.4: Raw data $P1_h$ HZ, scaled by a factor of 0.001 and plotted every 4th trace.

SPITS P2

After filtering $P2$, two onsets are visible. The first onset starts at 39.42 s and 256 km, it is observed at all offsets but with varying amplitude, see **Figure 2.6**, and lasts until t = 59.35 s and 418 km. A second onset comes in 6 s after the first onset and is well defined until an offset of 290 km. On all the vertical (BZ) and east-west (BE) components the amplitude increase in the range 280-290 km, before it decreases and disappears. The first onset is seen on all components, it is most well defined on BZ, and least on the north-south component (BN). The second onset occurs on BZ and BE components. Some og the high and very-high amplitude traces have not been removed by filtering.

SPITS P1

All the filtered vertical components (BZ) of $P1_s$ have a clear first onset starting at 26.19 s and ranging from an offset of 160 km to 190 km, on SPA1 the first onset can be seen at an offset of 210 km, see **Figure 2.7**. Another onset ranging from 230-260 km offset, starting at 37.5 s is visible on all stations except SPB4. On the vertical component of SPB4 noise is seen on large offsets and from 210-260 km nothing else than noise can be seen. On the vertical components from SPA3 and SPB4 an onset ~20 seconds below the first onset in the offset-range 160-190 km occurs.

On the horizontal components the first onset occurs at 26.19 s and ranges from 160-190 km, here BN have a more well defined first onset than BE. The onset ~20 seconds after the

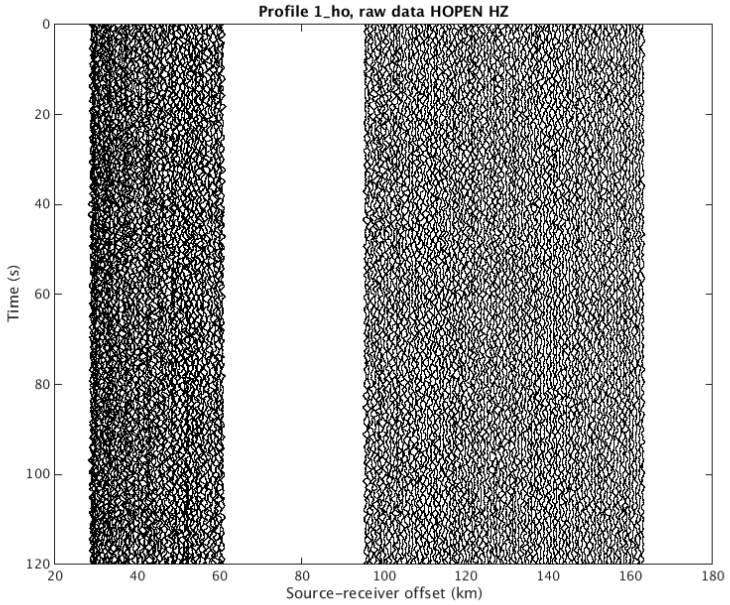

Figure 2.5: Raw data $P1_{ho}$ HZ, scaled by a factor of 0.001 and plotted every 4th trace.

onset at 26.19 s occurs on all the horizontal components, but most well defined on BE. An onset ranging from 230-260 km and 37.5-40 s occurs on SPB1 BN and SPB3 BE. From an offset of 255-260 km and ~39-40 s another onset occurs on SPB5 BN, SPB5 BE, SPB4 BN and SPB3 BE, see **Figure A.9**.

HSPB

The high amplitude noise on HSPB at ~90 and 110 km is still visible on all the components after filtering. An onset ranging from 60-126 km and 16-25 s can be seen on all components, most well defined on the horizontal component and least on the northern component. On the vertical component another onset occurs at 165-206 km and 29-34 s, this onset is contaminated by noise. Only noise is visible on the larger offsets of the northern and eastern components, **Figure A.14** and **A.15**.

HOPEN

At the vertical and east-west components of HOPEN the small offset part of the line are still more noise contaminated than the large offset part, see **Figure 2.9** and **A.16**. At the vertical component three onsets occur, two at small offsets: 40-44.6 km and 5.9-7.5 s, and 40-48 km and ~10-14 s. The third onset occurs at 107-167 km and 20-29 s. The east-west component has two onsets, one from 40-70 km and 10-23 s and a second one at 139-165 km and ~42-53 s. The north-south component of HOPEN has still a lot of high-amplitude noise after filtering.

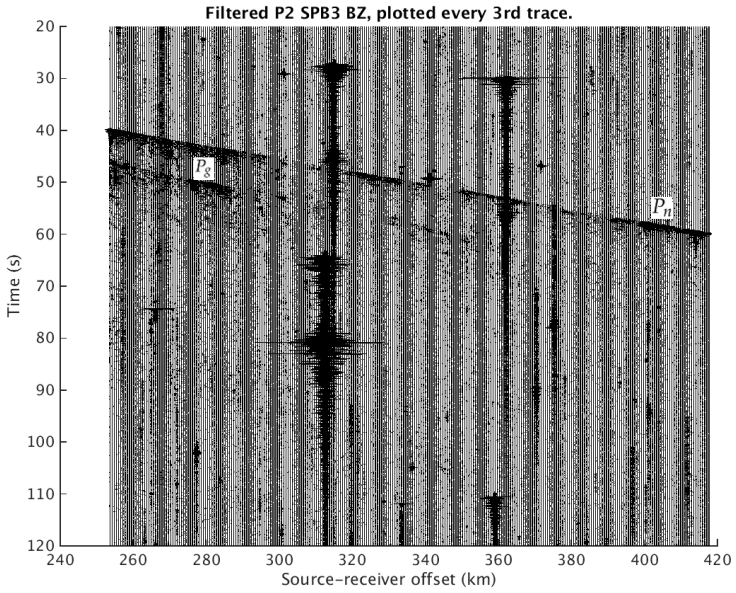

Figure 2.6: $P2$ SPB3 BZ, filtered and uncut. Scaled by a factor of 0.001 and plotted every 3rd trace.

On the small offset part of the line the traces are more noisy than the latter part of the line.

2.3.2 Cutting

High amplitude events that did not coincide with the data trend were cut away. $P2$ had originally 827 traces, 338 were cut away and the total number of traces after the cutting were 489. It is evident that the amplitude of the first two first onsets of $P2$ varies with offset.

$P1_s$ had 585 traces before cutting. Both high amplitude events and amplitudes that did not match the onsets were dominating before cutting. The large amplitude events occured on both small and large offsets, but noise with smaller amplitude dominated at smaller offsets and all data from 160 to 169 kilometers were cut away due to this. Total number of traces cut away in $P1_s$ were 227. Total number of traces for $P1_s$ after cutting were 358. The noise conditions on all the stations except SPB4 were quite similar so the same traces were cut away for all the stations.

$P1_h$ had 585 traces before cutting. Both the noise on the large offset and the high amplitude events were cut away, in total 412 traces were cut from each component leaving 173 traces. Traces with very large amplitudes were removed, but the majority of traces cut away came from large offsets.

$P1_{ho}$ had 585 traces before cutting, 28 traces were cut away leaving a 557 traces. Both traces from large and smaller offsets were removed.

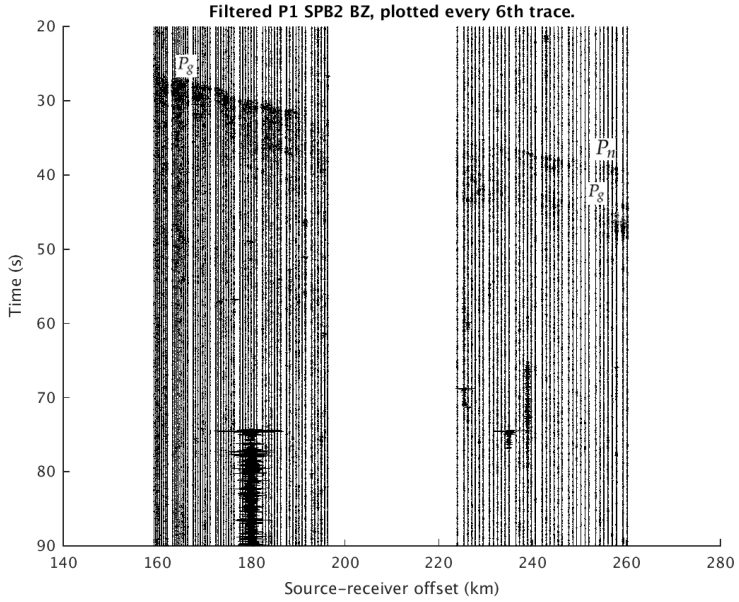

Figure 2.7: $P1_s$, SPB2 BZ, filtered and uncut dataset. Scaled by a factor of 0.001 and plotted every 6th trace.

2.3.3 Coordinate transformations

All three-component seismic stations were transformed from ZEN to ZRT and LQT. Incidence angles came from ray tracing, in cases where they did not produce a good rotated section they were adjusted.

SPITS P2

The stations SPB2, SPB3 and SPB5 were rotated for $P2$. The radial (R) and transversal (T) components can be seen in **Figure 2.10** and **A.37**, respectively. On all three R components the 39.42-59.35 s and 260-410 km onset occur, it is most well defined on SPB5 and least on SPB2. At SPB3 and SPB5 a second onset is defined ~7 s after the first, it is seen from 260-290 km. All the T components exhibits a weaker first onset (~40-60 s 260-410 km) than the radial components, in addition more noise is introduced at all the stations. Station SPB5, **Figure A.37** seems to have two new onsets starting at ~70 s and 260 km and lasts throughout the entire line, but this onset is not clearly defined. Another onset occurs after, at ~ 80 s, 260 km and can be seen until 370 km and 100 s.

Rotation to L and Q were performed with the incidence angles = 37.5-38°. The L components are very similar for all the three stations, see **Figure A.39**, the two onsets seen on R are here as well, but more well defined. On Q the two onsets occuring on L are visible but weaker, for SPB3 and SPB5 a very weak coherence trend at 80 - 100 s and in the offset-range 260-370 km occurs.

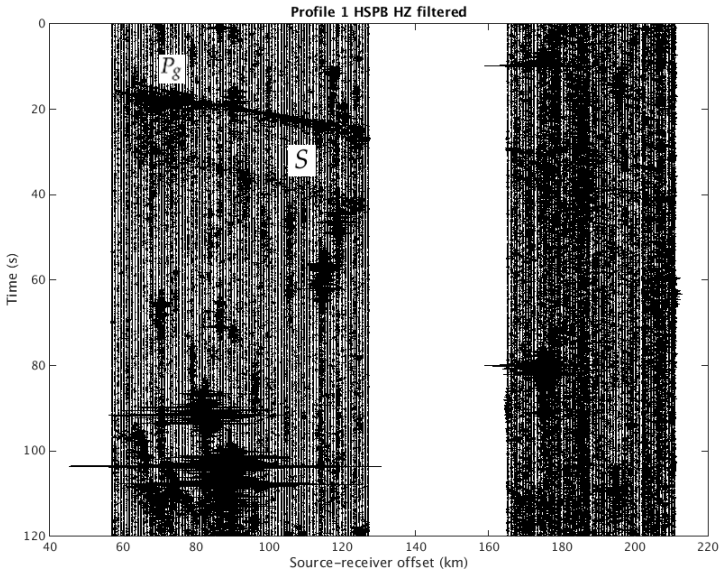

Figure 2.8: Filtered $P1_h$ HSPB HZ, scaled by a factor of 0.01. Every 4th trace is plotted.

SPITS P1

All the three-component stations for $P1_s$ were rotated. R and T rotated sections can be seen in **Figure 2.11** and **A.44**. The R component of SPA0, SPB1, SPB2, SPB3 and SPB4 have a first onset at 26.19-34 s 161-197 km, and a second one from ~47-57 s in the offset-range 163-197 km. SPB5 have these two onsets, but in addition it has high amplitudes at 225-330 km, ~40 s, and a possible onset at 225-260 km in the time range ~45-46 s. All the T components for SPA0, SPB1, SPB2, SPB3 and SPB5 have a weak first onset at 26.19-34 s 161-197 km, and a higher amplitude second onset at ~47-57 s in the offset-range 163-197 km. SPB4 exhibits high amplitudes at 180-192 km and ~30-32 s on an otherwise weak onset.

To transform to L and Q incidence angles of 26-39° were used. For all L components a clear first onset is defined at 26.19-34 s and 161-197 km, and a second onset can be seen from 225-260 and 36-38.67 s, below this onset another onset occurs at ~45-47 s and 245-260 km. Here there are very little noise on any of the stations, **Figure 2.12** and **A.46**. The Q component of SPA0, SPB1, SPB2, SPB3 and SPB5 have a weaker first onset than L at 161-190 km, but a well defined onset at ~47-57 161-197 km. Here there are more noise than on L. On SPB4 the first and second onset have equal amplitudes.

HSPB

Rotation to R, T, L and Q for HSPB can be seen in **Figures A.48**, **2.13**, **2.14** and **2.15**, respectively. On R three onsets can be seen, the first from 15.6-16.6 s and in the offset-range 72-78 km, the second and most prominent one at 16.3-23.5 s and in the offset range 63-116

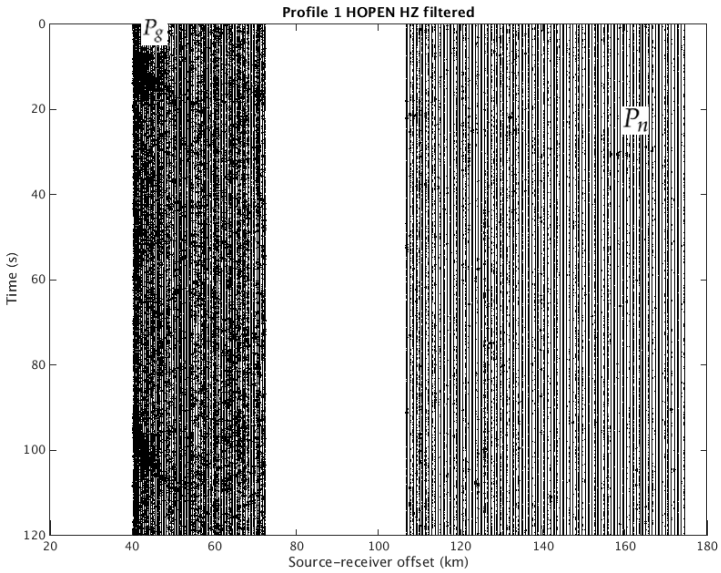

Figure 2.9: Filtered $P1_h$ HOPEN HZ, scaled by a factor of 0.01. Every 4th trace is plotted.

km. The third onset starts at 28 s and 68 km and lasts throughout the entire section to 39 s and 116 km. On the T component the onset at 16.3-23.3 s, 63-116 km occurs, but the dominating onset on T is in the range 28-39 s and 68-115 km.

To rotate to L and Q the incidence angles 28-39° were used. On L three onsets occur, two small offset onsets can be seen at 15.63-15.96 s and in the offset range 63.9-68.2 km, the second one are defined at 15.6-16.6 s in the offset-range 71-79 km. The third onset occur on all offsets and starts at 16.3 s and 63 km, and ends at 23.5 s and 116 km. On Q the onset at 16.3-23.5 s and 68-116 km is visible, but the highest amplitude onset can be seen at 28-39 s and in the offset-range 68-115 km.

HOPEN

Rotation to R, T, L and Q were performed as mentioned above, but due a lot of noise on N, only the large offsets of R, T and Q are plotted. The incidence angles used are: 15-30°. Both on R and T noise dominates and no onsets can be seen, see **Figure A.49** and **A.50**. On L, **Figure 2.16**, a onset is seen at 5.97-7.7 s and in the offset-range 40.53-45.55 km, a second onset are seen later at 10-14 s and in the offset-range 41-49 km. On the larger offsets one onset occur at 30.6-30.5 s in the range 156.7-161 km and another one at 28-29 s and in the offset-range 161-165 km. The Q component are quite similar to R and T, but there are some weak coherent onsets at ~50-52 s and in the offset-range 155-162 km, **Figure A.51**.

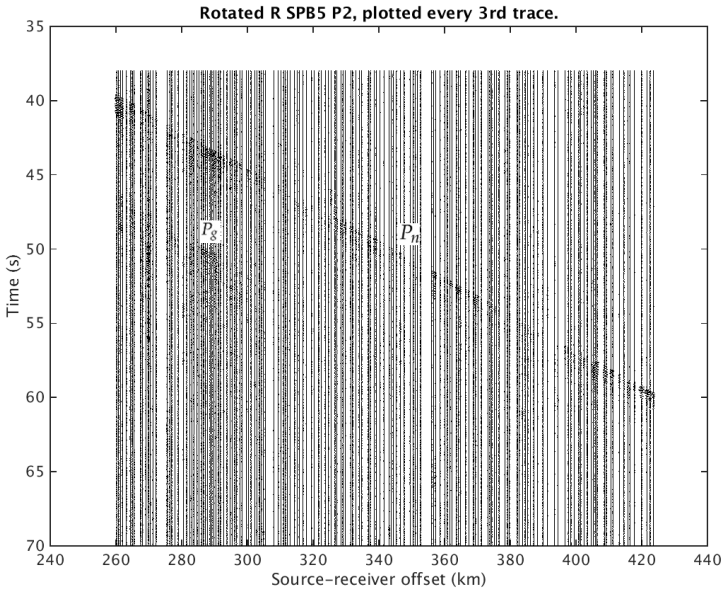

Figure 2.10: Rotated *P*2 SPB5 R, scaled by a factor of 0.001 and plotted every 6th trace.

2.3.4 Beamforming

Source-beams have been created for all components on all stations, while double-beams have been created for the three-component array data. Source- and double-beams have also been computed for the rotated data. In total 37 Z, E, N source-beams, 44 L,Q,T source-beams, 6 Z,E,N double-beams and 8 L,Q,T,R double-beams were calculated.

SPITS P2

Calculating the source- and double-beams for *P*2 were performed with an apparent velocity of 8 km/s, maximum distance between two traces was set to 30 m and SPB3 was used as the reference station in the double-beamforming. The onsets seen on all the components are as previously described in the previous sections, but with an improved SNR, the average SNR after filtering were 15, after source-beam it was 19 and after double-beamforming it was 25. The amplitude variations for the first and second onset are still visible on the double-beam.

The source-beam for SPB2 can be seen in **Figure A.54**, while the source-beam for the rotated data can be seen in **Figure A.76**.

For the east-west and vertical double-beams all three stations were utilized, the double-beam for the north-south component comprised SPB2 and SPB5. On all the double-beams the amplitude along the main offset still vary, but the SNR has increased. The R, T, L and Q double-beams were computed utilizing all the three-component stations.

In order to enhance S-waves an apparent velocity of 4 km/s was applied to the source- and subsequent double-beams, in **Figure A.80**, **A.85**, **A.70** and **A.75** the new apparent velocity

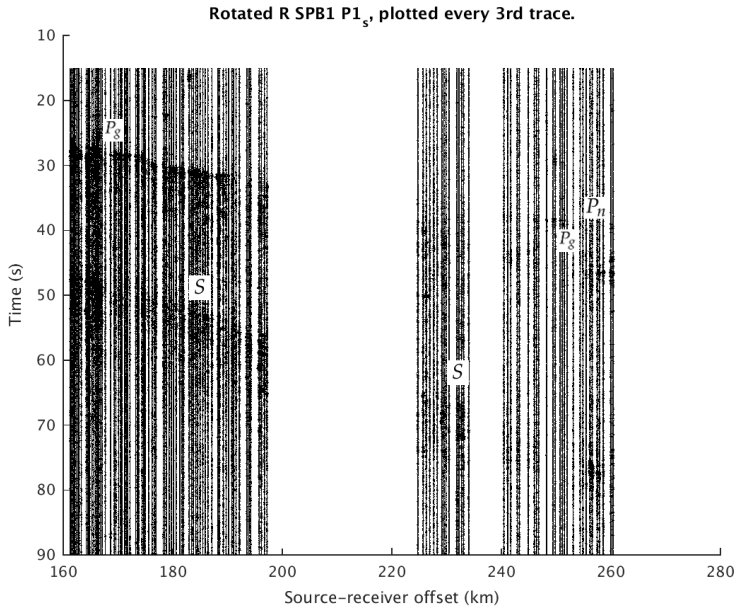

Figure 2.11: Rotated $P1_s$ SPB1 R plotted every 3rd trace.

has been applied on the rotated data. At the double beam of Q and T, **Figure A.84** and **A.74**, the two onsets seen on SPB3 and SPB5 at ~70 s and ~ 80-100s are slightly enchanced. On the vertical, eastern, northern and L double-beams the amplitude variations of the first onset has been decreased after the double beamforming.

SPITS P1

The beamforming for $P1_s$ was performed with an apparent velocity of 8 km/s and 4 km/s, maximum distance between two traces was set to 30 m and SPA0 was used as the reference station.

The vertical double-beam utilized all stations except SPB1, SPB4 and SPB5, the east-west and north-south components utilized all three-component stations. The source and receiver beams of SPB5 BZ shown in **Figure A.93** and **A.94** have an improved SNR, in addition the large offset arrivals are better defined on the double-beam. The source- and double-beam for the east-west component show an increase in amplitude of the second onset, this is also the case for the north-south component. The source- and double-beams computed with an apparent velocity of 4 km/s did not increase the SNR of any onsets on any of the beams. The SNR after filtering was 14, after the source-beam it was 17 and after the double-beamforming it was 22.

The rotated data utilized all three-component stations to compute the double-beam. The SNR increase on all the $P1_s$ double-beams, but the overall amplitude of the sections decrease.

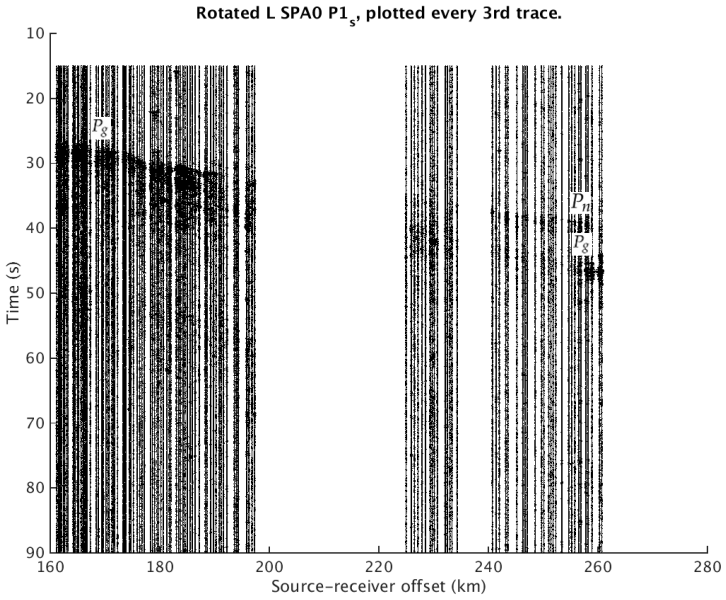

Figure 2.12: Rotated $P1_s$ SPA0 L, scaled by a factor of 0.001 and plotted every 3rd trace.

HSPB

HOPEN and HSPB are both single stations with 3-component broadband seismometers and hence only source-beams were possible to construct from these datasets. For both stations the apparent velocity was set to 6.5 km/s and 4 km/s, and maximum distance between two traces was set to 40 m.

412 traces were cut away at HSPB and this resulted in a source-beam where only the traces with close neighbouring traces were summed together. Although there is a slight improvement between the filtered data, cut datasets and the source-beams, the SNR for the filtered data was 14 while it is 16 after the beamforming. The east-west source-beam with an apparent velocity of 4 km/s has a slight decrease in amplitude for the first onset, while there is a slight increase in amplitude of the second one, see **Figure A.139** and **A.140**, this is not seen on the vertical nor north-south components.

HOPEN

At HOPEN not that many traces were cut away and the source-beams are better than the filtered dataset. The SNR after filtering were 11 while it increased to 13 after the beamforming. **Figure 2.17** displays the source-beam of the vertical components, here the random noise has decreased and the signal to noise ratio has increased. This is also the case for the two horizontal components and the rotated data. On the sourcebeam of L the large offset onset that was defined as several onset is visible as a more continuous onset ranging from 20.78-28.6 s and 107.2-167.1 km.

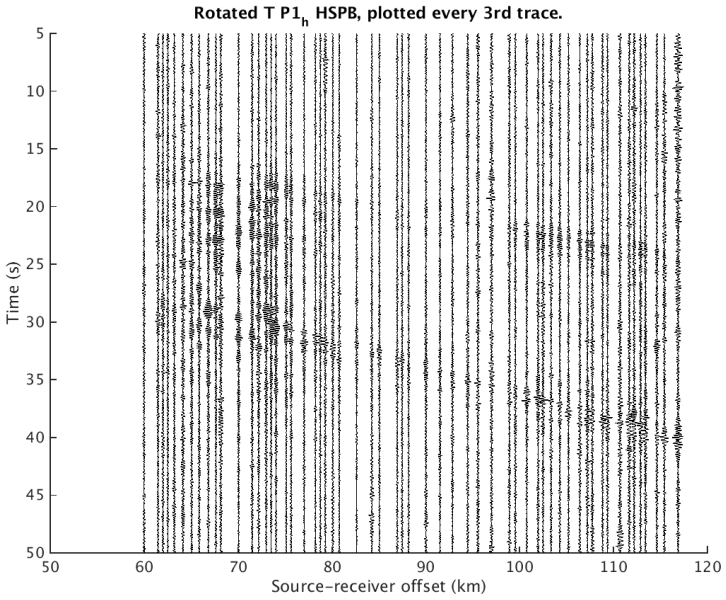

Figure 2.13: Rotated $P1_h$ T, scaled by a factor of 0.01 and plotted every 3rd trace.

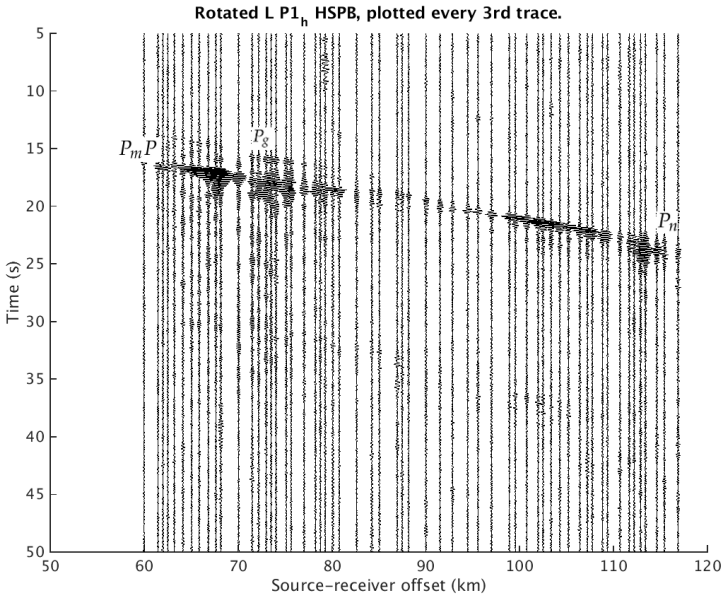

Figure 2.14: Rotated $P1_h$ L, scaled by a factor of 0.01 and plotted every 3rd trace.

The source-beams are not as good as the double-beams for $P2$ and $P1_s$ but there is an increase in signal-to-noise ratio on the source-beams for HOPEN and HSPB.

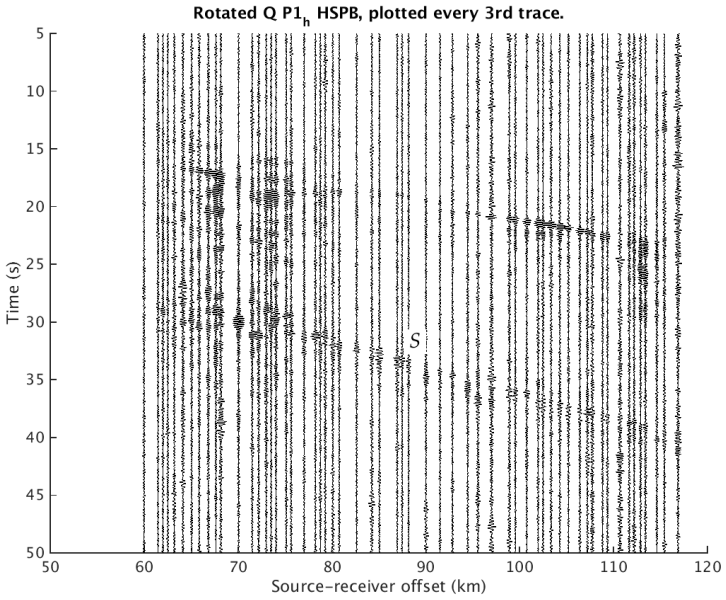

Figure 2.15: Rotated HSPB $P1_h$ Q plotted every 3rd trace.

2.3.5 Tau-v_{app} seismograms

Tau-p transformation has been performed on the Z, E, N data. To ease interpretation all the tau-p data are plotted as tau-apparent velocity. All components of HSPB and the vertical and east-west component of HOPEN have been scaled by a factor of 10, the rest are unscaled.

SPITS P2

The $\tau - v_{app}$ seismogram for $P2$ SPA1 BZ can be found in **Figure 2.18**, on this seismogram and all the other vertical components three curves occur. The first curve starts at $\tau = 0$ and $v_{app} = 5.8$ km/s and lasts until $\tau = 6$ s and $v_{app} = 8.5$ km/s. The largest amplitudes can be found in the apparent-velocity range 6.8-8 km/s. The second curve starts at $\tau = 0$ s and $v_{app} = 6.5$ km/s, it is a rather straight line and ends at $\tau = 5$ s and $v_{app} = 10.5$ km/s. This curve is intersected by a third one which starts at $\tau = 0$ s and $v_{app} = 7.3$ km/s. This curve can be followed until $\tau = 6.3$ s and $v_{app} = 10.5$ km/s. The largest amplitude of the two crossing curves occur in the area where they intersect. All the vertical components at all the stations are similar, but the curves at SPB5 have the largest amplitude, see **Figure 2.19**.

On the east-west components more noise occur at the small apparent velocities. The three curves from the vertical component are visible but with a lower amplitude. For small apparent velocities and τ there is a coherency trend along two curves, the first starts at $\tau = 1$ s and v_{app} = 3.5 km/s and lasts until $\tau = 8 - 12$ s and $v_{app} = 4.5 - 5$ km/s. The largest amplitude of the curve are found at smaller apparent velocities, the point where the curve ends is hard to define. The second curve starts at $\tau = 1.5$ s and $v_{app} = 4$ km/s and lasts until ~$\tau = 8 - 10$ s

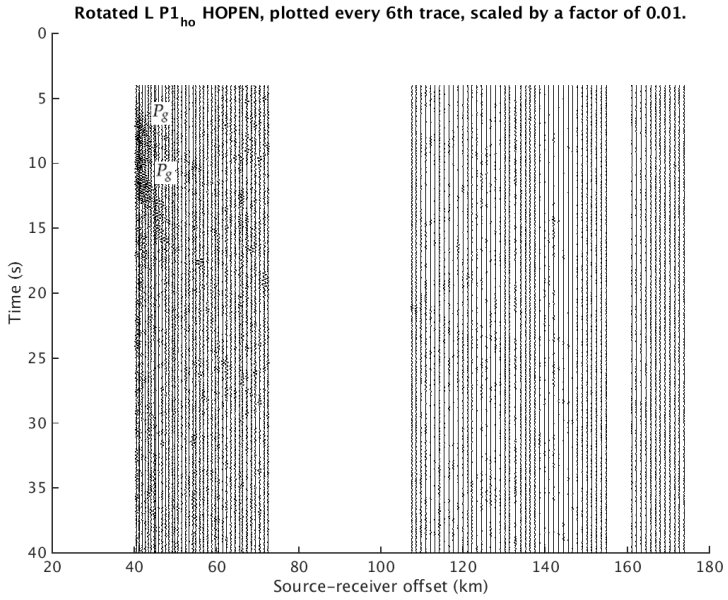

Figure 2.16: Rotated $P1_{ho}$ L, scaled by a factor of 0.01 and plotted every 3rd trace.

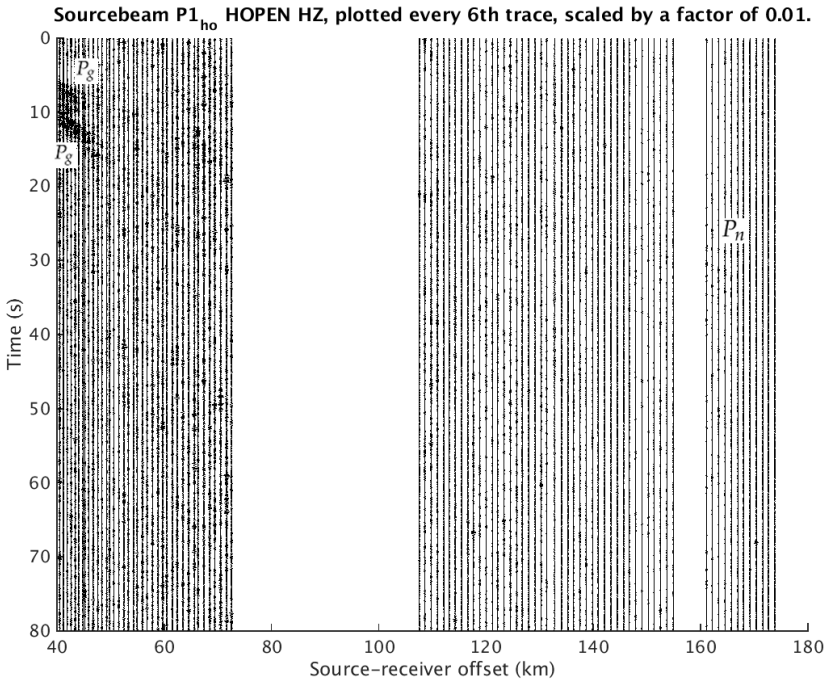

Figure 2.17: Source-beam $P1_ho$ HOPEN HZ, plotted every 3rd trace

and ~$v_app = 5.5 - 6$ km/s. At SPB2 both curves are well defined, at both SPB3 and SPB5 the second curve which ends at $v_{app} = 5.5 - 6$ km/s do not occur.

The north-south components are similar to the east-west components, both the curves starting at $\tau = 1$ s and $\tau = 1.5$ s can be seen at all the stations. The three curves found on the

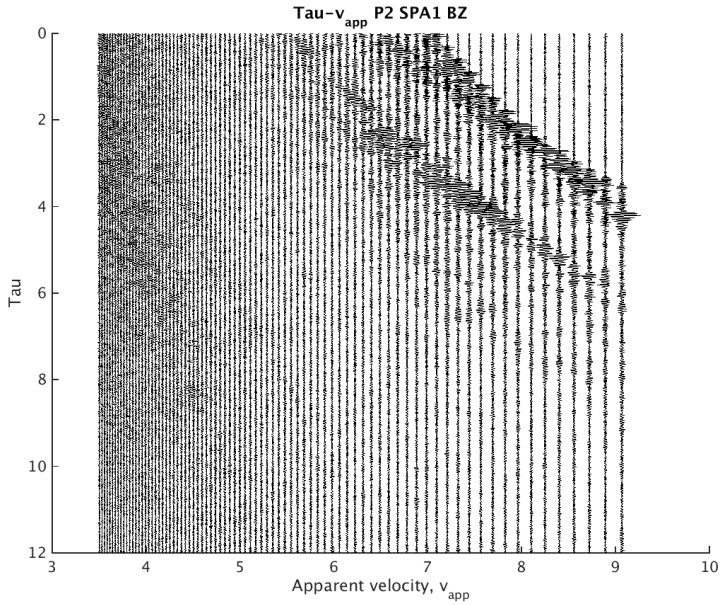

Figure 2.18: $\tau - v_{app}$ seismogram, $P2$ SPA1 BZ. Plotted every 10th trace

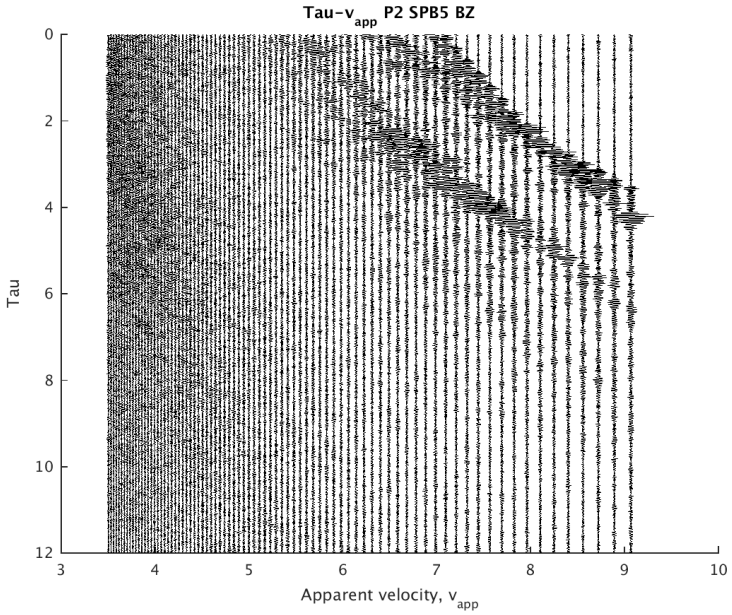

Figure 2.19: $\tau - v_{app}$ seismogram, $P2$ SPB5 BZ. Plotted every 10th trace

vertical component are weak amplitude curves here, see **Figure 2.21**.

SPITS P1

The vertical $\tau - v_{app}$ plots for $P1_s$ have all the same trend, the largest amplitudes are found in the τ-range 0-5.5 s and v_{app}-range 5-8.5 km/s. On SPA0 two curves are found in this range,

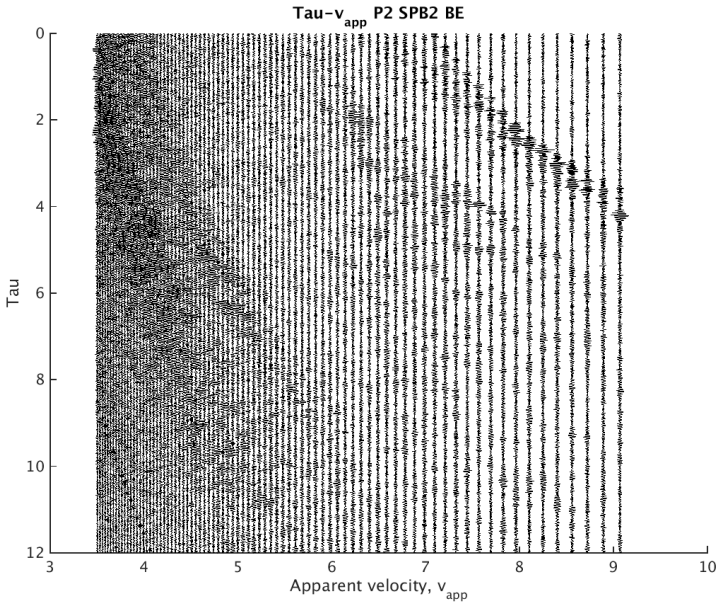

Figure 2.20: $\tau - v_{app}$ seismogram, $P2$ SPB2 BE. Plotted every 10th trace

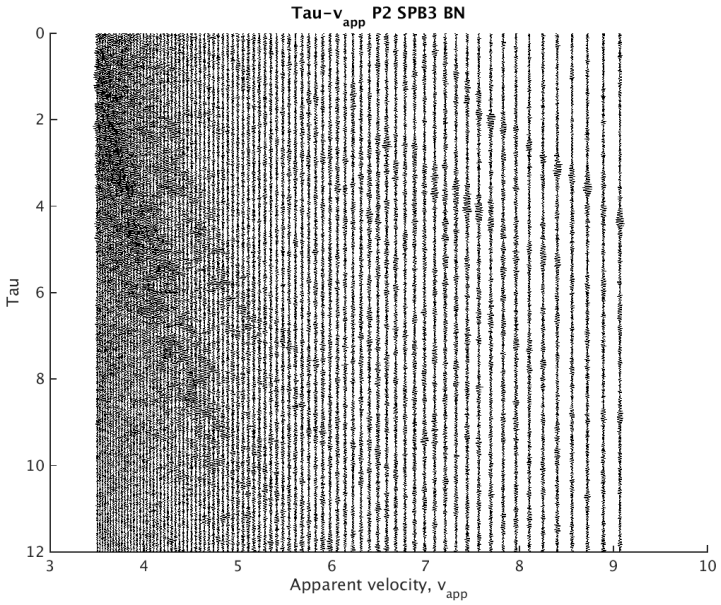

Figure 2.21: $\tau - v_{app}$ seismogram, P2 SPB3 BN. Plotted every 10th trace

the first one from $\tau = 0$ s and $v_{app} = 5.5$ km/s to $\tau = 5.5$ s and $v_{app} = 8.5$ km/s. A second curve is seen from $\tau = 0$ s and $v_{app} = 6$ km/s to $\tau = 5.5$ s and $v_{app} = 8.5$ km/s. At SPA1 there is better separation between the curves and a third curve is defined between the two previously described. It starts at $\tau = 0$ s and $v_{app} = 5.5$ km/s and lasts until $\tau = 2$ s and $v_{app} = 6.5$ km/s, this curve is also visible on SPB1 and SPB2 but with a weaker amplitude. For SPB3 the two

curves $\tau = 0 - 5.5$ s and $tau = 0 - 2$ s have small amplitudes, while the curve from $\tau = 0 - 4$ s and $v_{app} = 6 - 8.5$ km/s dominates. The three curves are also visible at SPB4, but the section is more noisy throughout. The three curves appear on SPB5, with the largest amplitudes at $v_{app} = 5.5 - 7$ km/s.

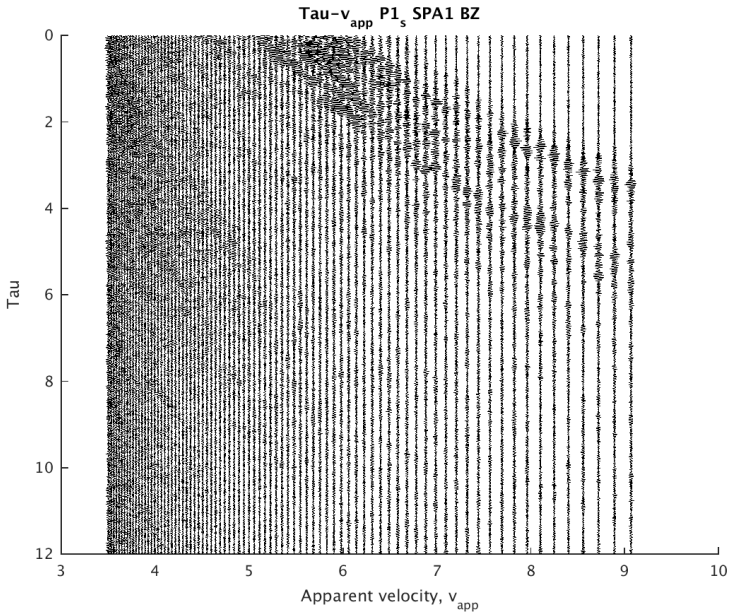

Figure 2.22: $\tau - v_{app}$ seismogram, $P1_s$ SPA1 BZ. Plotted every 10th trace

For the eastern components the three curves seen on the vertical component are not possible to discriminate. Here more noise are seen at small τ and v_{app}. On SPA0 a curve from $\tau = 0$ s to and $v_{app} = 3.5$ km/s to $\tau = 8$ s and $v_{app} = 6.5$ km/s is present, the largest amplitudes occurs from $v_{app} = 3.5 - 4.5$ km/s. On SPB1 the curve can be seen until $\tau = 6.5$ s and $v_{app} = 5.5$ km/s, this is also the case on SPB2 and SPB5, see **Figure 2.23**. For SPB3 two curves are defined, the one seen on SPA0, SPB1, SPB2 and SPB5, and a second curve starting at $\tau = 0$ s and $v_{app} = 4.2$ km/s to $\tau = 3$ s and $v_{app} = 5.5$ km/s, see **Figure 2.24**. On SPB4 there is more noise than on any of the other components, there is a trend from $\tau = 0 - 9$ s and $v_{app} = 3.5 - 5.5$ km/s but it is difficult to see any particular discrimination between possible curves due to noise.

The northern components are similar to the eastern components with high amplitudes at small τ and v_{app}. For all the stations two clear curves can be seen, except the three curves seen on the vertical components. One of the curves starts at $\tau = 2.5$ s and $v_{app} = 3.5$ km/s and can be followed until $\tau = 10$ s and $v_{app} = 5.5$ km/s, the other curve starts at $\tau = 0$ s and $v_{app} = 3.5$ km/s and lasts until $\tau = 7$ s and $v_{app} = 5.5$ km/s.

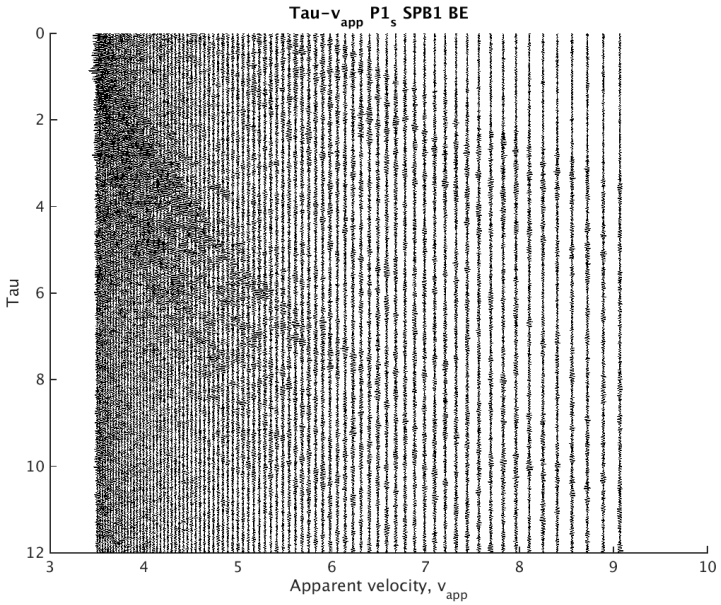

Figure 2.23: $\tau - v_{app}$ seismogram, $P1_s$ SPB1 BE. Plotted every 10th trace

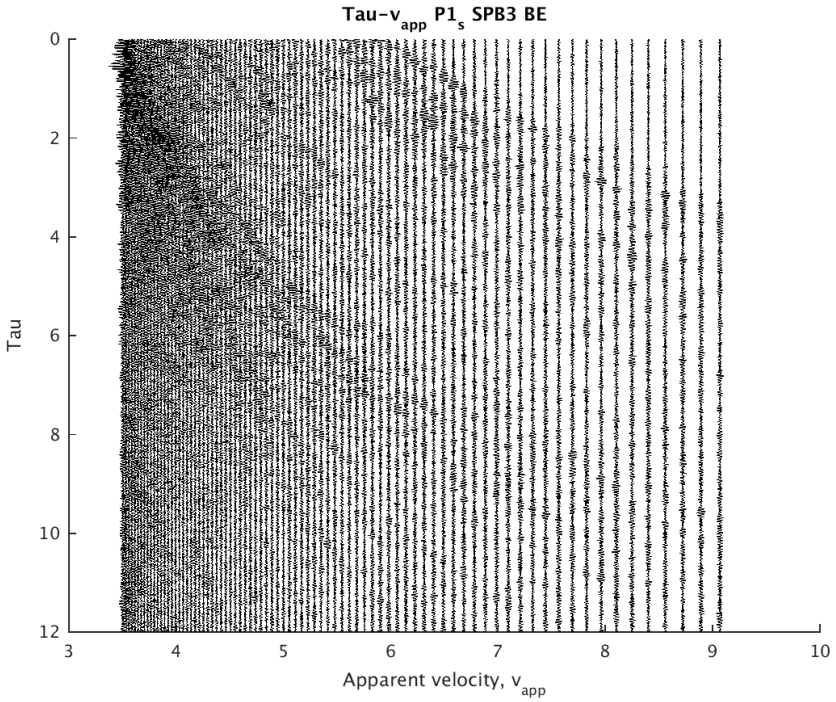

Figure 2.24: $\tau - v_{app}$ seismogram, $P1_s$ SPB3 BE. Plotted every 10th trace

HSPB

On the vertical component at HSPB there is a prominent large amplitude curve starting at $\tau = 1.5$ s and $v_{app} = 5.7$ km/s, the curve is rather wide and lasts until $\tau = 3.8$ s and $v_{app} = 8.5$

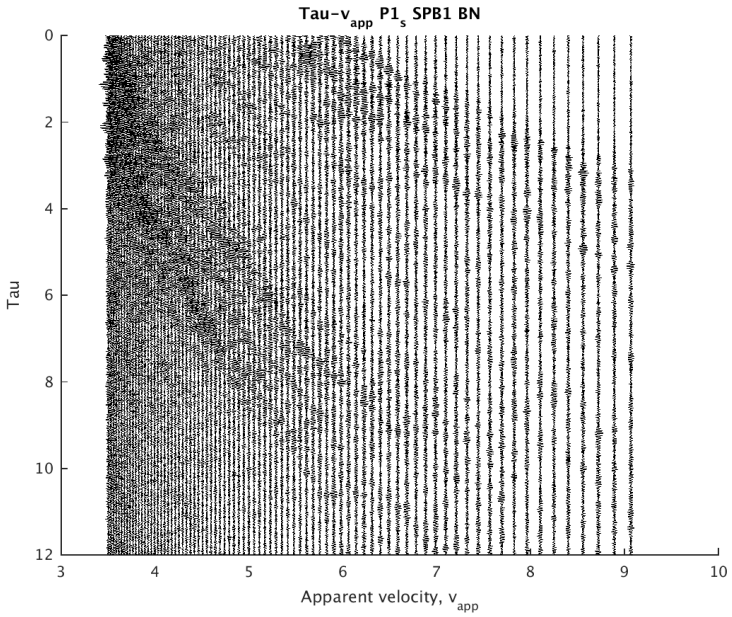

Figure 2.25: $\tau - v_{app}$ seismogram, $P1_s$ SPB1 BN. Plotted every 10th trace

km/s. This curve is abutting another curve at $\tau = 1.5$ s, the abutting curve starts at $\tau = 0$ s, $v_{app} = 4.7$ km/s and ends at ~$\tau = 2.5$ s and $v_{app} = 8$ km/s. At $\tau = 0$ s and $v_{app} = 4.1$ km/s another curve occurs, this curve occurs until $\tau = 2.5$ s and $v_{app} = 6$ km/s. The majority of large amplitudes occur at $v_{app} = 4.5 - 5.5$ km/s. A fourth curve is located at larger τ and small apparent velocities, this curve starts at $\tau = 3.5$ s, $v_{app} = 3.5$ km/s and ends at $\tau = 7$ s and $v_{app} = 6$ km/s. The amplitudes along this curve are generally low. On the eastern component two high amplitude curves are prominent. Both of them are seen on the vertical component, but here with different amplitudes. The first curve starts at $\tau = 3$ s, $v_{app} = 3.5$ km/s and lasts until $\tau = 7.5$ and $v_{app} = 6.5$. The curve has the highest amplitudes in the apparent velocity-range 3.5-5 km/s, in this range the thickness of the curve is at its largest. Another curve occurs at $\tau = 1.3$ s and $v_{app} = 5.6$ km/s, at $\tau = 1.5$ s the curve splits into two. One of the curves ends at $\tau = 1.8$ s, $v_{app} = 6.7$ km/s while the other curve ends at $\tau = 3.6$ s and $v_{app} = 9$ km/s. The high amplitudes can be found at the larger curve in the range $\tau = 2.2 - 3$ s and $v_{app} = 5.8 - 7.5$ km/s, see **Figure 2.27**. The north component of HSPB has two curves as the eastern component. The first one starts at $\tau = 2.5$ s and $v_{app} = 3.5$ km/s, the curve is quite thick and ends at $\tau = 8.2$ s and $v_{app} = 7$ km/s. From $\tau = 2$ s and $v_{app} = 6$ km/s to $\tau = 3.2$ s and $v_{app} = 8.2$ km/s a curve that increases in thickness and amplitude with increasing τ and v_{app} occur, the highest amplitudes can be found in the range: $\tau = 2.6 - 3.2$ s and $v_{app} = 6.5 - 7.4$ km/s.

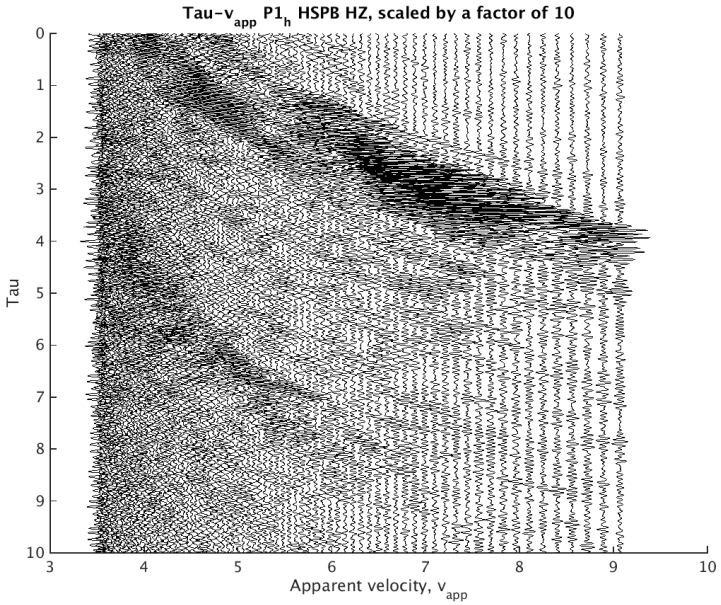

Figure 2.26: $\tau - v_{app}$ seismogram, $P1_h$ HZ. Plotted every 10th trace

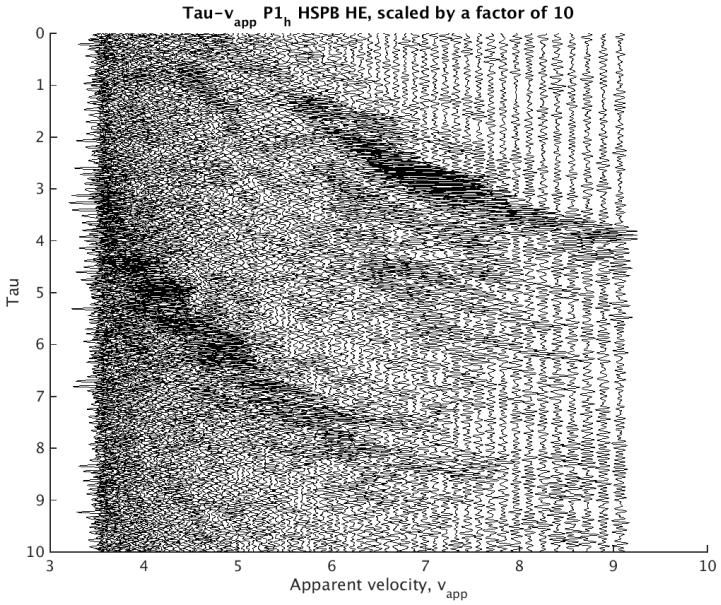

Figure 2.27: $\tau - v_{app}$ seismogram, $P1_h$ HE. Plotted every 10th trace

HOPEN

All components at HOPEN have very low amplitude $\tau - v_{app}$ transformations. There are no real high amplitude curves on the vertical component, but several curves can be seen at all apparent velocities and in the τ-range: 0-4 s. On the eastern component the amplitudes are slightly larger and some weak curves occur in the v_{app}-range 3.5-7.5 km/s and τ-range 0-4

s. For the northern component two curves can be seen, one starting at $\tau = 1$ s and $v_{app} = 3.5$ km/s and lasts until $\tau = 10$ s and $v_{app} = 7$ km/s. The second curve can be found at $\tau = 0$ s and $v_{app} = 3.5$ km/s and ends at $\tau = 2.6$ s and $v_{app} = 9$ km/s.

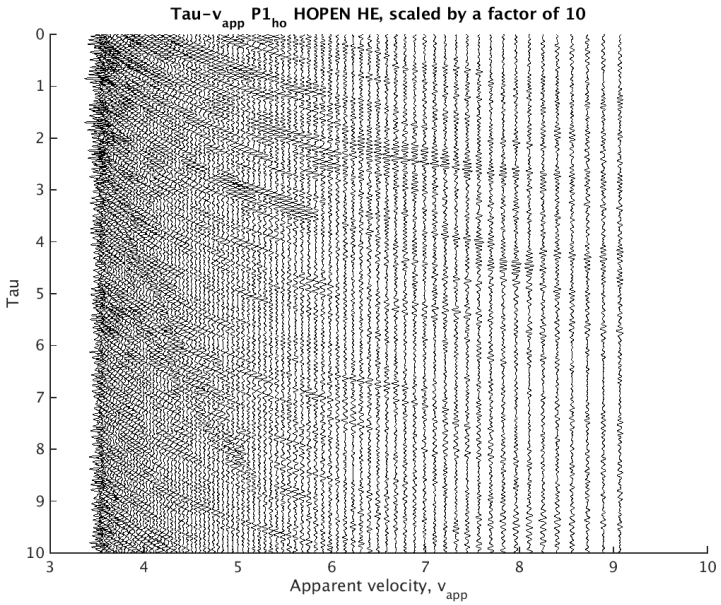

Figure 2.28: $\tau - v_{app}$ seismogram, $P1_{ho}$ HE. Plotted every 10th trace and scaled by a factor of ten.

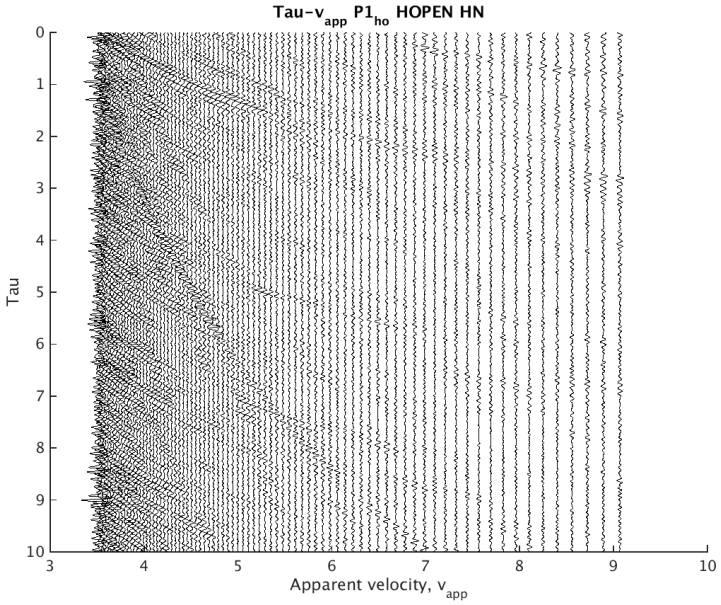

Figure 2.29: $\tau - v_{app}$ seismogram, $P1_{ho}$ HN. Plotted every 10th trace and scaled by a factor of ten.

2.3.6 Reduced seismograms

SPITS P2

From the tau-p transformation two main curves of apparent velocities occured at ~8 and ~ 6.5 km/s and hence the data from $P2$ have been reduced with these two apparent velocities. In figure 2.30 the double-beam of the vertical components of $P2$ are plotted with a reduction velocity of 8 km/s. The first onset aligns with the horizontal light grey line until an offset of 340 km, after this the onset are situated above the horizontal line. The distance between the horizontal line and the onset increases with offset. With a reduction velocity of 8 km/s the

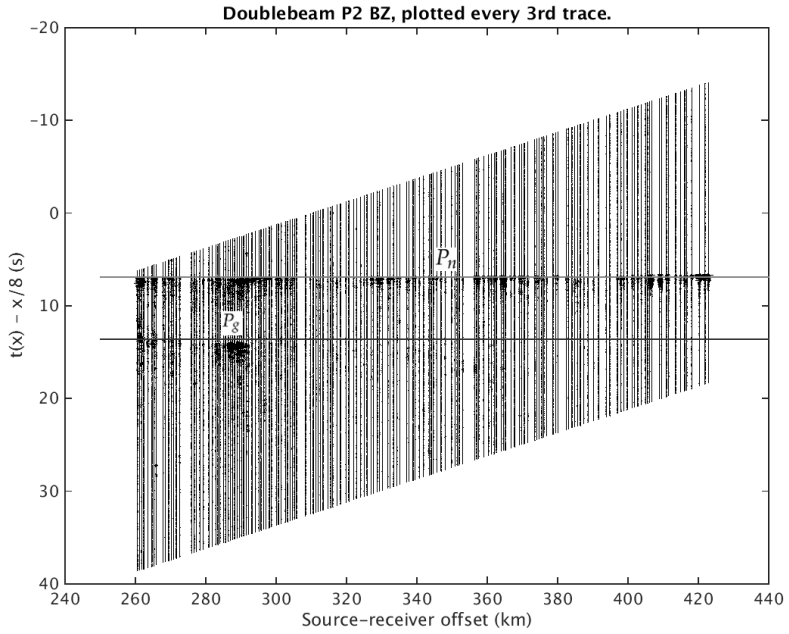

Figure 2.30: Doublebeam $P2$ BZ, plotted with a reduction velocity of 8 km/s. Every 3rd trace is plotted and scaled by a factor of 0.001. Horizontal light grey and dark grey lines has been fitted to the two onsets.

second onset plots below the dark grey horizontal line. In **Figure 2.31** the reduction velocity is set to 6.5 km/s, with this velocity the second onset aligns with the dark grey horizontal line. The first onset are aligned with the light grey horizontal line from 261-263 km, after this the onset can be found above the horizontal line.

SPITS P1

From the tau-p transformation of $P1_s$ the apparent velocties 5.5-8.5 and 3.5-5 km/s dominated. In **Figure 2.32** the vertical double-beam of $P1_s$ has been reduced by a velocity of 8 km/s. The horizontal line was fitted to the most horizontal part of the onset, the horizontal

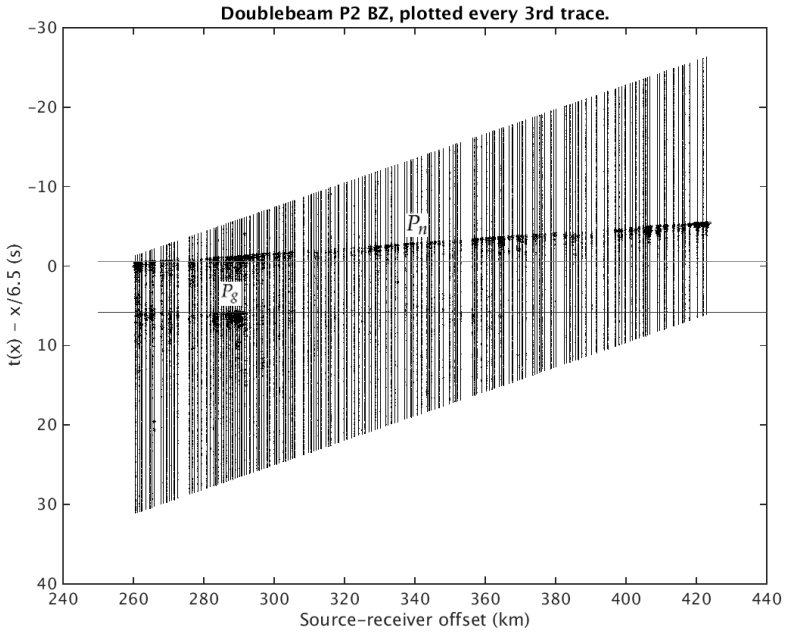

Figure 2.31: Doublebeam $P2$ BZ, plotted with a reduction velocity of 6.5 km/s. Every 3rd trace is plotted and scaled by a factor of 0.001. Horizontal light grey and dark grey lines has been fitted to the two onsets.

part of the onset is at 176-190 km. At large offsets the onset plots above the horizontal line. There is a visible jump in the onset at an offset of 176-186 km.

With a reduction velocity of 6.5 km/s the main onset align with the light grey horizontal line at 161-175 km.

The second onset on $P1_s$ is not that well defined, but with a reduction velocity of 4 km/s the onset aligns fairly well with the horizontal line, see **Figure 2.34**.

HSPB

From the tau-p transformation two apparent velocity trends were observed at ~4-5 km/s and ~6.5-8 km/s. In **Figure 2.35** the vertical source-beams of $P1_h$ are plotted with a reduction velocity of 8 km/s. The onset aligns with the light grey horizontal line for the larger offsets, on the smaller offset this onset is probably a Moho reflection, P_mP.

The source-beams of the east-west component, with a reduction velocity of 4.5 km/s, can be seen in **Figure 2.36**. The distance between the first onset and the horizontal line increases with offset while the second onset aligns well with the dark grey horizonal line.

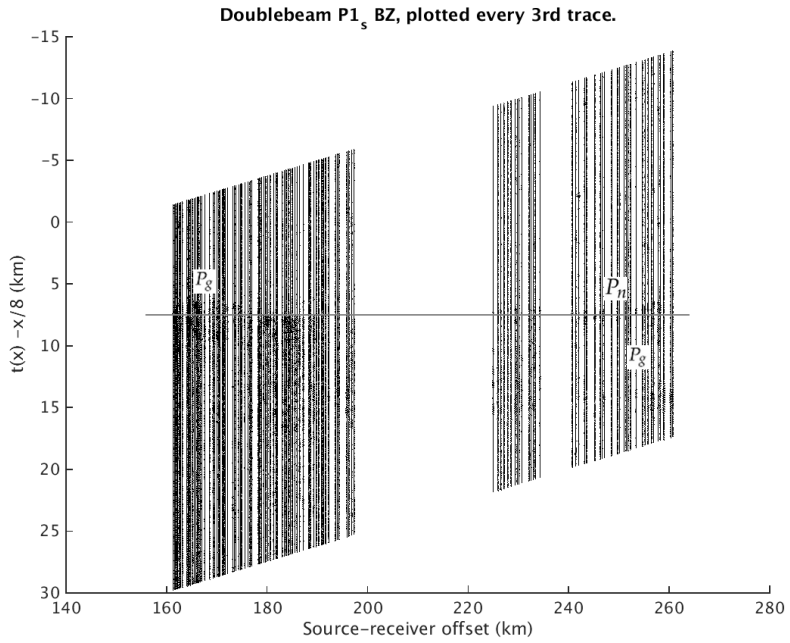

Figure 2.32: Doublebeam $P1_s$ BZ, plotted with a reduction velocity of 8 km/s. Every 3rd trace is plotted and scaled by a factor of 0.001. A horizontal light grey line is fitted to the onset.

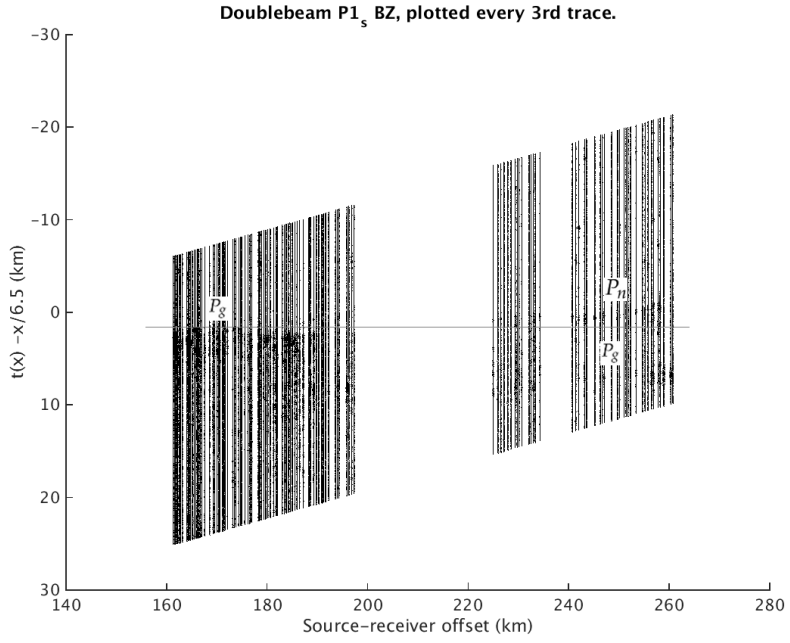

Figure 2.33: Doublebeam $P1_s$ BZ, plotted with a reduction velocity of 6.5 km/s. Every 3rd trace is plotted and scaled by a factor of 0.001. Horizontal light grey and dark grey lines have been fitted to the two onsets.

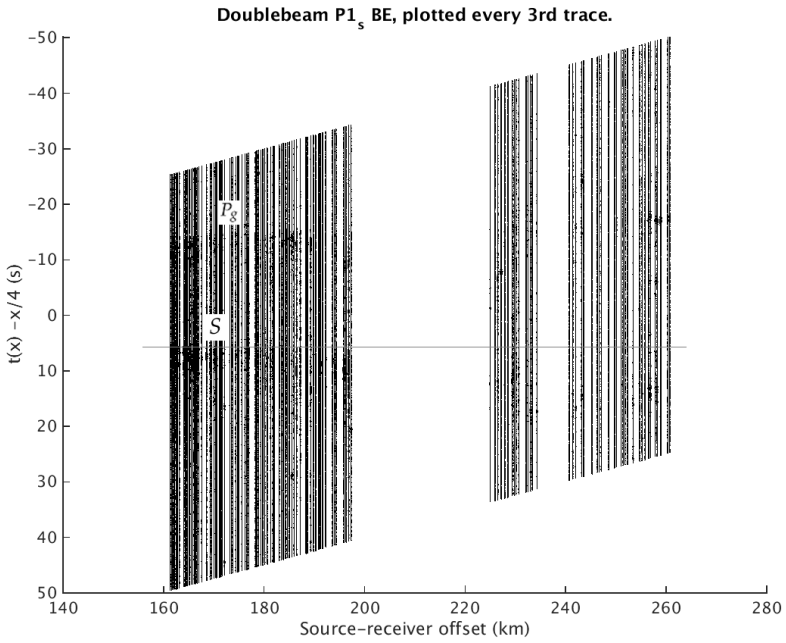

Figure 2.34: Doublebeam $P1_s$ BE, plotted with a reduction velocity of 4 km/s. Every 3rd trace is plotted and scaled by a factor of 0.001. Horizontal light grey and dark grey lines has been fitted to the two onsets.

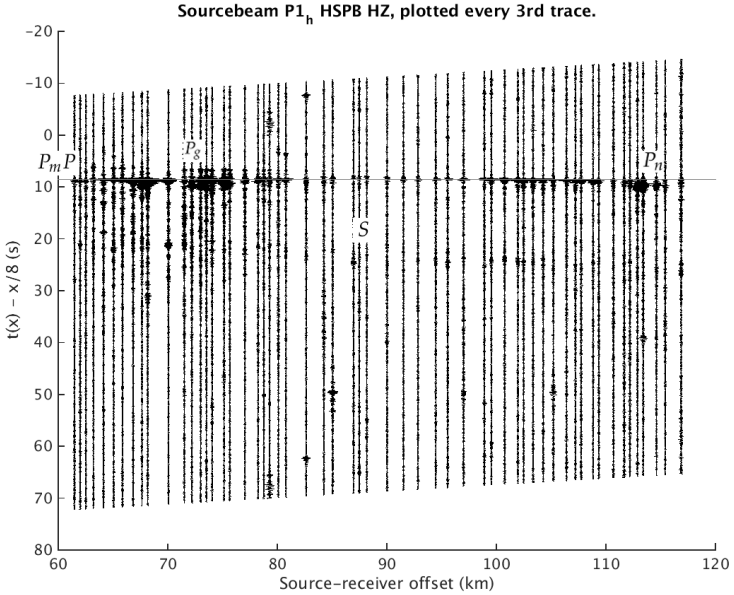

Figure 2.35: Sourcebeam $P1_h$ HZ, plotted with a reduction velocity of 8 km/s. Every 3rd trace is plotted and scaled by a factor of 0.05. A horizontal light grey line has been fitted to the onset.

HOPEN

The source-beams for HOPEN have been plotted with a reduction velocity of 2.3, 3 and 8 km/s. In **Figure 2.37** the source-beams of the vertical component of $P1_{ho}$ are plotted with a

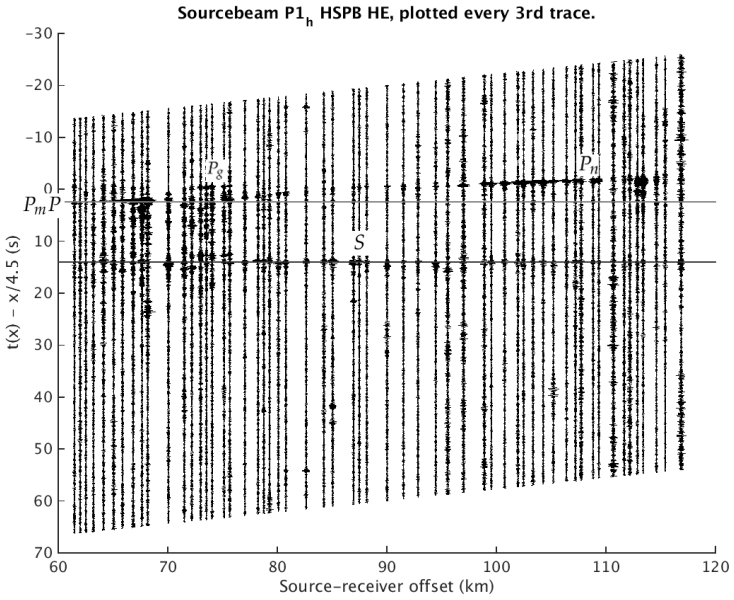

Figure 2.36: Sourcebeam $P1_h$ HE, plotted with a reduction velocity of 4.5 km/s. Every 3rd trace is plotted and scaled by a factor of 0.05. Horizontal light grey and dark grey lines has been fitted to the two main onsets.

reduction velocity of 2.3 km/s, here the second onset aligns with the horizontal dark grey line while the first onset plots slightly above the light grey horizontal line with increasing offset.

In **Figure 2.38** the vertical source-beams with a reduction velocity of 3 km/s are plotted. Here the first onset aligns quite well with the light grey horizontal line, the second onset however plots slightly below the dark grey horizontal line.

The source-beams for the east-west component with a reduction velocity of 8 km/s are plotted in **Figure 2.39**. At large offset the weak onset aligns with the light grey horizontal line.

2.3.7 Composite seismograms

The offsets of the different refraction lines are in some cases overlapping and composite seismograms of the vertical and L components can be seen in **Figure 2.40** and **2.41**. A grayscale composite seismogram to differentiate between the different refraction lines can be seen in **Figure A.161**. The composite plot of the vertical component comprises the vertical double-beams from $P2$ and $P1_s$ and the vertical source-beams of $P1_h$ and $P1_{ho}$. On the vertical composite plot the onset from $P2$ dominates and it seems to appear on both $P1_s$ and $P1_h$.

The composite plot of the L component comprises the L double-beams from $P2$ and $P1_s$ and the L source-beams for $P1_h$ and $P1_{ho}$, plotted with a reduction velocity of 8 km/s, see **Figure 2.41**. On this component it is evident that there is one main onset similar on $P2$, $P1_s$ and

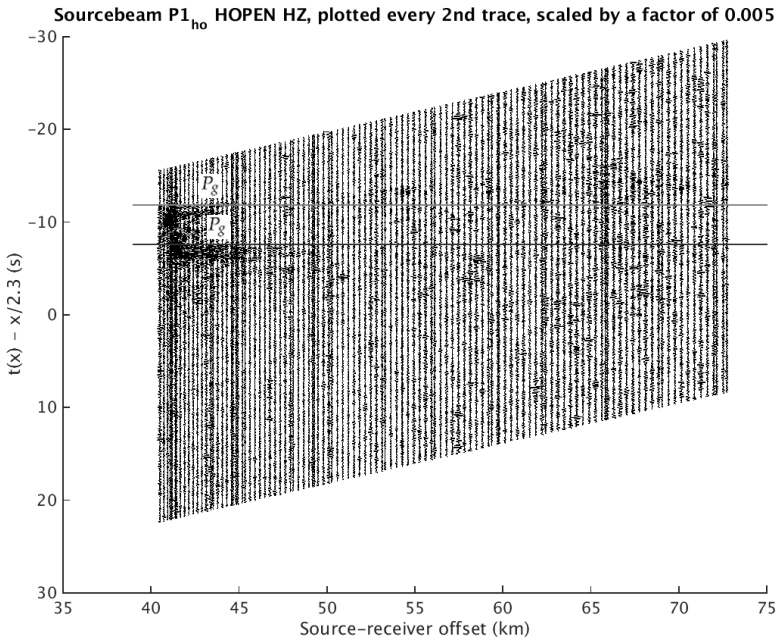

Figure 2.37: Sourcebeam $P1_{ho}$ HZ, plotted with a reduction velocity of 2.3 km/s. Every 2nd trace is plotted and scaled by a factor of 0.005. Horizontal light grey and dark grey lines are fitted to the two onsets.

$P1_h$. With a reduced time the first onset on $P2$ and the first onset on the large offset part of $P1_s$ aligns horizontally. The first onset on the smaller offset of $P1_s$ dips slightly down, but is generally plotted at the same reduced time as $P2$. The onset on $P1_h$ dips down as well, in addition it plots at a later time. The onsets on $P1_{ho}$ both dip significantly down. The second onset on $P2$ appears to be a continuation of the second onset seen on the large offset of $P1_s$, the onset dip slightly down.

The composite Q profile in **Figure 2.42** is plotted with a reduction velocity of 4.5 km/s. The light grey horizontal line is fitted to the onset seen on $P1_s$, this onset are rather well defined but appear to align approximately horizontal with a reduction velocity of 4.5 km/s. The most prominent onset on $P1_h$ plots later here as well i .e., a jump is seen her versus the S-wave arrival of $P1_s$. The large offset part of $P1_{ho}$ dips slightly down, but it plots before $P1_h$.

The S-wave arrival on $P2$ dip significantly down compared to the S-wave arrival on $P1_s$, it is evident that this S-wave must have been traveling in a slower media.

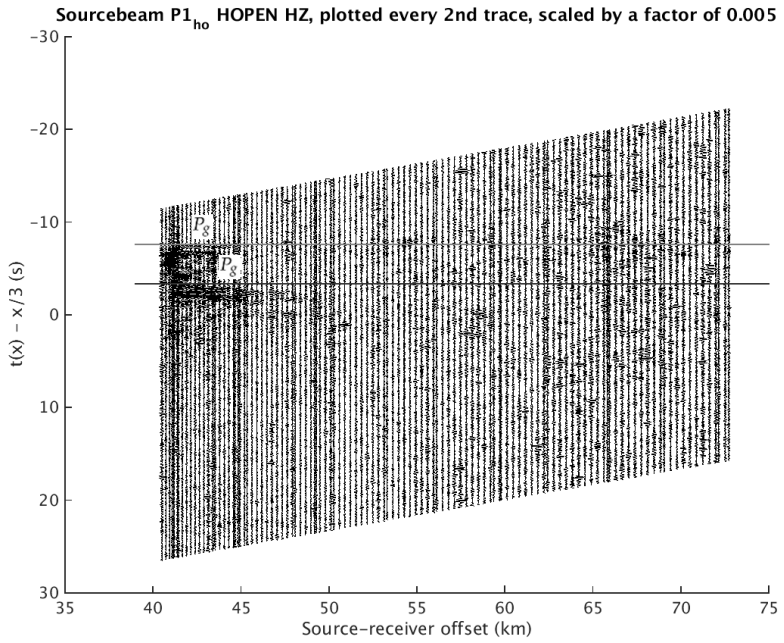

Figure 2.38: Sourcebeam $P1_{ho}$ HZ, plotted with a reduction velocity of 3 km/s. Every 2nd trace is plotted and scaled by a factor of 0.005. Horizontal light grey and dark grey lines are fitted to the two onsets.

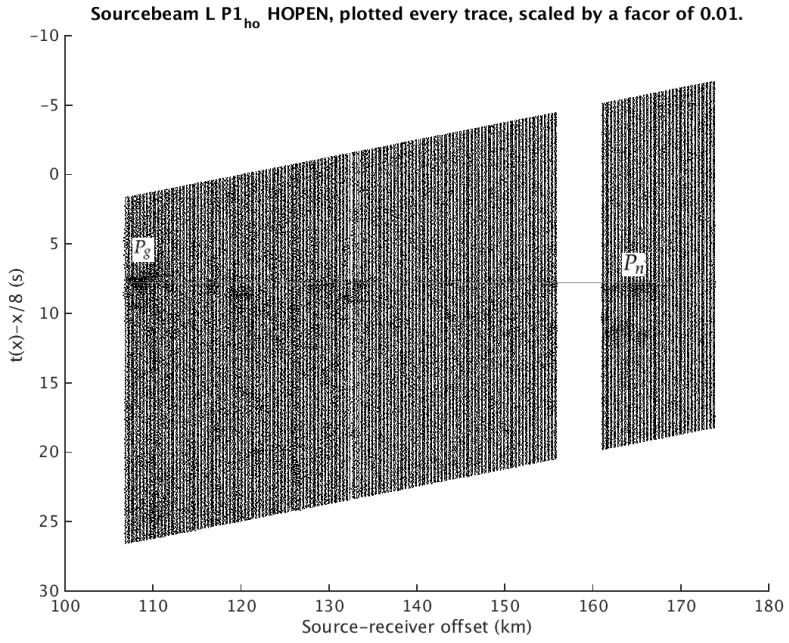

Figure 2.39: Sourcebeam $P1_{ho}$ L, plotted with a reduction velocity of 8 km/s. Every trace is plotted and scaled by a factor of 0.01.

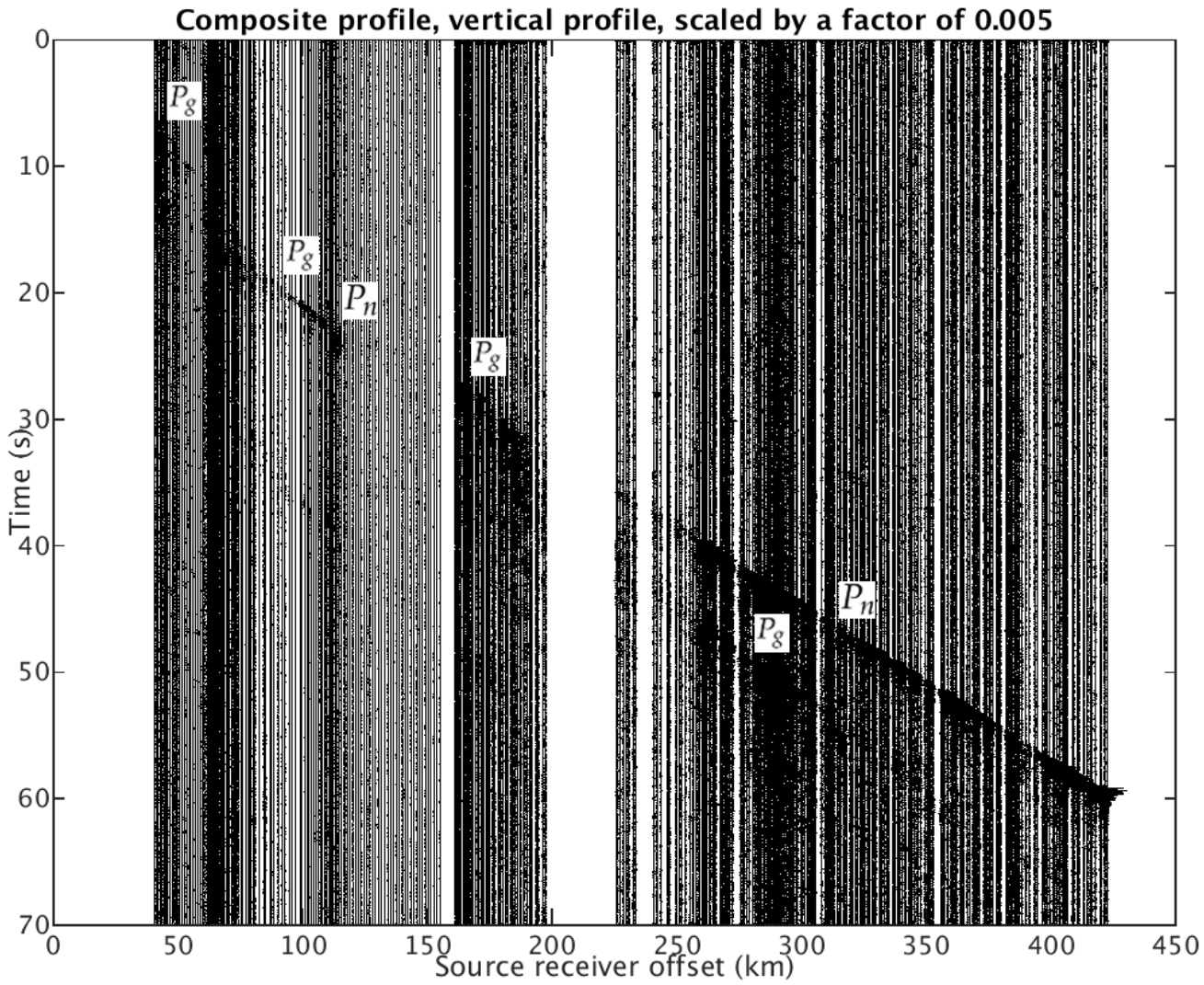

Figure 2.40: Composite seismogram of the vertical component of $P1_{ho}$, $P1_h$, $P1_s$ and $P2$. $P1_{ho}$ has been scaled by a factor of 0.01 while $P1_h$, $P1_s$ and $P2$ have been scaled by a factor of 0.005. For $P1_h$ and $P2$ every 3rd trace has been plotted, while for $P1_s$ and $P1_{ho}$ every 6th trace has been plotted.

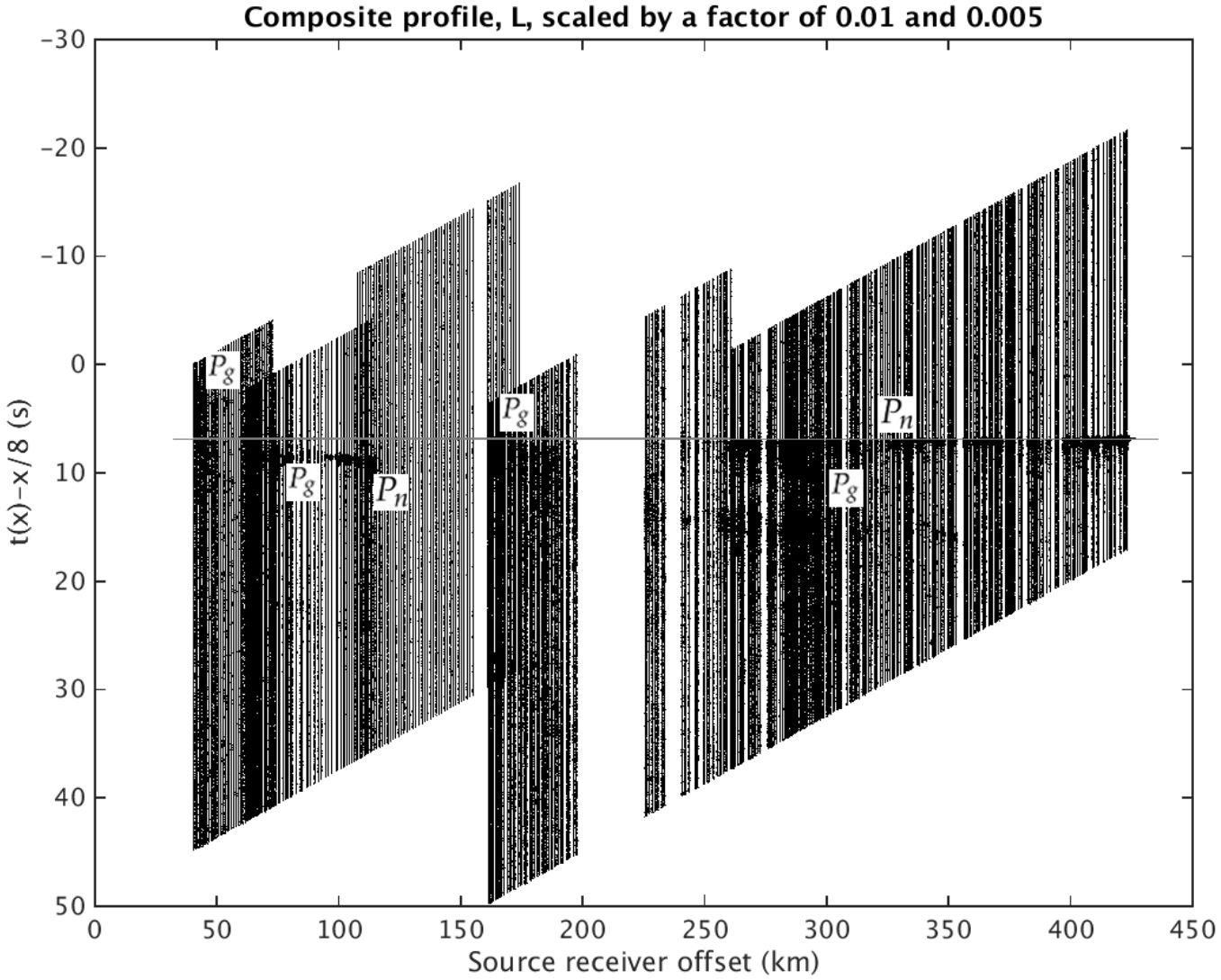

Figure 2.41: Composite seismogram of the L component of $P1_{ho}$ $P1_h$ $P1_s$ and $P2$. $P1_{ho}$ is scaled by a factor of 0.01 while $P1_h$, $P1_s$ and $P2$ are scaled by a factor of 0.005. $P1_h$ and $P2$ are plotted every 3rd trace, while $P1_s$ and $P1_{ho}$ are plotted every 6th trace. The light grey is a horizontal line fitted to $P2$. The seismograms are plotted in reduced time, with a reduction velocity of 8 km/s.

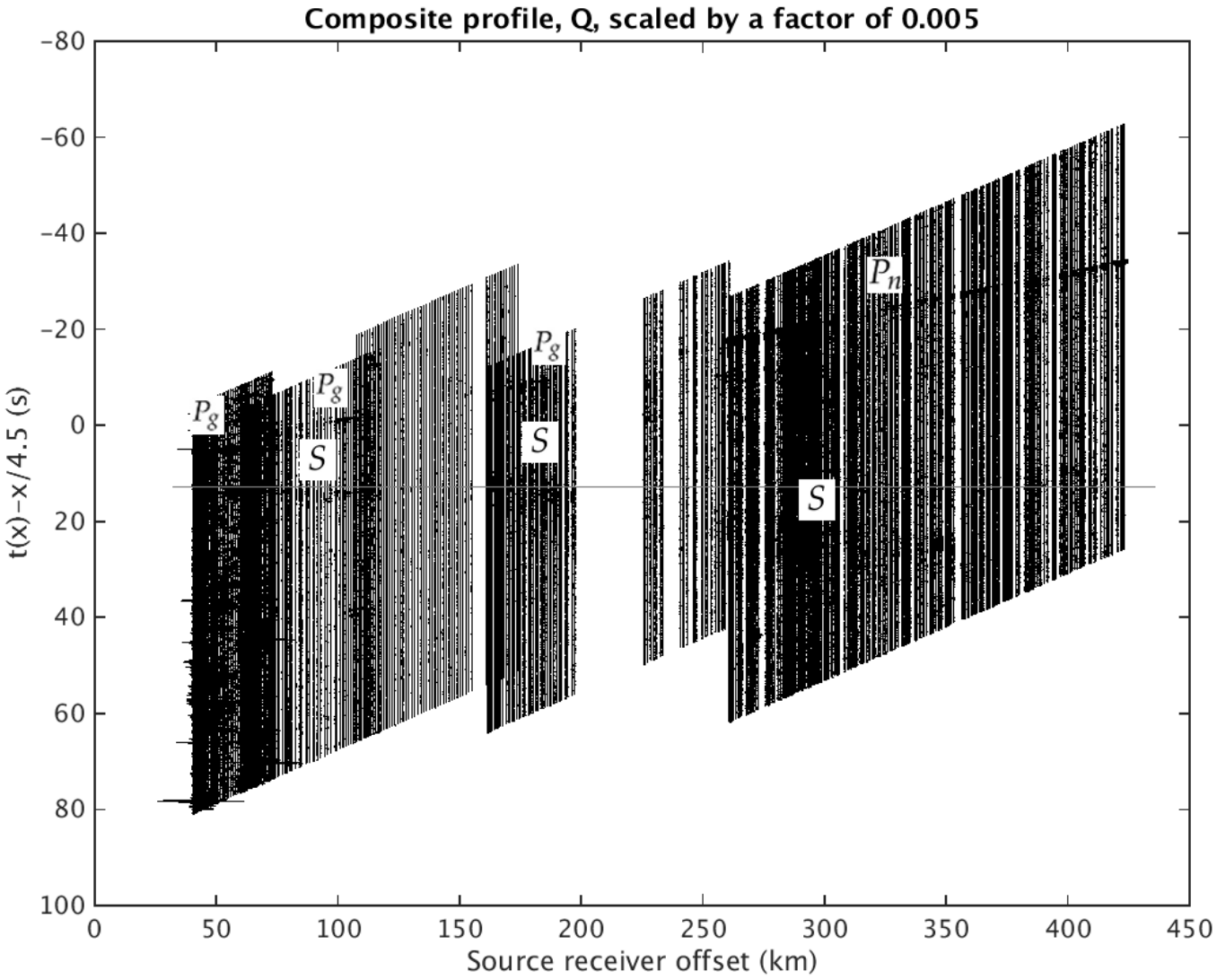

Figure 2.42: Composite seismogram of the Q component of $P1_{ho}$ $P1_h$ $P1_s$ and $P2$. All the stations have been scaled by a factor of 0.005. $P1_h$ and $P2$ are plotted every 3rd trace, while $P1_s$ and $P1_{ho}$ are plotted every 6th trace. The seismograms are plotted in reduced time, with a reduction velocity of 4.5 km/s.

3 Forward modelling

3.1 Methods

3.1.1 Travel-time modelling

Travel-time modelling was performed by kinematic raytracing. Ray tracing is a high-frequency modelling approach to solve the elastic wave equation with constant density (Cerveny, 2001; Boschi et al., 1996; Pujol, 2003). The high-frequency assumption cannot be used unless the seismic properties of the model do not vary much over the dominant wavelength of the seismic signal (Pujol, 2003).

The derivation below follows Cerveny (2001) and Boschi et al. (1996). The elastic wave equation (eq. 3.1) describes the propagation of waves in an elastic medium.

$$\nabla^2 P(\mathbf{x},t) - \frac{1}{c^2(\mathbf{x})}\frac{\partial^2 P(\mathbf{x},t)}{\partial t^2} = S(\mathbf{x},t), \tag{3.1}$$

Where ∇^2 is the Laplacian, P is the pressure in $\mathbf{x}$ at time t, S is the source function and $c(\mathbf{x})$ is the propagation velocity. The wave equation can also be represented in the frequency domain, then called Hemholtz equation:

$$\nabla^2 p(\mathbf{x},\omega) + \frac{\omega^2}{c^2(\mathbf{x})} p(\mathbf{x},\omega) = s(\mathbf{x},\omega) \tag{3.2}$$

The idea behind kinematic ray tracing is to approximate a high-frequency solution of the Hemholtz equation (eq. 3.2) to compute the travel-time of a ray. The frecuency domain 3-D Greens function, equation 3.3 is:

$$g(\mathbf{x},\omega) = A(\mathbf{x})e^{-i\omega T(\mathbf{x})} \tag{3.3}$$

This equation can be substituted into the Hemholtz equation (eq. 3.2) as a solution where the source term is set to 0, here with A(x) representing amplitude and T(x) for travel time:

$$\nabla^2 g(\mathbf{x},\omega) = -\frac{\omega^2}{c^2(\mathbf{x})} g(\mathbf{x},\omega) \tag{3.4}$$

The expression for $\nabla^2 g(\mathbf{x},\omega)$ can be written out as:

$$\nabla^2 g(\mathbf{x},\omega) = [\nabla^2 A(\mathbf{x}) + 2i\omega\nabla(A(\mathbf{x})T(\mathbf{x}) + iA(\mathbf{x})\omega(\nabla T(\mathbf{x}))^2)]e^{i\omega T(\mathbf{x})} \tag{3.5}$$

Inserting equation 3.5 into equation 3.4, rearranging the terms and dividing with $\omega^2 A(\mathbf{x})$ yields:

$$\left((\nabla T(\mathbf{x}))^2 - \frac{1}{c^2(\mathbf{x})}\right) - \frac{i}{\omega}\left(\frac{2}{A(\mathbf{x})}\nabla(A(\mathbf{x})T(\mathbf{x})) + \nabla^2 T(\mathbf{x})\right) - \frac{1}{\omega^2 A(\mathbf{x})}\nabla^2 A(\mathbf{x}) = 0 \tag{3.6}$$

For high frequencies the ω^{-1} and ω^{-2} terms of equation 3.6 will diminish, while the first term dominates. The first term is called the *eikonal equation* and can be written as:

$$(\nabla T(\mathbf{x}))^2 = \frac{1}{c^2(\mathbf{x})} \tag{3.7}$$

This equation is a first order ordinary differential equation for the travel-time $T(\mathbf{x})$. Then the kinematic ray equations are given by:

$$\frac{d\mathbf{x}(s)}{ds} = c(\mathbf{x})\mathbf{p}(s) \tag{3.8}$$

$$\frac{d\mathbf{p}(s)}{ds} = \nabla\frac{1}{c(\mathbf{x})} \tag{3.9}$$

Solving the kinematic ray equations (3.8 and 3.9) numerically is done by subsequent computation of the travel-time along the raypath (Cerveny, 2001). Kinematic ray equations can be solved by using the Runge-Kutta method, this method solve ordinary differential equations by progressing the solution one step at the time.

3.1.2 Amplitude modelling

Amplitude modelling was performed by frequency wavenumber (F-K) integration. Frequency wavenumber integration is an approach to model waveforms and create synthetic seismograms.

The derivation of the F-K integration follows Bouchon (1981) and Saikia (1994). In F-K integration two inverse transforms, frequency and wavenumber are evaluated.

$$F(\omega, r) = \int_0^\infty F(k, \omega) J_n(kr) k\, dk \tag{3.10}$$

$F(k, \omega)$ represents the medium response, $J_n(kr)$ is the nth order Bessel's function and k is the wavenumber. The integral in equation 3.10 can be evaluated using the polynomial approximations of the Bessel's functions combined with the Bouchon integration criteria (Bouchon, 1981). The Bouchon integration criteria defines the wavenumber interval $\Delta k = 2\pi/L$ given by:

$$L > 2r \tag{3.11}$$

and

$$\sqrt{(l-r)^2 + h^2} > v_{max} T \tag{3.12}$$

Here L is the source depth, v_{max} represents the highest velocity and T is the length of the time series.

Trimming the input parameters is important to avoid generating synthetic seismograms with numerical artifacts caused by oscillations and unwanted periodicities (Wang et al., 2003).

Several F-K integration packages developed for research purposes are available online. The University of Saint Louis has developed a fast and stable F-K integration software that is updated and maintained.

3.2 Implementation

The ray tracing was implemented in MATLAB R2014b, here the ode45 function has been used to solve differential equations employing the Runge-Kutta method. With keeping the source position constant and changing the take-off angle and azimuth rays have been traced throughout the medium. According to the reciprocity principle the direction the ray travel does not matter when modelling travel times. In order to minimize computing time the seismic stations are set as sources and rays have been traced in the direction of the seismic refraction lines. The velocity model (Barents50) was converted to UTM coordinates and smoothed with the smooth3 function in MATLAB, with box convolution-kernel set to 1. The model has been interpolated with a 2 km depth interval and 15 km intervals in x- and y-directions. The maximum travel time for the rays was set to 50 s and the source depth was set to 50 m.

The travel-time information was saved in matrices containing position, travel-time and slowness. In order to compute the travel-time to the exact position of the seismic line 2D interpolation was performed between rays that came up to the surface.

The frequency wavenumber integration software used to calculate the synthetic seismograms have been developed by the Earthquake Center at the University of Saint Louis (Herrmann, 2013). The input are 1D velocity models and distances, distances were set to 0-420 km, each step is 4 km. In order to create zero phase pulses the time vector started at -0.05 s, and the source time function was a Ricker wavelet with a maximum frequency of 100 Hz. There are no water layer in any of the models run through the FK integration, this is due to the fact that the program was unstable when v_s = 0 km/s.

Two seismograms have been created for the different 1D models, vertical and radial. Due to large offsets the Bessel function has been replaced by the Hankel function which is more stable at large distances and high frequencies (Herrmann, 2013). To scale the datasets, each trace has been divided by the max trace amplitude and subsequently multiplied by a factor of 10 or 20.

3.3 Results

3.3.1 Travel-time curves from 1D models

Frequency wavenumber integration was perfomed on 6 1D models; Fennoscandia, Barents, Barey, Barez, Barents50 at P1 and Barents50 at P2. The 1D models from Barens50 P1 and P2 are extracted from the 3D model at the specific refraction lines. The extracted 1D models from Barents50 comprises 110 layers down to a depth of 200 km. Both the P- and S-wave travel times for the different 1D models are plotted on top of the source- and double-beams from the different refraction profiles.

SPITS P2

In **Figure 3.1** the P- and S-wave travel times from Barents, Barey, Barez and Fennoscandia are plotted on top of the *P*2 vertical double-beam. The P-wave travel time are situated just below the first onset, see **Figure 3.1**. There are three visible curves: Barents, Barez and

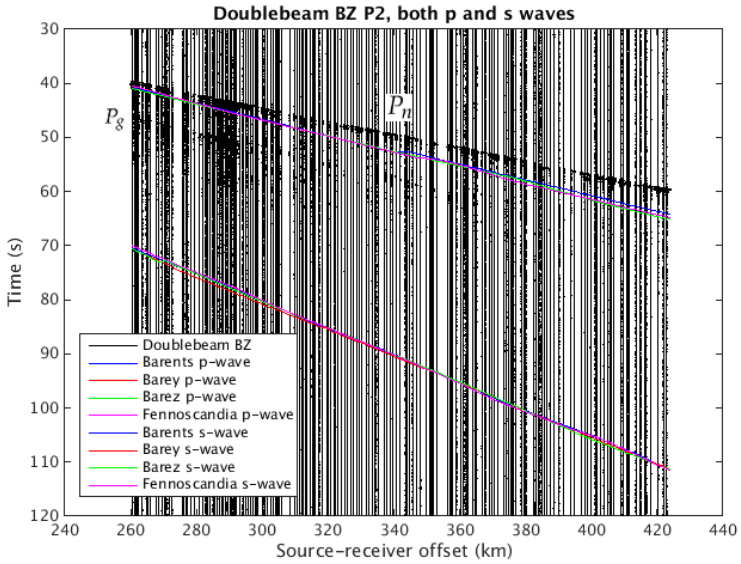

Figure 3.1: The double-beam of *P*2 BZ, where P- and S-wave travel-time curves from Barents, Barey, Barez and Fennoscandia are overlain.

Fennoscandia. And all the three curves have the same trend, the distance between the curves and the onset increase with offset. At the first offset the onset appear at 39.42 s, Fennoscandia at 40.5 s, Barents at 40.85 s and Barey at 40.99 s. Fennoscandia crosses both Barents and Barez after 17 and 30 km, respectively. Then Barez crosses Barents at 290.8 km and 45.43 s, subsequently Barents crosses Barez at 341.1 km and 52.75 s. Barez and Fennoscandia crosses three times at 349.5 km 52.75 s, 365.2 km and 55.96 s and 394.8 km 60.7 s, at the end of the refraction line at 422.9 km, Barents appear at 64.05 s, Fennoscandia at 64.67 s, Barez at 65 s, while the onset occur at 59.3 s.

S-wave travel times can also be found in **Figure 3.1**. Here all four travel-time curves are visible and they have the same overall trend. The travel-time curves plot ~10 s before the S-wave onset. At the start of the refraction profile, at Fennoscandia plots at 70.06 s, Barents at 70.46 s and Barez and Barey at 70.67 s. They all ends at 422.9 km , Barez plots at 111 s, Fennoscandia at 111.1 s, Barents at 111.2 s and Barey at 111.25 s.

SPITS P1

The P- and S-wave travel times for the 1D models are presented in **Figure 3.2**. The P-wave travel-time curves plots both before and after the onsets. Barey and Barez plot on top of each other throughout the entire section, they start at 27.33 s and 161 km and ends at 42.33 s and 260 km. Fennoscandia starts at 27.11 s and 161 km and ends at 41.71 s and 260 km. Barents starts at 27.17 s and 161 km and ends at 41.72 s and 260 km. These two curves do not cross each other. From an offset of 160 km to 175 km the first onset arrive before the three curves, from 175 to 196 km the three travel-time curves arrives before the onset. From 196 km and throughout the section the onset arrive before the travel-time curves. At the end of the line the three travel-time curves plot inbetween two onsets, the first at 38.67 s and a second at 45 s.

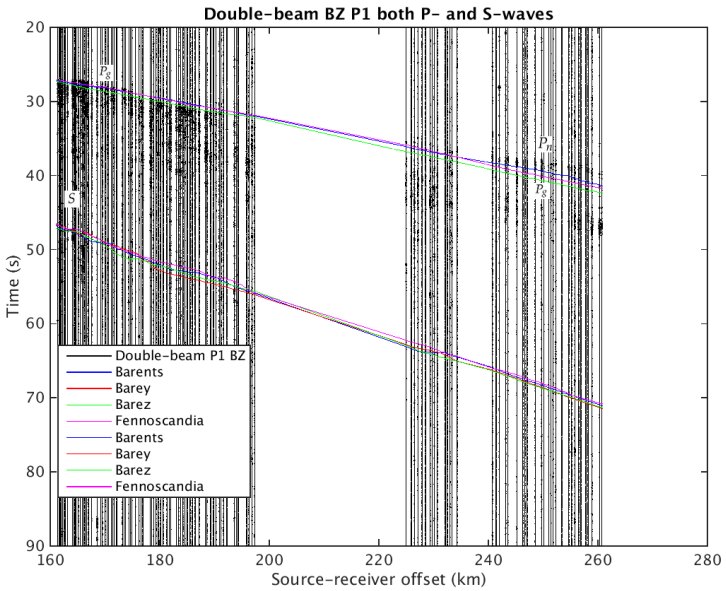

Figure 3.2: Double-beam of $P1_S$ BZ, where both P- and S-wave travel-time curves from Barents, Barey, Barez and Fennoscandia are plotted.

The S-wave travel time curves can be seen in **Figure 3.2**, here Fennoscandia start at 46.64 s, Barents at 46.92 s and Barey and Barez at 46.99 s. Fennoscandia and Barents crosses twice, Fennoscandia ends at 70.81 s and 260 km, Barents ends at 71.06 s and 260 km, Barez ends at 71.29 s and 260 km and Barey ends at 71.45 s and 260 km. From 160-175 km the onset arrives before any of the travel-time curves, the onset starts at 45.74 s at 160 km, after ~175 km all the four travel-time curves arrive before the onset.

HSPB P1

On refraction profile $P1_h$ the P-wave travel-time curves are plotted on top of the source-beam of the vertical component. All the P-wave travel-time curves plots on top of each other throughout the entire section, the curve starts at 10.26 s and 61.48 km, 6.01 s before the main onset at 16.27 s and ends at 18.88 s and 116 km, 3.94 s before the main onset at 22.82 s. The three S-wave travel-time curves for Barents, Barey, Barez and Fennoscandia plots on top of each other until an offset of ~90 km, after this the Barents, Barey and Barez plot on top of each other throughout the section, while Fennoscandia plots below, see **Figure 3.3**. The S-wave travel-time curves starts at 16.88 s and 61.48 km, 0.31 s after the main onset and 10.98 s before the second onset. The travel-time curves plot ontop of each other throughout the enitire section and ends at 31.19 s, while the second onset can be found 8.07 s after.

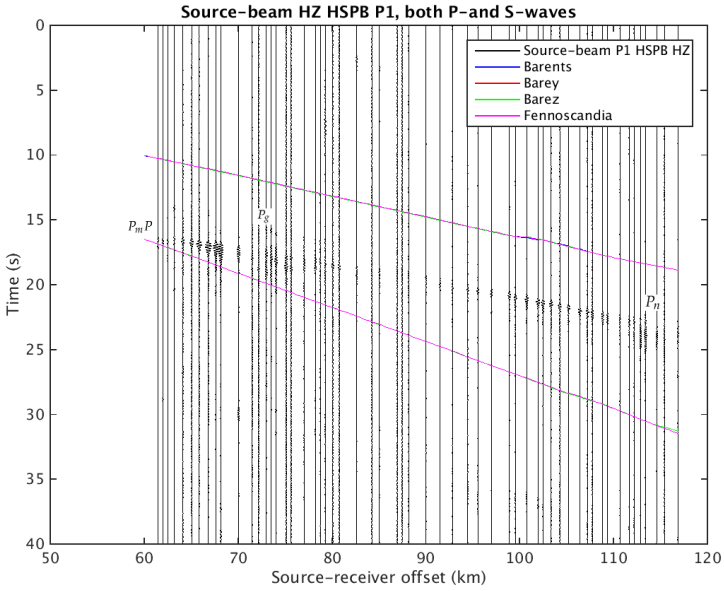

Figure 3.3: Source-beam of P1_h HZ, where P- and S-wave travel-time curves from Barents, Barey, Barez and Fennoscandia are plotted.

HOPEN P1

Travel times for the 1D models plotted on top of the vertical source-beam from $P1_{h0}$ can be seen in **Figure 3.4**. As on HSPB both the different P- and S-wave travel-time curves are overlapping the first 90 km, i.e., until an offset of 130 km.

After 135 km the travel-time curves for the P-waves are plotted in in the order: Fennoscandia, Barez, Barey and Barents throughout the section. Fennoscandia ends at 27.89 s, Barez at 27.9 s, Barey at 27.9 s and Barents at 27.92 s. The S-wave travel-time curves are plotted

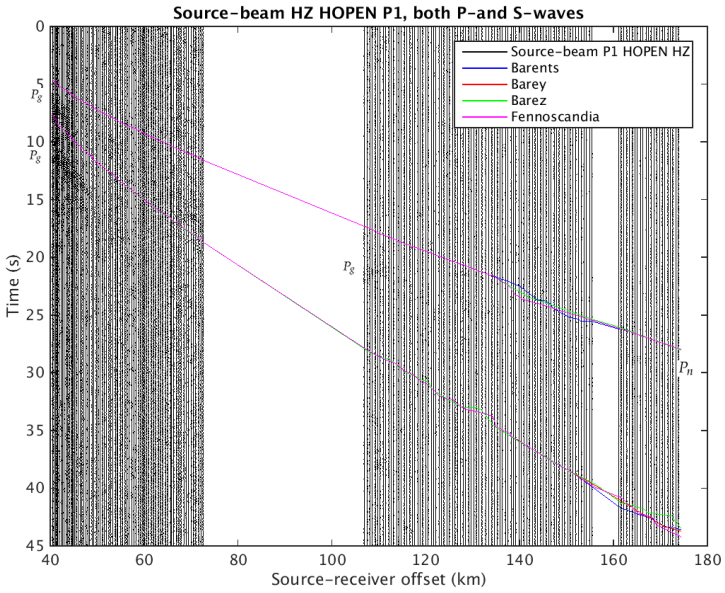

Figure 3.4: Source-beam of $P1_{ho}$ HZ, where both P- and S-wave travel-time curves from Barents, Barey, Barez and Fennoscandia are plotted.

in the order Barez, Barents, Barey and Fennoscandia, they end at 43.2 s, 43.48 s 44.23 s and 44.08 s, respectively.

3.3.2 Travel-time curves from Barents50

The P- and S-wave travel times from Barents50 plotted on top of $P2$ can be found in **Figure 3.5**. The P-wave travel-time curve starts at 37.64 s, 1.82 s before the onset and ends at 57.86 s, 1.49 s before the onset. The S-wave comes in at 65.58 s and ends at 100.8 s, this travel-time curve plots ~ 15 s before the weak S-wave onset starting at ~80 s.

The travel-time curves for P- and S-waves from Barents50 plotted on top of $P1_s$ can be seen in **Figure 3.6**. The P-wave travel-time curve starts at 24.61 s and 161.4 km, 1.66 s before the onset and ends at 37.3 and 260.7 km, 1.45 s above the onset. The S-wave travel-time curve starts at 45.52 s and 161.4 km, 1.3 s above the onset. The curve ends at 68 s and 260.7 km, here there are no onset in the vicinity.

The travel-time curves for the P- and S-waves from Barents50 plotted on top of the vertical source-beam for $P1_h$ can be seen in **Figure 3.7**. The P-wave travel-time curve starts at 11.43 s, 4.84 s before the first onset and it ends at 19.67 s 3.15 s before the onset. The S-wave travel-time curve starts at 20.08 s, 7.48 s before the second onset and ends at 34.46 s, 4.80 s before the second onset. The travel-time curve for the S-wave crosses the first onset at 20.7 s and 63.9 km.

In **Figure 3.8** the P- and S-wave travel times for Barents50 can be found on top of the

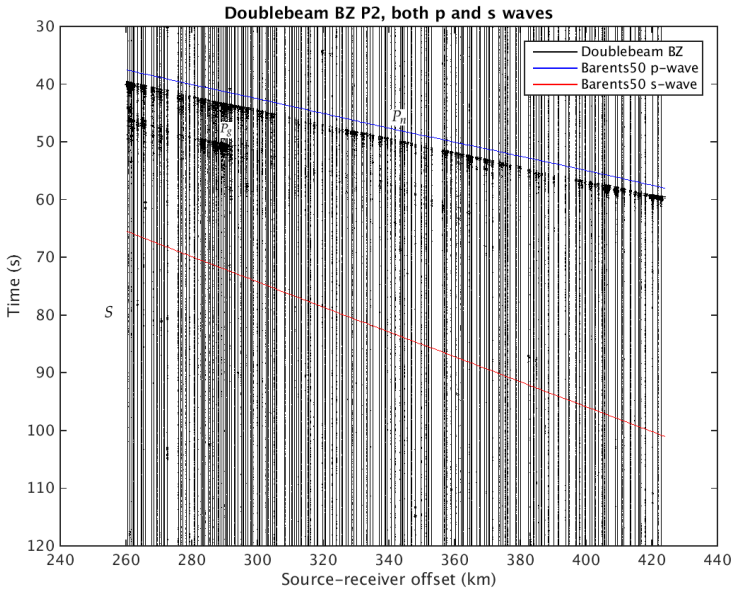

Figure 3.5: Double-beam of $P2$ BZ, travel-time curves from Barents50, P-wave travel-time curve in blue and S-wave travel-time curve in red.

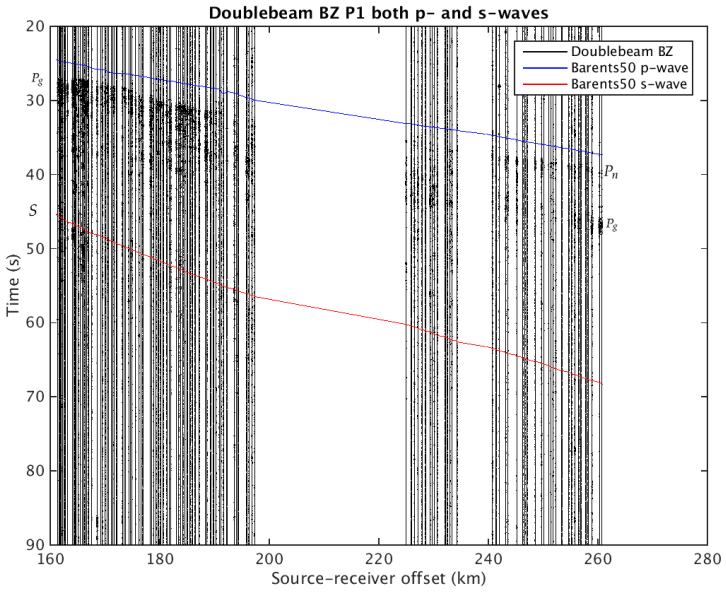

Figure 3.6: Double-beam of $P1_S$ BZ, travel-time curves from Barents50, P-wave travel-time curve in blue and S-wave travel-time curve in red.

vertical source-beam of $P1_{h0}$. The P-wave travel-time curve starts at 6.11 s, 0.47 s after the first onset at 5.64 s, the travel-time curve ends at 28.24 s, 0.87 s before the onset. The travel-time curve for the S-wave plots at 11.19 s, 0.71 s after the onset at 10.48 s and it ends at 49.21 s, the S-wave onset is not that well defined here. In **Figure 3.9** the large offset S-wave

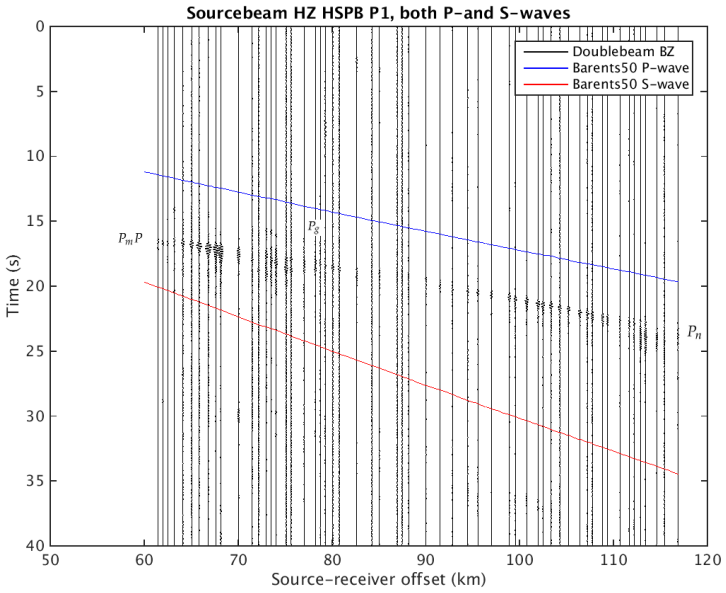

Figure 3.7: Source-beam of $P1_h$ HZ, travel-time curves from Barents50, P-wave travel-time curve in blue and S-wave travel-time curve in red.

onset is visible at 35.3 s and 108.2 km, the travel-time curve plots 0.9 s before the onset here.

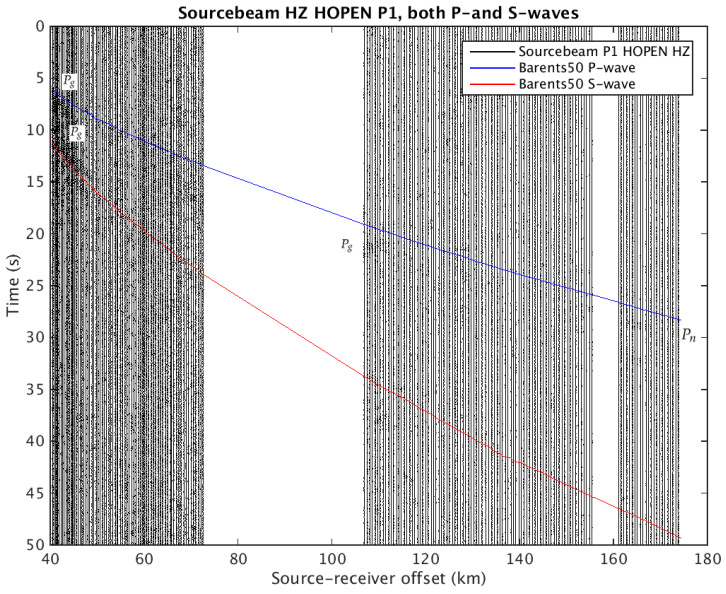

Figure 3.8: Source-beam of $P1_{ho}$ HZ, travel-time curves from Barents50, P-wave travel-time curve in blue and S-wave travel-time curve in red.

On the larger offsets the P-wave travel-time curve plots ~0.8 s before the onset from 20.78-

28.6 s and 107-165 km.

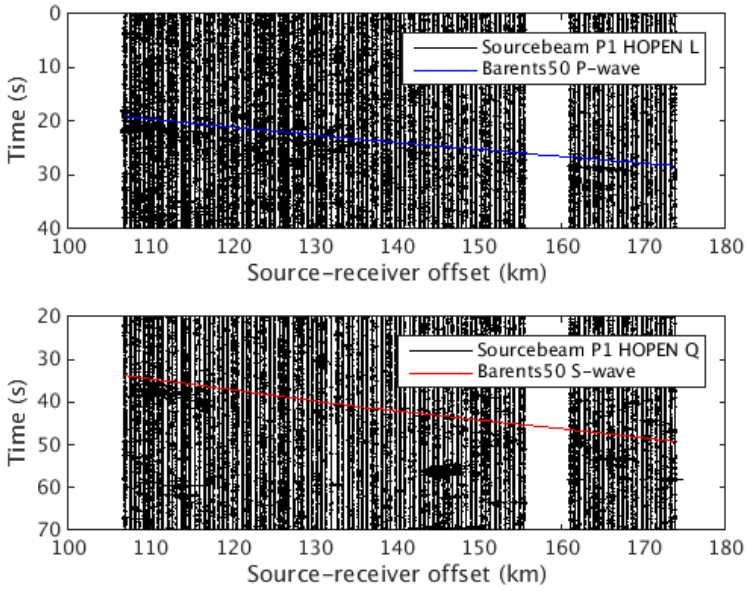

Figure 3.9: Top: source-beam of $P1_{ho}$ L, every trace is plotted and scaled by a factor of 0.02. Bottom: source-beam of $P1_{ho}$ Q, every trace is plotted and scaled by a factor of 0.01. P-wave travel-time curve in blue and S-wave travel-time curve in red.

3.3.3 Raypaths in the Barents50 3D model

An overview of the area the velocity and density model covers and different rayfans for all the different refraction lines can be seen in **Figure 3.10**. A topographic map has been overlain and shifted up.

SPITS P2

In **Figure 3.11** and **A.163** the raypats through Barents50 for P- and S-waves are plotted. All the upgoing P-waves have been refracted at a depth of ~40 km and ~8 km/s, the S-wave travel paths are quite similar but the velocity at ~40 km is ~4.5 km/s. Both the P- and S-wave rayfans have shadow zones in the middle part of the line, the incidence angles for the upcomming rays at the line are 37.5-38 °.

The three dimensional view of raypaths can be found in **Figure A.162**.

SPITS P1

The raypaths through Barents50 from the central station of SPITS and to the refraction line $P1_s$ can be seen in **Figure 3.13** and **A.164**. The upcoming rays in the western most section

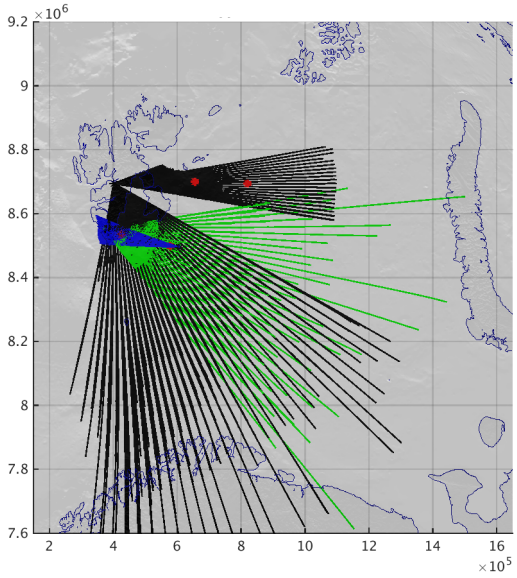

Figure 3.10: Rayfans from SPITS in black, green are raypaths from HSPB and blue are raypaths from HOPEN. The small red crosses are the end points of the aqcusition lines. The map has been plotted in UTM coordinates, UTM zone 34.

of refraction line $P1_S$ have travelled with a maximum velocity of ~7 km/s, at the eastern more parts of the line the upcoming rays have travelled with a maximum velocity of ~8 km/s. The rays travelling in 3D can be seen in **Figure 3.12**.

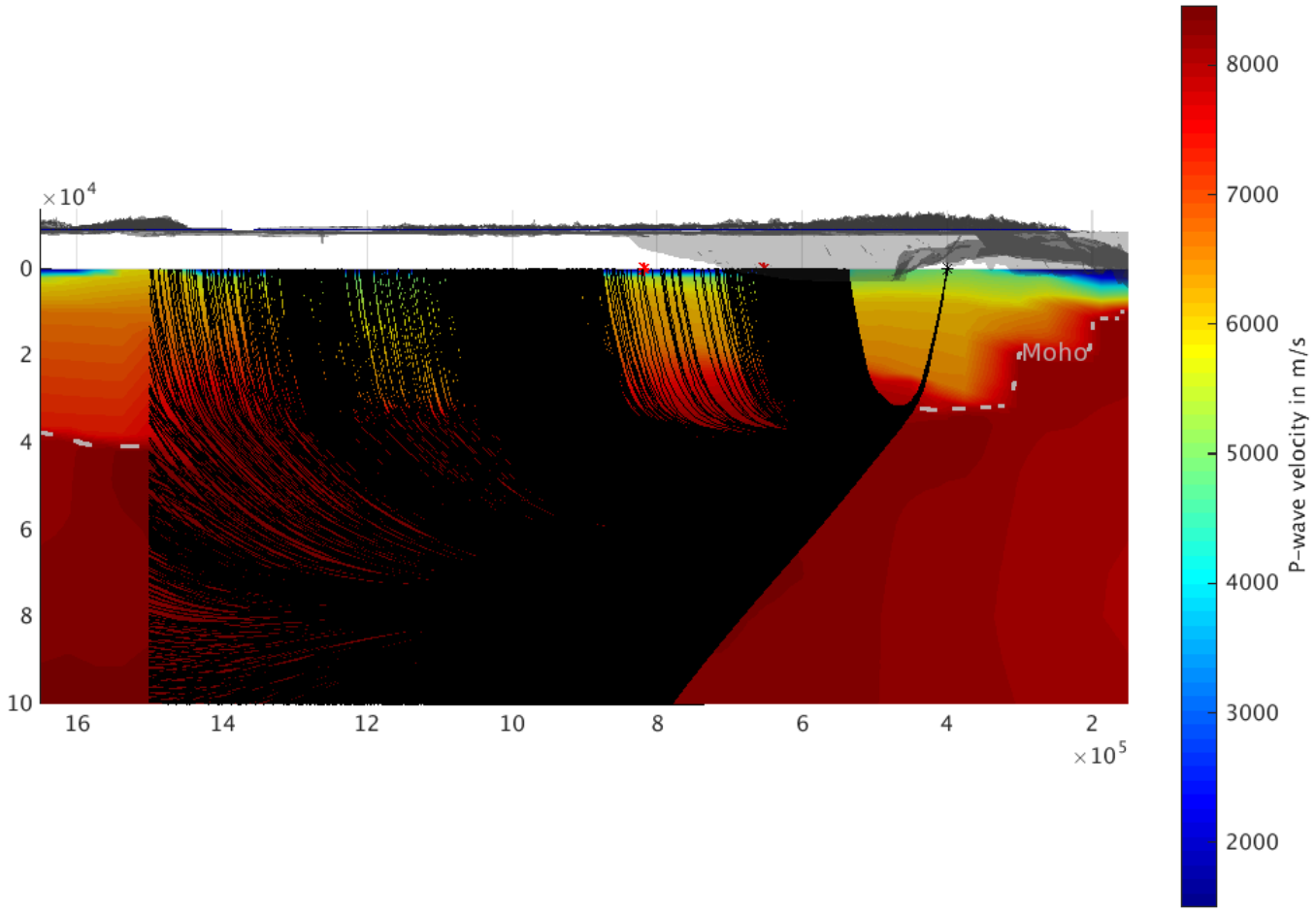

Figure 3.11: Raypaths of P-waves from SPITS (SPB3) towards *P*2, plotted every 10th ray. Endpoints of *P*2 are red crosses. View towards south. The depth is in meter and the velocity is in meter per second. The velocity cube is plotted in UTM coordinates, UTM zone 34.

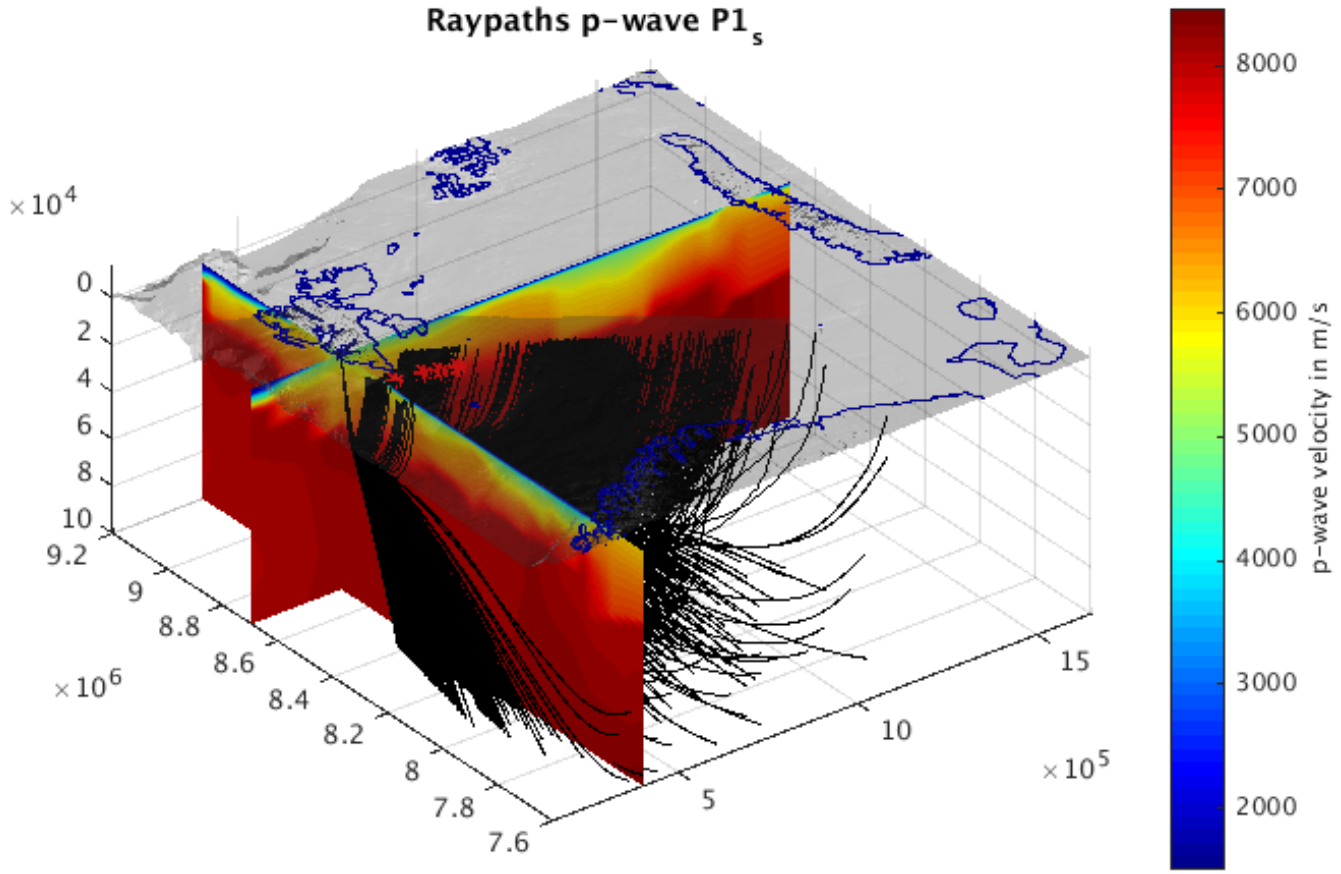

Figure 3.12: Raypaths of P-waves from SPA0 towards $P1_s$ through the Barents50 3D model with Etopo bathymetry slightly shifted up. Endpoints of the two sections of $P1_s$ plotted as red crosses. View towards north-west. The z-axis is depth in meters positive downward. The velocity cube is plotted in UTM coordinates, UTM zone 34

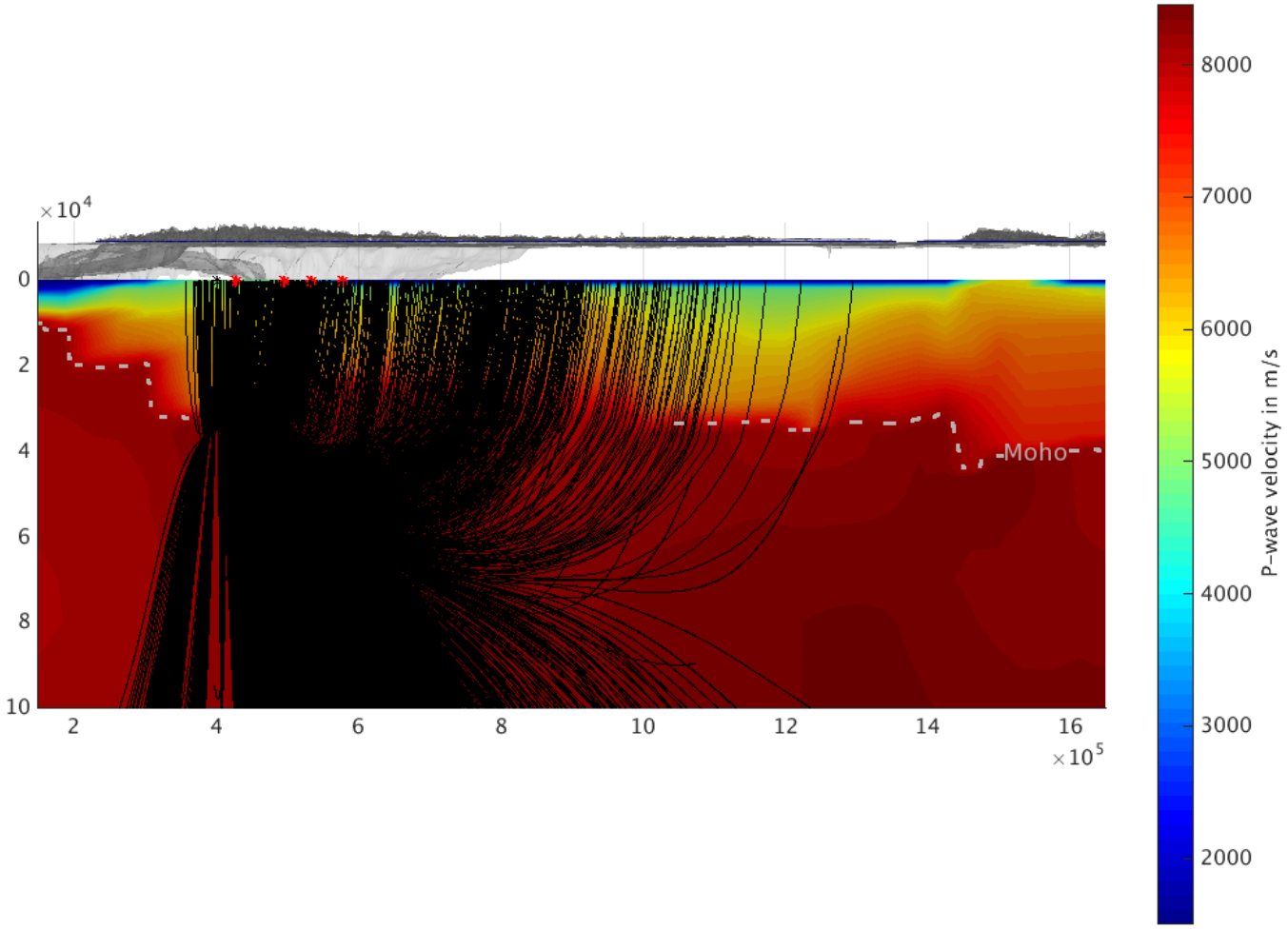

Figure 3.13: Raypaths of P-waves from SPITS (SPA0) towards $P1_s$. Endpoints of the two sections of $P1_s$ plotted as small red crosses. View towards north. The depth is in meter and the velocity is in meter per second. The velocity cube is plotted in UTM coordinates, UTM zone 34.

The S-waves for the small offsets of line $P1_s$ travels with a maximum velocity of 3.5-4 km/s. In the second part of the line the waves travel with a maximum velocity greather than 4 km/s, see **Figure A.164**.

HSPB

Raypaths for P- and S-waves from HSPB to the line $P1_h$ can be seen in **Figure 3.14** and **A.165**. The P-wave rays travel both in crust and upper mantle, all rays up to an incidence angle of 29°travels in the upper mantle. Rays with a larger incidence angle travel in the crust. In

vicinity of the second cross the reflected waves and the refracted waves arrive at the same time, this is both seen for P- and S-waves. The S-wave raypaths have similarities with the

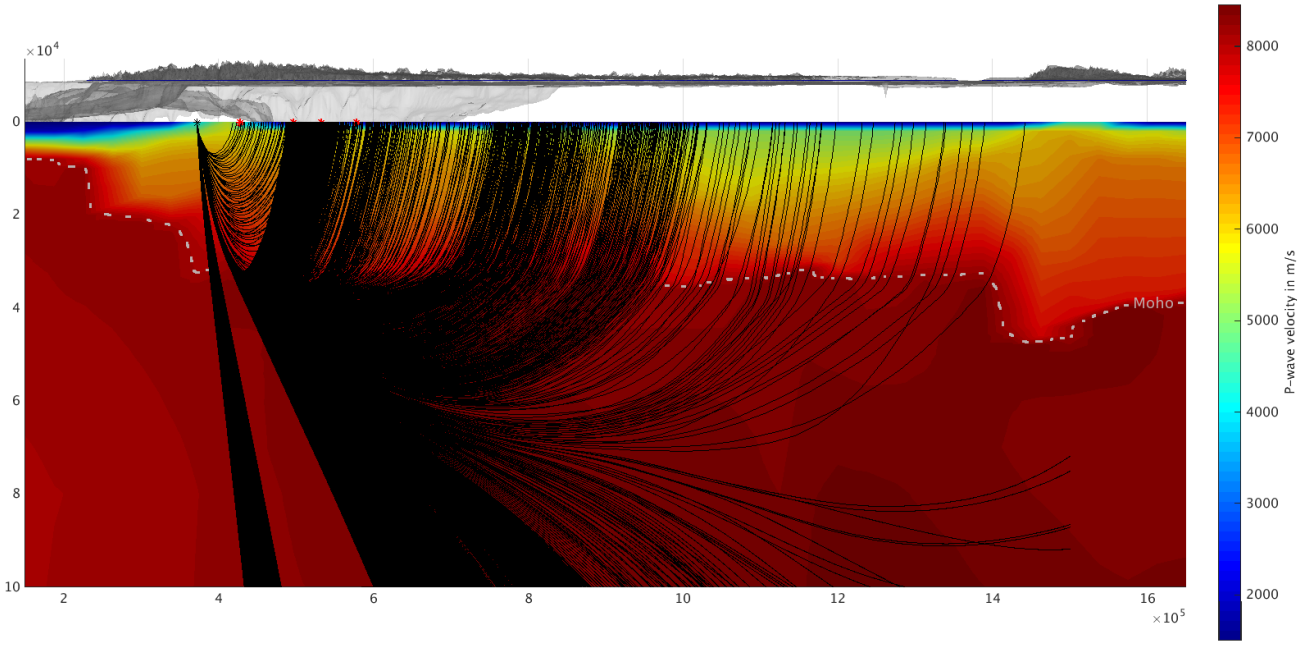

Figure 3.14: Raypaths of S-waves from HSPB towards $P1_h$. Endpoints of the two sections of $P1_h$ plotted as small red crosses. View towards north. The depth is in meter and the velocity is in meter per second. The velocity cube is plotted in UTM coordinates, UTM zone 34.

P-wave raypaths, only the rays comming up at the largest offsets of $P1_h$ have travelled in the mantle. The upcomming rays for the western most part of the line have mainly travelled in the upper and lower crust, the upcomming rays at the latter part of the line have travelled both in the crust and upper mantle, see **Figure A.165**.

A plot of the three dimensional view can be found in **Figure A.166**.

HOPEN

The raypaths for P- and S-waves can be seen in **Figure 3.15** and **A.167**. The P-wave rays travel in the upper crust the first part of the line, with a velocity of ~3.5-6 km/s. While the rays arriving at the second part of the line travel in the lower crust/upper mantle with a velocity of ~6-8 km/s. The S-wave rays travel as the P-waves both in the upper crust and the lower crust/mantle. The S-wave velocities vary between ~2.5-4.4 km/s, see **Figure A.167**.

The general shape of the different wave phases are very similar for the P- and S-waves traveling towards $P1_{ho}$. A 3D plot of the raypaths can be seen in **Figure A.168**.

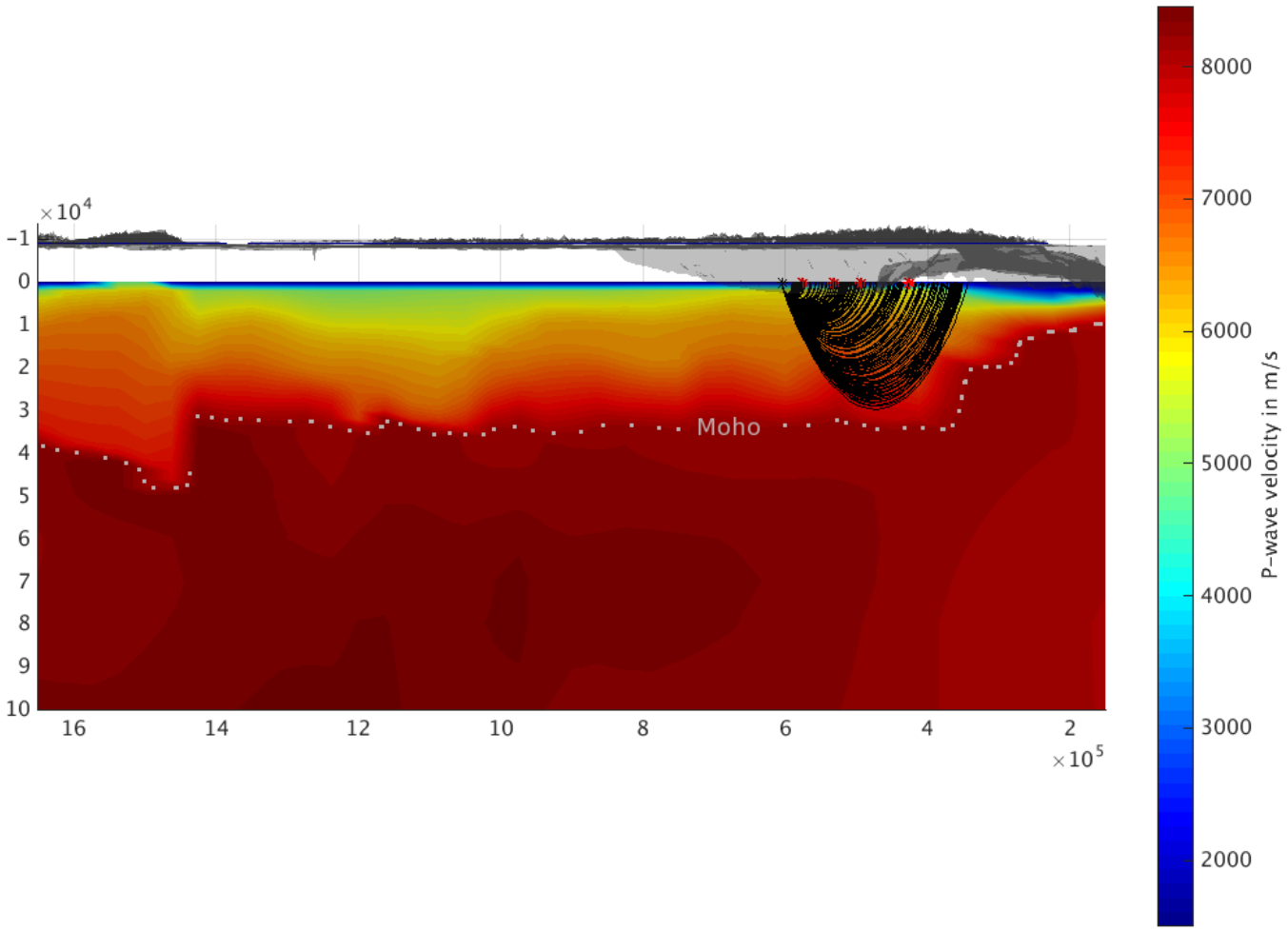

Figure 3.15: Raypaths of P-waves from HOPEN towards $P1_{ho}$. Endpoints of the two sections of $P1_{ho}$ plotted as small red crosses, every 25th ray are plotted. View towards south. The depth is in meter and the velocity is in meter per second. The velocity cube is plotted in UTM coordinates, UTM zone 34.

3.3.4 Synthetic seismograms

Frequency wavenumber integration was performed on all the 1D models and synthetic seismograms were created. In addition data from Barents50 were extracted along the refraction lines and subsequent 1D models were created and frequency wavenumber integration was performed to create synthetic seismograms. All the synthetic seismograms have been scaled by a factor of 10 in this section.

The 1D velocity models of Barents, Barey, Barez and Fennoscandia can be found in **Table A.1, A.2, A.3** and **A.4**.

Synthetic seismogram Barents, Barey, Barez and Fennoscandia

In **Figure 3.16** the synthetic seismogram for Barents is plotted in reduced time. FK- integration produces both body waves and surface waves. One arrival that can be seen throughout the section, it starts at t = 0 s and ends at t = 79.7 s. Another onset are also visible throughout the entire section, it starts at t = 0 s and ends at 11 s. This onset is however intersected by another arrival below which starts at 52 km and 5.95 s they seem to intertwine at 336 km and 12.53 s. From this offset the onset are rather flat throughout the section. At an offset of 63.76 km and 9.28 second another arrival appears, this arrival can be followed until 156.8 km and 12.89 s, here the amplitude interfere with the amplitudes from the two onsets above and there is not that clear is the onset continues or not. Two other arrivals can also be seen, at 146.7 to 430 km in the time-range 22.48-25.93 s, this arrival is rather flat. The arrival below ranges from 223.1-430 km and in the time-range 38.11-45.38 s, this onset is slightly dipping. The same onsets are also seen for the models Barey, Barez and Fennoscandia.

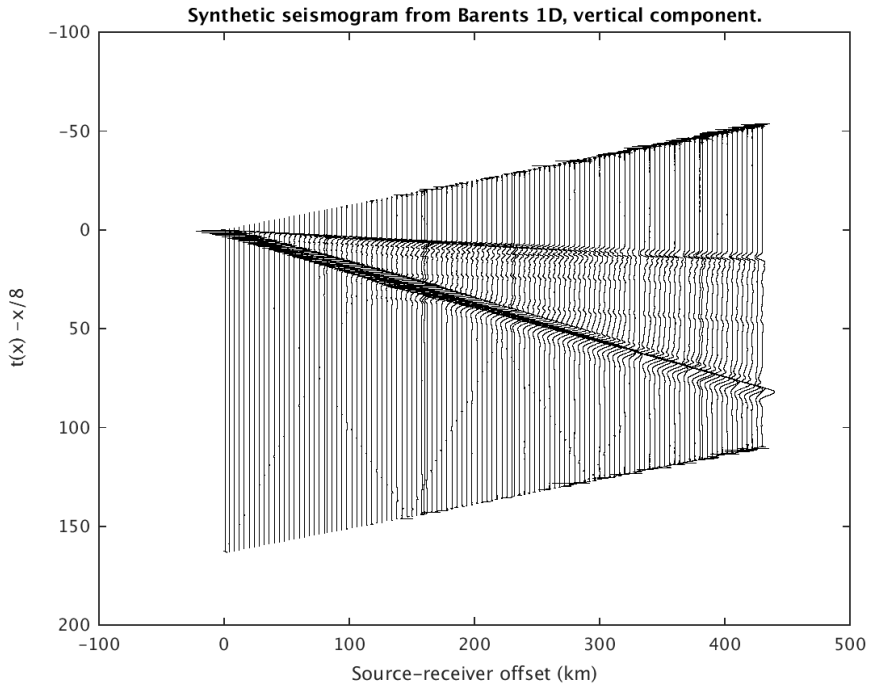

Figure 3.16: Synthetic seismogram from the 1D model Barents, vertical component.

Synthetic seismogram for Barents50 $P1_S$

The synthetic seismogram for the 1D model for Barents50 at line P1 can be seen in **Figure 3.17**. A clear arrival can be seen throughout the entire section, it starts at t = 0 and ends at 75.98 s, the phase of the arrival changes throughout the section. Another onset starts at 0 s and 0 km and are clearly defined until 116 km and 9.77 s, the onset seems to continue

but the amplitude and phase is now affected by another onset that appears above from 79.99 km and 5.79 s, this onset are almost flat and can be followed until 282 km and 13.32 s. At an offset of 38.78 km and 7.415 s another arrival appears, it is well defined until an offset of 90 km and 11.03 seconds, here it interfere with the two onsets above, it does not seem to cross the closest curve above. Below this two onsets occurs, the first starts at 58.39 km and 12.48 s, this onset ends at 205.9 km and 25.04 s. The other starts at 122.4 km and 22.7 s, it appears until the end pf the section at 258 km and 33.45 s.

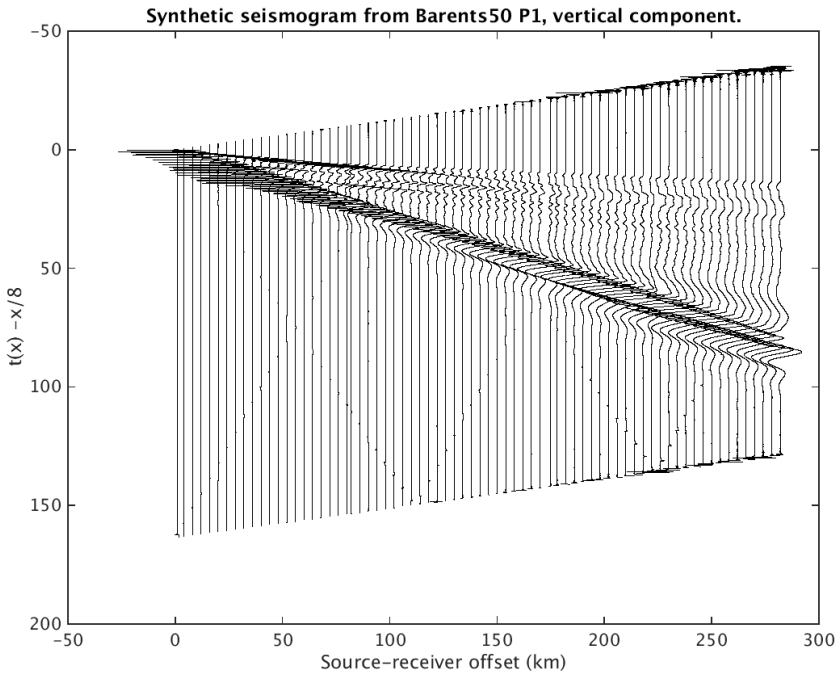

Figure 3.17: Synthetic seismogram from the an extracted 1-D model for P1 from Barens50, vertical component.

On all the synthetic seismograms there are minor numerical artifacts, at offsets larger than 100 km high amplitudes occur in the beginning and end of each trace, in addition there are also some minor artifacts appearing as chevron lines beneath and crossing some of the arrivals.

4 1D inversion

4.1 1D inversion method

Inversion of refraction profiles can be done in several ways and two methods will be presented here, following Diebold and Stoffa (1981) and Clayton and McMechan (1981). Diebold and Stoffa (1981) extracts travel-time information from the data and perform a Wiechert-Herglotz integration subsequently creating a velocty-depth profile.

The travel-time equation, **Equation 4.1**, can be described as a sum of the functions of horizontal and vertical ray slowness. The horizontal component can be found from the slope, also denoted ray parameter. While the vertical component is the interept time. The intercept time is a rather simple function of the ray parameter and in reality a function of the velocity depth structure, hence mapping the data into $\tau - p$ domain makes velocity-depth inversion much easier (Diebold and Stoffa, 1981).

The ray parameter and the intercept time is determined by the slope and intercept of travel-time data and the travel-time data comes from travel-time picking. The derivation below follows Diebold and Stoffa (1981), Bessonova et al. (1974) and Stein and Wysession (2013). The traveltime equation decomposed in vertical and horizontal components can be expressed as:

$$\Delta T = p\Delta X + q\Delta Z \tag{4.1}$$

Where the total travel-time for a stack of homogenous horizontal layers is:

$$T = pX + n\sum_{j=1}^{n} q_j Z_j \tag{4.2}$$

Equation 4.2 describes a line that is tangent to the travel-time curve at (T, X), with corresponding slope p and intercept time:

$$\tau = 2\sum_{j=1}^{n} q_j Z_i = T - pX \tag{4.3}$$

The travel-time inversion can be found by taking the recursive solution of the intercept time equation, **Equation 4.3**, when $p_k > p_{k+1}$ i.e., the velocity must increase with depth. Where each p represents the slowness of some layer and $u_1 = p_1$.

$$Z_1 = \frac{\tau(p_2)/2}{(u_1^2 - p_2^2)^{1/2}} \tag{4.4}$$

and:

$$Z_2 = \frac{\tau(p_3)/2 - Z_1(u_1^2 - p_3^2)^{1/2}}{(u_2^2 - p_3^2)^{1/2}} \tag{4.5}$$

The general τ-sum recursion can then be written as:

$$Z_k = \frac{\tau(p_{k+1})/2 - \sum_{j=1}^{k-1} Z_j(u_j^2 - p_{k+1}^2)^{1/2}}{(u_k^2 - p_{k+1}^2)^{1/2}} \tag{4.6}$$

Travel-time picking may bias the inversion result and pick uncertainty should be determined. Zelt and Forsyth (1994) define the pick uncertainty in milliseconds (ms) as the square root of the ratio of the trace energy in a 250 ms window before and after the pick, see **Table 4.1**.

Table 4.1: Pick uncertainty σ in milliseconds found by taking the square root of the ratio of the trace energy on either side of the pick. Table modified from Zelt and Forsyth (1994).

r	σ (ms)
> 10	20
> 4	35
> 2	50
> 1.75	75
> 1.5	100
$\leq$ 1.5	125

4.2 Implementation

An inversion routine was written in MATLAB and travel-time picks were made with the ginput2 program written by Carlos Adrian Vargas Aguilera. A simple pick uncertainty script following Zelt and Forsyth (1994) was made to calulate the uncertainty related to each picked datapoint.

4.3 Results

4.3.1 1D velocity models

On all the profiles P-wave onsets were picked, only on $P1_h$ the S-wave onset was well enough defined to pick.

Number of points picked for the inversion varied between the different refraction profiles, for $P2$ 330 points were picked, for $P1_s$ 271 points, for $P1_h$ 104 points were picked at the P-wave onset and 88 points were picked at the S-wave onset, and for $P1_{ho}$ 166 points were picked. The root mean square (rms) can be found in **Table 4.2**. For P2 and $P1_s$ the pick uncertainity were slighly lower than 75 ms, i.e., r was above 1.75. The uncertainty for $P1_h$ P-wave, $P1_h$ S-wave and $P1_{ho}$ were a bit lower than 100 ms, i.e., r was above 1.5. Picks with a pick uncertainty less than 0.8 were removed i.e., 12 picked points from $P2$ were removed, from $P1_s$, $P1_h$ P-wave and $P1_h$ S-wave 37, 24, and 18 picks werre removed, respectively. For $P1_{ho}$ 34 picks had a pick uncertainty less than 0.8, 27 of them came from the large offset and they were re-picked. After re-picking the 27 picks had a mean pick uncertainty of 0.88, in order to have data from the large offset these picks were used in the inversion and total number of removed picks for $P1_{ho}$ were 7.

Table 4.2: Pick rms for the different profiles

Profile	Mean rms	Maximum rms	Minimum rms
$P2$	1.7729	3.8624	0.5367
$P1_s$	1.7234	2.1271	0.5861
$P1_h$ P-wave	1.6897	2.6951	0.5145
$P1_h$ S-wave	1.6011	3.8752	0.5542
$P1_{ho}$	1.1654	3.4175	0.1361

All 1-D velocity models from the inversion have been plotted together in **Figure 4.1**. In all four models the velocities the first 10 km lie between 4 and 5.5 km/s, from 10-20 km the velocities ranges between 5.5 and 6.5 km/s. The last depth point for $P1_h$ is at 23.9 km and 6.35 km/s. From 20-35 km depth the velocities ranges from 6.5-8.1 km/s. The 1-D model from $P1_{ho}$ has the highest velocities the first 20 km, at ~20-25 km depth all the models have velocities between 6.2 and 6.4 km/s, $P1_{ho}$ ends at 29.8 km and 8.03 km/s. The 1-D model for $P2$ has the lowest velocities in the first 15 km, the next 15 km $P2$ has velocities between 6.2 and 6.6 km/s, the 1-D model for $P1_s$ are in between $P1_{ho}$ and $P2$ with the last point at 30.9 km and 8.06 km/s. Upper crustal velocities for HOPEN surpass the three other inverted models with ~0.7 km/s at a depth of 3 km.

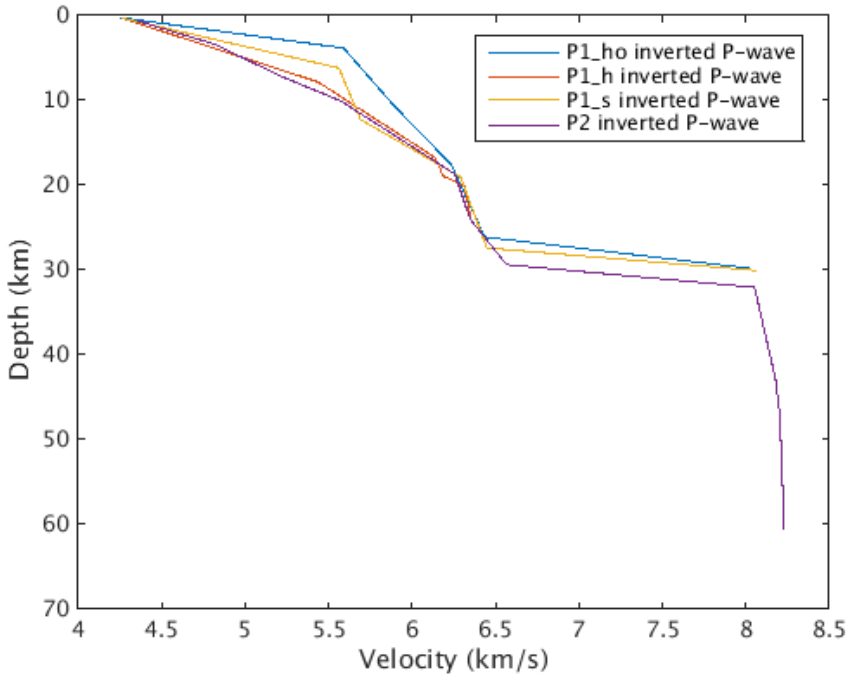

Figure 4.1: 1D velocity models from inversion, the blue line = HOPEN, red line = HSPB, the yellow line = SPITS $P1_s$ and the purple line = SPITS $P2$

All the different 1D velocity models used in the FK integration can be seen in **Figure 4.2** and **4.3**. In both figures the inverted 1D velocity models are plotted in bold. The S-wave inversion of $P1_h$ in **Figure 4.3** the

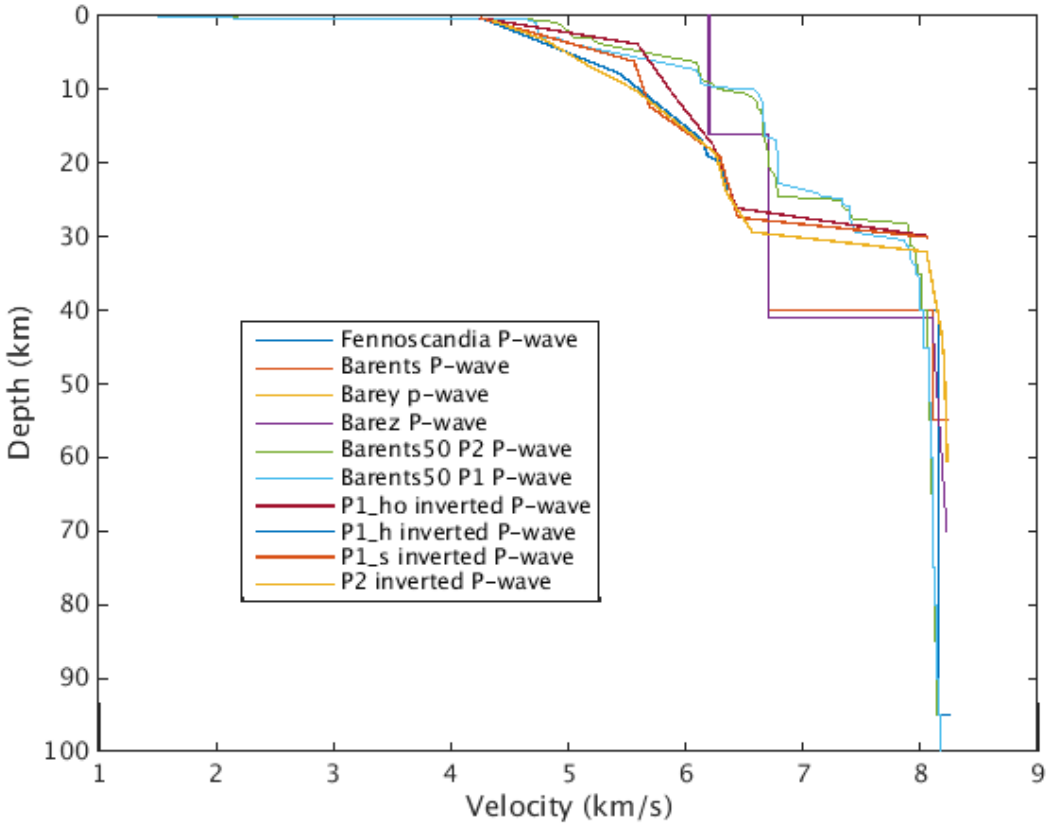

Figure 4.2: 1D velocity models for P-waves, the inverted 1D models are the models with low crustal velocities.

4.3.2 Synthetic seismograms

The synthetic seismograms has been calculated with the inverted P-wave velocity. The density and S-wave velocity values is an average of Barents, Barey, Barez, Fennoscandia and the two 1D models from Barents50 at the specified depths. The P-, S-wave and density values used in the inversion can be found in table A.5, A.6, A.7 and A.8. All the seismograms in this section are plotted in reduced time, for the x-t seismograms see **Figure A.172, A.173, A.174** and **A.175**. The synthetic seismograms in this section have been scaled by a factor of 20 in addition to a maximum trace amplitude scaling.

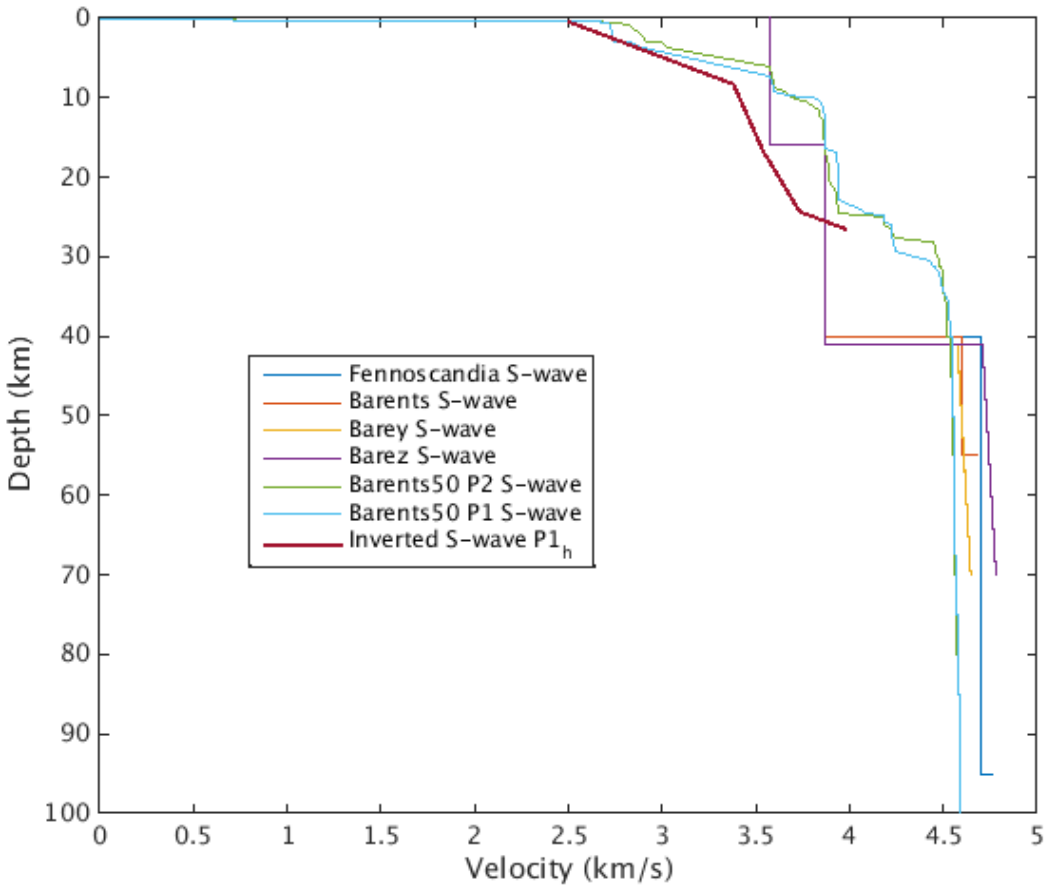

Figure 4.3: 1D models for S-waves, the inverted S-wave for HSPB can be seen in bold.

SPITS P2

The synthetic seismogram for an inverted 1-D velocity model for *P*2 can be seen in **Figure 4.4**. A high amplitude onset can be seen throughout the entire section, it starts at 0s and 0 km, and ends at 78.8 s and 430 km. Another onset is clearly defined from 0s 0 km at this 217 km and 14 s the onset changes phase and seems to interfere with an onset starting at 145 km and 7.97 s this onset is rather flat and ends at 430 km and 17.57 s, the onset below is ends at 430 km and 24.7 s. Three other possible onsets can also be found at 78-158 km and 9.5-13.3 s, 146.6-428.8 km and 18.9-34.8 s and in the range 138-429 km and 22.9-50.6s. The onset in the range 138-429 km starts as a dipping onset, after 249 km and 39.4 s the onset flattens out and remain rather flat throughout the section.

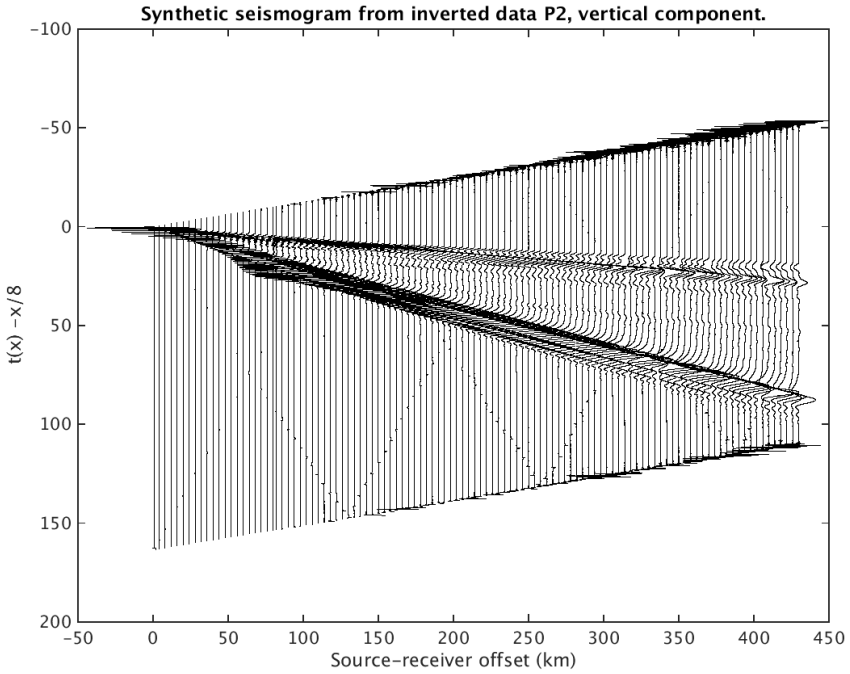

Figure 4.4: Synthetic seismogram from the 1-D inverted velocity of $P2$.

SPITS P1

In **Figure 4.5** the synthetic seismogram for $P1_s$ can be found. As in the synthetic seismogram for $P2$ there are two main onsets dominating throughout the section. One of the two onsets starts at 0 s and 0 km and lasts until an offset of 282 km and 51.2 s. The other well defined onset starts at 0 km and 0 s as well, and can be followed throughout the entire section until 282 km and 11.12 s. This onset interfere with another onset from ~150-160 km and ~7.5-10 s, this onset is rather flat, and the distance beteen the two increases with offset. This onset is approximately flat and ends at 282 km and 11.1 s. A third onset, appears at 165.6 km and 16.9 s, this onset has much smaller amplitude than all the three other. This onset are flat, and interferes with the onset above that ranges from 0-282 km and 0-15.2 s, this interference makes it hard to see where the onset actually ends.

HSPB P1

Synthetic seismogram for $P1_h$ can be found in **Figure 4.6**. As in **Figure 4.4** and **4.5** two onsets dominate with their high amplitude, they both start at 0 km and 0 s, the upper most of them lasts until 118 km and 16.8 s while the other ends at 118 km and 59.4 s. In addition two other onsets can be identified, the upper most seem to intersect the onset from 0-16.8 s. It is not possible to find a well defined start position of this onset, but it crosses the 0-16.8 s onset at ~160-170 km and ~7-11 s, this onset lasts throughout the rest of the section and ends up

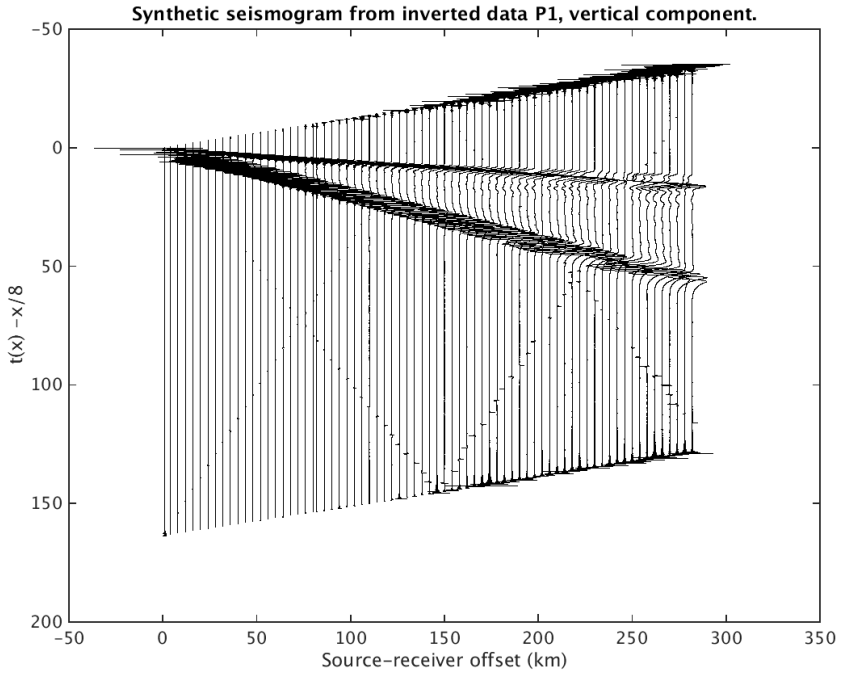

Figure 4.5: Synthetic seismogram from the 1-D inverted velocity of $P1_s$.

at 118 km and 14.3 s. Several small amplitude features appear below the interfearing onsets.

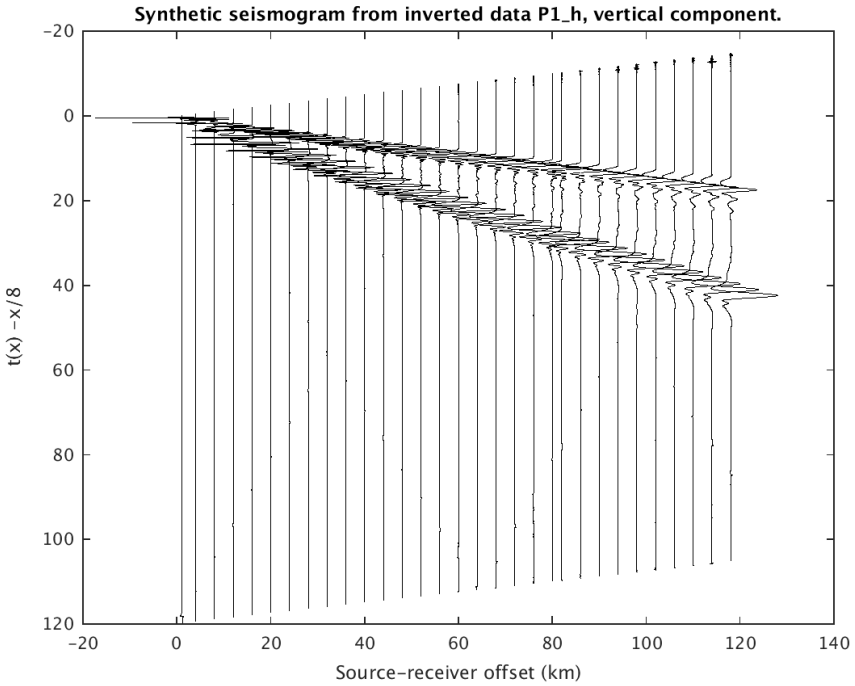

Figure 4.6: Synthetic seismogram from the 1-D inverted velocity of $P1_h$.

HOPEN P1

The synthetic seismogram for $P1_{ho}$ with a reduction velocity of 8 km/s can be seen in **Figure 4.7**. Here two large amplitude onsets dominates, one which starts at 0 s and 9 km and ends at 21.6 s and 282 km. The second large amplitude onset starts at 0 s and 0 km as well and ends at 5.3 s and 282 km, another onset appear to start at 0.6 s and 40 km, this onset is situated just above the large amplitude onset and the amplitudes interfere, this onset ends at 3.7 s and 282 km. In between the two large amplitude onsets there are three small amplitude

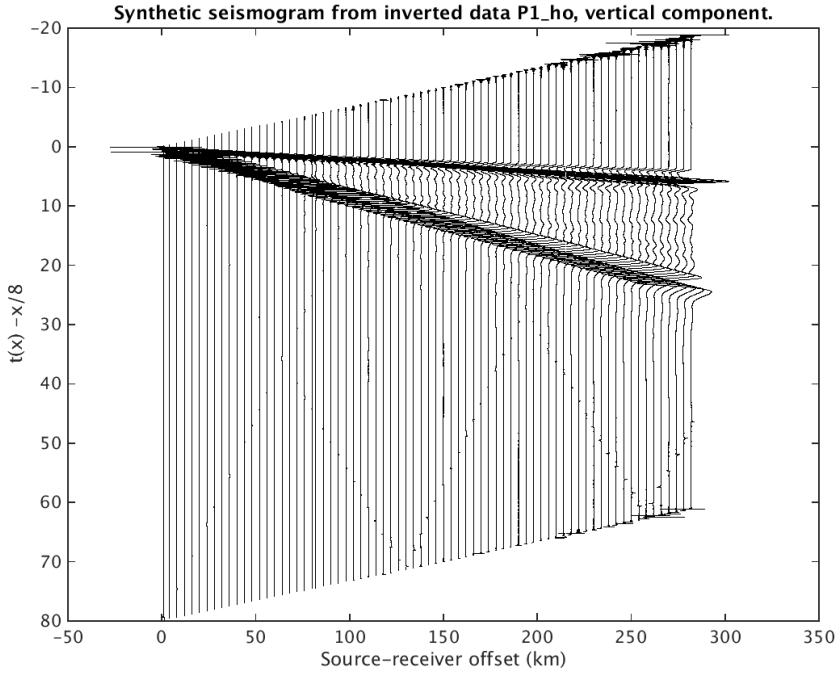

Figure 4.7: Synthetic seismogram from the 1-D inverted velocity of $P1_{ho}$.

onsets, one starts at 4.9 s and 76 km, this onset is rater flat and starts to interfere with the large amplitdue onset above at 160 km. Another onset can be seen at 12 s and 194 km, it could possibly have started before that, but it does then interfere with the onset below. This onset is flat throughout and ends at 11.9 s and 282 km. Above the lower most large amplitude onset another onset occur, this onset can be seen from 14.6 s and 214 km and until 17.5 s and 282 km.

The real data plotted on top of the synthetic data for $P2$ can be seen in **Figure 4.8**. On the far offset: 260-420 km the data from $P2$ are plotted on top, the first onset on the real data plots almost exactly on top of the synthetic first arrival, however with offset the synthetic onset plots further down than the real onset.

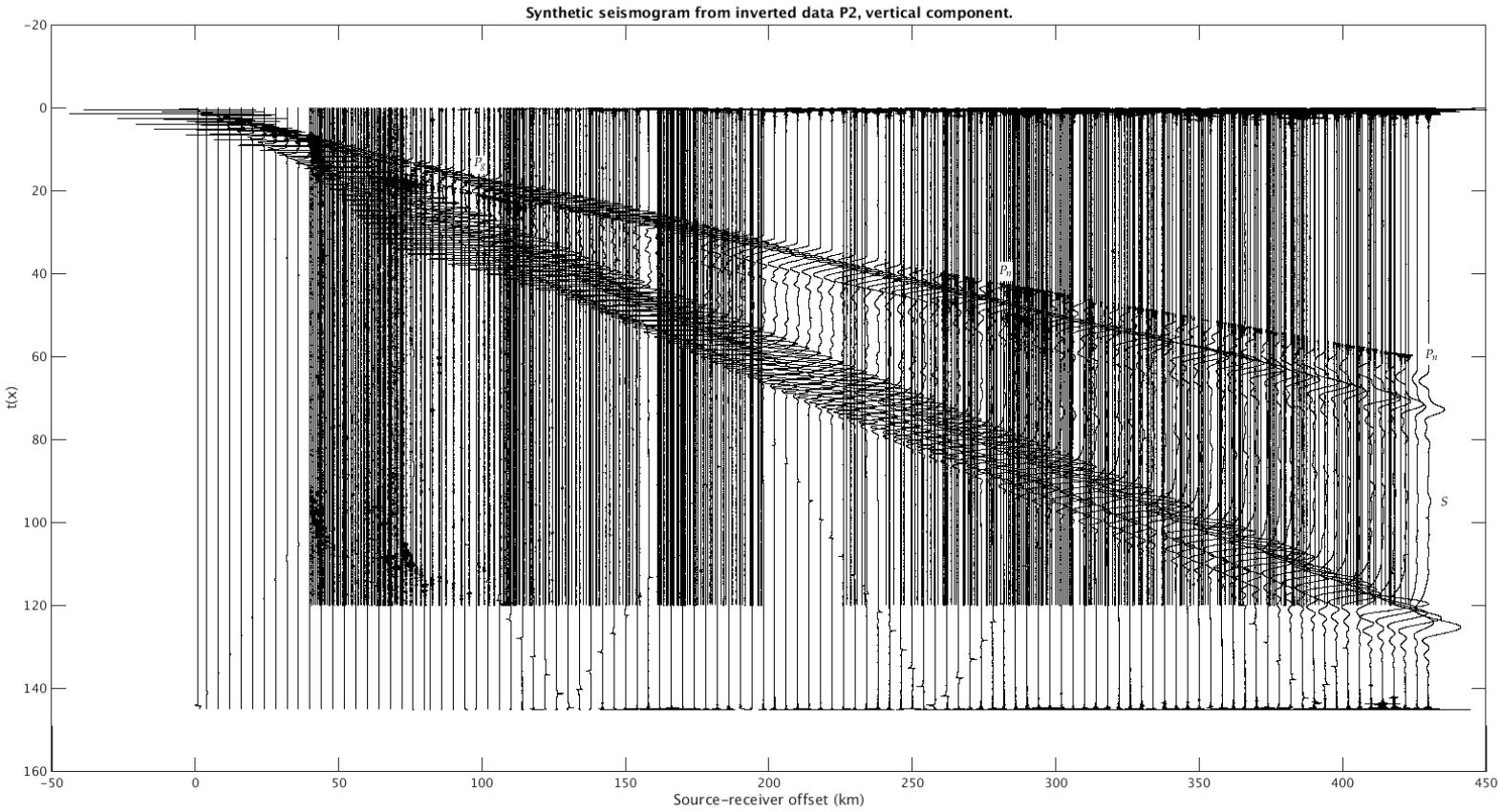

Figure 4.8: Synthetic seismogram from the 1D inverted velocity of $P2$. The double-beams of $P2$, $P1_s$ and source-beams of $P1_h$ and $P1_{ho}$ are plotted on top.

5 Discussion

From the coordinate transformations, tau-p transformations and the reduced travel-time plots it was evident that both P and S-wave phases occurred on all the four refraction profiles. Ray tracing revealed ray paths mainly through the lower crust and upper mantle for the refraction profiles. All theoretical travel-time curves from the previously published 1D models and the 3D model deviated from the real data. For $P2$ and the large offsets of $P1_s$ and $P1_{ho}$ the travel-time curves from Barents50 appeared to be shifted up 1.5-2 s, with a constant shift throughout the entire section. Unlike these profiles the two travel-time curves from Barents50 plotted ontop of $P1_h$ deviated significantly from the onsets. As indicated by the velocities the onsets on $P1_h$ had apparent velocities in the range of what would be expected from rays traveling in the crust, while P2 and the larger offsets of $P1_s$ and $P1_{ho}$ have mainly upper mantle apparent velocities. The smaller offset arrivals of $P1_s$ and $P1_{ho}$ have apparent velocities of rays traveling in the upper and lower crust. From the 1D inversion of the profiles a discrepancy in the upper to middle crustal velocities was detected. $P1_h$ was the only profile with well enough defined S-wave arrivals and hence this was the only profile with a 1D S-wave velocity model.

5.1 General velocity structure

The general velocity structure inferred from the tau-p transformations and inversion revealed similarities in crustal and upper mantle velocities between the four profiles. The composite profiles in **section 2.3.7** show how the different arrivals align with an apparent velocity of both P- and S-waves in the upper crust, lower crust and upper mantle. In **Figure 2.41** it is evident that the P-wave arrival of $P2$ and $P1_s$ matches very well in the area where they overlap, in addition they align fairly horizontally with the same reduction velocity of 8 km/s. The waves from $P2$ and $P1_s$ travel in east-west and south-north directions. Large velocity variations would have caused differences in the travel time and hence the variations in mantle velocity and or depth cannot be large between the two profiles. The P-wave onsets from $P1_h$ and $P1_{ho}$ do not align with the P-waves for $P2$ and $P1_s$, it is evident that these two onsets have travelled in the crust.

A substantial difference between the first onsets of $P1_h$ and $P1_{ho}$ occurs in the area where they overlap, here there is a visible jump between the P-wave onsets and it is evident that the crustal properties vary between these two profiles. This is also seen from the 1D inversion. Differences in shallow crustal velocities between Hornsund and Hopen are also seen in Czuba et al. (2008) and Breivik et al. (2005).

5.2 The upper mantle

The upper mantle was sampled in three directions, south-north ($P1_s$), east-west ($P2$) and west-east ($P1_{ho}$). The inverted velocities have a maximum difference in upper mantle velocity of 0.03 km/s. However the upper mantle velocity of $P2$ deviates from both the previously published 1D models and the 3D model. In previous publications of the upper mantle in the western Barents Sea the upper mantle velocities vary between 7.9-8.3 km/s and the Moho depth varies between 28-36 km (Hauser et al., 2011, and references therein). $P2$ was the only profile which sampled the upper mantle to a depth of 60 km.

The large scale change from a thin oceanic plate to a thicker continental plate is evident in the west-east section of Barents50 as seen in **Figure 5.1**. The crustal thickness increases toward east, which is also seen from tomographic models from this region. From **Figure 5.1** underplating is evident just east of Spitsbergen, this is not the case further south, e.g., at $P1$. From Barents50 it is also evident that between SPITS and the refraction line the velocity is 6 km/s or larger at ~10 km depth, faster than the inverted models in this thesis.

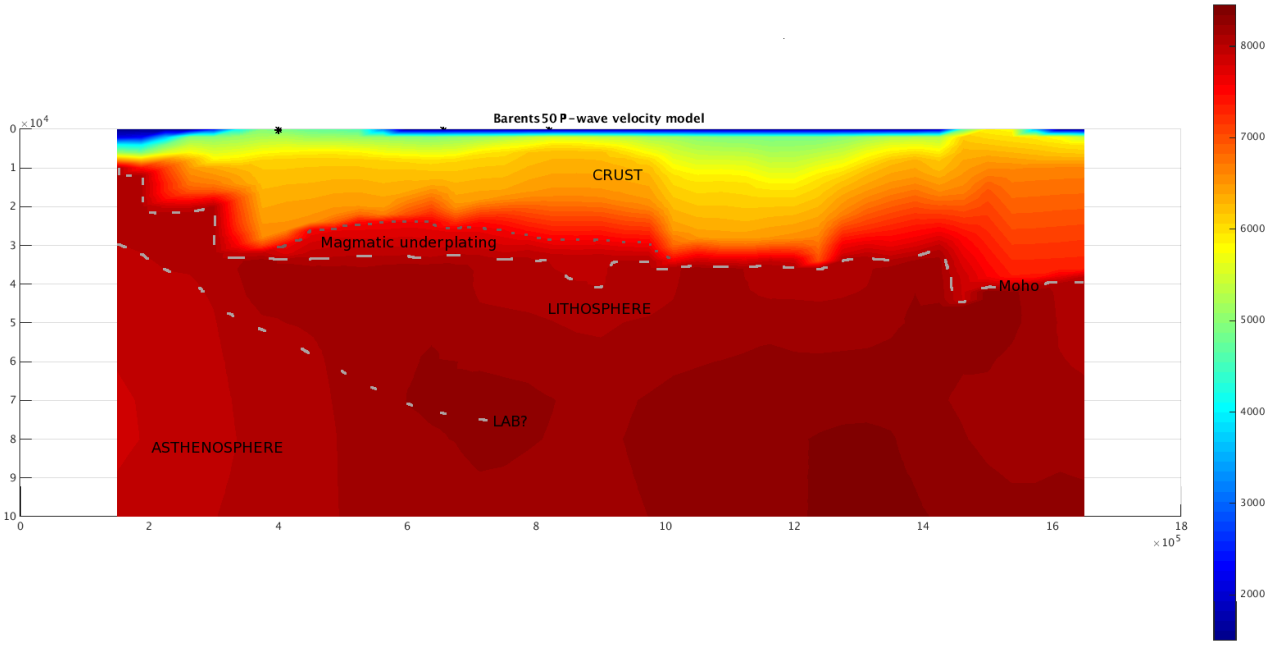

Figure 5.1: Barents50 cross section through $P2$, view towards north. Black crosses are the locations of SPITS (left) and the endpoints of acqusition line $P2$. Note the underplating in the lower crust between the station and the acqusition line. The y-axis is depth in meters, positive downwards, while the x-axis is the UTM coordinates in west-east direction.

5.2.1 Moho depth

The inverted Moho depths for both $P2$ and $P1_s$ are within the uncertainty range of the Moho depths in both Ritzmann et al. (2007) and Hauser et al. (2011). The inverted Moho depth of $P1_{ho}$ at 29.8 km is close to the Moho depth found in Czuba et al. (2008) of 27-30 km, but deviate from the depth found in the closest line to Hopen in Breivik et al. (2005) of 30-35 km, with an increasing depth towards Hopen. Furthermore the composite synthetic seismograms for $P2$ with refraction profiles plotted on top matches quite well. The Moho refraction seen on $P1_s$ and $P2$ plots at the same time as the synthetic refraction, but it plot slightly earlier than the synthetic arrival at the largest offsets. This deviation could be related to lateral variation in Moho depth along the profile which is not accounted for in a 1D structure.

A shorter profile in Breivik et al. (2005) in the western part of Storfjorden has a Moho depth of ~29.5-33.8 km, the shallow section of this line crosses $P1_{ho}$. This profile however was too short to constrain the upper mantle velocities, but Breivik et al. (2005) emphasised that they have good control on the Moho surface. The inverted data from Hopen had an increasing uncertainty of picked onset times with increasing offset and the shallow Moho depth compared to profile 2 in Breivik et al. (2005) could be related to the pick uncertainty. However the Moho depth is within the uncertainty range of Hauser et al. (2011). In Hauser et al. (2011) the Moho depth are ~35 km in the vicinity of Hopen while it decreases to ~28 km in the vicinity of Tusenøyane, i. e., the Moho depth in the vicinity of Hopen increases. The rays from the large offsets of $P1_{ho}$ have travelled in both the lower crust and the upper mantle. It is reasonable to assume that an inversion not accounting for a dipping Moho and an increased pick uncertainty have biased the inversion result and that the actual Moho depth is deeper than what is estimated from the inversion.

5.2.2 Travel-time differences

The travel-time curves from the four different 1D models were all affected by high upper crustal velocities, and a large depth-to-Moho. Naturally the travel-time curves from the modelled data arrived before the real data for the small to intermediate offsets, i. e., entire $P1_h$ and $P1_{ho}$ and the first part of $P1_s$. On the latter part of $P1_s$ and throughout the entire $P2$ the P-wave travel-time curve arrived after the first arrivals. The discrepancy between the data from $P1_{ho}$ and the modelled travel-time is ~1 s for the P-wave and ~2 s for the S-wave. The difference is substantially larger for the data from $P1_h$, here the difference between the model and the data is ~6 s at the start of the line and ~3.9 s at the end of the line. The two travel-time curves for $P1_h$ and $P1_{ho}$ overlap where they have overlapping offset and hence errors related to travel-time computation are probably minor.

The upper crustal P-wave velocities in all the four previously published 1D models are high, 6.2 km/s. For the first 8 km the difference between the four 1D models and the inverted

1D model for $P1_h$ is as much as 2 km/s. The difference between the inverted 1D model of $P1_h$ and $P1_{ho}$ is as much as 1.4 km/s from 4-8 km. The difference between the onset and the travel-time curve for the onset both on $P1_h$ and $P1_{ho}$ is then most likely due to variations in upper crustal velocities.

On the smaller offsets of $P1_s$ the P-wave travel-time curves for all the 1D models arrived ~1 s after the onset. The travel-time curves cross the onset at 175 km and from 175-200 km the travel-time curves arrive before the onset. On the latter part of the line the travel-time curve arrive after the onset with increasing distance as the offset increases, this is also the case for $P2$. The difference between the large offsets and the small offsets can probably be explained by the fact that for the large offset waves spend a short amount of time traveling through the upper crustal layers, while they mainly travel through the mantle. With a much shallower upper mantle the rays will travel faster e.g. the large offset waves will arrive before the modelled rays.

Another factor affecting the travel-time is that rays were only traced to the surface, i.e. 0 m above sea level. HOPEN and HSPB are situated just above sea level while SPITS is situated 200-340 m above sea level. With a P-wave velocity of 3.5 km/s for the 340 m of rock beneath SPITS the travel-time from sea level to SPITS would be 0.1 s.

The Moho depth in Barents50 was quite similar to the inverted Moho depth for both $P1_s$ and $P2$, so a better fit between the modelled travel time and the data was expected. The difference between the travel-time curves and the real data was ~2-1.5 s e.g., the distance between them decreased with offset. From the ray tracing through Barents50 it is evident that the Moho depth is shallowing in the middle part of $P2$, a shallowing in the Moho depth for $P1_s$ is also evident beneath the latter part of the line. The change in Moho depth is in the range of 1-4 km, this would produce a travel-time difference of 0.1-0.2 s and in addition the upper mantle velocity vary slightly throughout both profiles. However, any strong velocity anomalies would not have resulted in such a linear travel-time curve seen for $P1_s$ and $P2$. In addition the only dataset in the vicinity of $P2$ originates from Høgden (1999), he has higher velocities in the lower crust i.e., magmatic underplating. The velocities from Høgden (1999) is used to constrain the crust and upper mantle in vicinity of $P2$ in Barents50. The first arrival of $P2$ travel rather vertical through the lower crust, the lower crustal velocity from Høgden (1999) is 7.5 km/s while the maximum crustal velocity from the inversion of $P2$ is 6.56 km/s, if the maximum thickness of the underplate is 10 km a Moho refraction travelling in a crust without underplating will travel 0.4 s slower than in the case of underplating in the crust.

Hence 0.3-0.4 s discprepancy between $P1_s$ and Barents50 can be explained by the differences in depth to Moho, Moho topography, underplating and correction for station elevation in the raytracing, while 0.6-0.8 s discprepancy between $P2$ and Barents50 can be explained by these factors. This indicates that 1-1.3 s travel time difference between the modelled data

and the real data comes from differences in crustal velocities, not including the underplating. These effects will be discussed in section 5.3.

5.2.3 Uncertainties related to inversion

The inversion method from Diebold and Stoffa (1981) requires strictly increasing velocities with depth. Minakov et al. (2011) imaged lower Cretaceous lavas and mafic intrusions with the same survey as for $P2$. They modelled high-velocity anomalies in both the upper and lower crust and interpreted them as intrusive bodies. Such bodies can have higher velocities than the adjacent rock and hence velocities would not be strictly increasing with depth.

The 1D inversion did not account for any dipping layers. From Ritzmann et al. (2007), Hauser et al. (2011), Breivik et al. (2005) and Czuba et al. (2008) it is known that there are dipping sedimentary layers and Moho topography. In addition there are shallow dipping sedimentary layers beneath SPITS (Schweitzer, 2001). This could especially have affected the inversion of $P1_{ho}$ since it appears to be a substantial increase in crustal thickness towards Hopen.

5.2.4 Magmatic underplating

Dörr et al. (2013) and Høgden (1999) both argued for underplating beneath Svalbard and east of Svalbard, respectively. The data from Høgden (1999) are just west of $P2$. Høgden (1999) used both gravimetric data and refraction data to argue for underplating in the vicinity of Kong Karl's Land. However Minakov et al. (2011) related gravity anomalies in this area to sills in the upper crust and dikes in the lower crust. The second arrival on $P2$ and on the latter part of $P1_s$ revealed a reduction velocity of 6.5 km/s, the secondary arrival could have travelled as a head wave in the lower crust. In addition the travel-time difference between the first and second arrival should have been ca. 3 s if the wave travelled in the lower crust of a velocity of 7-7.5 km/s. This is further supported by the inversion, where there are no crustal velocities above 6.5 km/s. The dikes imaged in the vicinity of $P2$ by Minakov et al. (2011) are too small to have been imaged with the frequencies of the waves in this thesis.

Dörr et al. (2013) linked regional magmatic underplating in the vicinity of the Yermak Plateau to the uplift of Svalbard the last 10 Ma and thermal erosion of the mantle lithosphere under the western Spitsbergen, even though it is not supported by several recent refraction surveys (Ritzmann and Jokat, 2003). The data from Dörr et al. (2013) support the absence of a magmatic underplate east of the Central Tertiary Basin (CTB), i.e., all the refraction lines in this thesis except $P1_h$ are east of the CTB. In addition Huismans and Beaumont (2011) states that seismic data is an important tool to study underplating due to the high lower crustal velocities.

Amundsen et al. (1987) studied xenoliths derived from the lower crust and upper mantle

in the Bockfjord area. They calculated pressure and temperature to construct a geotherm and computed seismic velocities from the petrological data. In the lower crust they found mafic granutlites which they estimated originated from a depth of 17-20 km and with a velocity of 6.46±0.2 km/s, slightly above the velocities found from the inversion of the refraction profiles in this thesis. In addition they have defined a transition zone from mafic granulites in the lower crust to spinel lherzolite and pyroxenite in the upper mantle between 27 and 32 km which they interpret as a transition zone from lower crust to upper mantle. Their velocity estimate of the upper mantle is 7.9-8 km/s, close to what has been found from the inversion, see **Figure 5.2**. The last inverted depth for *P*2 are at 60.5 km, this depth could be related to the transition between spinel lherzolite and granulite lherzolite, see **Figure 5.2**.

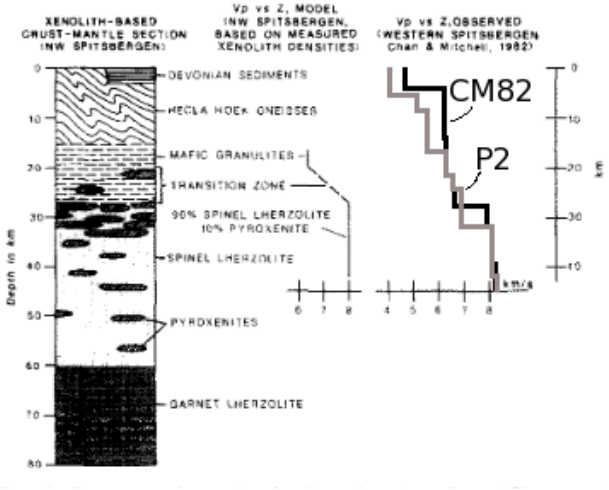

Figure 5.2: The petrological section modified from Amundsen et al. (1987). The black velocity model is from Chan and Mitchell (1982), denoted CM82. The grey velocity model is from the inversion of *P*2, denoted P2.

It should be noted that the velocity model used in Amundsen et al. (1987) sampled the crust and upper mantle west of Svalbard. The discprepancy between the crustal velocity of the model in Amundsen et al. (1987) and *P*2 comes from the fact that the crust west of Svalbard is more deformed and there are no sedimentary basins there. This leads to higher crustal velocities compared to the crust east of Svalbard.

5.2.5 Azimuthal anisotropy

Both 3D models from Klitzke et al. (2015) and Ritzmann et al. (2007) comprise reflection and refraction data in addition to surface wave tomography. Reflection and refraction data have limited offsets and the velocity structure is only constrained in the crust and by Moho

reflections and refractions while the data from surface wave tomography is well constrained from a depth of ~70 km. The inverted velocity of $P1_s$ and $P2$ revealed difference in the upper mantle velocities. $P2$ have higher mantle velocities than the regional models, while velocities and depths obtained for $P1_s$ are more consistent with the average 1D models and Barents50. In the upper mantle the difference between $P2$ and the 1D models extracted from Barents50 is 1.5 - 2%, with slowest velocities in Barents50. The previously published 1D models also have a lower velocity in the upper mantle, about 0.5%, the difference between the 1D model of $P2$ and Barey and Barez decrease from 40 km, and it appears as the Barey/Barez and $P2$ would have converged at ca 70 km depth. Directional dependent velocity variations in this area could be a result of elastic anisotropy, i.e., velocities across the north-south Caledonian basement and Eocene compression structures are higher than along the structures, see **Figure 5.3**. However a better azimuthal coverage is necessary to define any elastic anisotropy in this region.

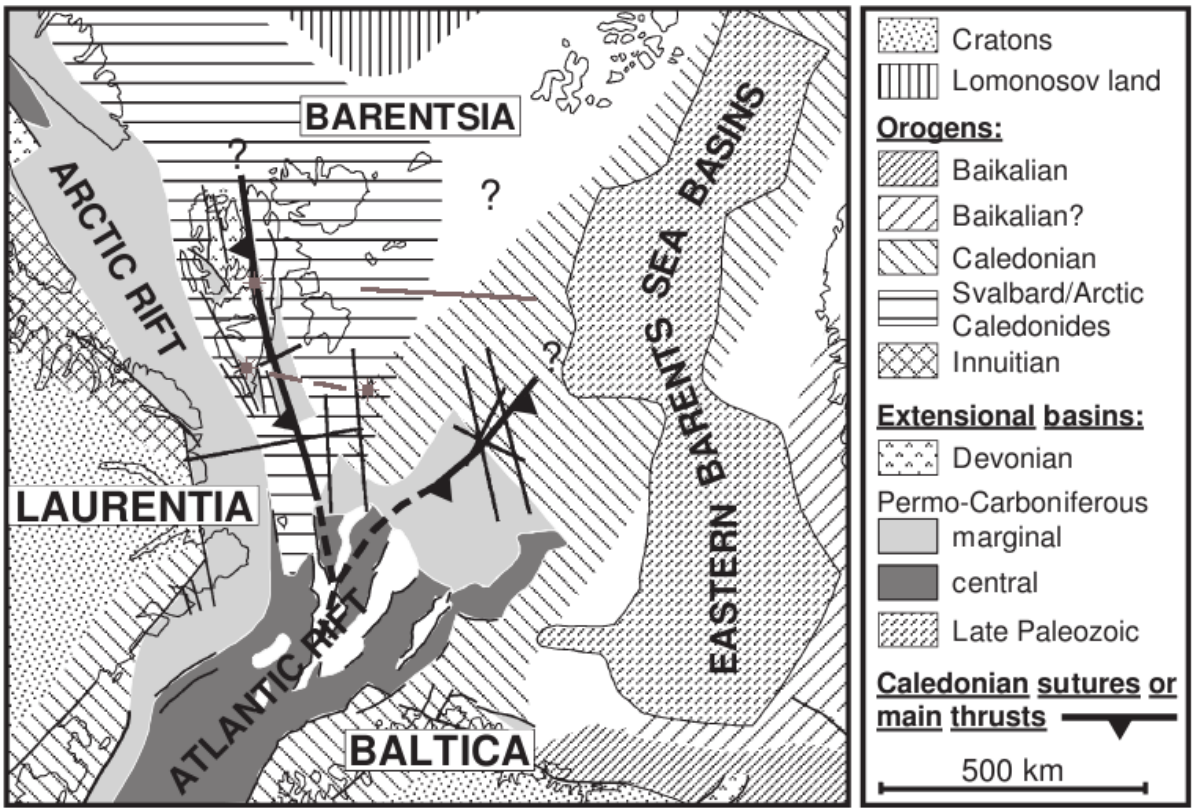

Figure 5.3: Figure showing the mainly north-south pattern of structures in the Spitsbergen region. The three grey crosses are the seismic array SPITS and the seismic stations HSPB and HOPEN, the two grey lines are the two refraction profiles used in this thesis. $P1$ is crossing the N-S Caledonian sutures close to HSPB. Figure modified from Breivik et al. (2005).

5.3 Crustal structure

From ray tracing of $P2$ and $P1_s$ the majority of the rays travelled in the lower crust and upper mantle, hence the upper and middle crust are poorly imaged in these profiles. On the other hand, $P1_h$ and $P1_{ho}$ had rays traveling in the upper and middle crust and they have imaged these areas. The difference in crustal velocities of the four inverted 1D models is found in the upper crust, here the velocity of $P1_{ho}$ is 5.6 km/s at 3.8 km depth while the other profiles have a velocity of 4.2-4.8 km/s. The main differences between the inverted models and the models from Kremenetskaya et al. (2001), Schweitzer and Kennett (2002), Mykkeltveit and Ringdal (1981) and Ritzmann et al. (2007) are found in the upper to middle crust.

The crustal velocities at shallow depths of the 1D model of $P1_{ho}$ are generally high e.g., at 3.8 km depth the P-wave velocity is 5.6 km/s. The pick uncertainty for this part of $P1_{ho}$ were rather stable. Breivik et al. (2005) argued that high crustal velocities, i.e., highly consolidated sedimentary rocks, >5.4 km/s at shallow depths in this area could indicate a seismic velocity of the fast Triassic strata, which again could be an indication of missing Cretaceous strata. In this area it has been 2-2.5 km of net erosion due to the Late Cenozoic uplift. The onsets of $P1_{ho}$ are the only one who arrive close to the travel-time curve from Barents50. The first onset arrive 0.47 s before the P-wave travel-time curve, the S-wave travel-time curve plot in the vicinity of the second onset. The second onset on $P1_{ho}$ is a P-wave and the discrepancy between the models and the data is expected. The data from Breivik et al. (2005) was included into the 3D model of Ritzmann et al. (2007), generally a high upper crustal velocity is found in the lines close to Hopen as opposed to the more slow upper crust just east of Hornsund, see Czuba et al. (2008), Breivik et al. (2005) and $P1_h$. The resolution of Barents50 is 1x1°, and high velocity at shallow depths found both south and west of Hopen are widespread enough to be presented in the model, while smaller features as the lower velocity of the upper crust in $P1_h$ will not be resolved in such a model even though the model is based on data that have shown the same local trend.

Mid crustal reflectors (MCR) at ~16-18 km and 6.2 km/s as found in Czuba et al. (2008), Breivik et al. (2005) and Chan and Mitchell (1982) are also imaged with the datasets in this thesis. Amundsen et al. (1987) argued that the MCR at depth ~14 km and with a velocity of 6.2 km/s may consist of granulite-facies rocks with a higher proportion of felsic granulites than in the deeper layers. Assigning the MCR as granulite-facies rock would be dubious, but it is possible that the MCR could represent the Conrad discontinuity. The geological significance of the discontinuity is debated, but it has been argued that it represents the transition from amphibolite facies to granulite facies (Lowrie, 2007).

The deviation of crustal velocities can also be related to undersampling of the crust, especially for $P1_s$ and $P2$. An interesting phenomenon here is that the average crustal velocity is lower than what is found for the data from Barents50, but close to the previously published

1D models. The area of which all the profiles have sampled is considered a part of the HALIP (Maher, 2001). In Ritzmann et al. (2007) gravity modelling is provided together with the refraction and reflection data to constrain the crustal velocities. Refraction and reflection data, at smaller offsets than the datasets in this thesis, do not travel vertically through the crust but more horizontally and hence it can better image crustal features than the datasets in this thesis. From Minakov et al. (2011) and Breivik et al. (2005) it was found sills and dikes in the upper and lower crust. Igneous intrusions will increase the average crustal velocity. In cases where the crustal sampling is more sparse and not performed together with gravity modelling it is reasonable to assume that the average crustal velocity will be lower than what is found from combined gravity modelling and refraction data.

5.4 S-waves

On all profiles S-phases were present. The travel-time differences between the modelled S-waves and the real S-wave arrivals are in the same range as the differences between the P-waves. But on $P2$ the S-phase occurs 5-10 s before the S-wave arrival, in addition the arrival is most well defined on the transversal component. As previously mentioned the main energy on the transversal component originates from SH-waves, P- and SV-waves are coupled for horizontal layered media while SH-waves are separate. The energy found on the transversal component could be a result of anisotropy and shear wave splitting. However the arrival on the transversal component could also be an effect of scattering, i.e., defining the correct incidence angle in coordinate transformations is crucial. If there are slightly leakage of energy between the components of scattering this would produce an apparent SH- and SV-wave arrival (Stein and Wysession, 2013).

S-waves are affected by viscosity changes. Partial melting in the upper mantle will affect the potential viscosity and hence it can be detected by the S-waves. From the S-wave inversion of $P1_h$ the largest inverted depth is 23.91 km. In addition the inversion routine would not pick up on a velocity decrease. The S-wave velocity is however consistent with the mid crustal reflectors found for the P-wave phase for $P1_h$.

5.5 Amplitude variations

Amplitudes of seismic waves decay as a result of geometrical spreading and attenuation. Even at small offsets of $P1_{ho}$ it is evident that the amplitude decreases when the offset increases. On $P1_s$ the amplitude of the first arrival decrease with increasing offset. This is however not seen on $P1_h$ and the two first onsets on $P2$, here the amplitude decreases but also increases with offset.

The first arrival on $P2$ has similar amplitude variations at all the different stations which could be a result of problems during acquisition. Minakov et al. (2011) reported on minor air

gun issues during acquisition of $P2$, however this does not explain an increase in amplitude at an offset of ~400 km. Air gun issues were also reported during aquisition of $P1_h$.

From ray tracing of $P1_h$ it is evident that on the larger offsets of the first part of the line the reflected rays arrive at the same time as the refracted waves, see **Figure 3.11**, this kind of focusing effect could have caused an increase in amplitude. To reveal any frequency dependence of the amplitudes the data were re-filtered, originally the data were filtered with a 3-6 Hz Butterworth filter. The test was perfomed with a 3-4 Hz, 4-5 Hz and 5-6 Hz filter, the amplitudes were higher for the higher frequencies. It should however be noted that the frequency range is rather narrow and compared to the amplitude variations of $P2$ these amplitude variations are minor and they can be an effect of the air gun issues. The same amplitude variations occur on the S-wave arrival. Since P- and S-waves are coupled it is reasonable to assume amplitude variations due to the air gun or features at the seabottom or in the uppermost layers just below the seabottom.

The apparent velocity range for the first onset of $P2$ is within a upper mantle velocity. Generally the amplitude will decrease significantly when it travels at these distances. Schweitzer (2001) detected large slowness variations at SPITS and found large Pn apparent velocities towards northeast and smaller towards southwest. These variations were explained as an effect of dipping sedimentary layers in the shallow crust beneath the array. The layers dip in north-west direction and could create a focusing effect. The raypaths for $P1_s$ are mainly in south-southeast to north-northwest, the same direction as the dip of the upper crustal sedimentary layers. However no large amplitude variations are seen for this profile even though the incidence angles are in the same range as the large offset rays for $P2$.

Paul et al. (1996) related amplitude anomalies for Pn to changes in crustal thickness and Moho topography, Moho topography will cause focusing and defocusing of seismic energy and amplitudes. From ray tracing of $P2$ one can see that anomalies in the upper mantle cause defocusing and slight focusing at the end of the line, but not to the degree as seen from the ray tracing of $P1_h$. The presence of Moho topography is found in both Ritzmann et al. (2007), Minakov et al. (2011) and Hauser et al. (2011). Minakov et al. (2011) imaged the Moho in 2D in the vicinity of $P2$, in addition Hauser et al. (2011) calculated the probabilistic depth of the Moho in this area. In Ritzmann et al. (2007) the Moho topography varies with 5 km in the area of which the rays travel in. In Minakov et al. (2011) the Moho depth vary with 4 km in the 160 km long transect. The Moho dip towards west with slight Moho topography. In Hauser et al. (2011) the Moho depth varies with 6 km in the area where the rays travel through the upper mantle, here the Moho also has an overall trend where it dips towards east.

The amplitudes could be frequency dependent, hence the data were re-filtered with both high (10-15 Hz) and low bandpass filters (5-7 Hz). Re-filtered data from $P2$ can be seen in **Figure 5.4**. The large amplitudes of $P2$ on both the large offset part of the first arrival and the

second onset are not present for the higher frequencies, but present for lower frequencies. The low frequency and large amplitudes can be an effect of scattering. Another factor affecting the amplitudes is the structure of the sediments found just below the surface beneath the source. If there are mud layers, undulations or even shallow gas pockets they will have an effect on the amplitude.

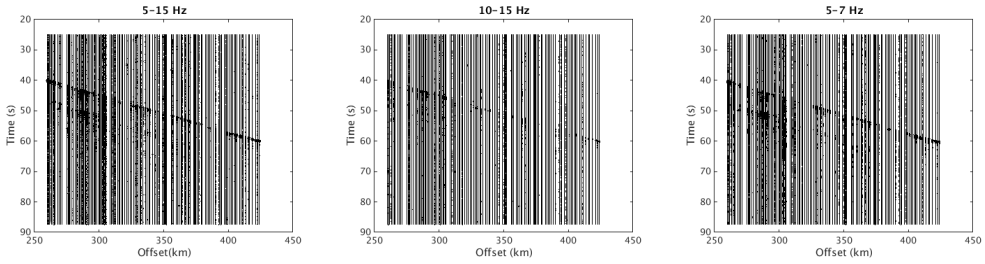

Figure 5.4: Filtered sections of *P*2. From left to right the sections are filtered with 5-15 Hz, 10-15 Hz and 5-7 Hz Butterworth bandpass filters.

6 Conclusion

In this thesis the lower crust and upper mantle in the western Barents Sea and Svalbard have been imaged by an active source and recorded at seismological stations. With offsets up to 420 km the upper mantle has been imaged, processed, modelled and interpreted. This method has proved well in imaging the lower crust upper mantle, especially at offsets larger than 200 km. In addition to imaging the upper mantle the datasets have provided crustal velocities below what is predicted from previous 3D models from Ritzmann et al. (2007) and Klitzke et al. (2015). It is evident that the crust is undersampled in this study, but the discrepancy between the models and the data is also an effect of sparse seismic coverage east of Svalbard and their resolution.

Due to the known crustal structure in the Western Barents Sea any 1D model will be a limited description of the crustal velocities in the region. However it is evident that the previous models from the Barents Sea have quite substantial deviations in crustal velocities and some deviations in upper mantle velocities. Most of these models were initially constructed to improve the event location in the Barents Sea region, evidently there are still deviations in the crustal velocities and furter constrains are necessary.

This method presented in this thesis has proven useful in imaging the lower crust and upper mantle. The upper mantle has high uncertainties from the Moho boundary to 70-80 km depth with reflection/refraction data and surface wave tomography. With active source seismology this zone is imaged and fills a gap in the velocity of the upper mantle.

6.1 Further work

However more wide-angle data are necessary to constrain the upper mantle and the crustal structure. East of Svalbard the crust is poorly constrained and more data is necessary to have sufficient control of the velocities and densities. In addition better azimuthal coverage would help determine possible elastic anisotropy.

The amplitudes at the large offsets of $P2$ suggests that the profile could have been continued. Naturally it would have been very interesting to have continued this profile, not only to investige the upper mantle but also to possibly image the lithosphere - astenosphere boundary (LAB).

References

Aki, K. and Richards, P. G. (2002), *Quantitative Seismology*, 2 edn, University Science Books.

Amundsen, H. E. F., Griffin, W. L. and O'Reilly, S. Y. (1987), 'The lower crust and upper mantle beneath northwestern Spitsbergen: evidence from xenoliths and geophysics', *Tectonophysics* **139**, 169–185.

Bessonova, E. N., Fishman, V. N., Ryaboyi, V. Z. and Sitnikova, G. A. (1974), 'The tau method for inversion of travel times. I. Deep seismic sounding data', *Geophys. J. R. Astr. Soc* **36**, 377–398.

Blinova, M., Faleide, J. I., Gabrielsen, R. H. and Mjelde, R. (2012), 'Seafloor expression and shallow structure of a fold-and-thrust system, Isfjorden, west Spitsbergen', *Polar Research* **31**.

Boschi, E., Ekström, G. and Morelli, A. (1996), *Seismic Modelling of Earth Structure*, Editrice Compositori, chapter 6: Seismic ray tracing, pp. 223–274.

Bouchon, M. (1981), 'A simple method to calculate Green's function for elastic layered media', *Bulletin of the Seismological Society of America* **71**(4), 959–971.

Breivik, A. J., Mjelde, R., Gorgan, P., Shimamura, H., Murai, Y. and Nishimura, Y. (2005), 'Caledonide development offshore-onshore Svalbard based on ocean bottom seismometer data', *Tectonophysics* **410**, 79–117.

Cerveny, V. (2001), *Seismic Ray Theory*, Cambridge University Press, chapter 3: Seismic Rays and Travel Times, pp. 99–210.

Chan, W. W. and Mitchell, B. J. (1982), 'Synthetic seismogram and surface wave constraints on crustal models of Spitsbergen', *Tectonophysics* **89**, 51–76.

Clayton, R. W. and McMechan, G. A. (1981), 'Inversion of refraction data by wave field continuation', *Geophysics* **46**(6), 860–868.

Cocks, L. R. M. and Torsvik, T. H. (2006), 'European geography in a global context from the Vendian to the end of the Palaeozoic', *European Lithosphere Dynamics, Geological Society, London, Memoirs* **32**, 83–95.

Czuba, W., Grad, M., Guterch, A., Majdański, M., Malinowski, M., Mjelde, R., Moskalik, M., Środa, P., Wilde-Piórko, M. and Nishimura, Y. (2008), 'Seismic crustal structure along the deep transect horsted'05, svalbard', *Polish Polar Research* **29**(3), 279–290.

Diebold, J. B. and Stoffa, P. L. (1981), 'The traveltime equation, tau-p mappting, and inversion of common midpoint data', *Geophysics* **46**(3), 238–254.

Dörr, N., Clift, P., Lisker, F. and Spiegel, C. (2013), 'Why Svalbard is an island? Evidence for two-stage uplift, magmatic underplating, and mantle thermal anomalies', *Tectonics* **32**, 473–486.

Faleide, J. I., Tsikalas, F., Breivik, A. J., Mjelde, R., Ritzmann, O., Øyvind Enger, Wilson, J. and Eldholm, O. (2008), 'Structure and evolution of the continental margin off Norway and the Barents Sea', *Episodes* **31**(1), 82–91.

Faleide, J. I., Vågnes, E. and Gudlaugsson, S. T. (1993), 'Late Mesozoic-Cenozoic evolution of the southwestern Barents Sea in a regional rift shear tectonic setting', *Marine and Petroleum Geology* **10**(3), 186–214.

Gabrielsen, R. H., Færseth, R. B., Jensen, L. N., Kalheim, J. E. and Riis, F. (1990), 'Structural Elements of the Norwegian Continental Shelf. part I: The Barents Sea Region', *Norwegian Petroleum Directorate Bulletin* .

Gernigon, L. and Brönner, M. (2012), 'Late Palaeozoic architecture and evolution of the south-western Barens Sea: Insights from a new generation of areomagnetic data', *Journal of the Geological Society, London* pp. 449–459. DOI: 1144/0016-76492011-131.

Gibbons, S. J., Schweitzer, J., Ringdal, F., Kværna, T., Mykkeltveit, S. and Paulsen, B. (2011), 'Improvements to Seismic Monitoring of the European Arctic Using Three-Component Array Processing at SPITS', *Bulletin of the Seismological Society of America* **101**(6), 2737–2754. DOI 10.1785/0120110109.

Grogan, P., Nyberg, K., Fotland, B., Myklebust, R., Dahlgren, S. and Riis, F. (1998), 'Cretaceous Magmatism South and East of Svalbard. Evidence from Seismic Reflection and Magnetic Data', *Polarforschung* .

Gudlaugsson, S. T., Faleide, J. I., Johansen, S. E. and Breivik, A. J. (1998), 'Late palaeozoic structural developement of the south-western Barents Sea', *Marine and Petroleum Geology* **15**, 73–102.

Haskov, J. and Alguacil, G. (2004), *Instrumentation in Earthquake Seismology*, Vol. 22 of *Modern Approaches in Geophysics*, 1 edn, Springer Netherlands. DOI: 10.1007/978-1-4020-2969-1.

Hauser, J., Dyer, J. M., Pasyanos, M. E., Bungum, H., Faleide, J. I., Clark, S. A. and Schweitzer, J. (2011), 'A probabilistic seismic model for the european arctic', *Journal of Geophysical Research* **116**.

Herrmann, R. B. (2013), 'Computer programs in seismology: An evolving tool for instruction and research', *Seism. Res. Letters.* **84**, 1081–1088.

Huismans, R. and Beaumont, C. (2011), 'Depth-dependent extension, two-stage breakup and cratonic underplating at rifted margins', *Nature* **473**, 74–79.

Høgden, S. (1999), Seismotectonics and crustal structure of the Svalbard region, Master's thesis, University of Oslo.

Johansen, S. E., Henningsen, T., Rundhovde, E., Sæther, B. M., Fichler, C. and Rueslåtten, H. G. (1994), 'Continuation of the Caledonides north of Norway: Seismic reflectors within the basement beneath the southern Barents Sea', *Marine Petroleum Geology* **11**, 190–201.

Johansen, S. E., Ostisty, B. K., Birkeland, O., Fedorovsky, Y. F., Martitosjan, V. N., Christensen, O. B., Cheredeev, S. I., Ignatenko, E. A. and Margulis, L. S. (1992), Hydrocarbon potential in the Barents Sea region: play distribution and potential, *in* T. O. Vorren, E. Bergsager, O. A. Dahl-Stamnes, E. Holter, B. Johansen, E. Lie and T. B. Lund, eds, 'Arctic Geology and Petroleum Potential', Vol. 2, Norwegian Petroleum Society, Special Publication, pp. 273–320.

Klitzke, P., Faleide, J. I., Scheck-Wenderoth, M. and Sippel, J. (2015), 'A lithosphere-scale structural model of the Barents Sea and Kara Region', *Solid Earth* **6**, 153–172.

Kremenetskaya, E. O., Asming, V. and Ringdal, F. (2001), 'Seismic location calibration of the european arctic', *Pure and Applied Geophysics* **158**, 117–128.

Krüger, F., Weber, M., Scherbaum, F. and Schlittenhardt, J. (1993), 'Double beam analysis of anomalies in the core-mantle boundary region', *Geophysical Research Letters* **20**(14), 1475–1478.

Larsen, G. B., Elvebakk, G., Henriksen, L. B., Kristensen, S. E., Nilsson, I., Samuelsberg, T. J., Svåna, T. A., Stemmerik, L. and Worsley, D. (2005), 'Upper Palaeozoic lithostratigraphy of the southern part of the Norewgian Barents Sea', *Norges Geologiske Undersøkelse Bulletin* **444**.

Levshin, A., Schweitzer, J., Weidle, C., Shapiro, N. and Ritzwoller, M. (2007), 'Surface wave tomography of the Barents Sea and surrounding regions', *Geophysical Journal International* **170**, 441–459.

Lowrie, W. (2007), *Fundamentals of Geophysics*, Cambridge University Press, chapter 3, pp. 186–187.

Maher, H. D. (2001), 'Manifestations of the Cretaceous High Arctic Large Igneous Province in Svalbard', *Journal of Geology* **109**(1), 91–104.

Marello, L., Ebbing, J. and Gernigon, L. (2013), 'Basement inhomogenities and crustal setting in the Barents Sea from combined 3D gravity and magnetic modelling', *Geophysical Journal International* **193**, 557–584. DOI: 10.1093/gji/ggt018.

McKerrow, W. S., Niocaill, C. M. and Dewey, J. F. (2000), 'The Caledonian Orogeny redefined', *Journal of the Geological Society, London* **157**, 1149–1154.

Minakov, A., Mjelde, R., Faleide, J. I., Flueh, E. R., Dannowski, A. and Keers, H. (2011), 'Mafic intrusions east of Svalbard imaged by active-source seismic tomography', *Tectonophysics* **518-521**, 106–118.

Mykkeltveit, S. and Ringdal, F. (1981), *Identification of seismic sources - earthquake or underground explosion*, Reidel Publishing Company, chapter Phase identification and event location at regional distance using small aperture array data, pp. 467–481.

Mørk, A., Knarud, R. and Worsley, D. (1982), 'Depositional and diagenetic environments of the Triassic and Lower Jurassic succesion of Svalbard', *Arctic Geology and Geophysics, Canadian Society of Petroleum Geologists Memoir* **8**, 371–398.

NORSAR (2015), 'Spits array'.
URL: *http://www.norsardata.no/NDC/stations/SPI/, retrieved 10. April 2015*

Olovyanishnikov, V. G., Roberts, D. and Sidlecka, A. (2000), 'Tectonics and Sedimentation of the Meso- to Neoproterozoic Timan-Varanger Belt along the Northeastern Margin of Baltica', *Polarforschung* **68**, 267–274.

Oppert, S. and Perez, M. (2001), 'Radon transform functions for matlab'.
URL: *http://www.crewes.org/ForOurSponsors/archive/AnnuRepSoftware/2001/software/radon/readme.htm, last visited 24. April 2015*

Paul, A., Jongmans, D., Campillo, M., Malin, P. and Baumont, D. (1996), 'Amplitudes of regional seismic phases in relation to crustal structure of the Sierra Nevada, California', *Journal of Geophysical Research* **101**(B11), 25,243–25,254.

Pujol, J. (2003), *Elastic wave propagation and generation in seismology*, Cambridge University Press, chapter 4-8.

Ringdal, F. (1999), Semiannual technical summary, Technical report, The Reasearch Council of Norway and NORSAR.

Ritzmann, O. and Faleide, J. I. (2007), 'Caledonian basement of the western Barens Sea', *Tectonics* **26**. DOI: 10.1029/2006TC002059.

Ritzmann, O. and Jokat, W. (2003), 'Crustal structure of northwestern Svalbard and the adjacent Yermak Plateau: Evidence for Oligocene detachment tectonics and non-volcanic break-up', *Gephysical Journal International* **152**, 139–159.

Ritzmann, O., Maercklin, J. I., Faleide, J. I., Bungum, H., Mooney, W. and Detweile, S. T. (2007), 'A three-dimensional geophysical model of the crust in the Barents Sea region: Model

construction and basement characterization', *Geophysical Journal International* **170**, 417–435.

Roberts, D. and Sidlecka, A. (2002), 'Timanian orogenic deformation along the northeastern margin of Baltica Northwest Russia and Northeast Norway and Avalonian-Cadomian connections', *Tectonophysics* **352**(1-2), 169–184.

Rost, S. and Thomas, C. (2002), 'Array Seismology: Methods and Applications', *Reviews of Geophysics* **40**(3).

Saikia, C. K. (1994), 'Modified frequency-wavenumber algorithm for regional seismograms using Filon's quadrature: modelling of Lg waves in eastern North America', *Geophysical Journal International* **118**, 142–158.

Schweitzer, J. (2001), *Monitoring the Comprehensive Nuclear Test-Ban Treaty: Source Location*, Springer, chapter HYPOSAT - An Enhanced Routine to Locate Seismic Events, pp. 277–289.

Schweitzer, J., Fyen, J., Mykkeltveit, S., Gibbons, S. J., Pirli, M., Kühn, D. and Kværna, T. (2012), *In: New Manual of Seismological Observatory Practice (NMSOP-2)*, GFZ German Research Centre for Geosciences, chapter 9: Seismic Arrays, pp. 1–80. DOI: 10.2312/GFZ.NMSOP-2.

Schweitzer, J. and Kennett, B. L. N. (2002), Comparison of local procedures - the Kara Sea event of 16 August 1997, Technical Report 1-2002, NORSAR.

Schweitzer, J., Mjelde, R., Krüger, F., Guterch, A., Schmidt-Aursch, M., Grad, M. and Faleide, J. I. (2009), The IYP Project: The Dynamic Continental Margin Between the Mid-Atlantic-Ridge System (Mohs Ridge, Knipovich Ridge) and the Bear Island Region, Presented at the annual meeting of the Geological Society of Norway (NGF).

Shipilov, E. V. and Vernikovsky, V. A. (2010), 'The Svalbard-Kara plates junction: structure and geodynamic history', *Russian Geology and Geophysics* **51**, 58–71.

Smelror, M., Basov, V. A., Ebbing, J., Gernigon, L., Korchinskaya, M. V., Koren, T., Kosteva, N. V., Kotljar, G. V., Larssen, G. B., Litoviova, T., Negrov, O. B., Olesen, O., Pascal, C., Pchelina, T. M., Petrov, O. V., Petrov, Y. O., Sjulstad, H.-I., Sobolev, N. N., Vasiliev, V. and Werner, S. C. (2009), *Geological History of the Barents Sea*, Geological Survey of Norway, chapter 2-21, pp. 14–126.

Spengler, D., Brueckner, H. K., van Roermund, H. L. M., Drury, M. R. and Mason, P. R. D. (2009), 'Long-lived, cold burial of Baltica to 200 km depth', *Earth and Planetary Letters* **281**(27-35).

Stein, S. and Wysession, M. (2013), *An Introduction to Seismology, Earthquakes and Earth Structure*, 13 edn, Blackwell Publishing.

Torsvik, T. H., Smethurst, M. A., Meert, J. G., der Voo, R. V., McKerrow, W., Brasier, M. D., Sturt, B. A. and Walerhaug, H. J. (1996), 'Continental break-up and collision in the Neoproterozoic and Palaeozoic- A tale of Baltica and Laurentia', *Earth Science Reviews* **40**(3-4), 229–258.

Wang, R., Martín, F. L. and Roth, F. (2003), 'Computation of deformation induced by earthquakes in a multi-layered elastic crust - fortan programs edgrn/edcmp', *Computers and Geosciences* **29**, 195–207.

Wilde-Piorko, M., Grad, M., Wiejacz, P. and Schweitzer, J. (2009), 'HSPB seismic broadband station in Southern Spitsbergen: First results on crustal and mantle structure from reciever functions and SKS splitting', *Polish Polar Research* **30**(4), 301–316.

Worsley, D. (2008), 'The post-Caledonian developement of Svalbard and the western Barents Sea', *Polar Research* **27**, 298–317.

Zelt, C. A. and Forsyth, D. A. (1994), 'Modeling wide-angle seismic data for crustal structure: Southeastern Grenville Province', *Journal of Geophysical Research* **99**, 11,687–11,704.

A Appendix

A.1 Data processing

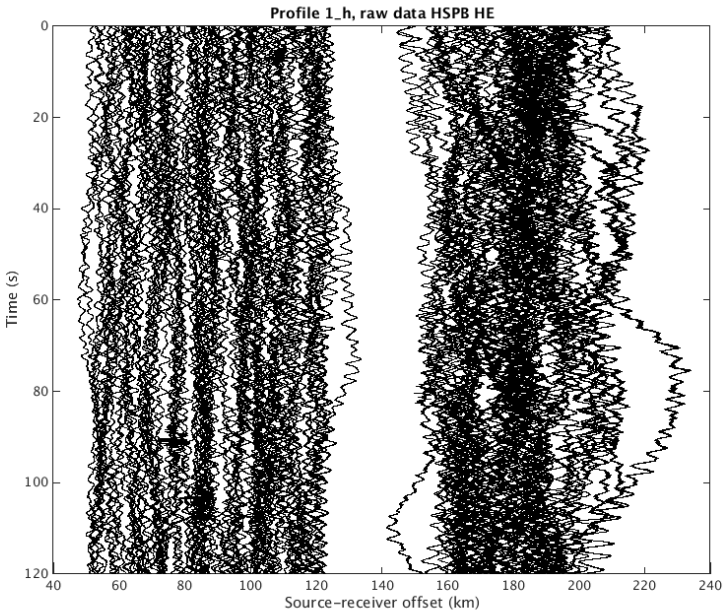

Figure A.1: Raw data $P1_h$ HSPB HE, scaled by a factor of 0.001. Every 4th trace is plotted.

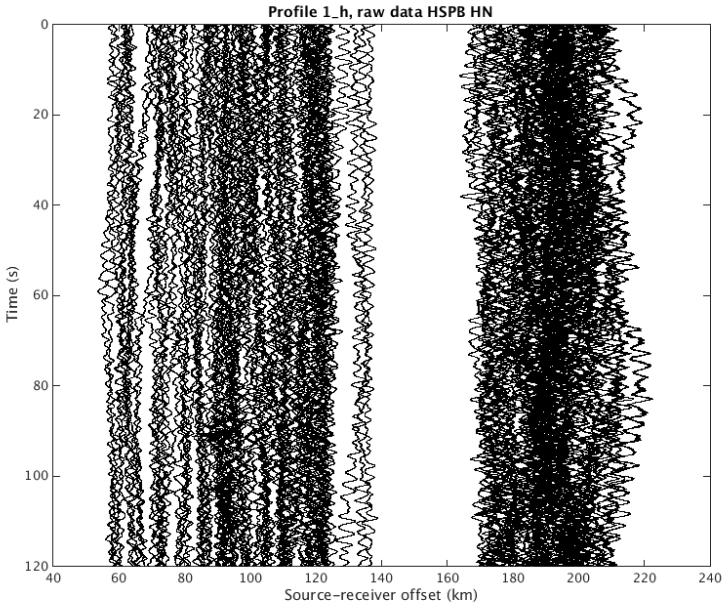

Figure A.2: Raw data $P1_h$ HSPB HN, scaled by a factor of 0.001. Every 4th trace is plotted.

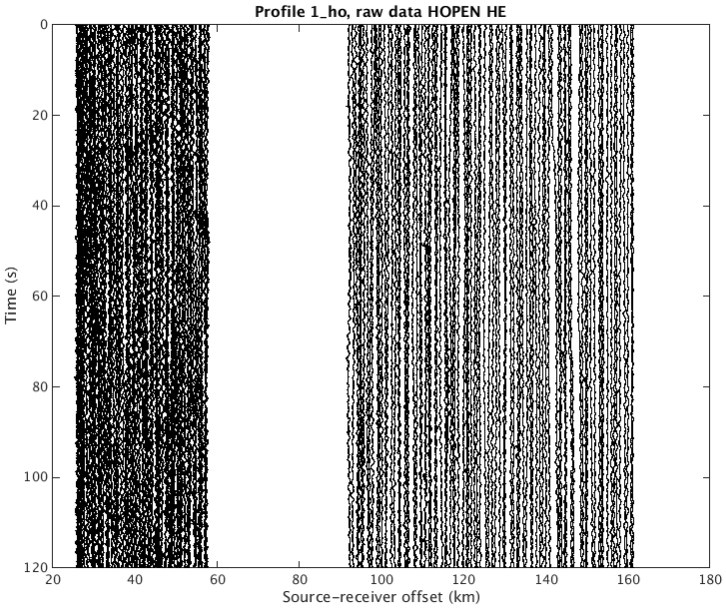

Figure A.3: Raw data $P1_{ho}$ HOPEN HE, scaled by a factor of 0.001. Every 4th trace is plotted.

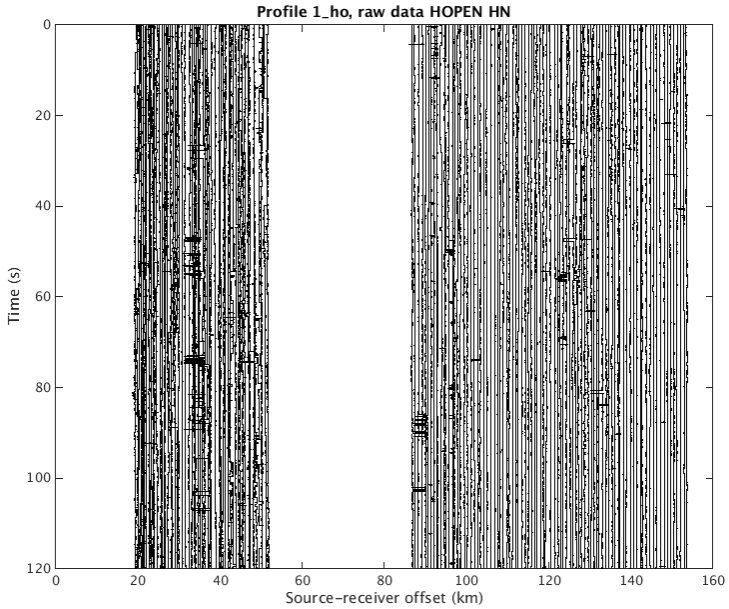

Figure A.4: Raw data $P1_{ho}$ HOPEN HN, scaled by a factor of 0.0001. Every 4th trace is plotted.

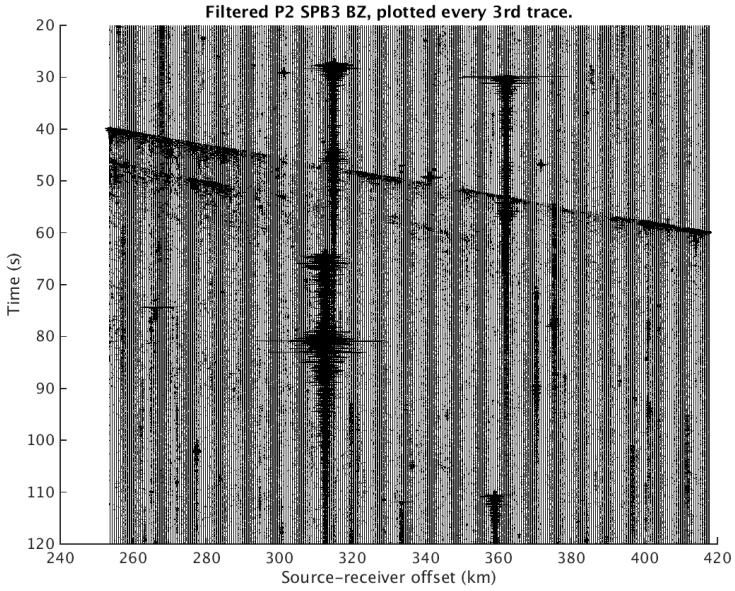

Figure A.5: Filtered data $P2$ SPB3 BZ, scaled by a factor of 0.001. Every 3rd trace is plotted.

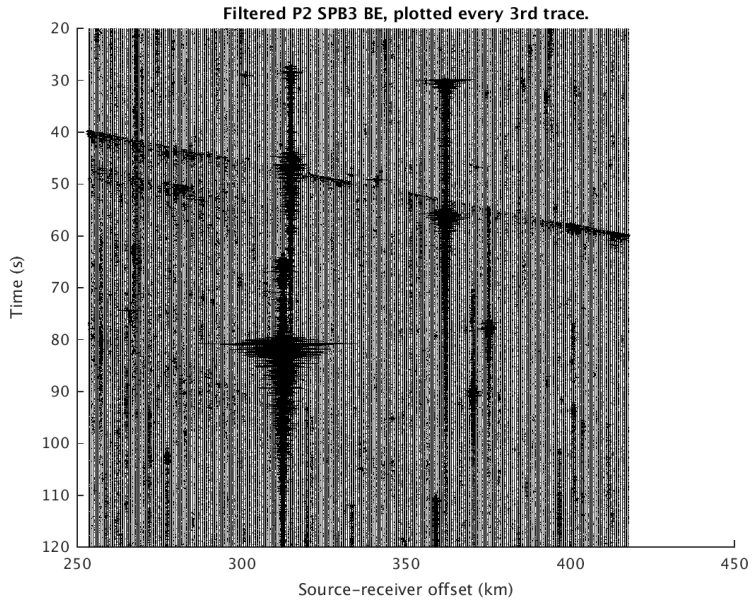

Figure A.6: Filtered data *P*2 SPB2 BE, scaled by a factor of 0.001. Every 3rd trace is plotted.

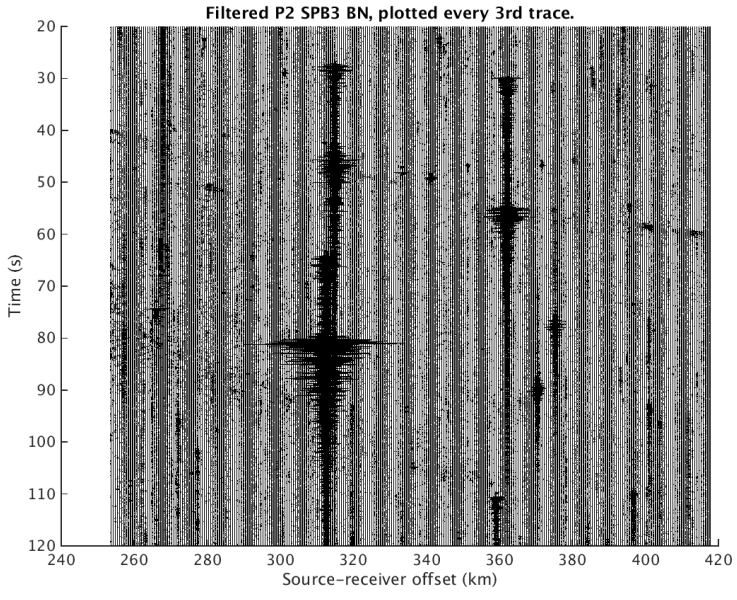

Figure A.7: Filtered data *P*2 SPB3 BN, scaled by a factor of 0.001. Every 3rd trace is plotted.

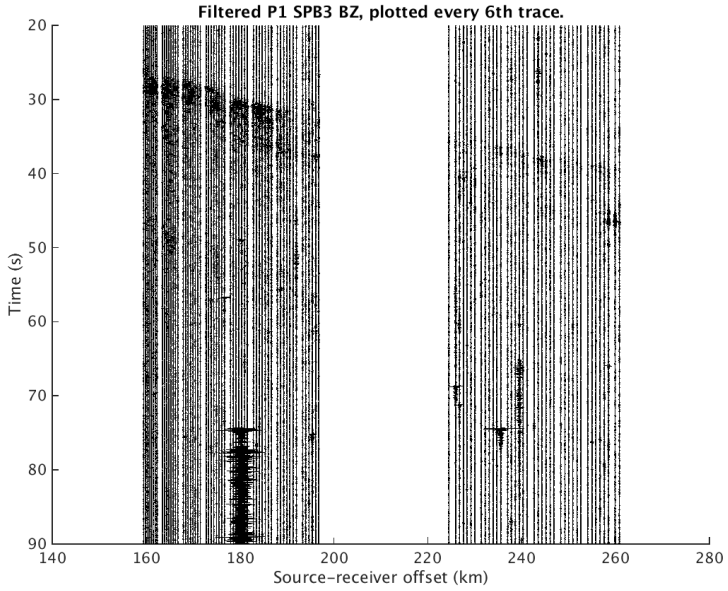

Figure A.8: Filtered data $P1_s$ SPB3 BZ, scaled by a factor of 0.001. Every 3rd trace is plotted.

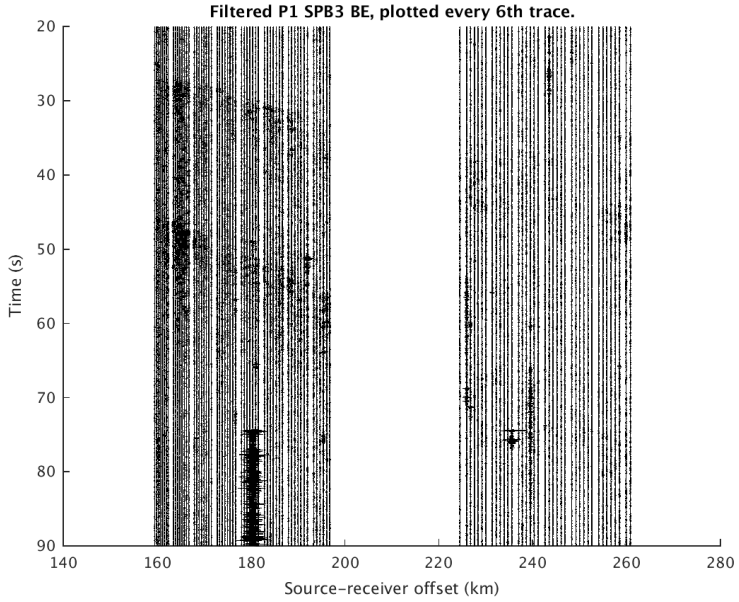

Figure A.9: Filtered data $P1_s$ SPB3 BE, scaled by a factor of 0.001. Every 3rd trace is plotted.

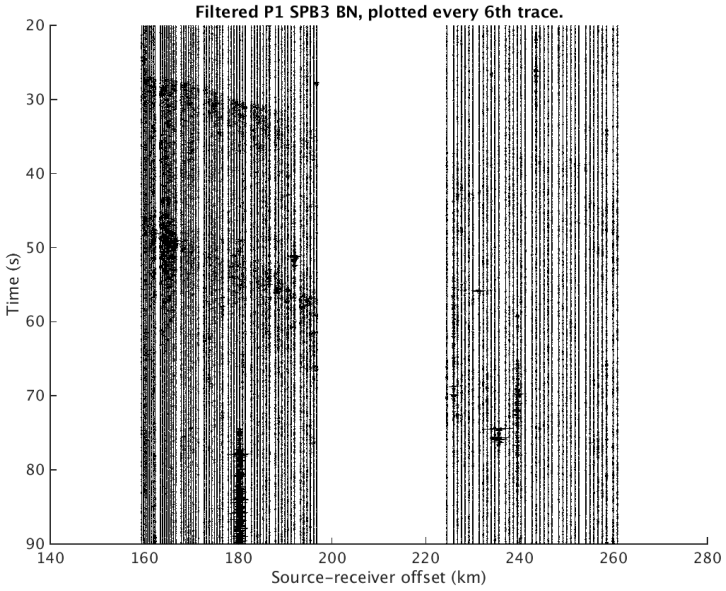

Figure A.10: Filtered data $P1_s$ SPB3 BN, scaled by a factor of 0.001. Every 3rd trace is plotted.

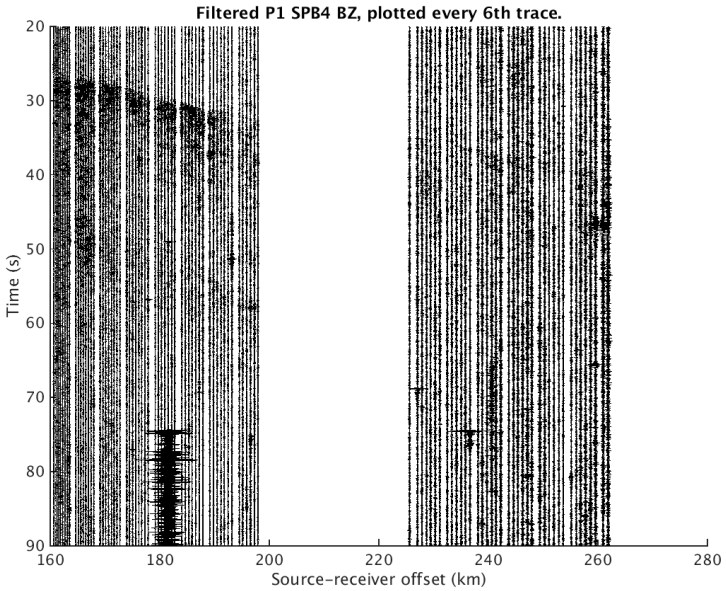

Figure A.11: Filtered data $P1_s$ SPB4 BZ, scaled by a factor of 0.001. Every 3rd trace is plotted.

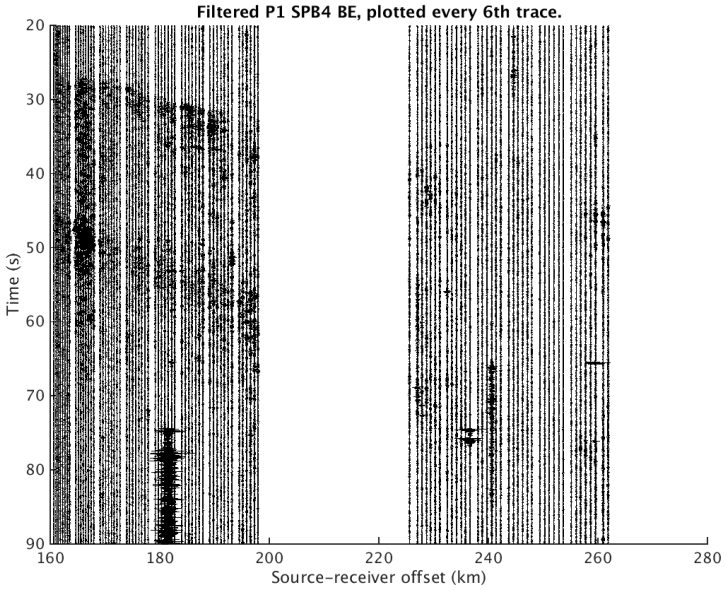

Figure A.12: Filtered data $P1_s$ SPB4 BE, scaled by a factor of 0.001. Every 3rd trace is plotted.

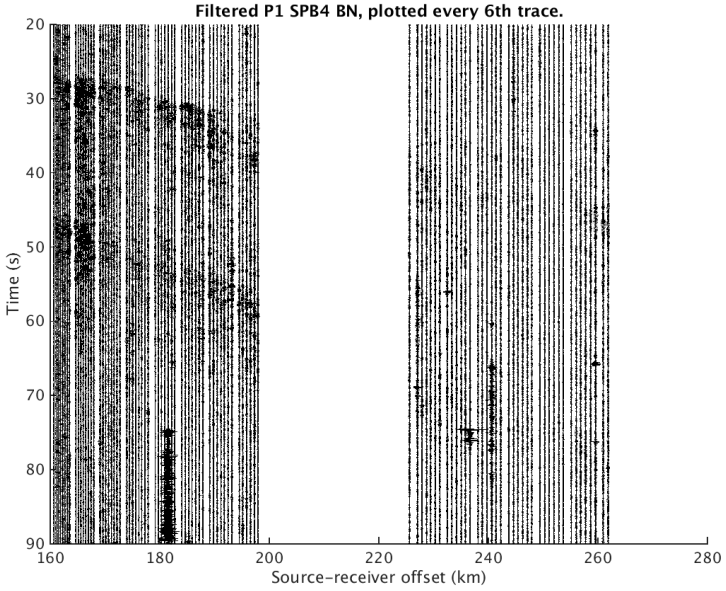

Figure A.13: Filtered data $P1_s$ SPB4 BN, scaled by a factor of 0.001. Every 3rd trace is plotted.

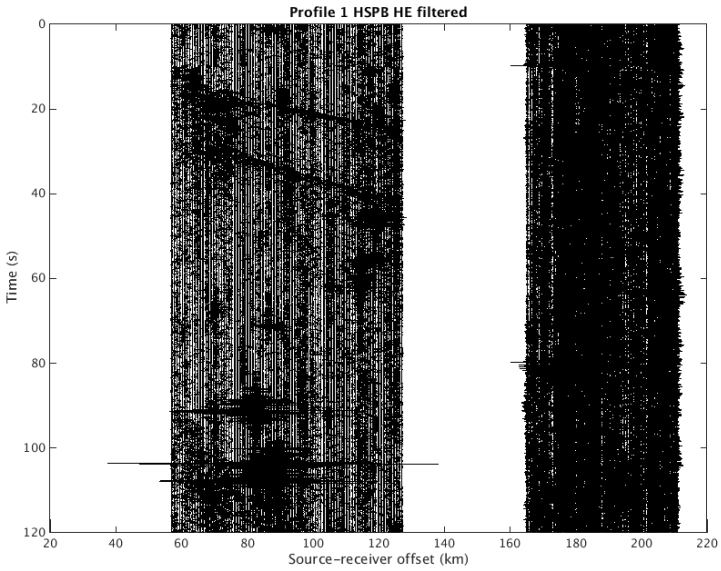

Figure A.14: Filtered $P1_h$ HSPB HE, scaled by a factor of 0.01. Every 4th trace is plotted.

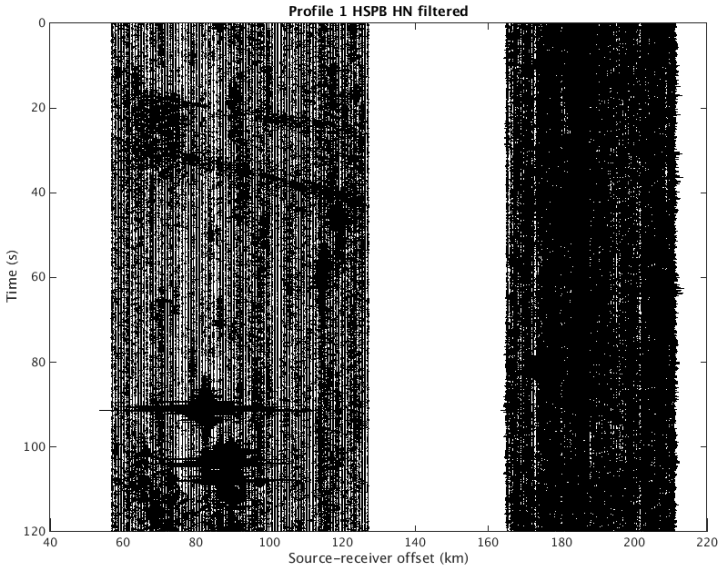

Figure A.15: Filtered $P1_h$ HSPB HN, scaled by a factor of 0.01. Every 4th trace is plotted.

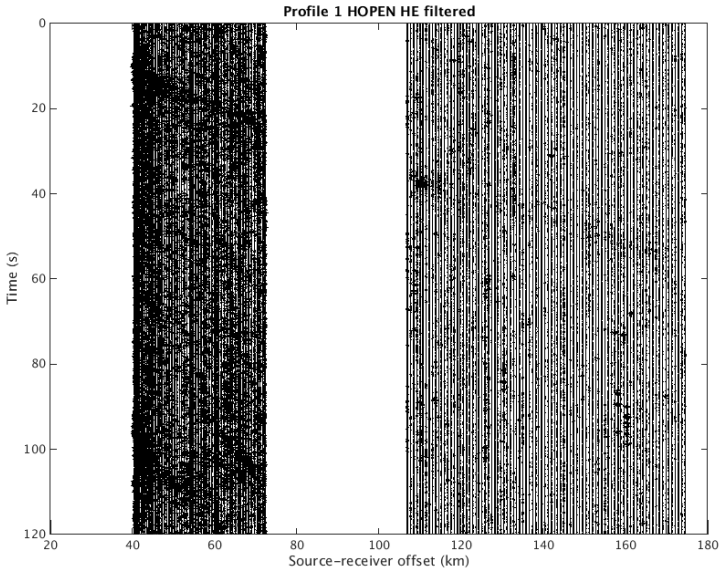

Figure A.16: Filtered $P1_h$ HOPEN HE, scaled by a factor of 0.01. Every 4th trace is plotted.

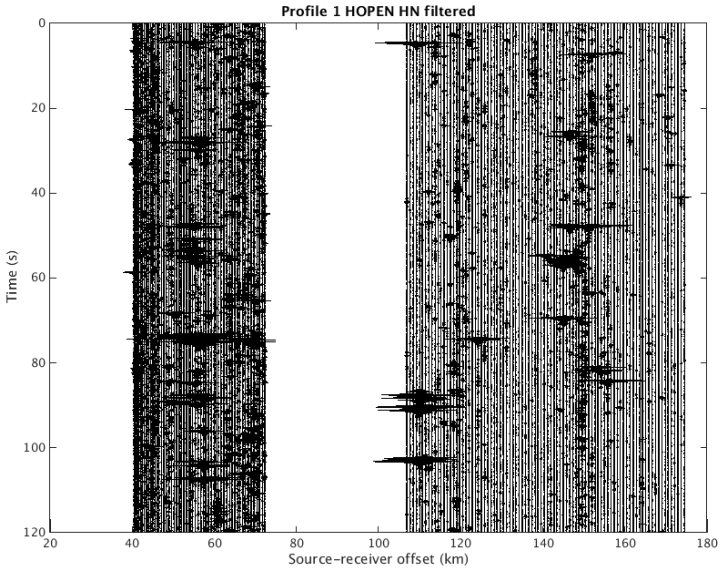

Figure A.17: Filtered $P1_h$ HOPEN HN, scaled by a factor of 0.001. Every 4th trace is plotted.

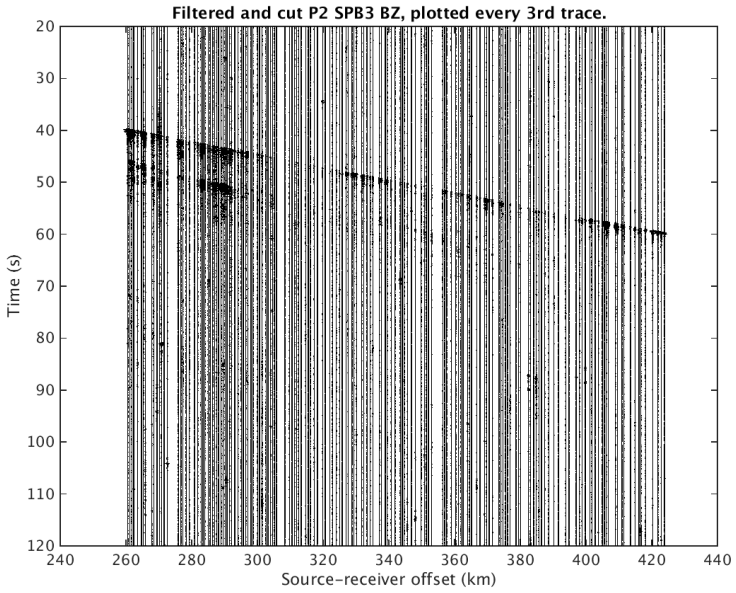

Figure A.18: Filtered and cut *P*2 SPB3 BZ, scaled by a factor of 0.001. Every 3rd trace is plotted.

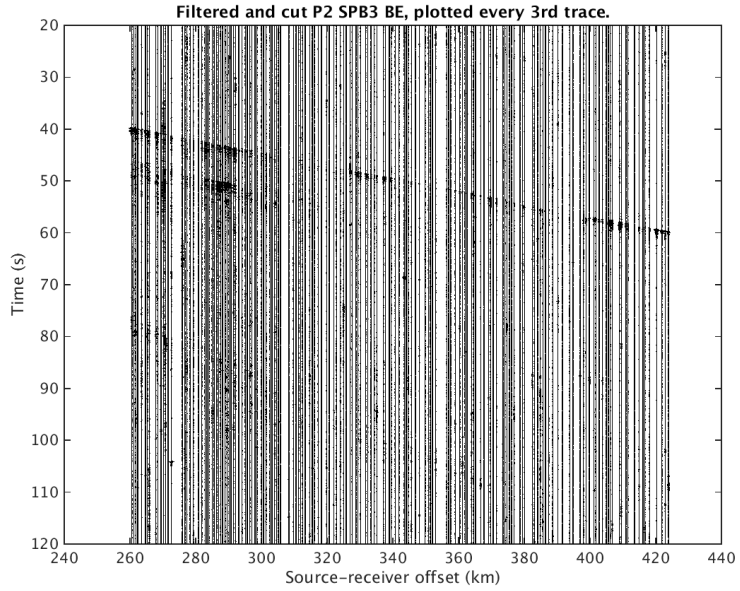

Figure A.19: Filtered and cut *P*2 SPB2 BE, scaled by a factor of 0.001. Every 3rd trace is plotted.

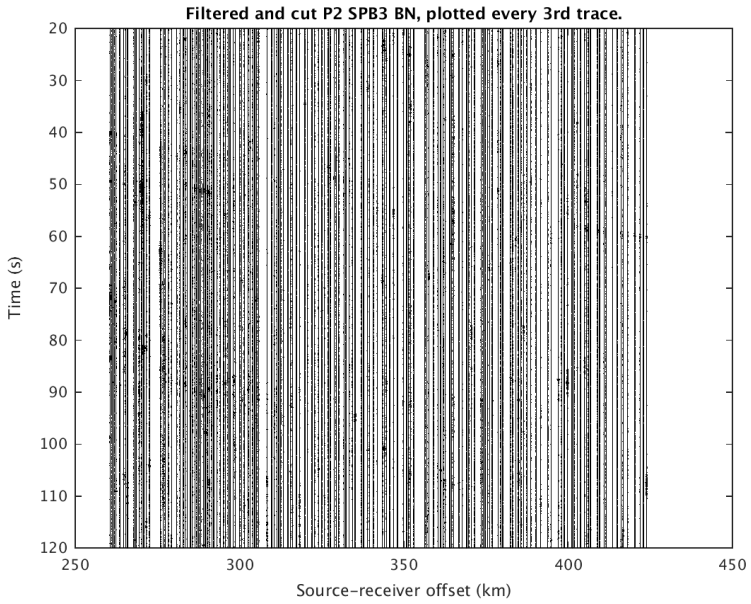

Figure A.20: Filtered and cut *P*2 SPB3 BN, scaled by a factor of 0.001. Every 3rd trace is plotted.

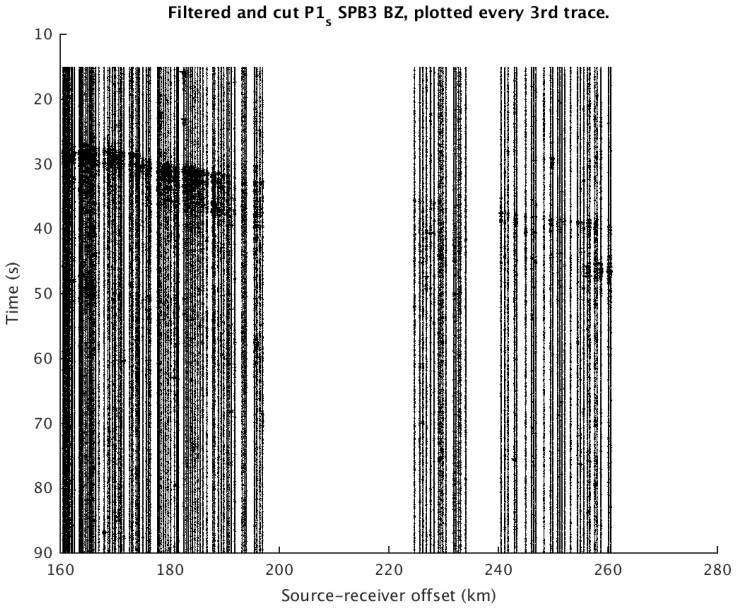

Figure A.21: Filtered and cut $P1_s$ SPB3 BZ, scaled by a factor of 0.001. Every 3rd trace is plotted.

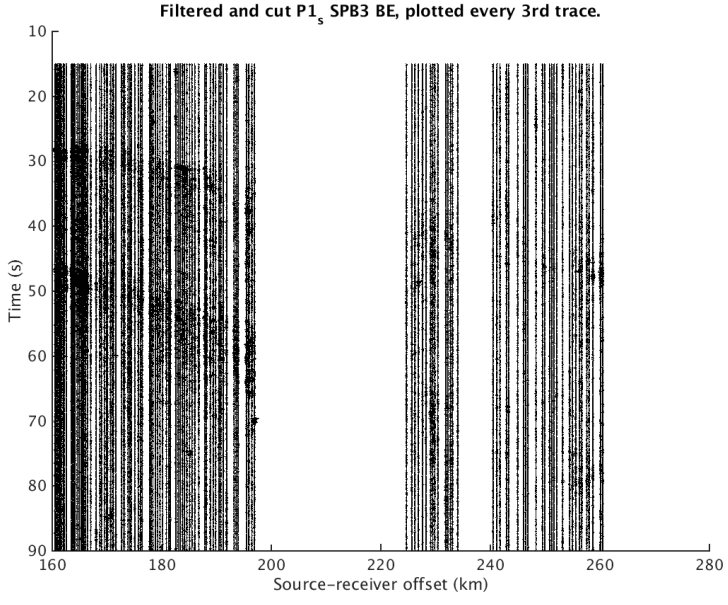

Figure A.22: Filtered and cut $P1_s$ SPB3 BE, scaled by a factor of 0.001. Every 3rd trace is plotted.

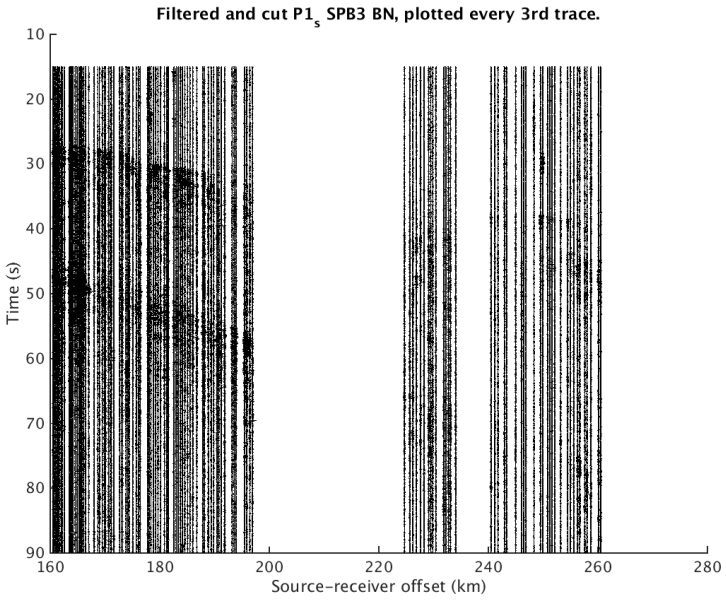

Figure A.23: Filtered and cut $P1_s$ SPB3 BN, scaled by a factor of 0.001. Every 3rd trace is plotted.

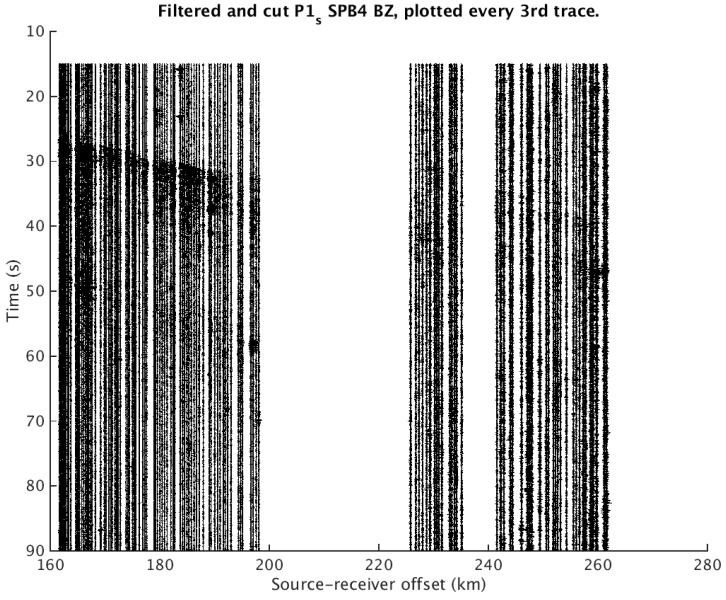

Figure A.24: Filtered and cut $P1_s$ SPB4 BZ, scaled by a factor of 0.001. Every 3rd trace is plotted.

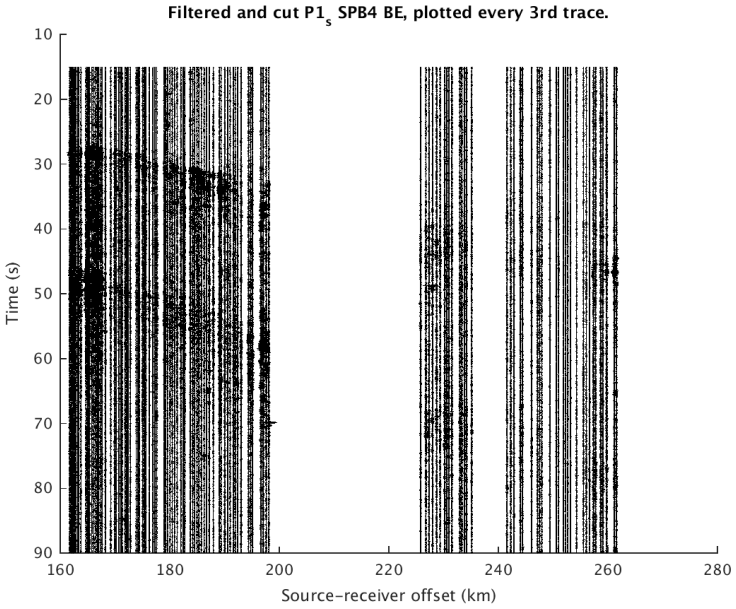

Figure A.25: Filtered and cut $P1_s$ SPB4 BE, scaled by a factor of 0.001. Every 3rd trace is plotted.

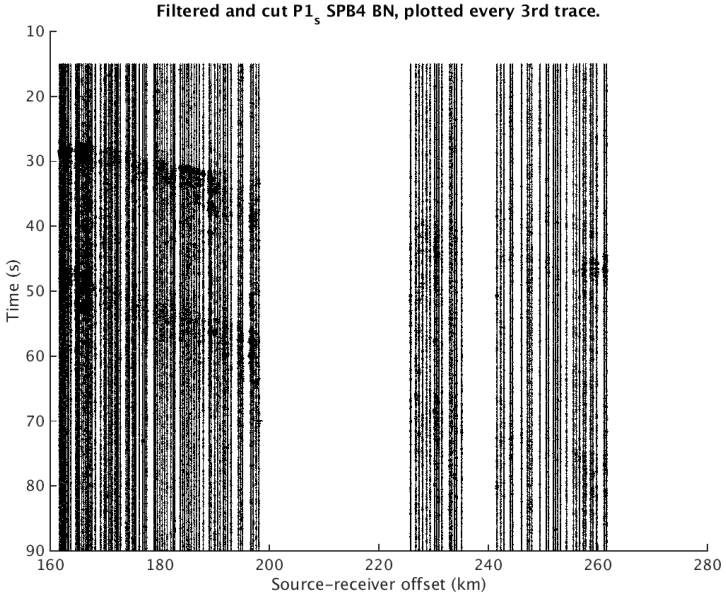

Figure A.26: Filtered and cut $P1_s$ SPB4 BN, scaled by a factor of 0.001. Every 3rd trace is plotted.

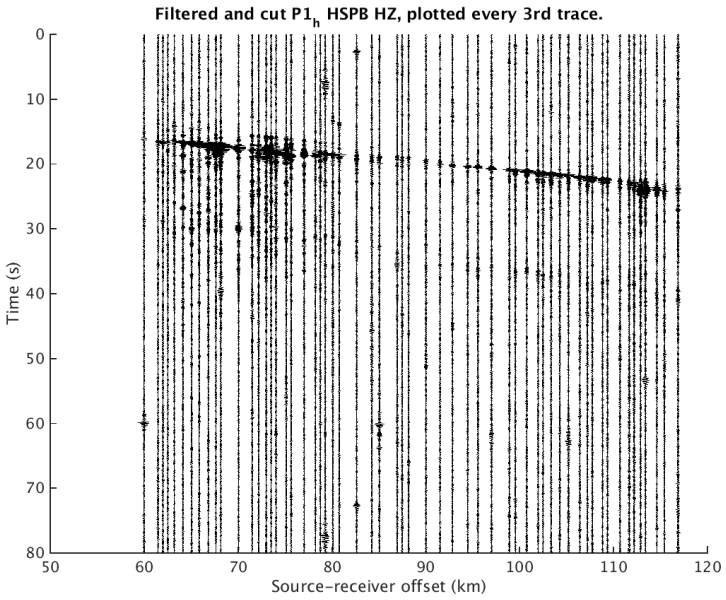

Figure A.27: Filtered and cut $P1_h$ HSPB HZ, scaled by a factor of 0.01. Every 4th trace is plotted.

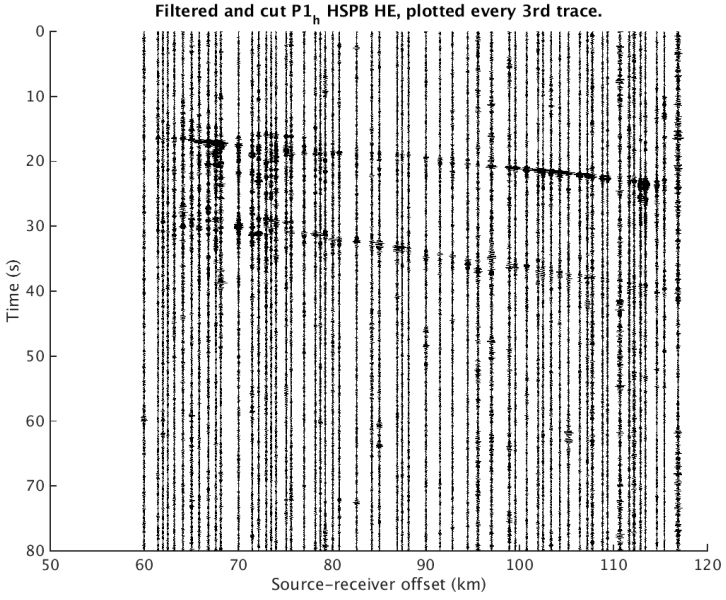

Figure A.28: Filtered and cut $P1_h$ HSPB HE, scaled by a factor of 0.01. Every 4th trace is plotted.

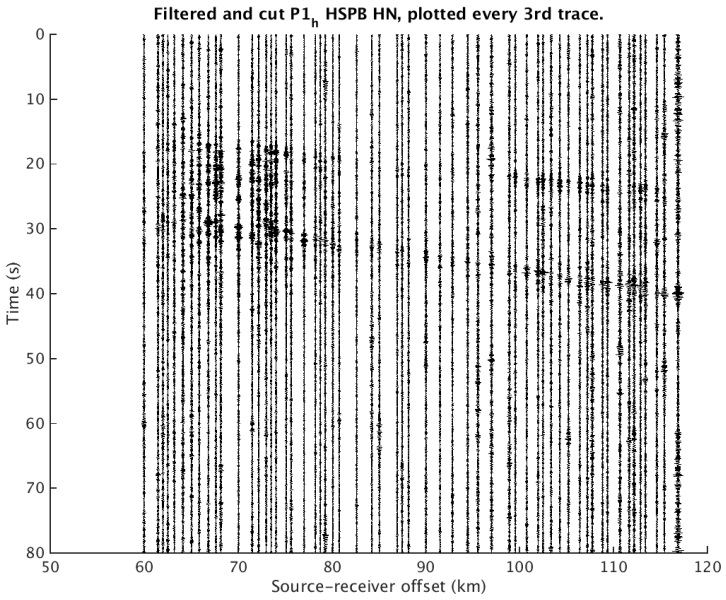

Figure A.29: Filtered and cut $P1_h$ HSPB HN, scaled by a factor of 0.01. Every 4th trace is plotted.

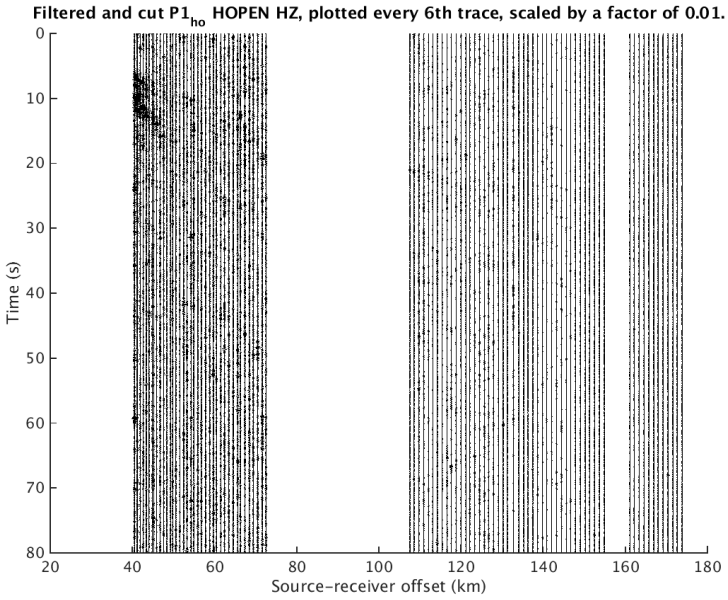

Figure A.30: Filtered and cut $P1_{ho}$ HOPEN HZ, scaled by a factor of 0.01. Every 4th trace is plotted.

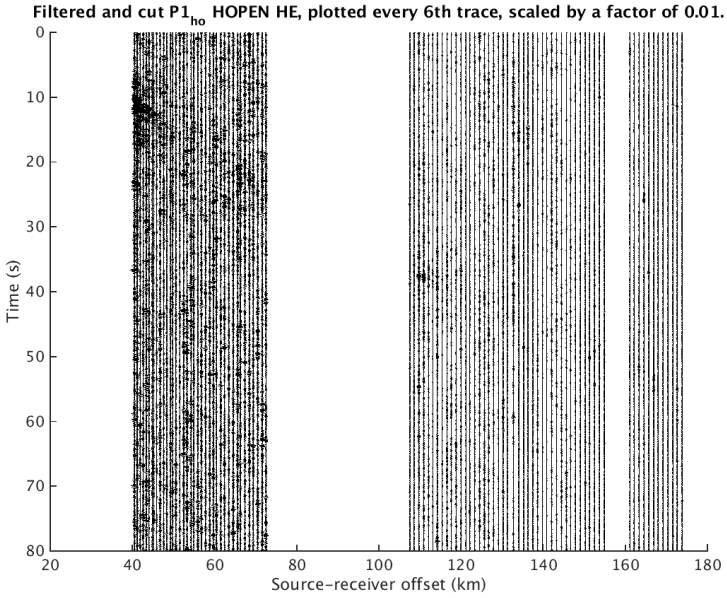

Figure A.31: Filtered and cut $P1_{ho}$ HOPEN HE, scaled by a factor of 0.01. Every 4th trace is plotted.

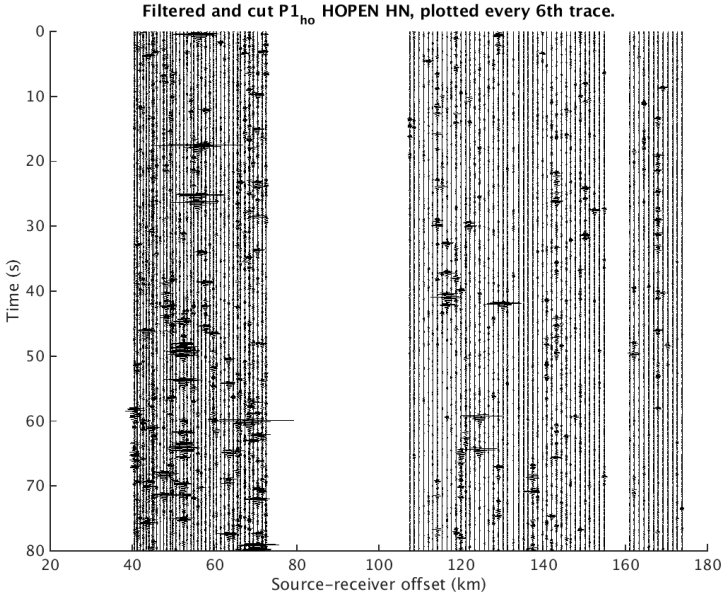

Figure A.32: Filtered and cut $P1_{ho}$ HOPEN HN, scaled by a factor of 0.001. Every 4th trace is plotted.

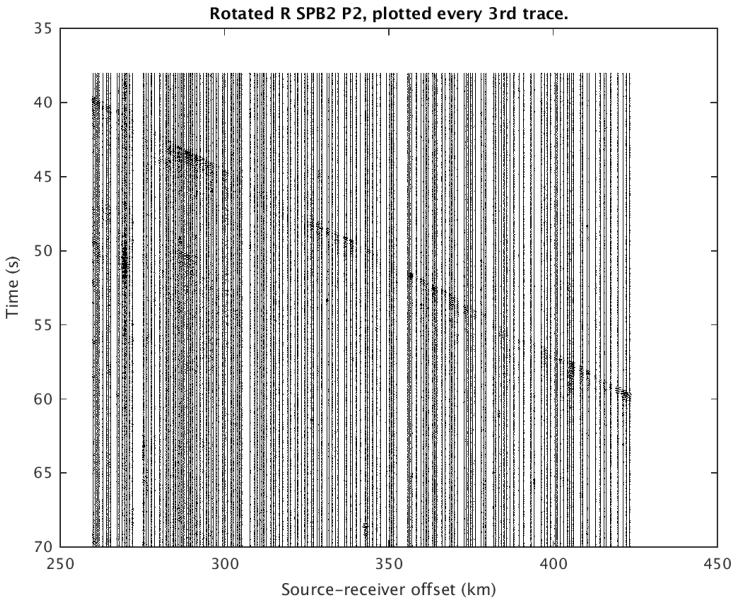

Figure A.33: Rotated SPB2 R, plotted every 6th trace.

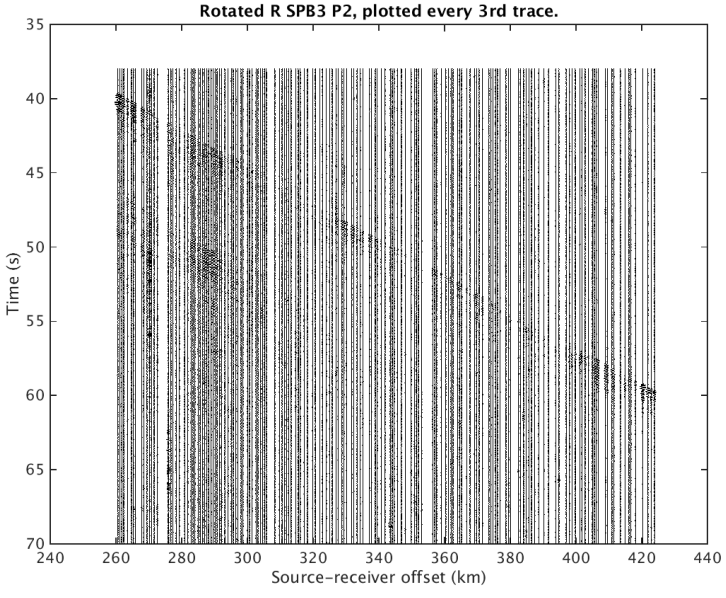

Figure A.34: Rotated SPB3 R, plotted every 6th trace.

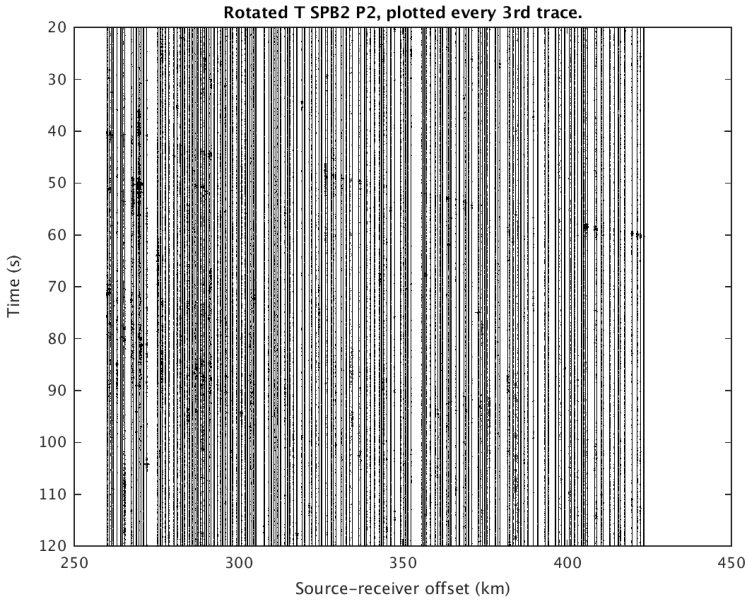

Figure A.35: Rotated SPB2 T plotted every 6th trace.

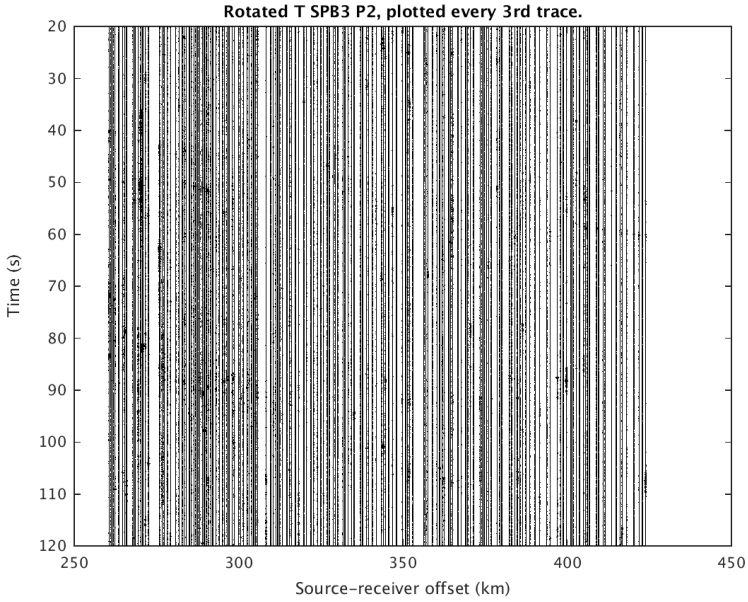

Figure A.36: Rotated SPB3 T plotted every 6th trace.

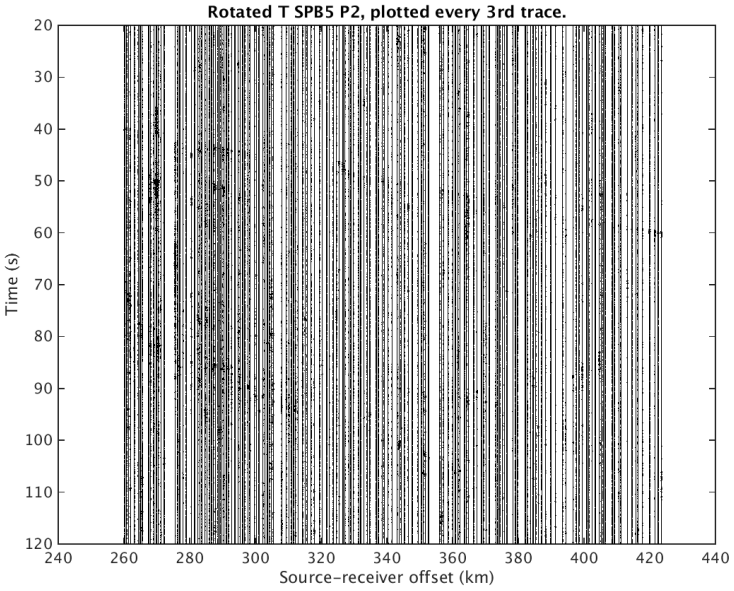

Figure A.37: Rotated SPB5 T plotted every 6th trace.

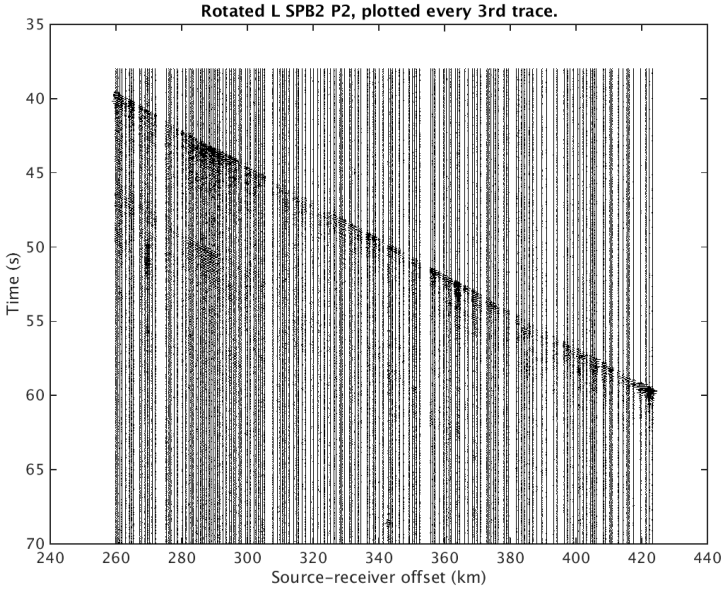

Figure A.38: Rotated SPB2 L plotted every 6th trace.

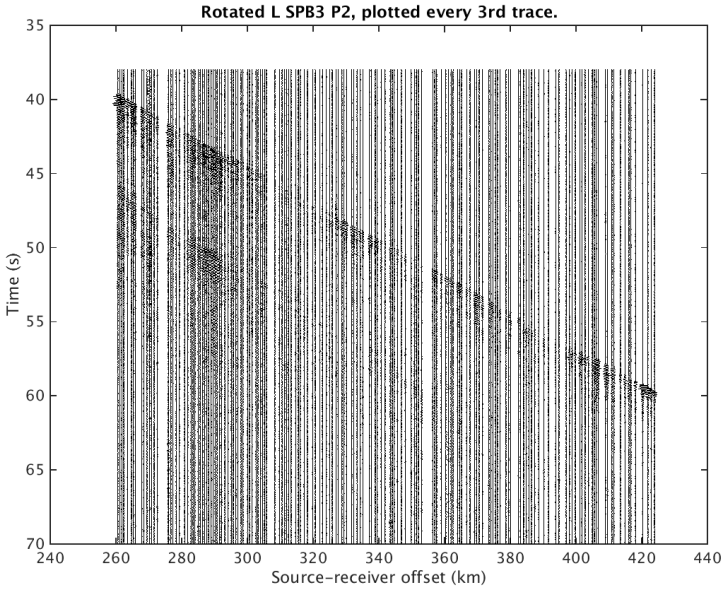

Figure A.39: Rotated SPB3 L plotted every 6th trace.

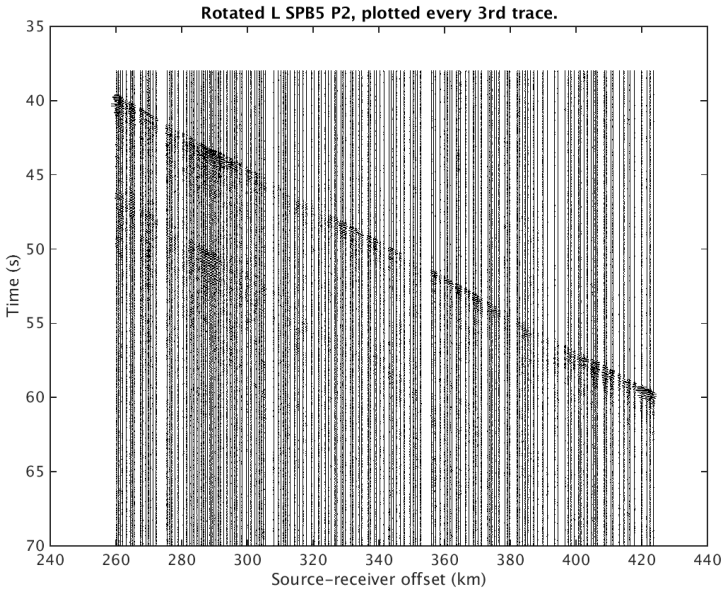

Figure A.40: Rotated SPB5 L plotted every 6th trace.

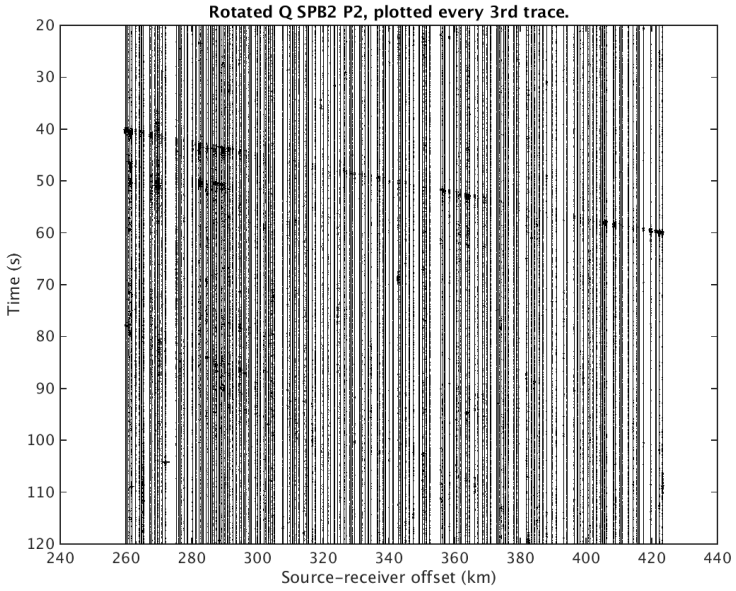

Figure A.41: Rotated SPB2 Q plotted every 6th trace.

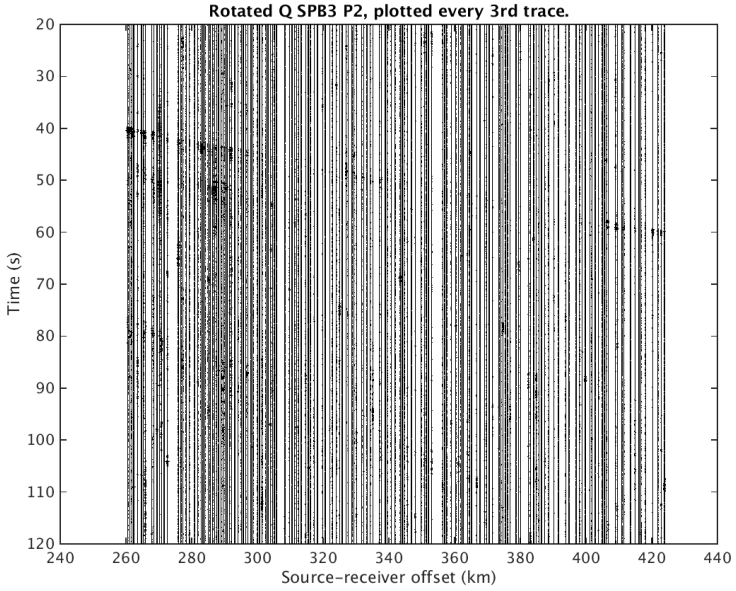

Figure A.42: Rotated SPB3 Q plotted every 6th trace.

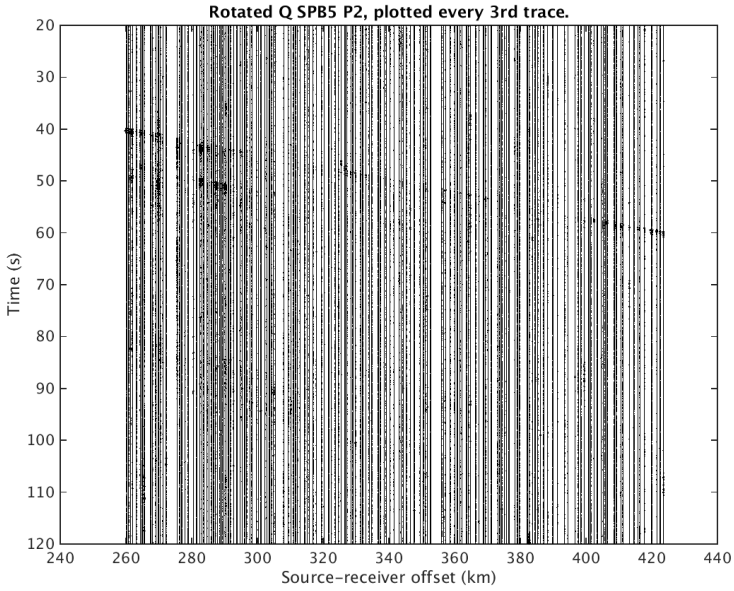

Figure A.43: Rotated SPB5 Q plotted every 6th trace.

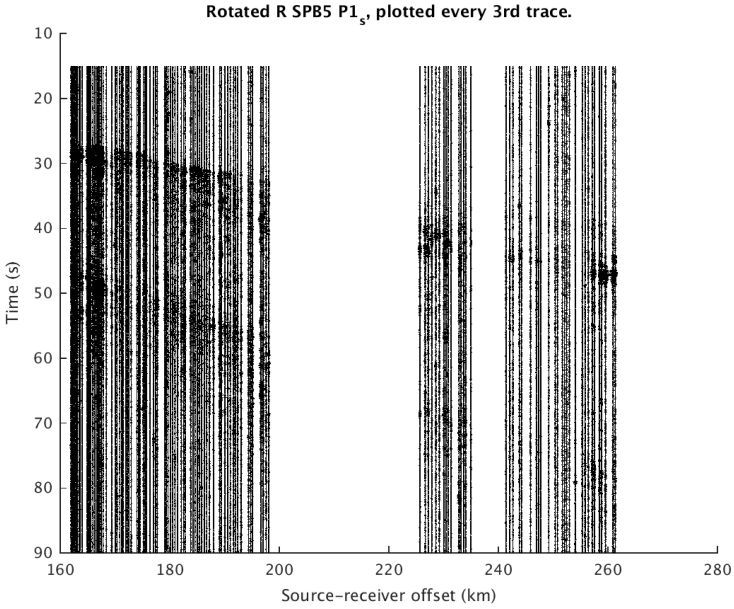

Figure A.44: Rotated SPB5 $P1_S$ R plotted every 3rd trace.

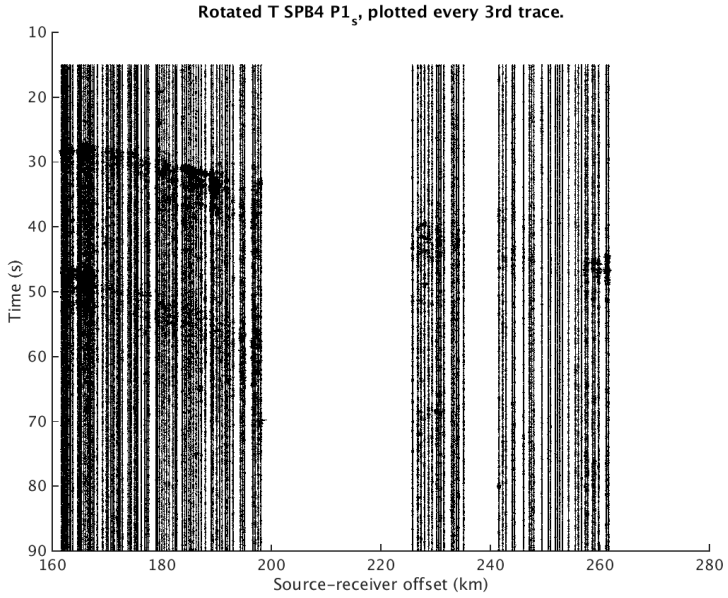

Figure A.45: Rotated SPB4 $P1_s$ T plotted every 3rd trace.

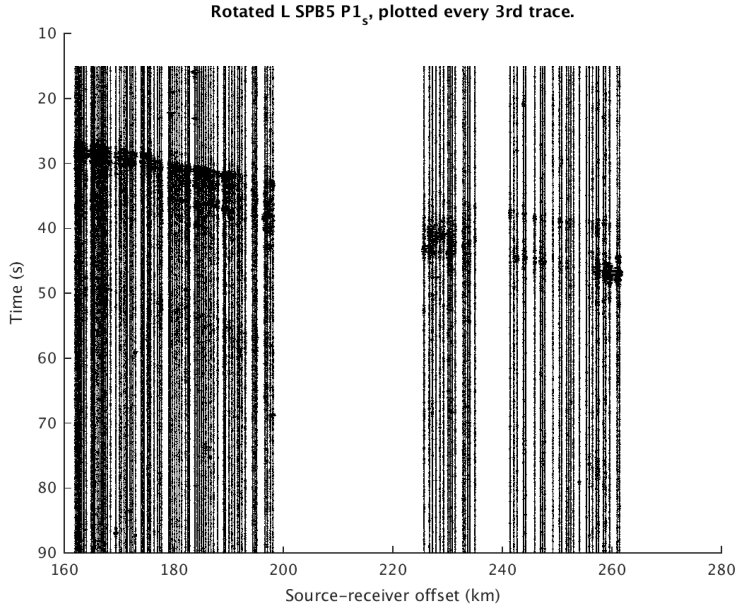

Figure A.46: Rotated SPB5 $P1_s$ L plotted every 3rd trace.

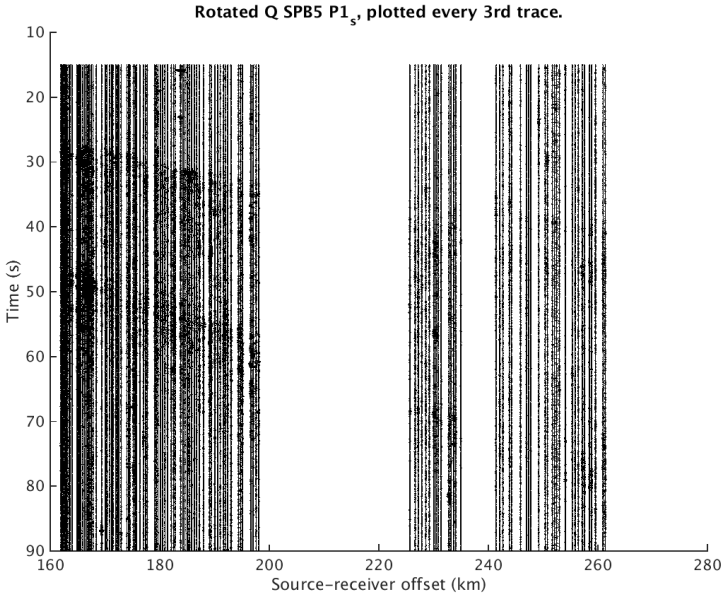

Figure A.47: Rotated SPB5 $P1_s$ Q plotted every 3rd trace.

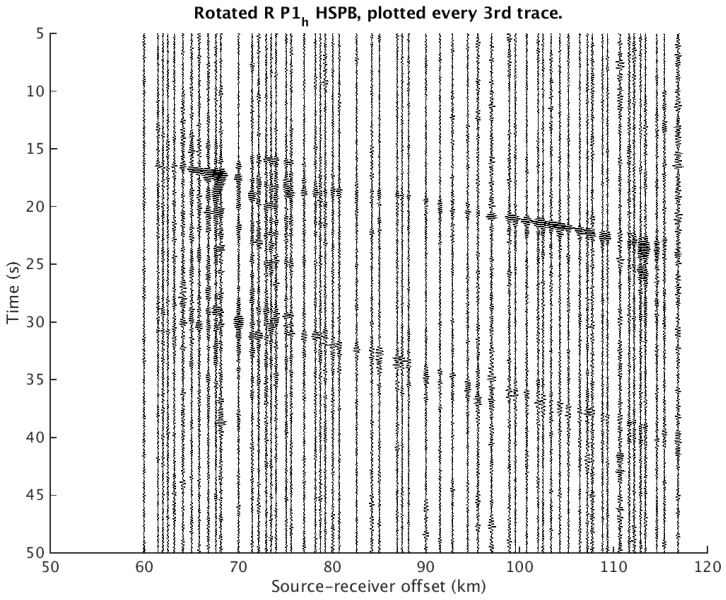

Figure A.48: Rotated HSPB $P1_h$ R plotted every 3rd trace.

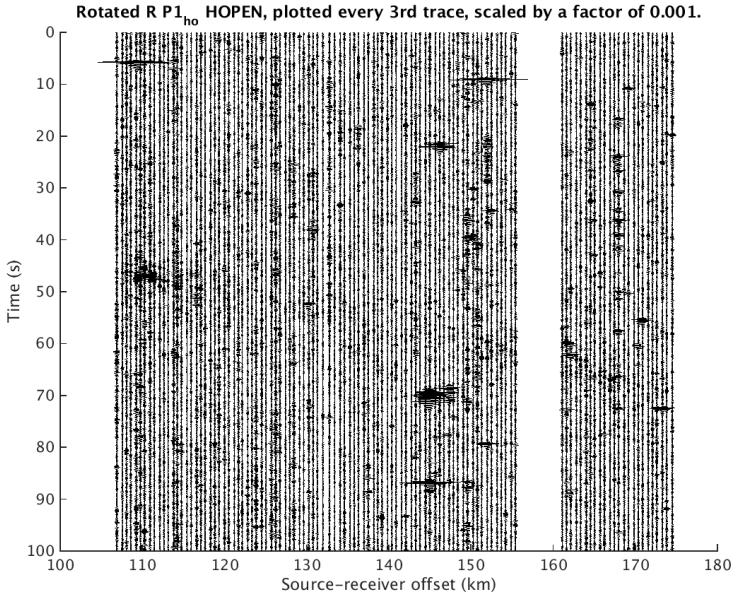

Figure A.49: Rotated HOPEN $P1_{ho}$ R.

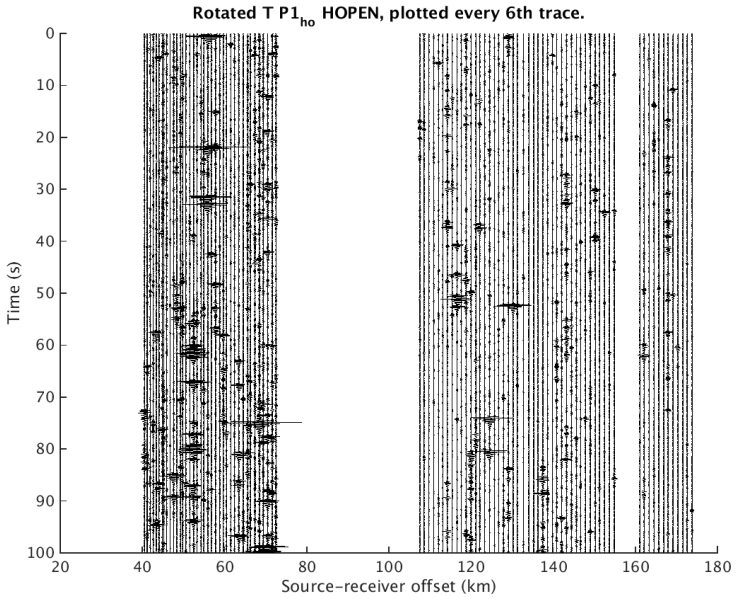

Figure A.50: Rotated HOPEN $P1_{ho}$ T.

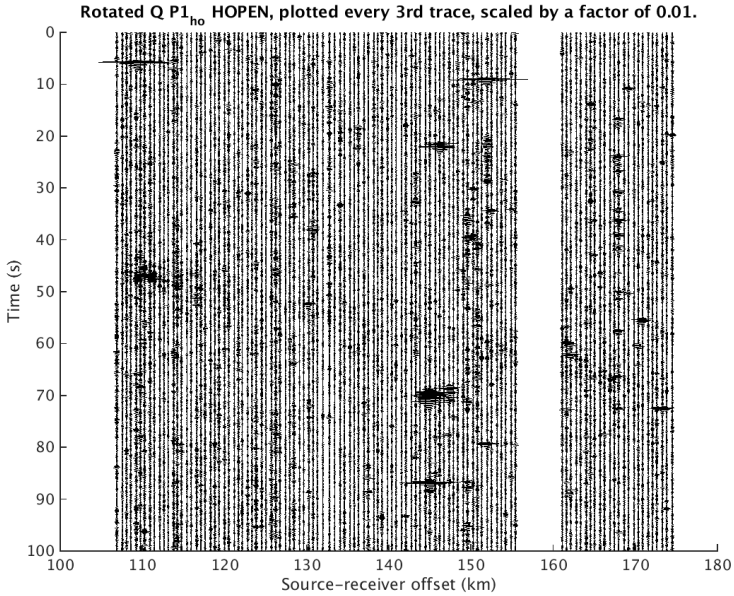

Figure A.51: Rotated HOPEN $P1_{ho}$ Q.

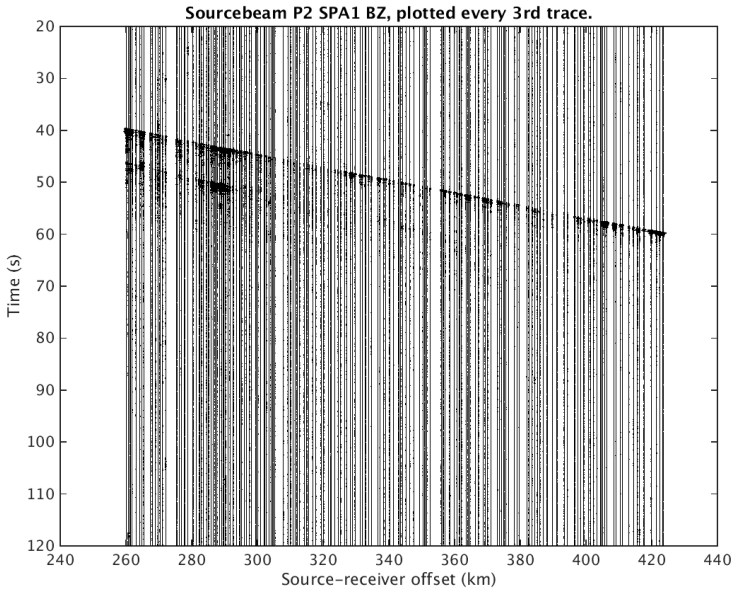

Figure A.52: Source-beam P2 SPA1 BZ, plotted every 6th trace

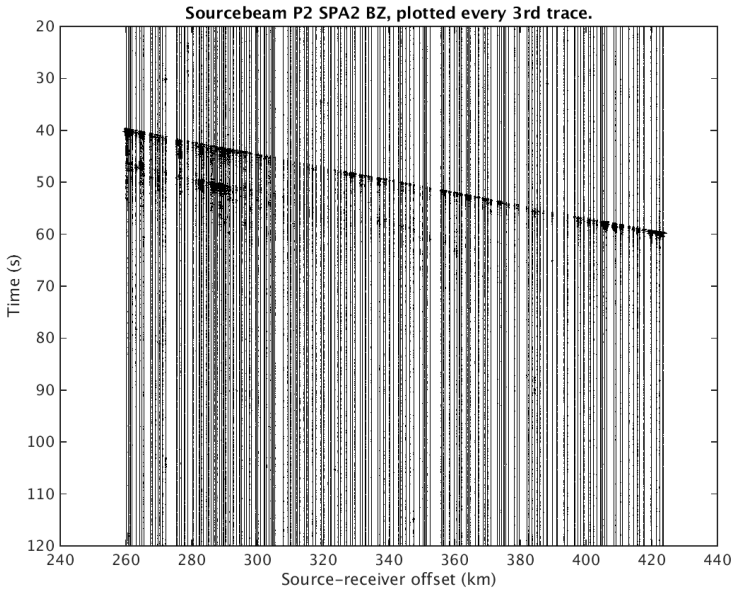

Figure A.53: Source-beam P2 SPA2 BZ, plotted every 6th trace

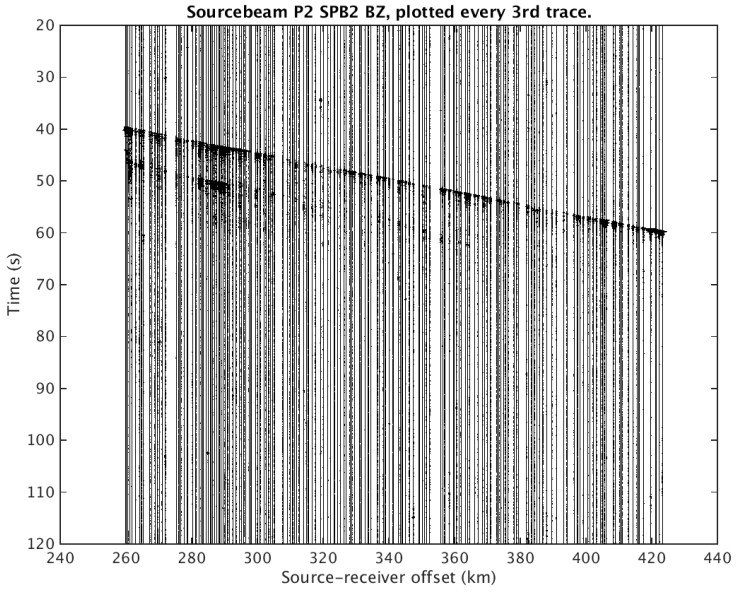

Figure A.54: Source-beam P2 SPB2 BZ, plotted every 6th trace

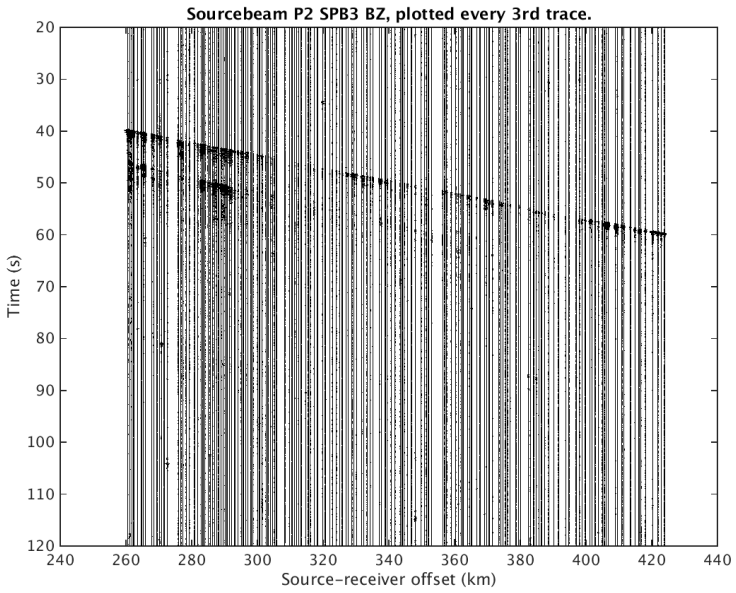

Figure A.55: Source-beam P2 SPB3 BZ, plotted every 6th trace

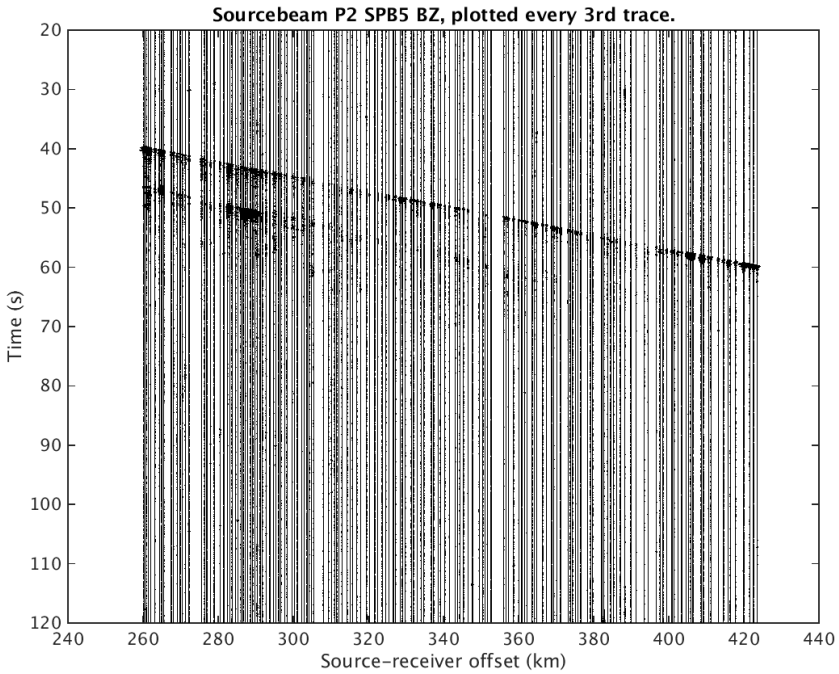

Figure A.56: Source-beam P2 SPB5 BZ, plotted every 6th trace

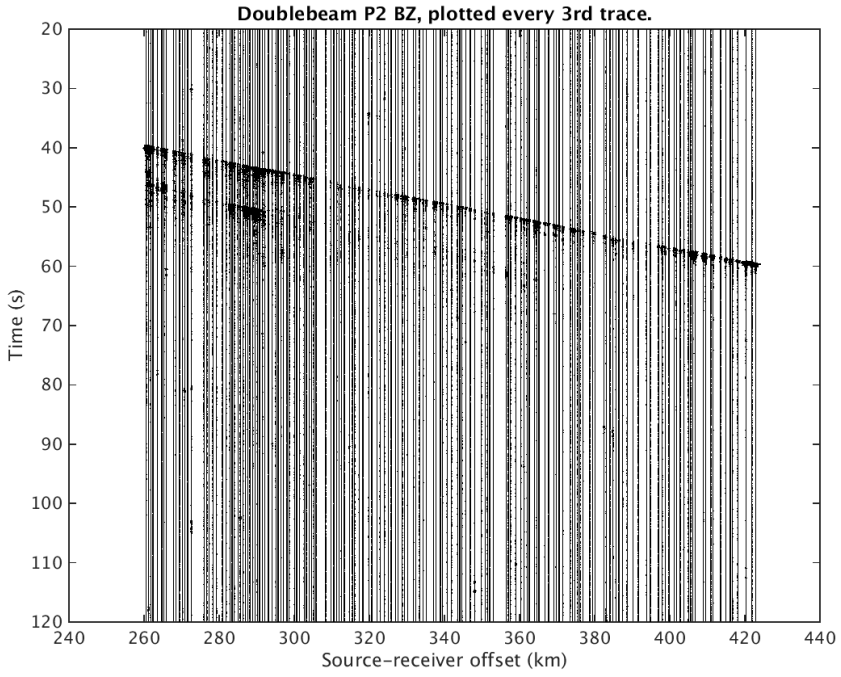

Figure A.57: Double-beam P2 BZ, plotted every 6th trace

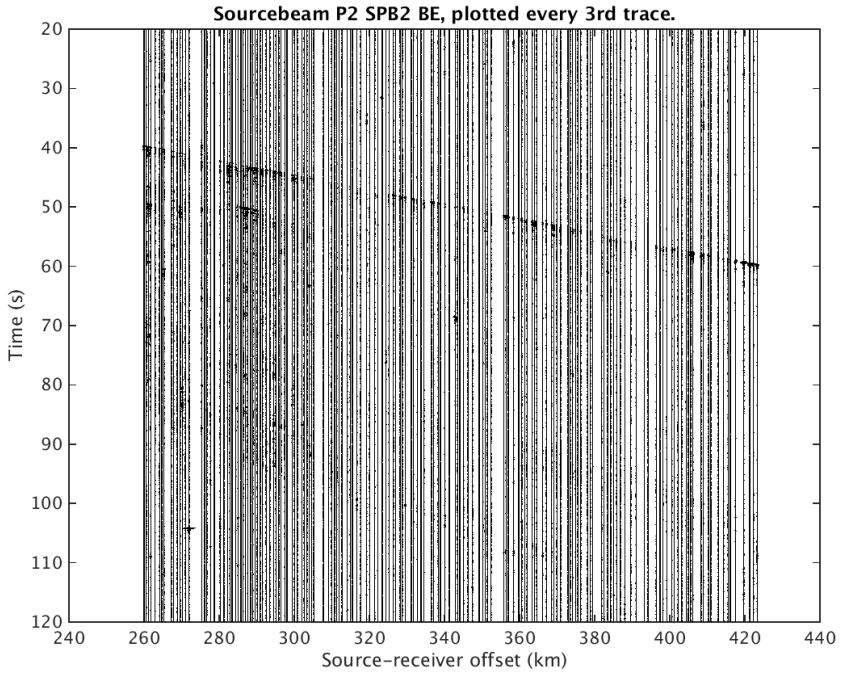

Figure A.58: Source-beam P2 SPB2 BE, plotted every 6th trace

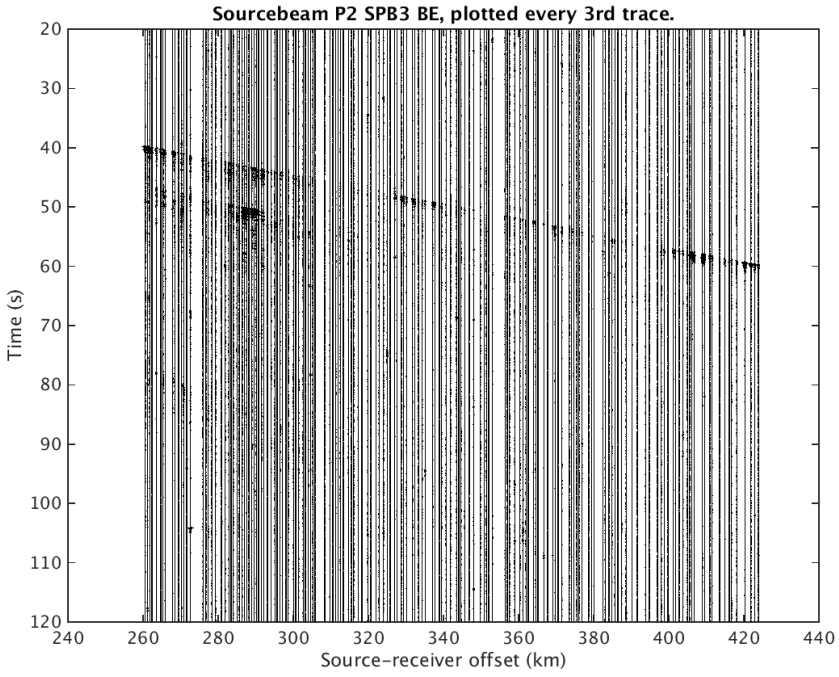

Figure A.59: Source-beam P2 SPB3 BE, plotted every 6th trace

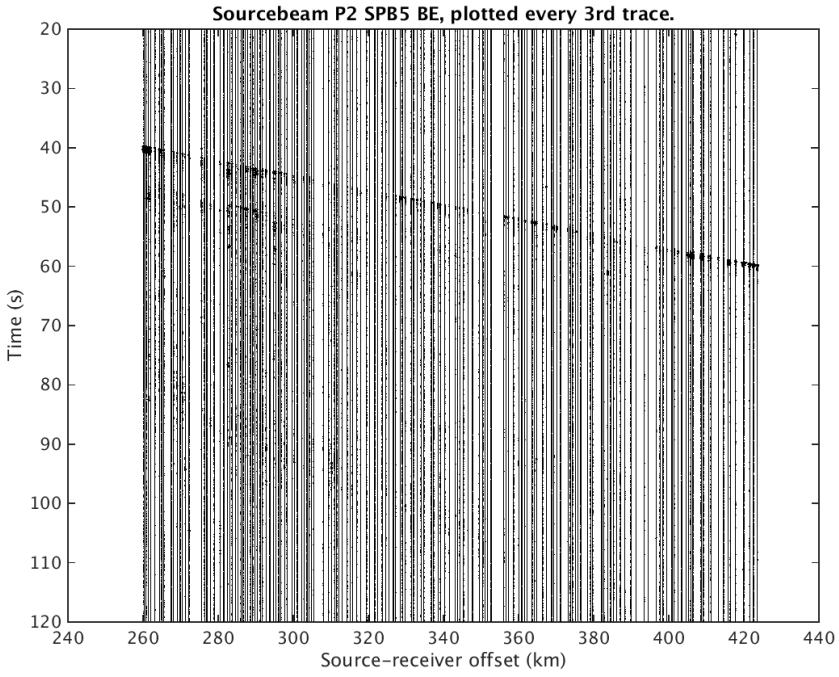

Figure A.60: Source-beam P2 SPB5 BE, plotted every 6th trace

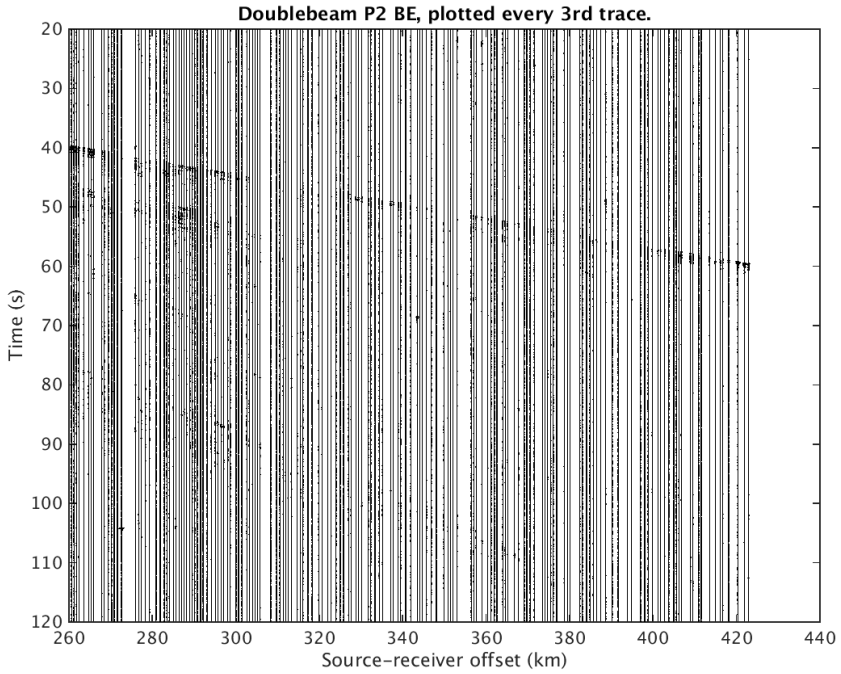

Figure A.61: Double-beam P2 BE, plotted every 6th trace

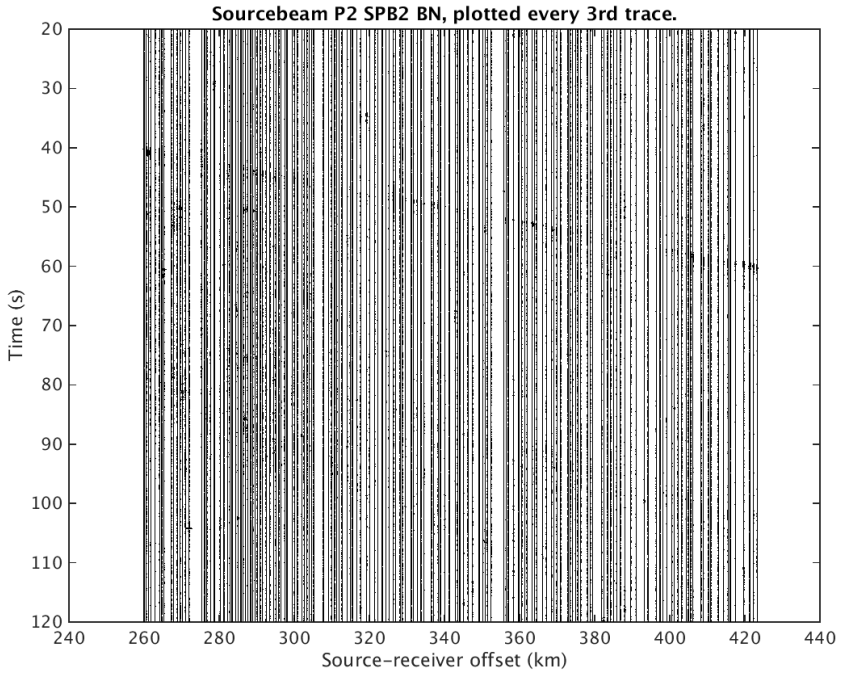

Figure A.62: Source-beam P2 SPB2 BN, plotted every 6th trace

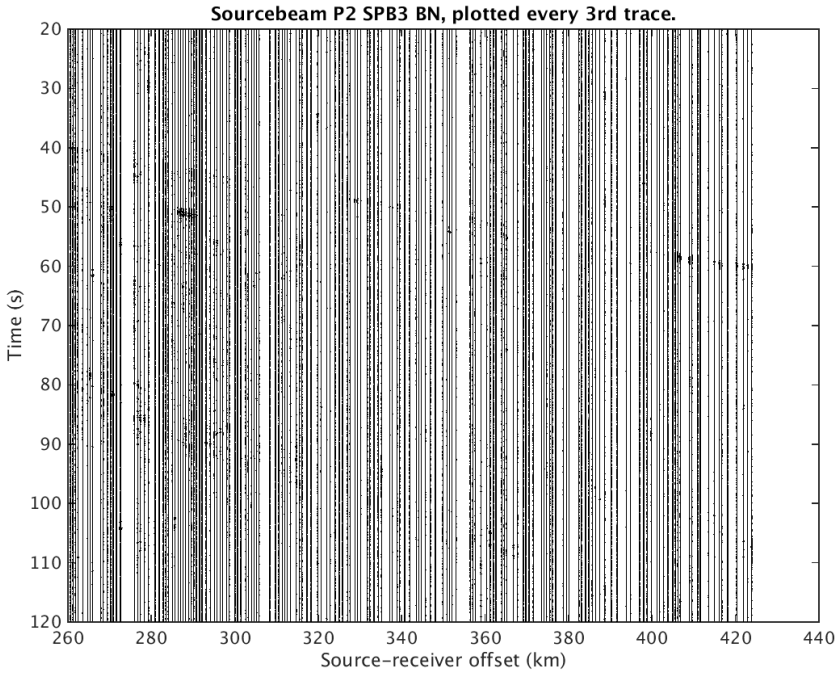

Figure A.63: Source-beam P2 SPB3 BN, plotted every 6th trace

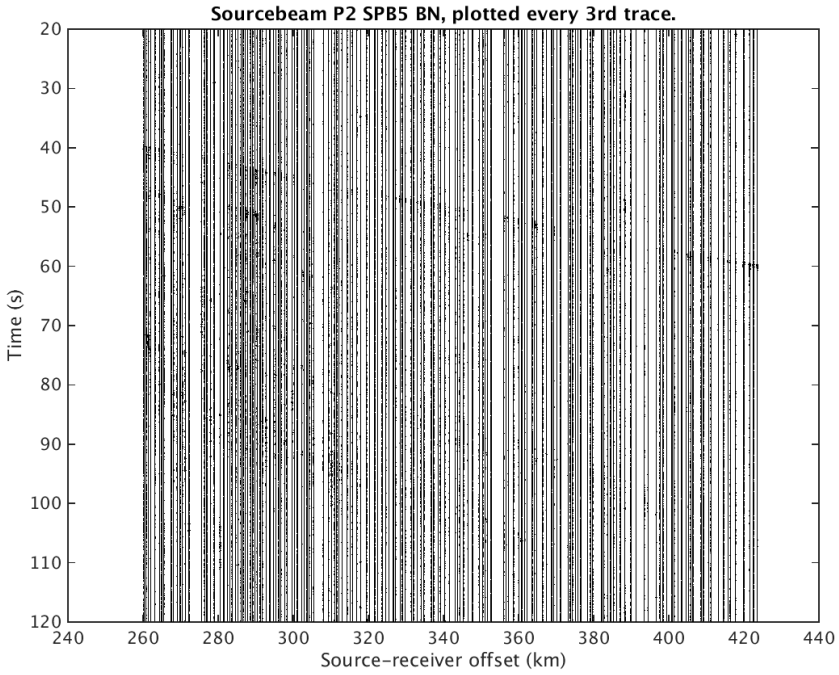

Figure A.64: Source-beam P2 SPB5 BN, plotted every 6th trace

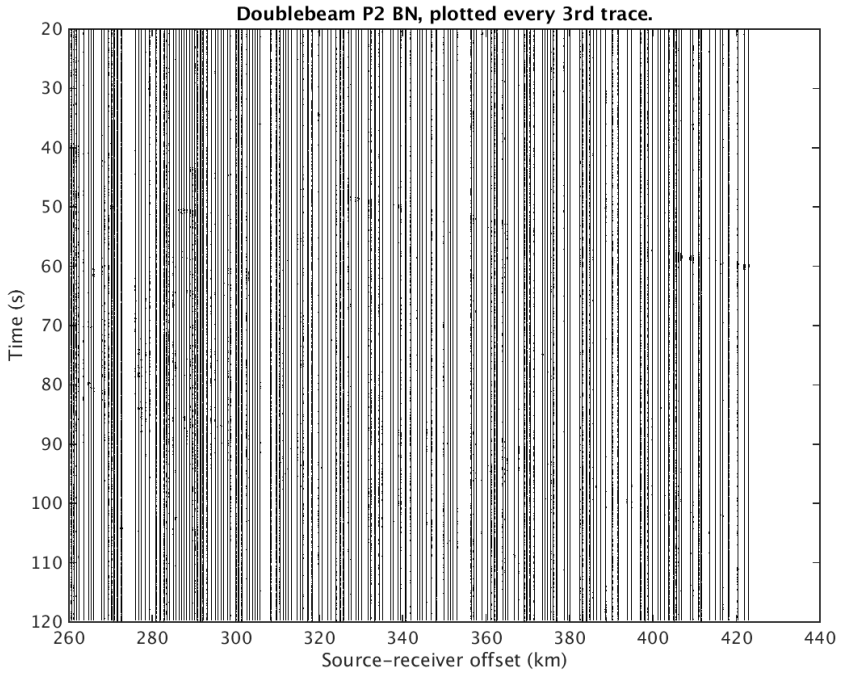

Figure A.65: Double-beam P2 BN, plotted every 6th trace

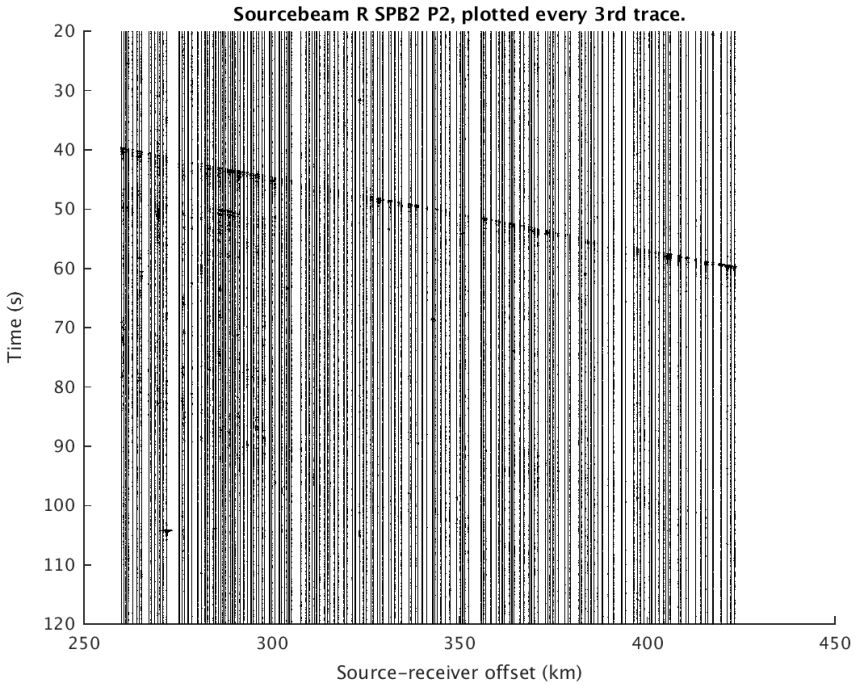

Figure A.66: Source-beam P2 SPB2 R, plotted every 6th trace

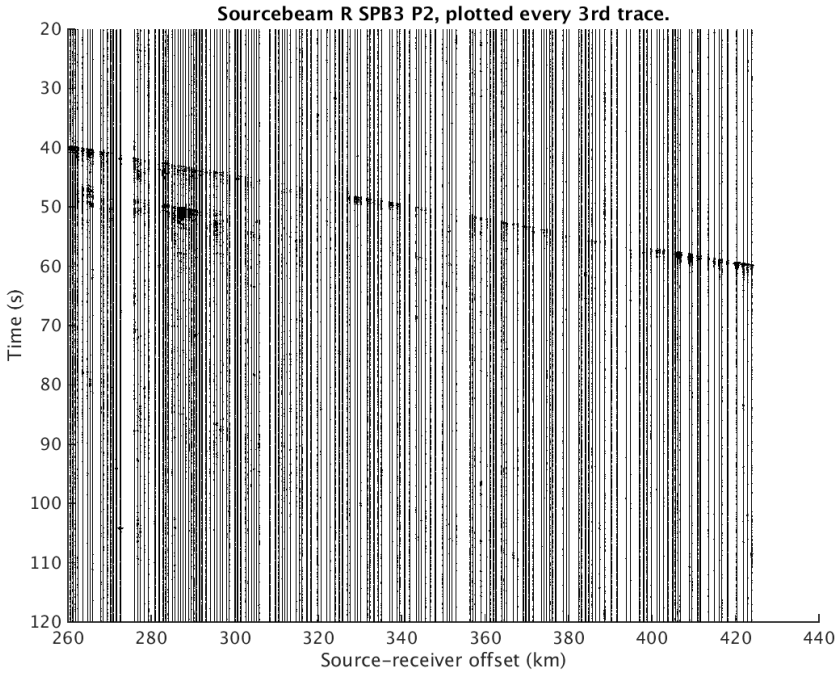

Figure A.67: Source-beam P2 SPB3 R, plotted every 6th trace

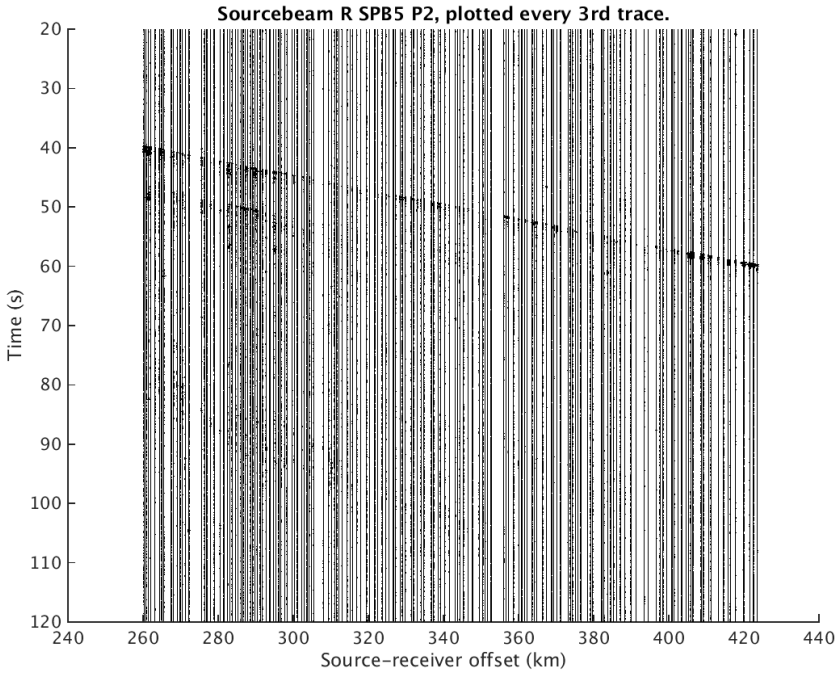

Figure A.68: Source-beam P2 SPB5 R, plotted every 6th trace

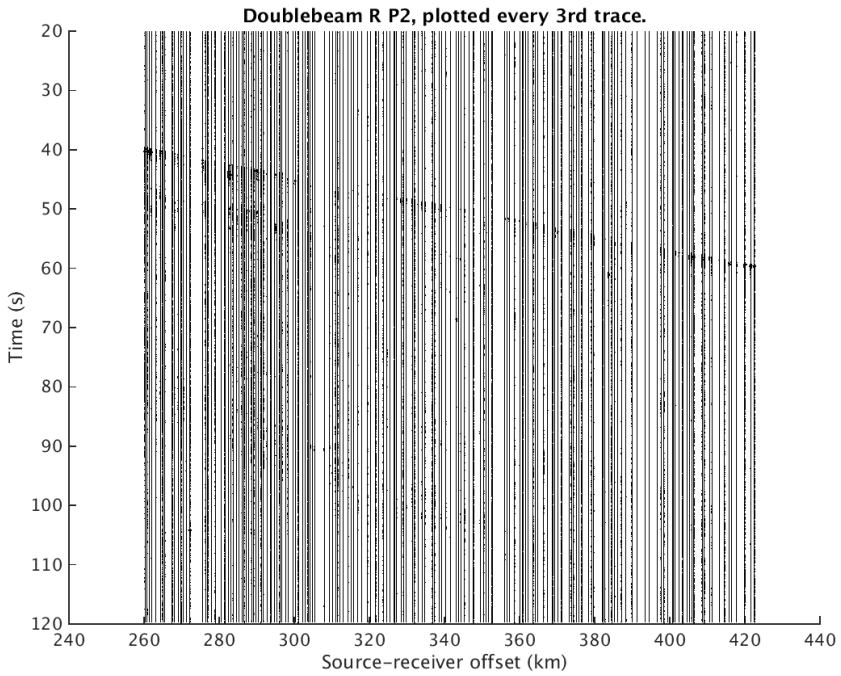

Figure A.69: Double-beam P2 R, plotted every 6th trace

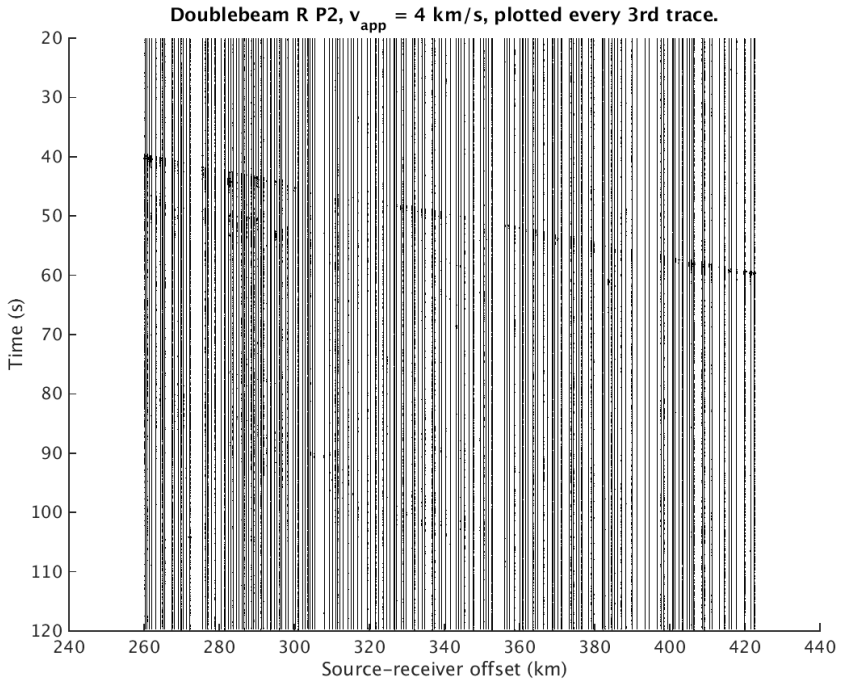

Figure A.70: Double-beam P2 R, apparent velocity = 4 km/s, plotted every 6th trace

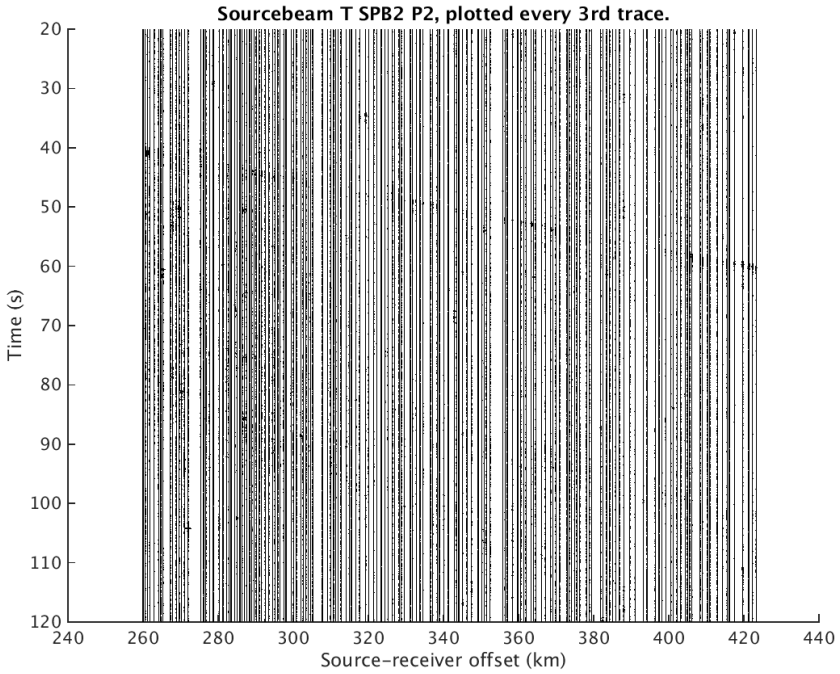

Figure A.71: Source-beam P2 SPB2 T, plotted every 6th trace

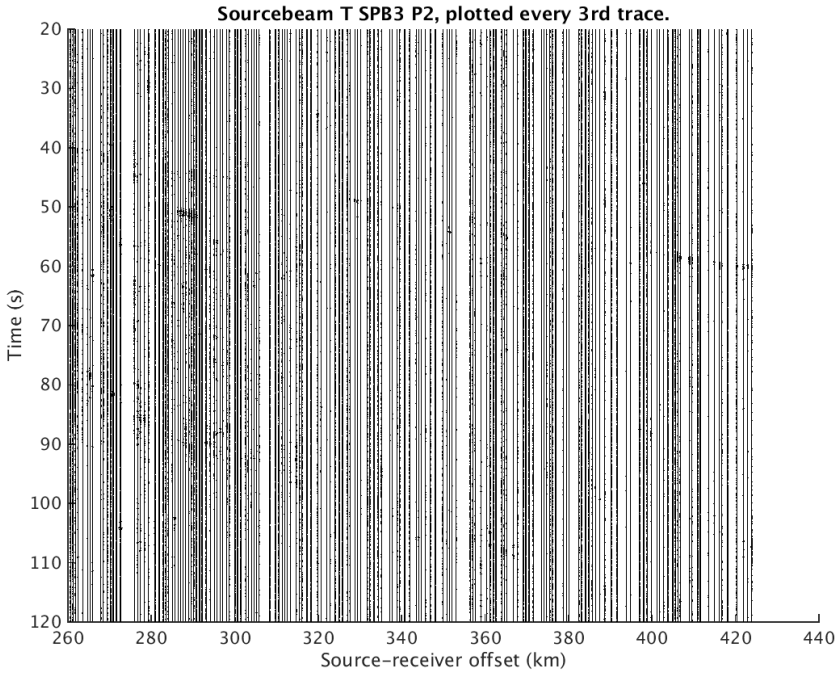

Figure A.72: Source-beam P2 SPB3 T, plotted every 6th trace

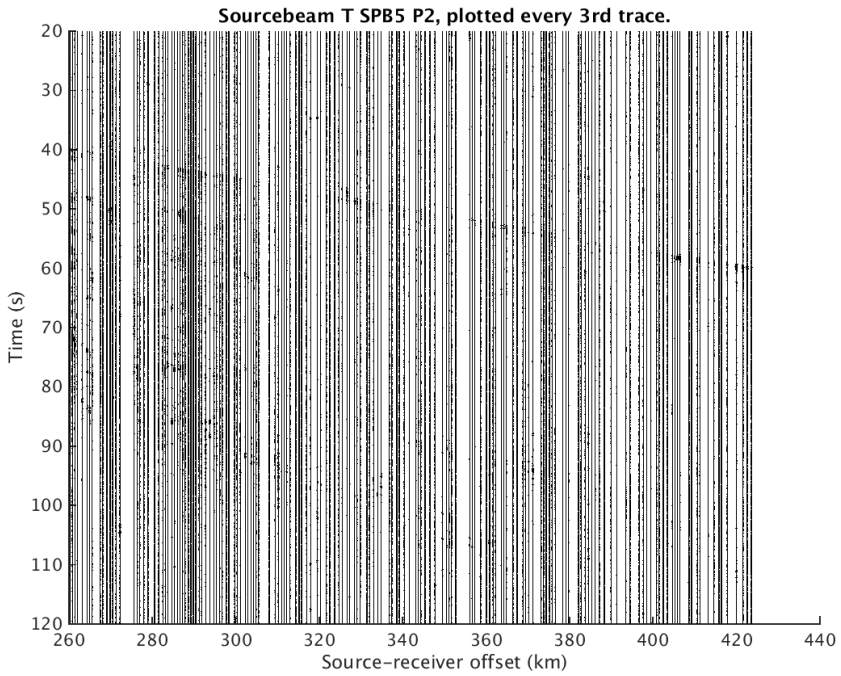

Figure A.73: Source-beam P2 SPB5 T, plotted every 6th trace

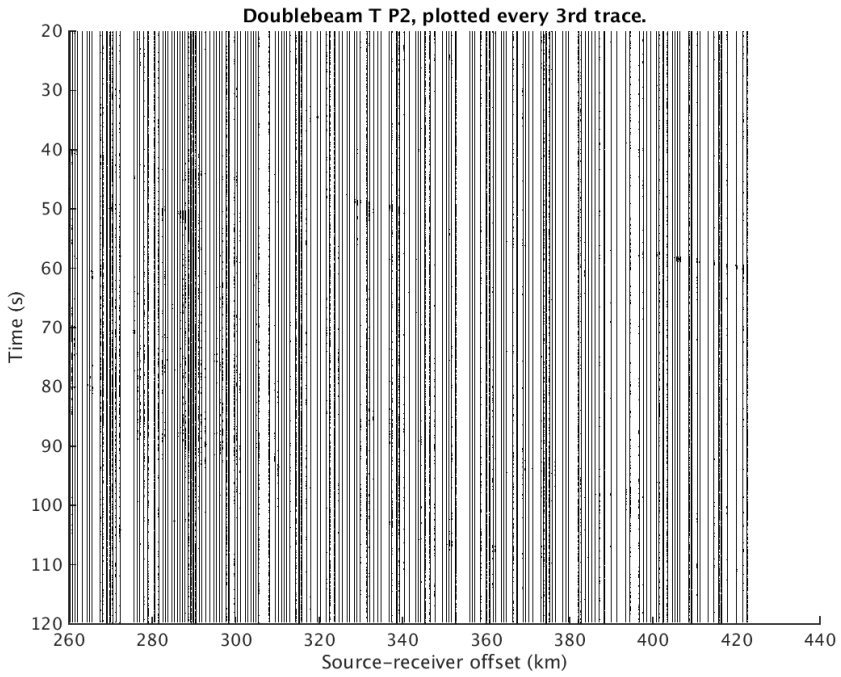

Figure A.74: Double-beam P2 T, plotted every 6th trace

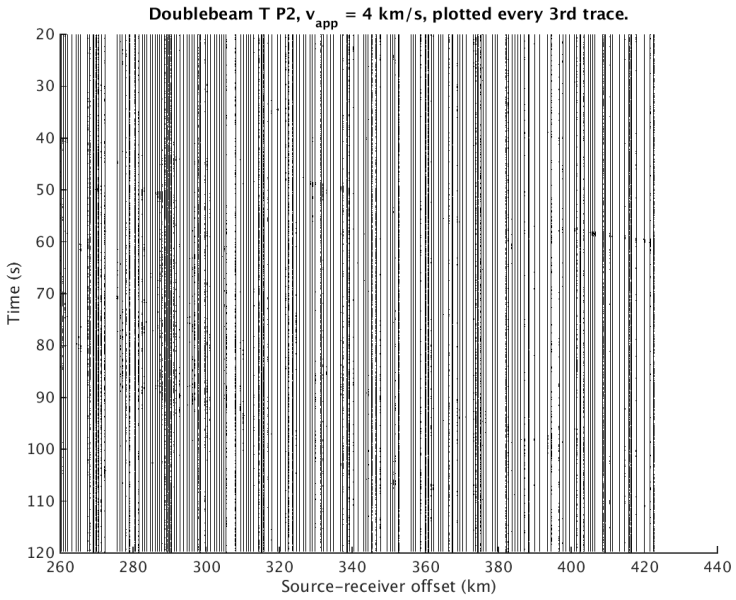

Figure A.75: Double-beam P2 T,apparent velocity = 4 km/s, plotted every 6th trace

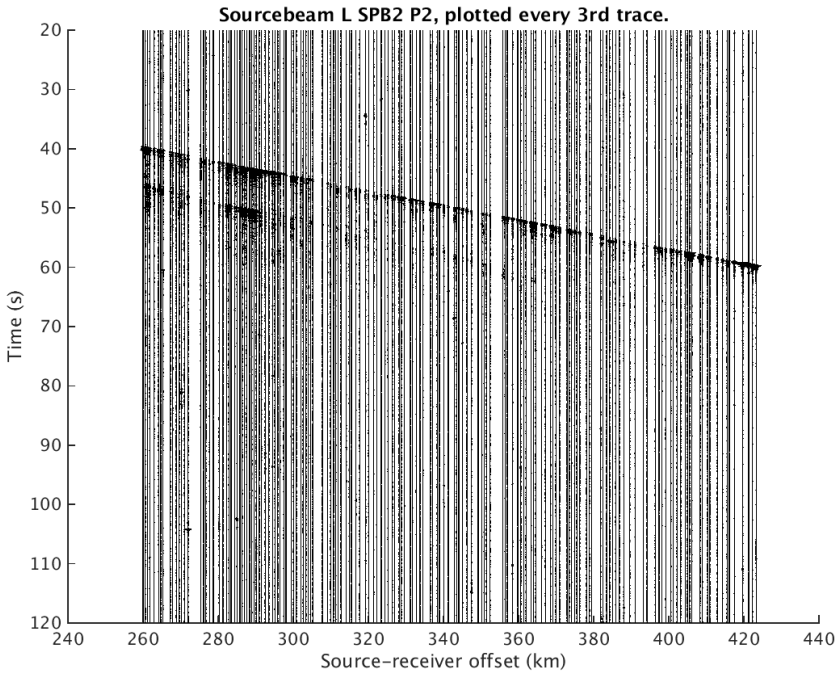

Figure A.76: Source-beam P2 SPB2 L, plotted every 6th trace

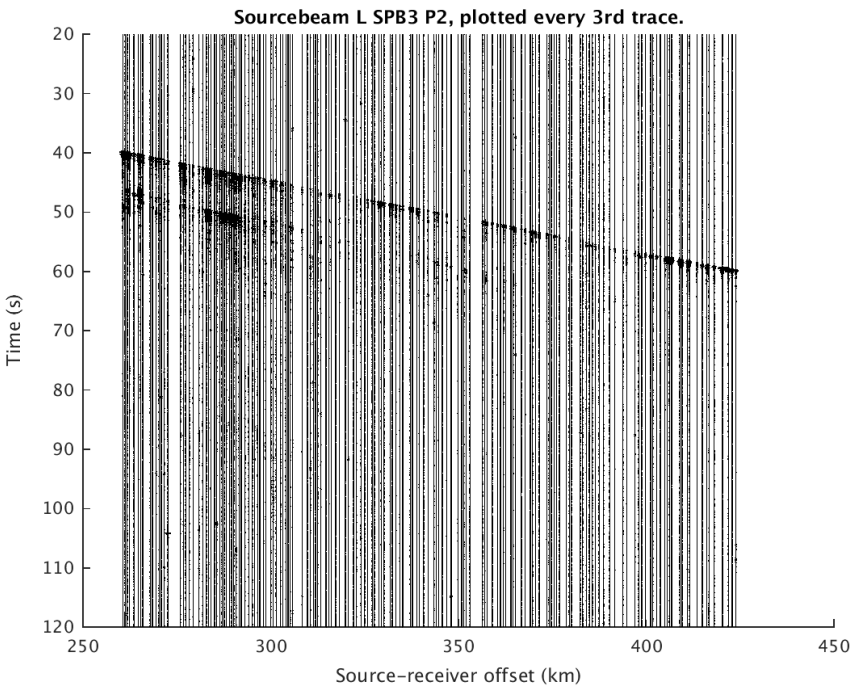

Figure A.77: Source-beam P2 SPB3 L, plotted every 6th trace

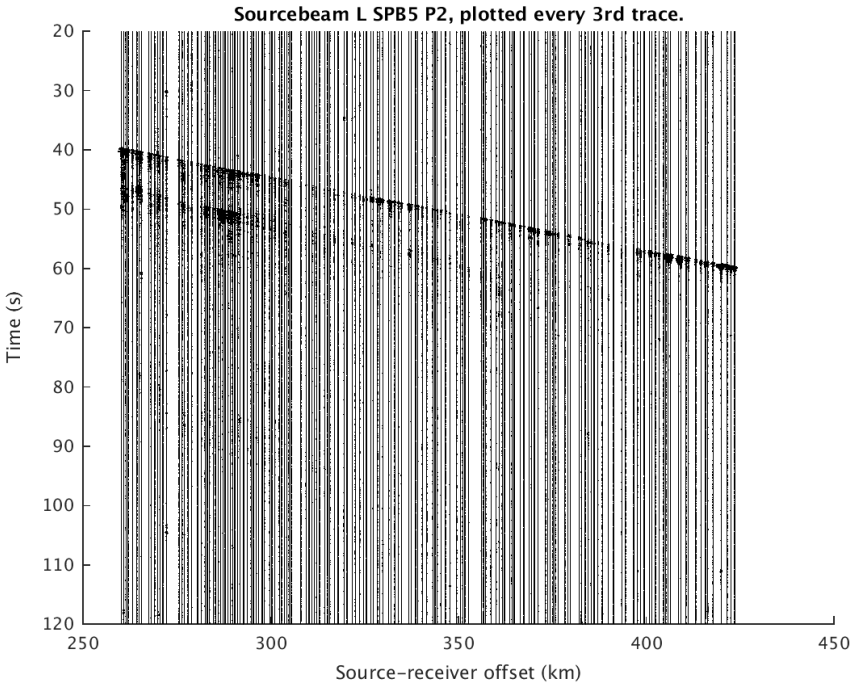

Figure A.78: Source-beam P2 SPB5 L, plotted every 6th trace

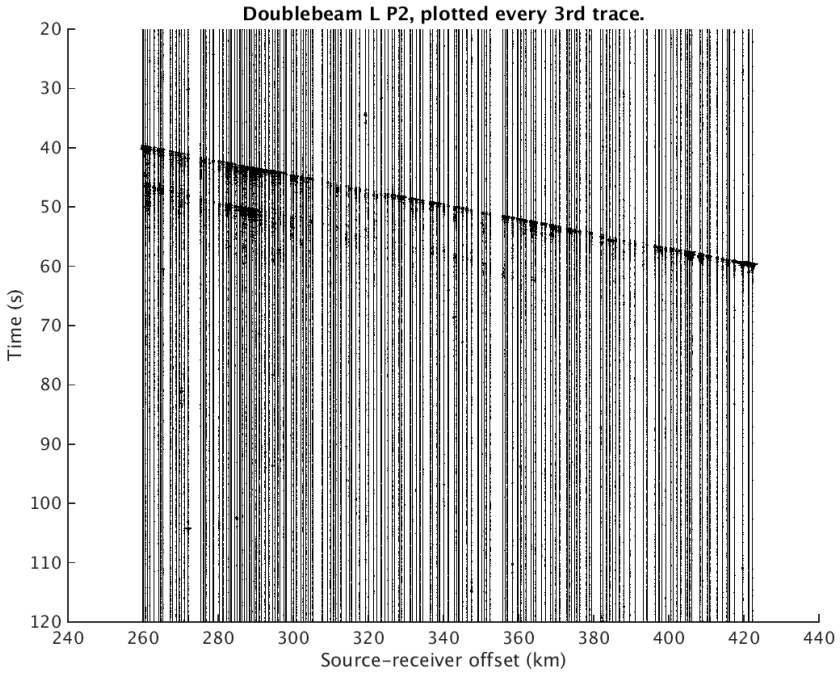

Figure A.79: Double-beam P2 L, plotted every 6th trace

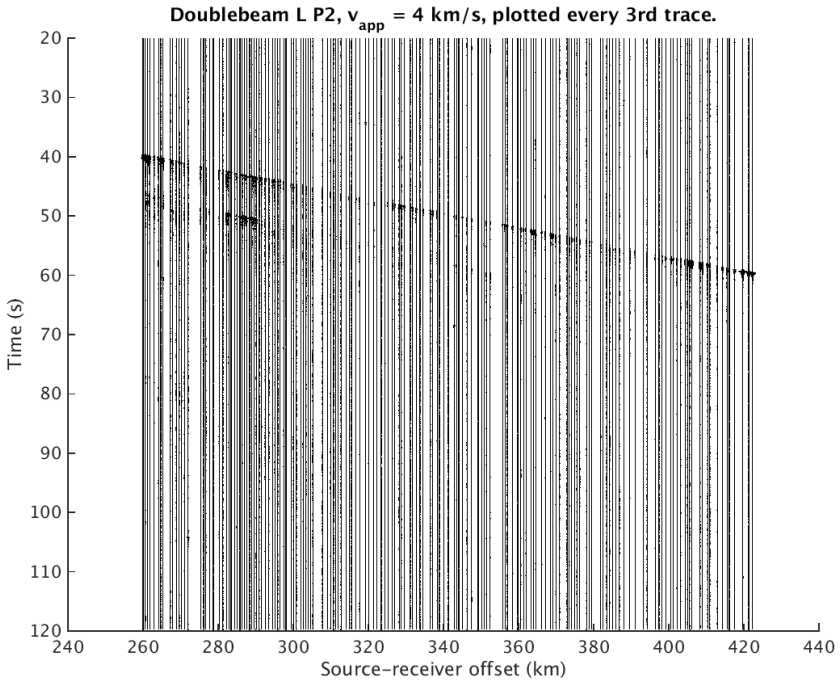

Figure A.80: Double-beam P2 L, apparent velocity = 4km/s, plotted every 6th trace

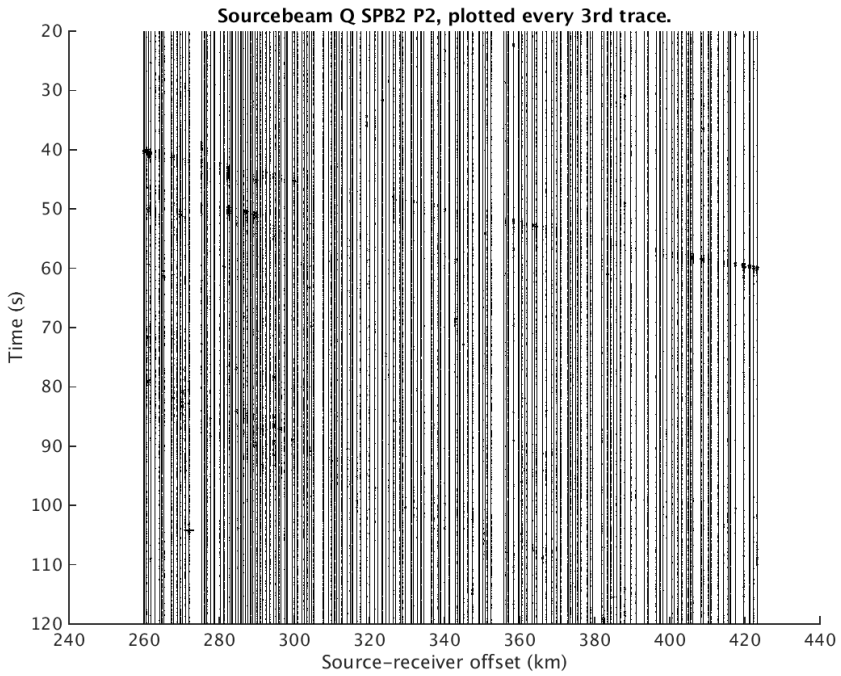

Figure A.81: Source-beam P2 SPB2 Q, plotted every 6th trace

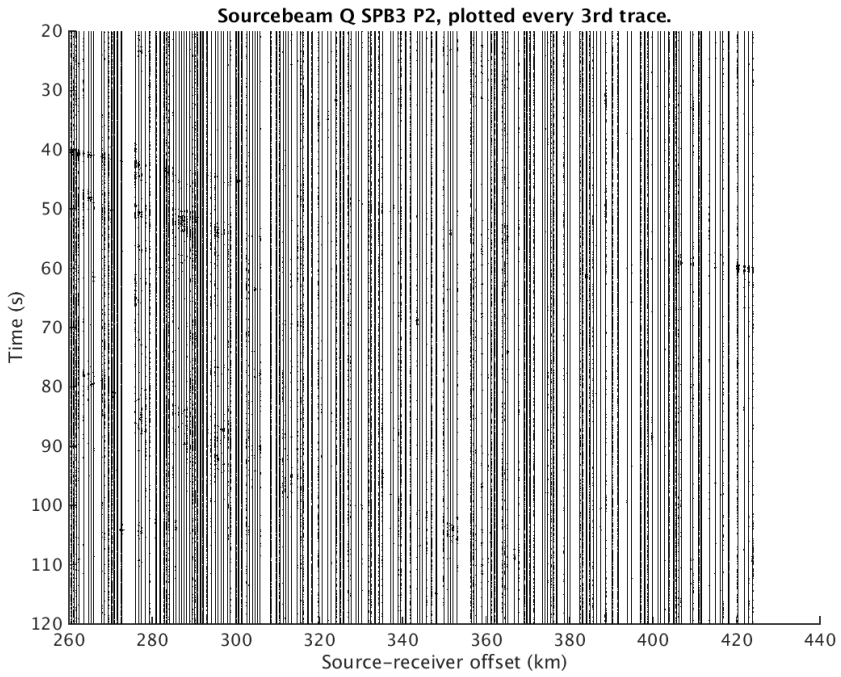

Figure A.82: Source-beam P2 SPB3 Q, plotted every 6th trace

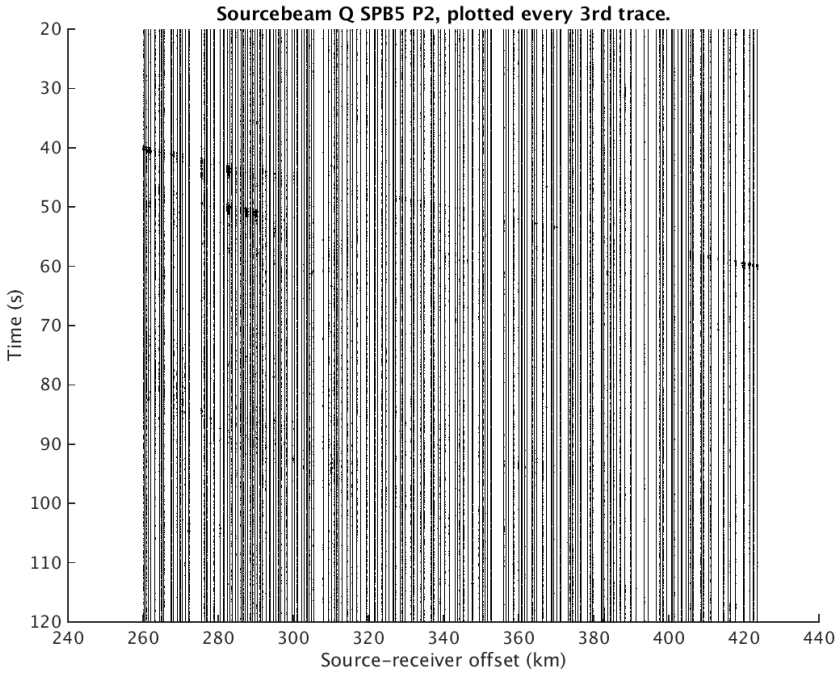

Figure A.83: Source-beam P2 SPB5 Q, plotted every 6th trace

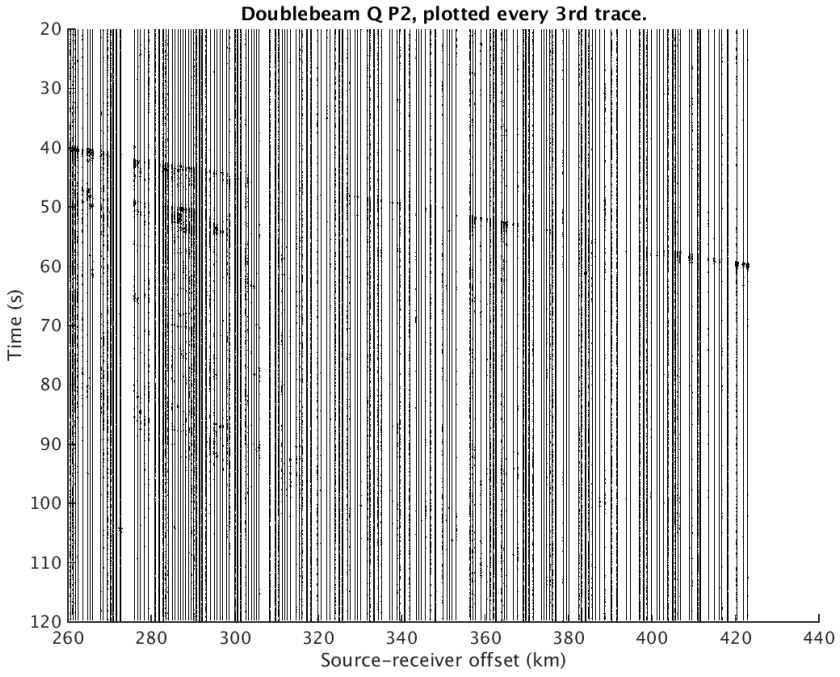

Figure A.84: Double-beam P2 Q, plotted every 6th trace

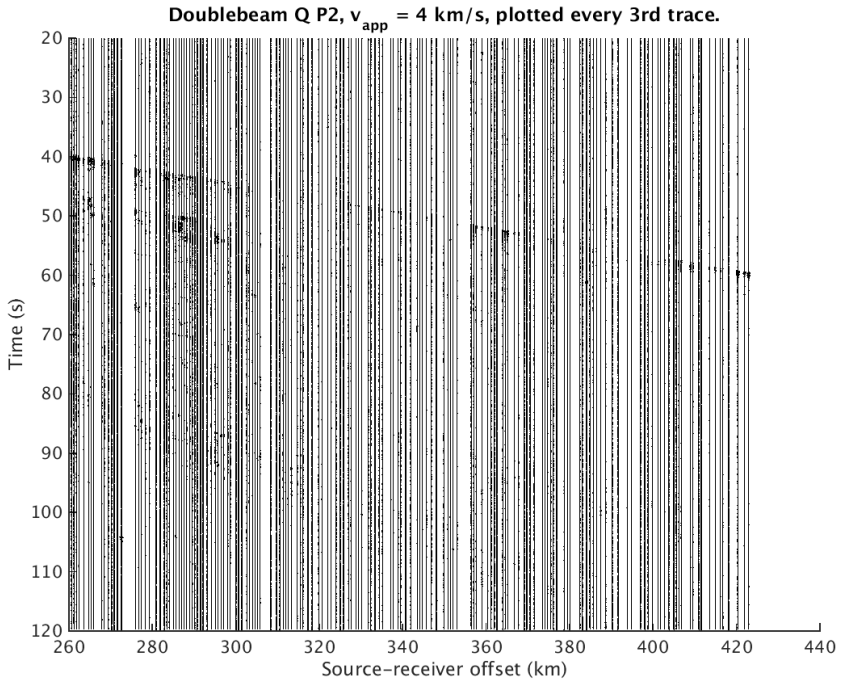

Figure A.85: Double-beam P2 Q, apparent velocity = 4km/s, plotted every 6th trace

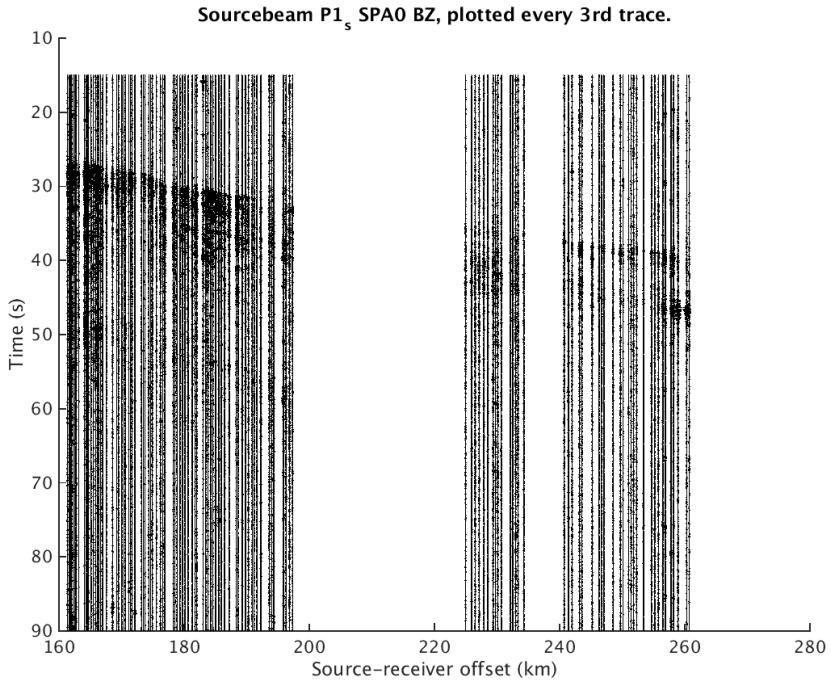

Figure A.86: Source-beam $P1_s$ SPA0 BZ, plotted every 3rd trace

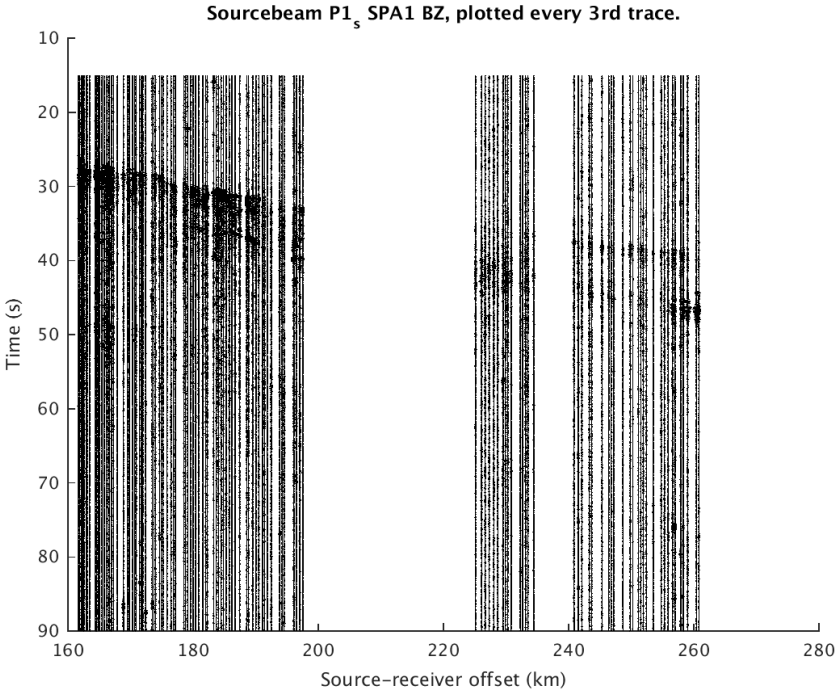

Figure A.87: Source-beam $P1_s$ SPA1 BZ, plotted every 3rd trace

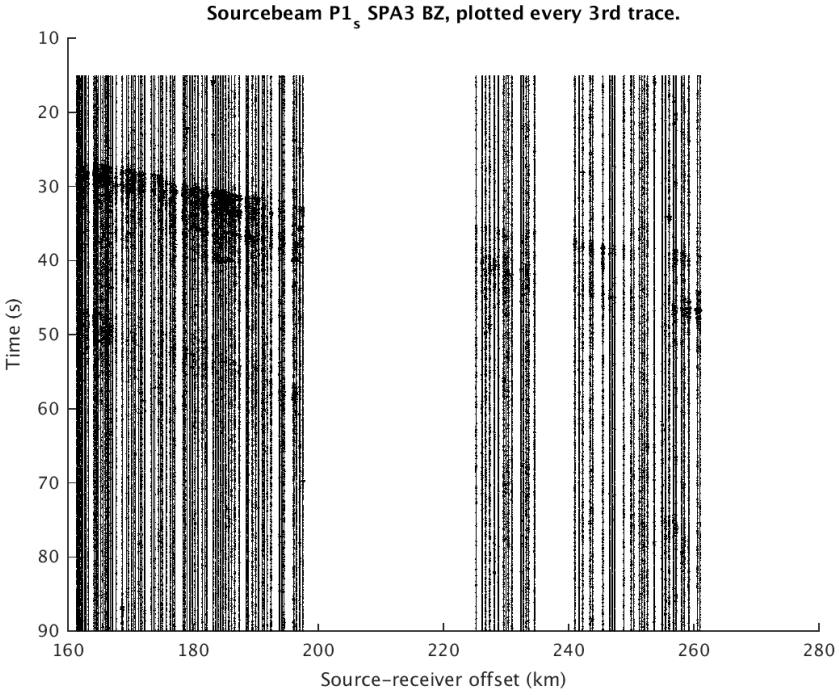

Figure A.88: Source-beam $P1_s$ SPA3 BZ, plotted every 3rd trace

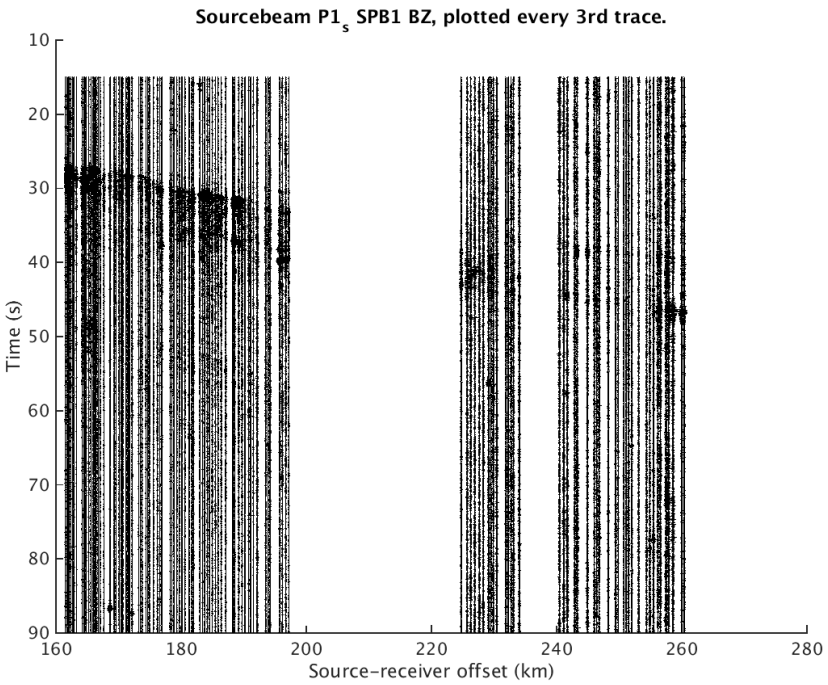

Figure A.89: Source-beam $P1_s$ SPB1 BZ, plotted every 3rd trace

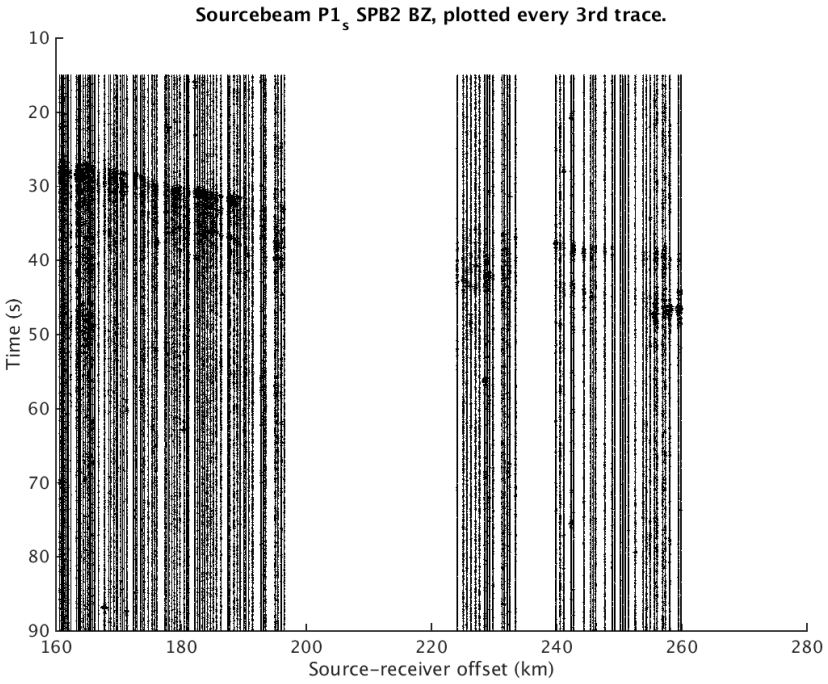

Figure A.90: Source-beam $P1_s$ SPB2 BZ, plotted every 3rd trace

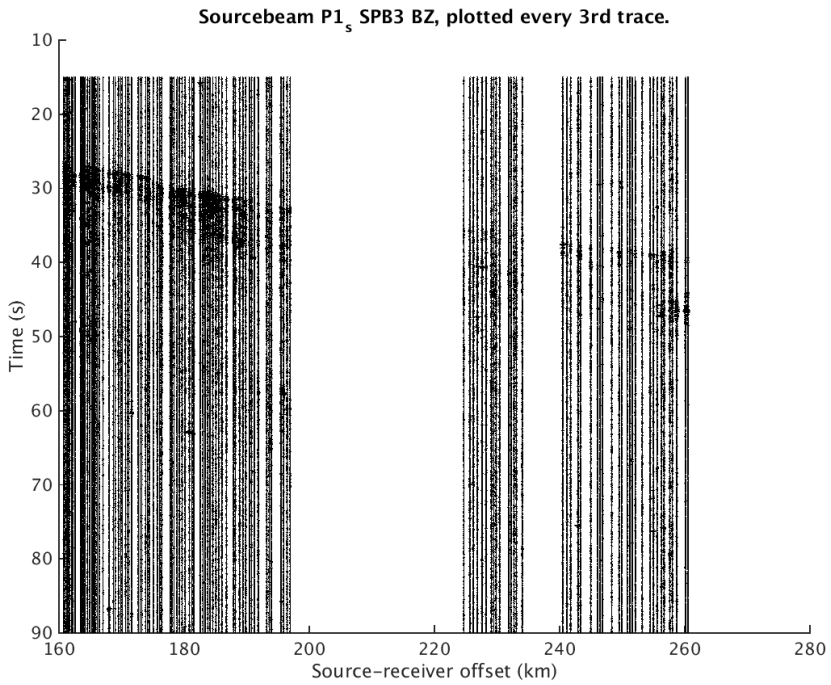

Figure A.91: Source-beam $P1_s$ SPB3 BZ, plotted every 3rd trace

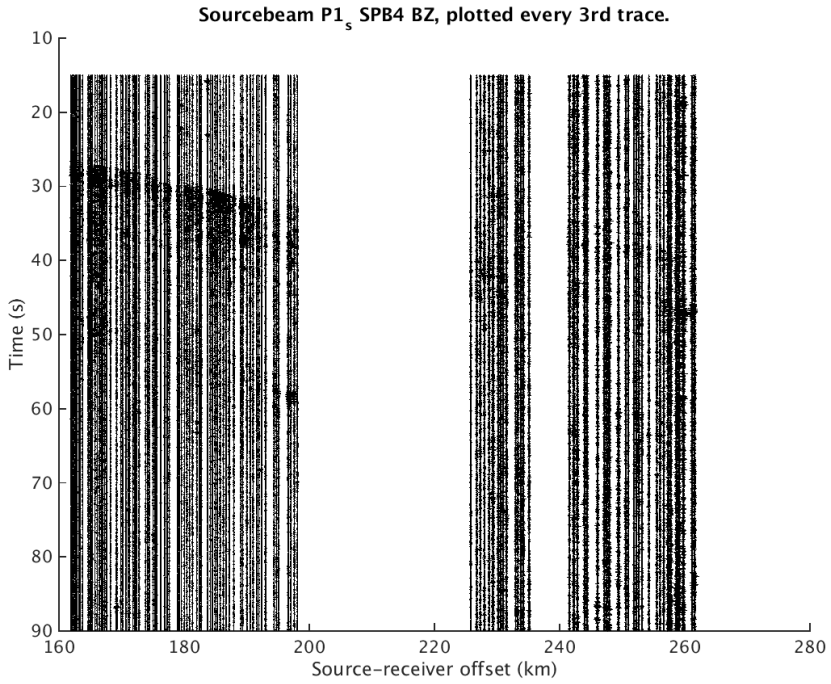

Figure A.92: Source-beam $P1_s$ SPB4 BZ, plotted every 3rd trace

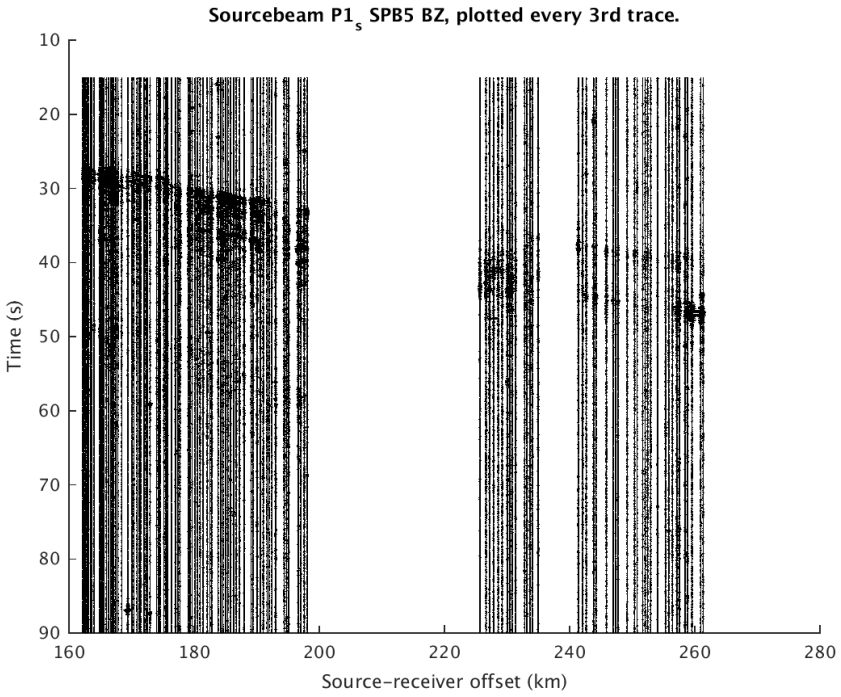

Figure A.93: Source-beam $P1_s$ SPB5 BZ, plotted every 3rd trace

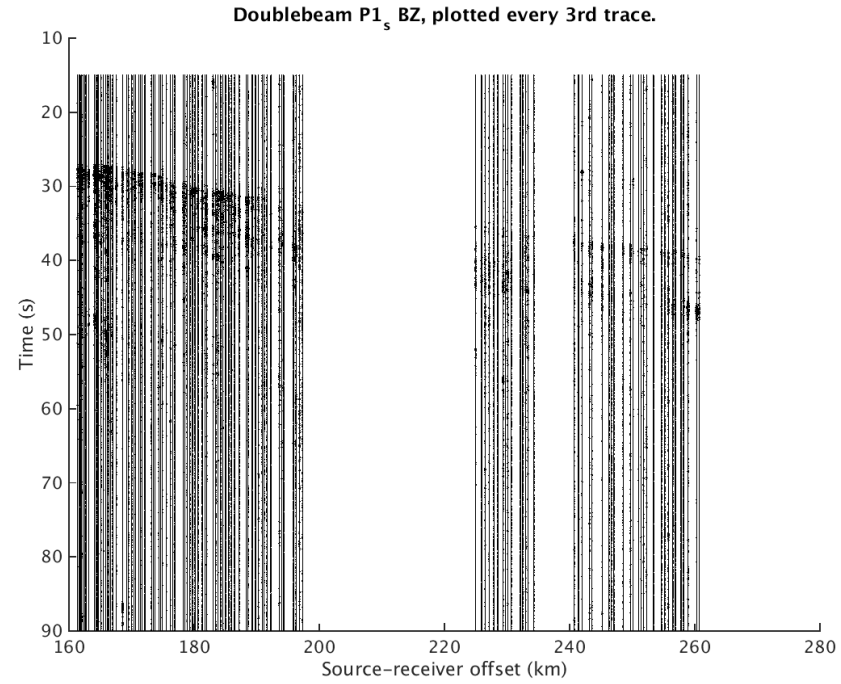

Figure A.94: Double-beam $P1_s$ BZ, plotted every 3rd trace

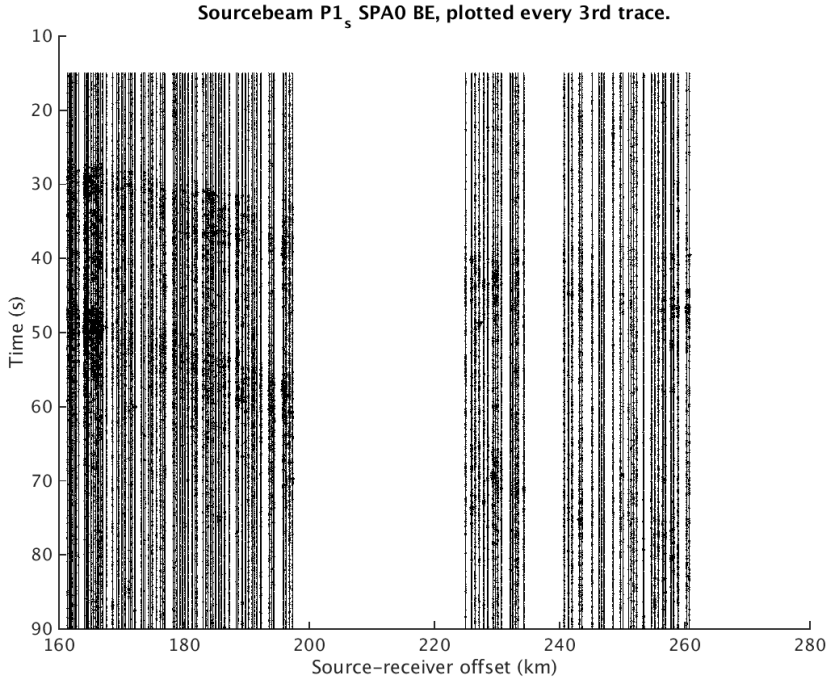

Figure A.95: Source-beam $P1_s$ SPA0 BE, plotted every 3rd trace

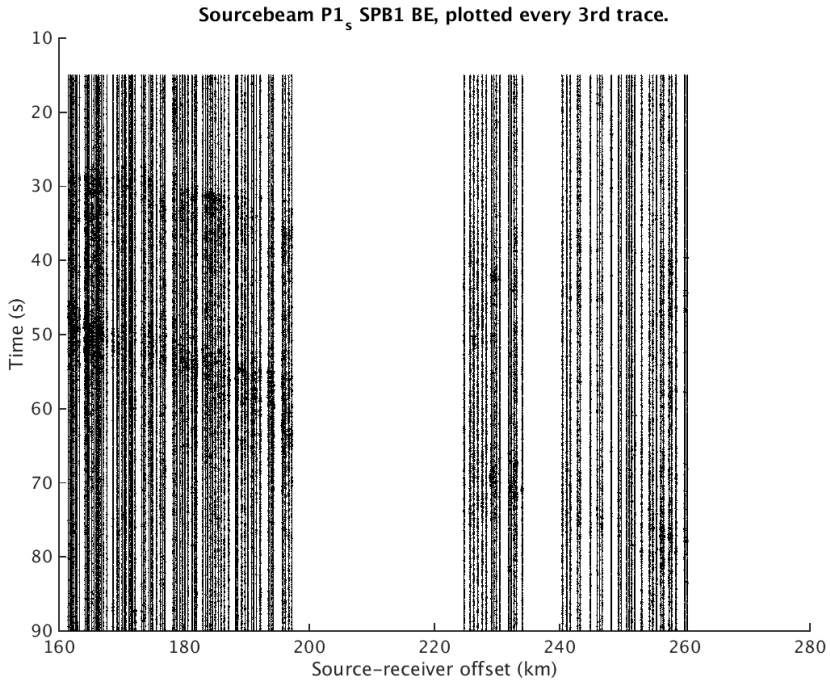

Figure A.96: Source-beam $P1_s$ SPB1 BE, plotted every 3rd trace

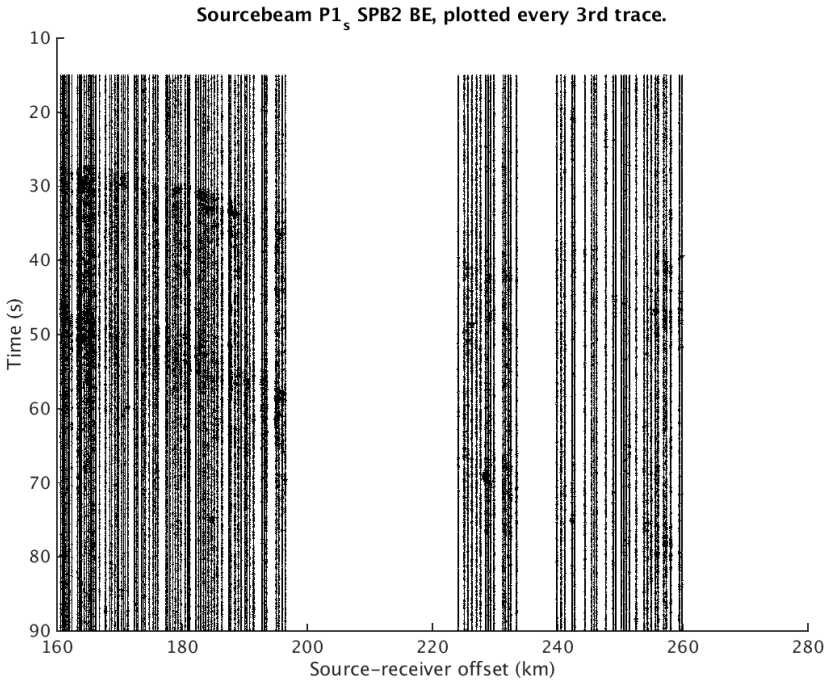

Figure A.97: Source-beam $P1_s$ SPB2 BE, plotted every 3rd trace

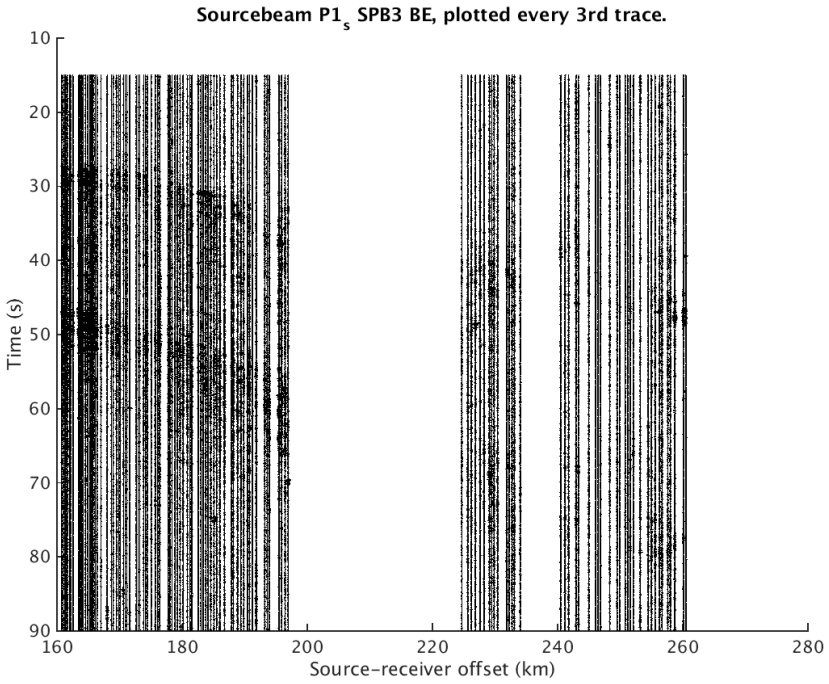

Figure A.98: Source-beam $P1_s$ SPB3 BE, plotted every 3rd trace

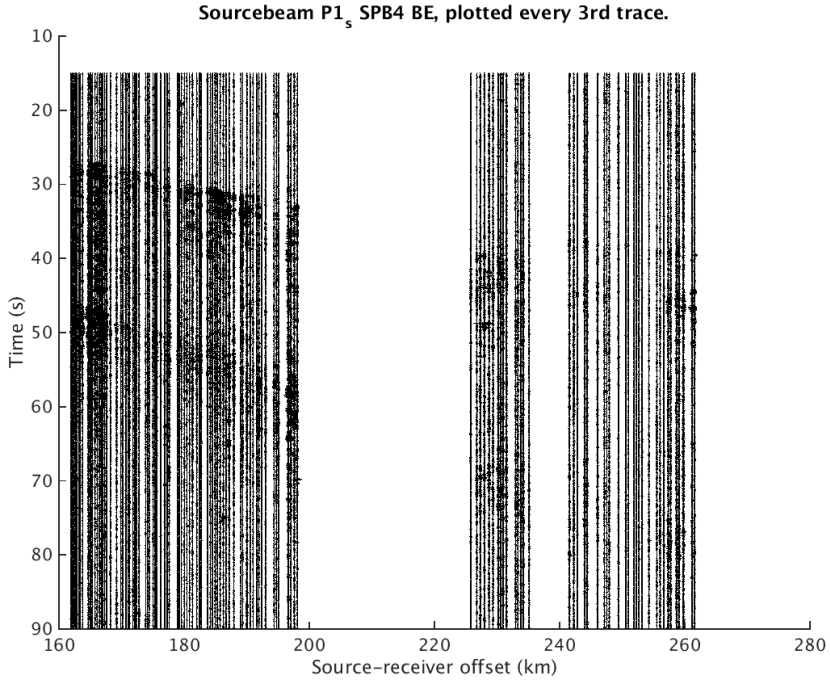

Figure A.99: Source-beam $P1_s$ SPB4 BE, plotted every 3rd trace

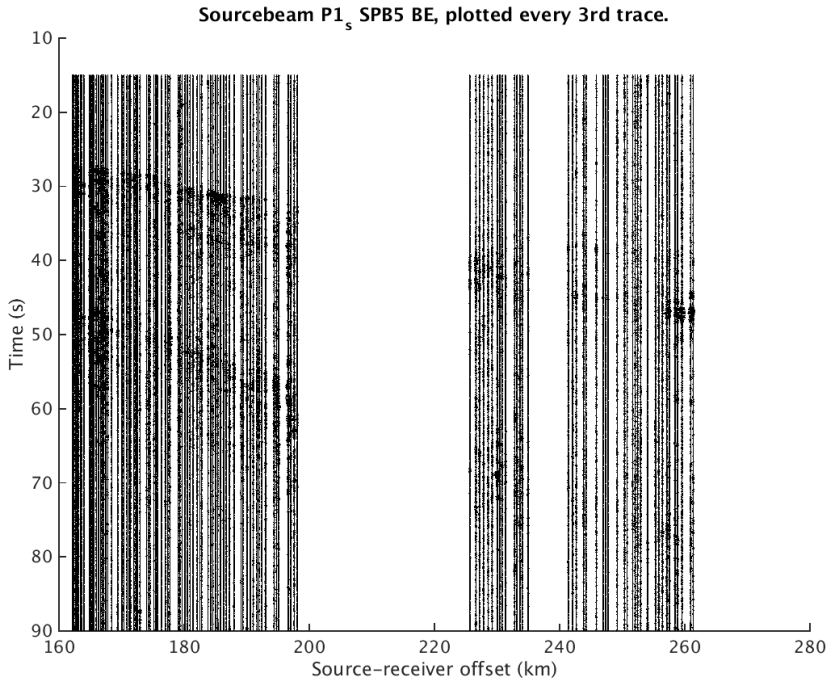

Figure A.100: Source-beam $P1_s$ SPB5 BE, plotted every 3rd trace

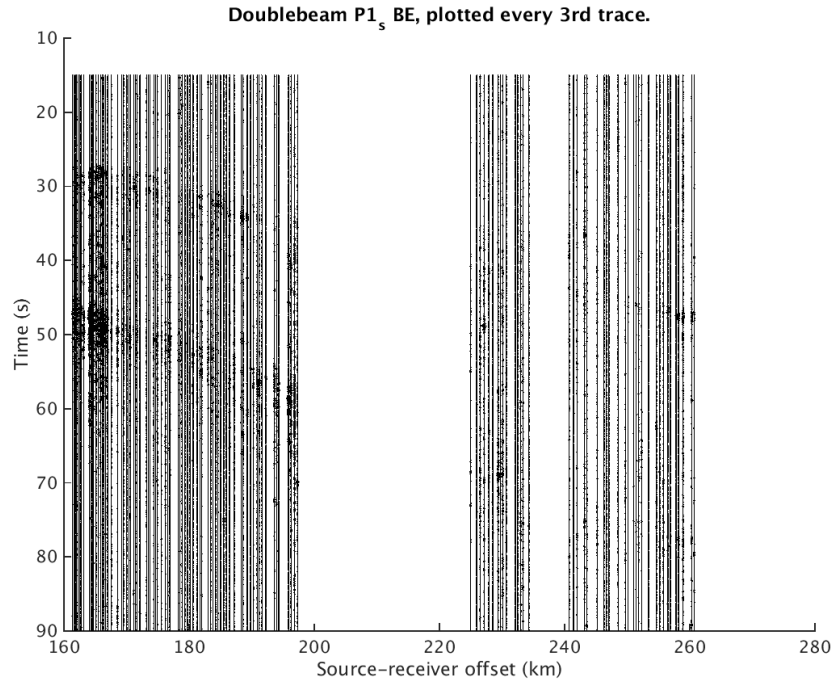

Figure A.101: Double-beam $P1_s$ BE, plotted every 3rd trace

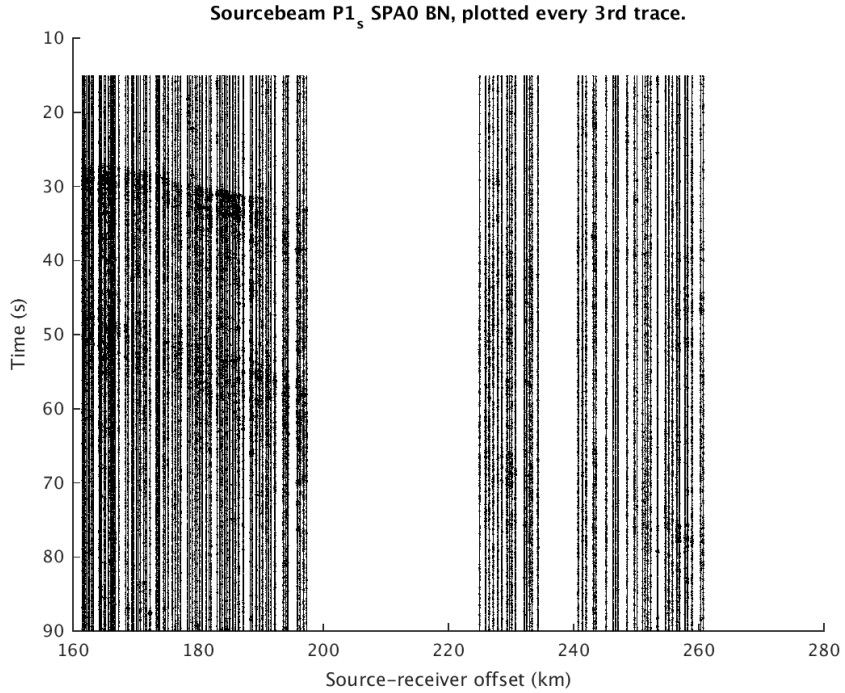

Figure A.102: Source-beam $P1_s$ SPA0 BN, plotted every 3rd trace

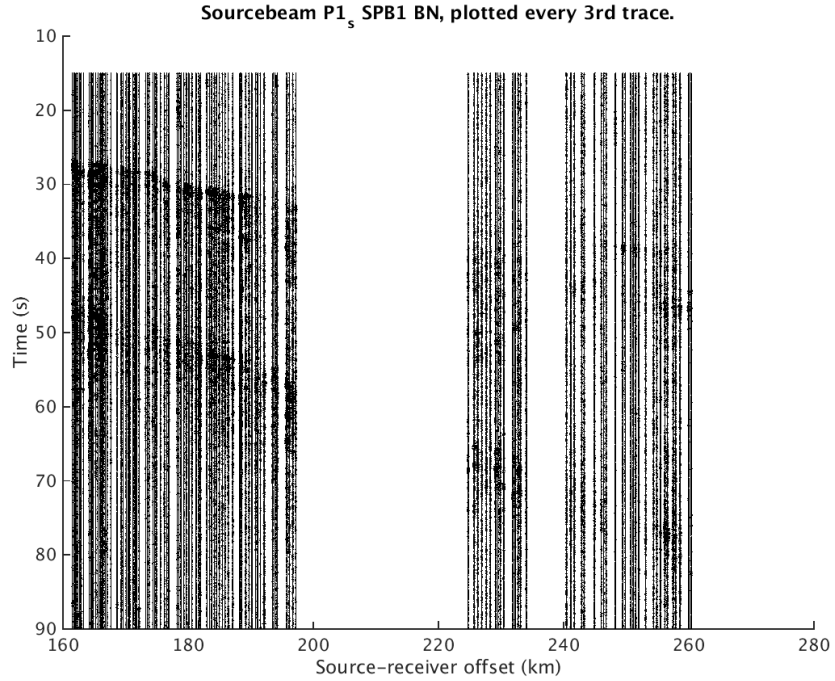

Figure A.103: Source-beam $P1_s$ SPB1 BN, plotted every 3rd trace

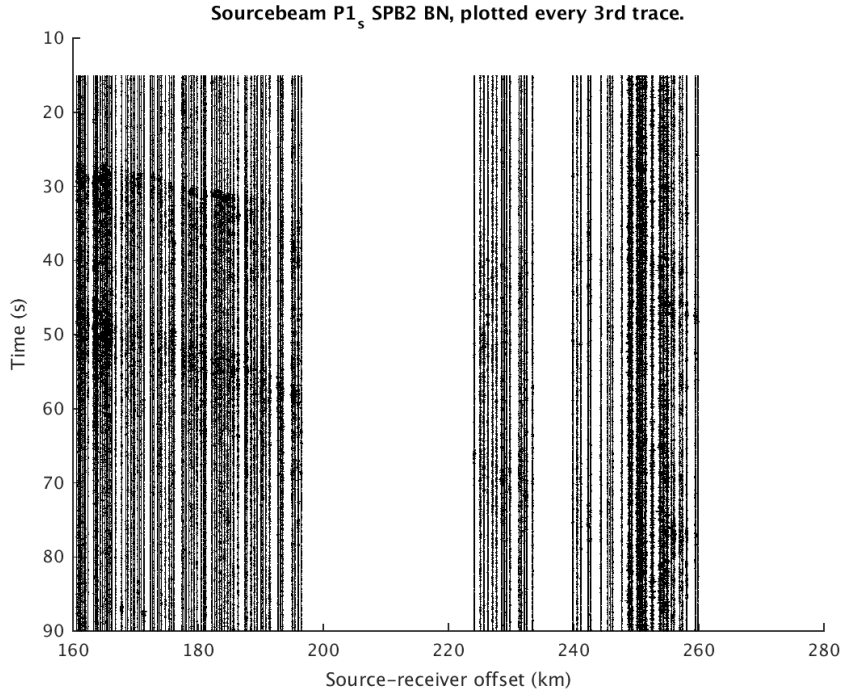

Figure A.104: Source-beam $P1_s$ SPB2 BN, plotted every 3rd trace

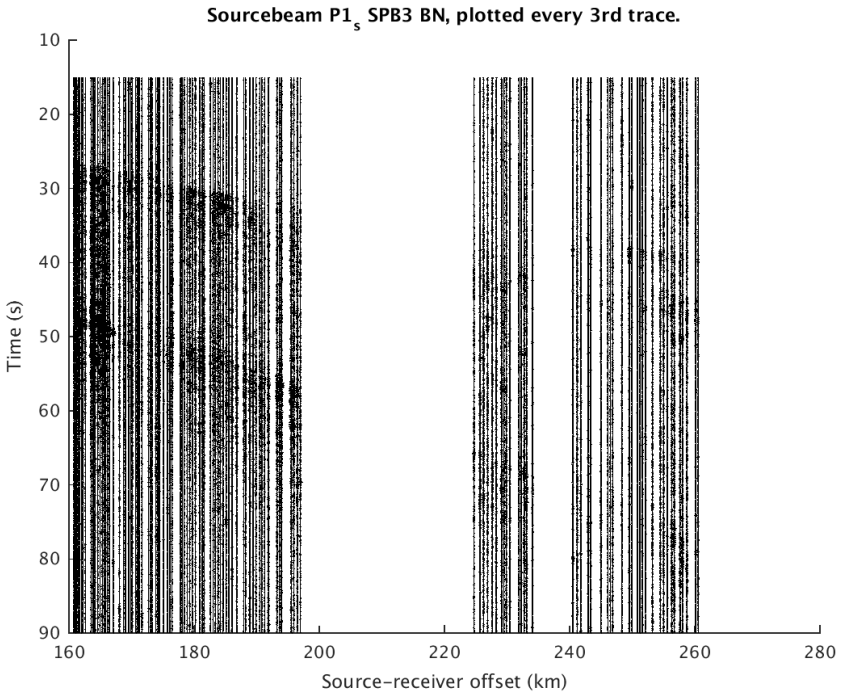

Figure A.105: Source-beam $P1_s$ SPB3 BN, plotted every 3rd trace

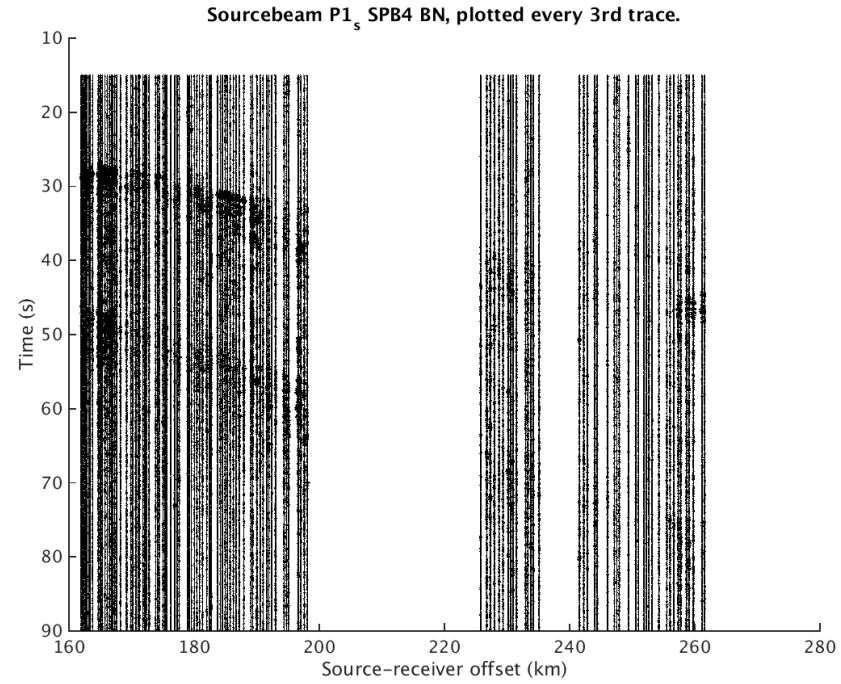

Figure A.106: Source-beam $P1_s$ SPB4 BN, plotted every 3rd trace

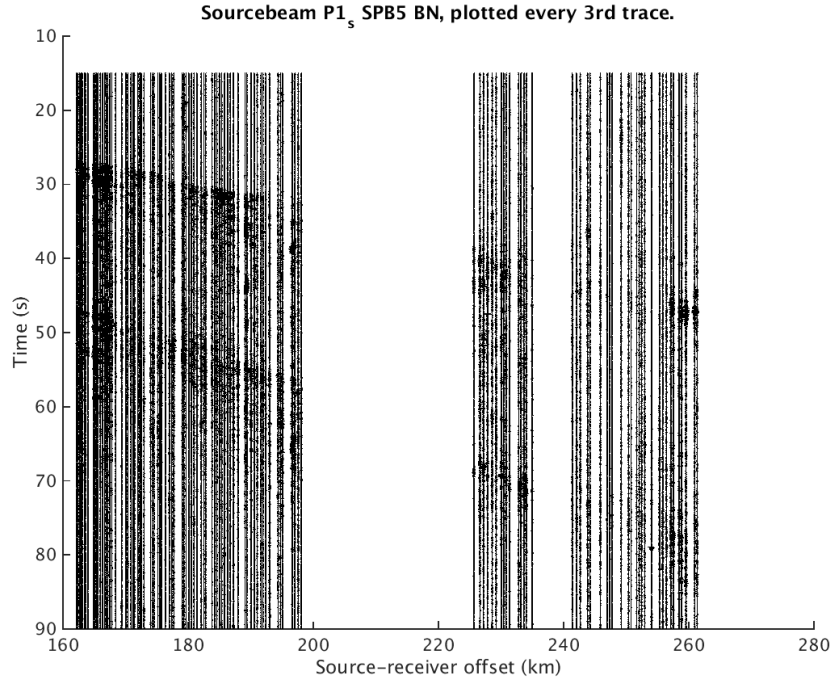

Figure A.107: Source-beam $P1_s$ SPB5 BN, plotted every 3rd trace

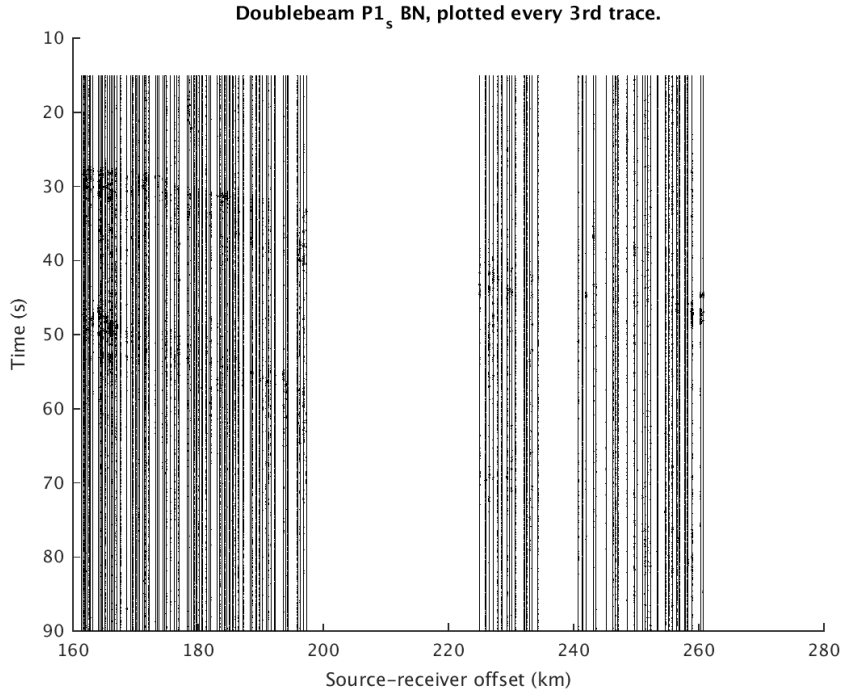

Figure A.108: Double-beam $P1_s$ BN, plotted every 3rd trace

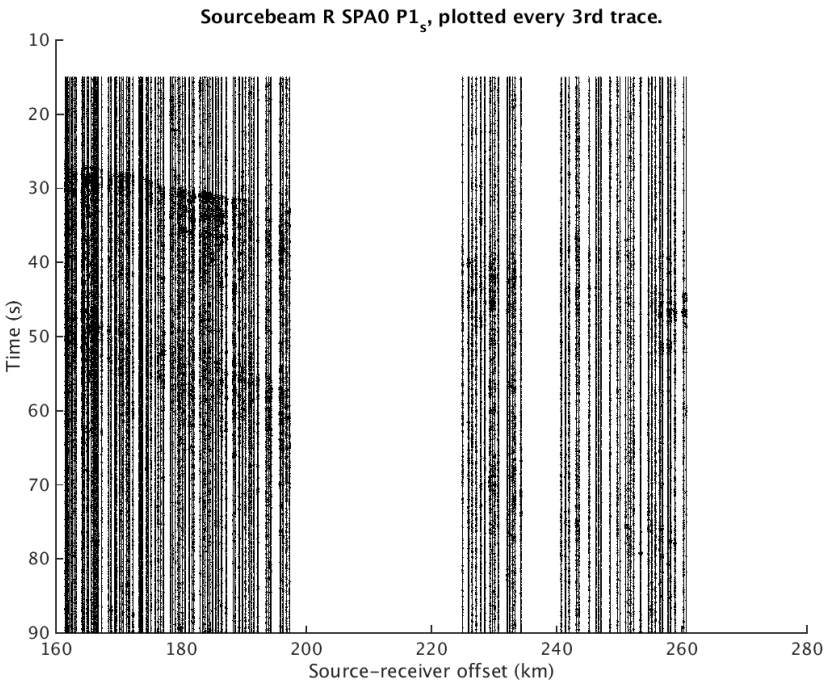

Figure A.109: Source-beam $P1_s$ SPA0 R, plotted every 3rd trace

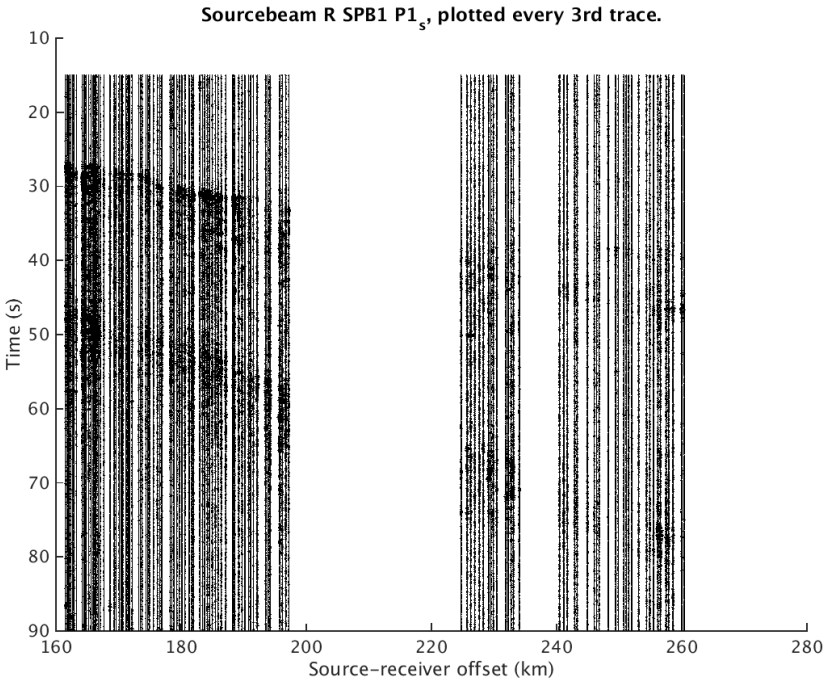

Figure A.110: Source-beam $P1_s$ SPB1 R, plotted every 3rd trace

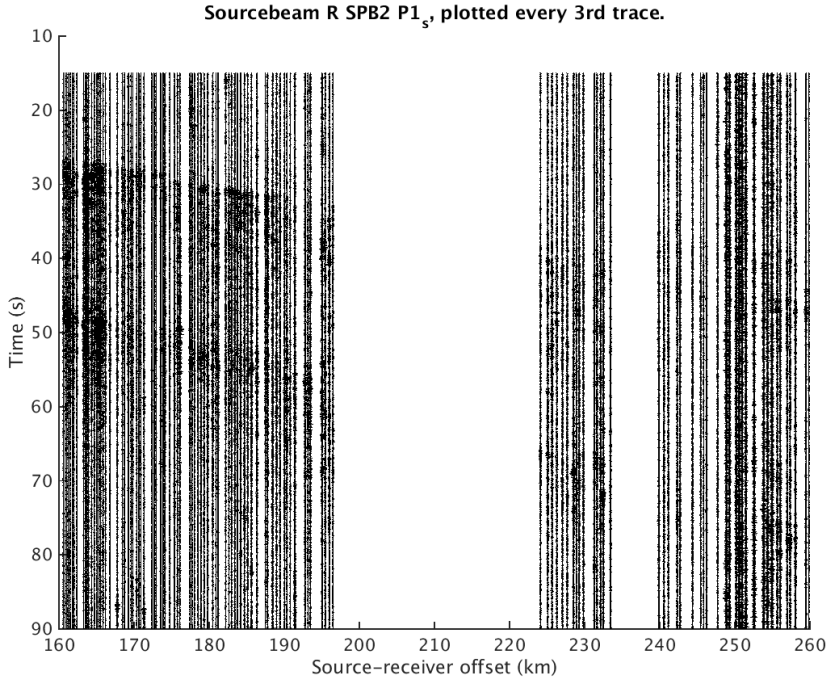

Figure A.111: Source-beam $P1_s$ SPB2 R, plotted every 3rd trace

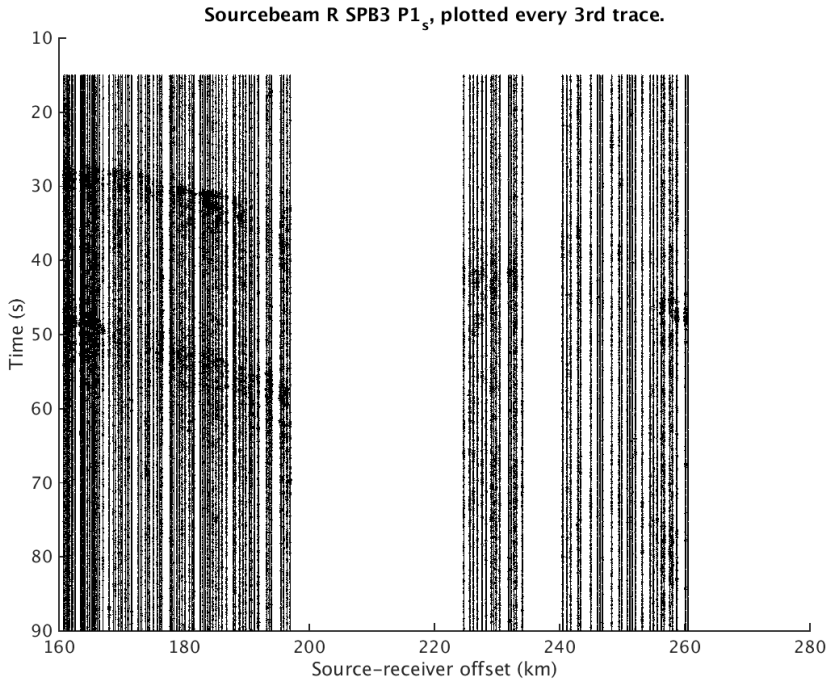

Figure A.112: Source-beam $P1_s$ SPB3 R, plotted every 3rd trace

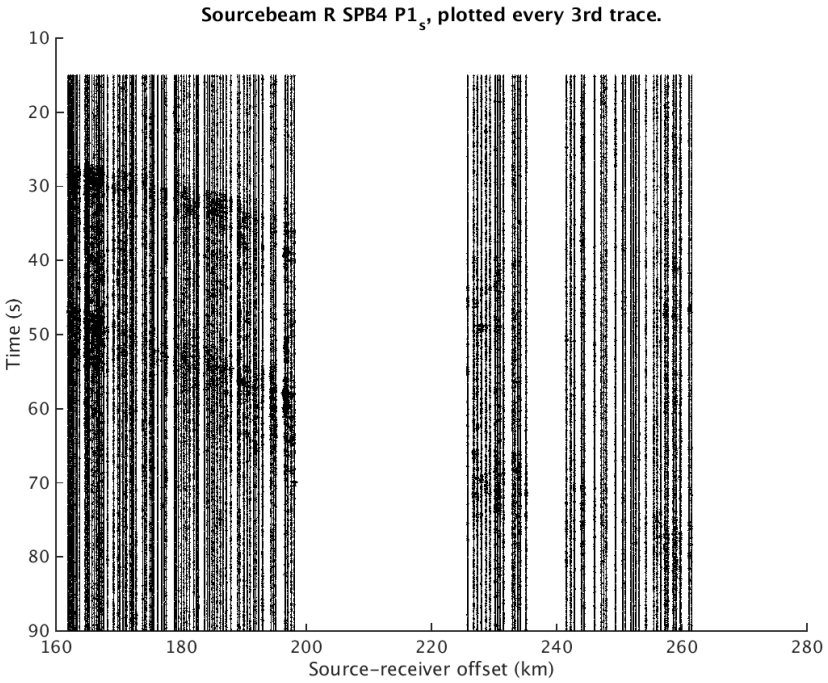

Figure A.113: Source-beam $P1_s$ SPB4 R, plotted every 3rd trace

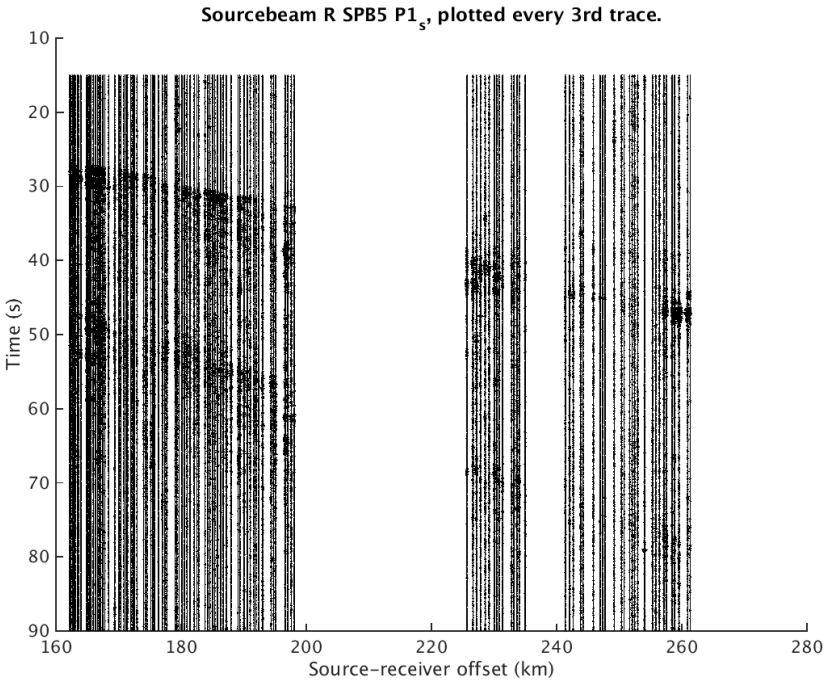

Figure A.114: Source-beam $P1_s$ SPB5 R, plotted every 3rd trace

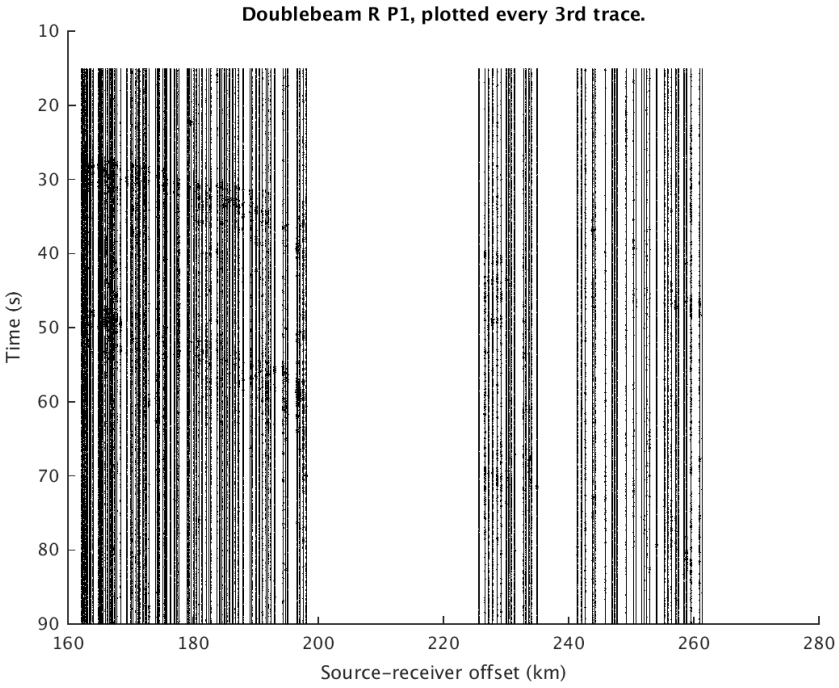

Figure A.115: Double-beam $P1_s$ R, plotted every 3rd trace

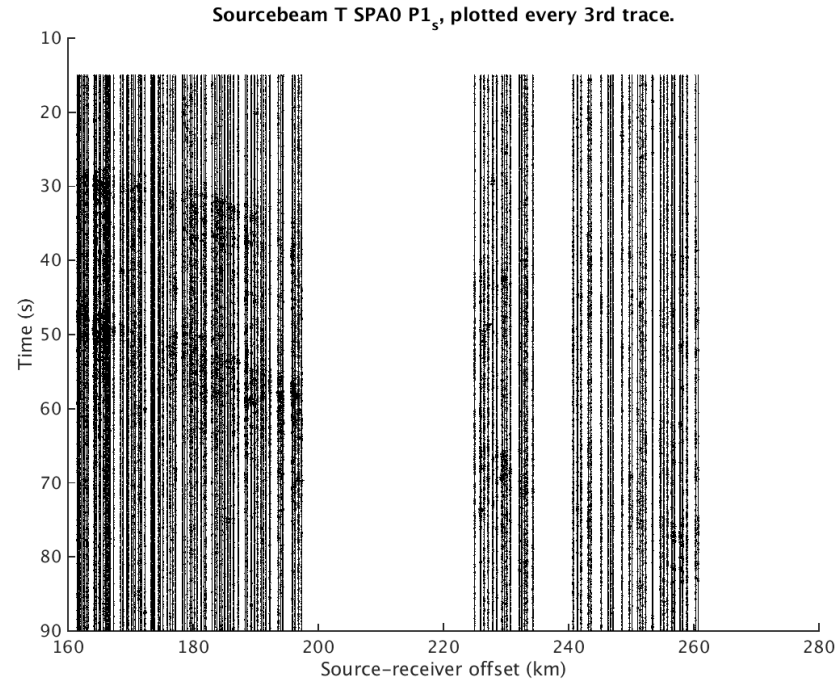

Figure A.116: Source-beam $P1_s$ SPA0 T, plotted every 3rd trace

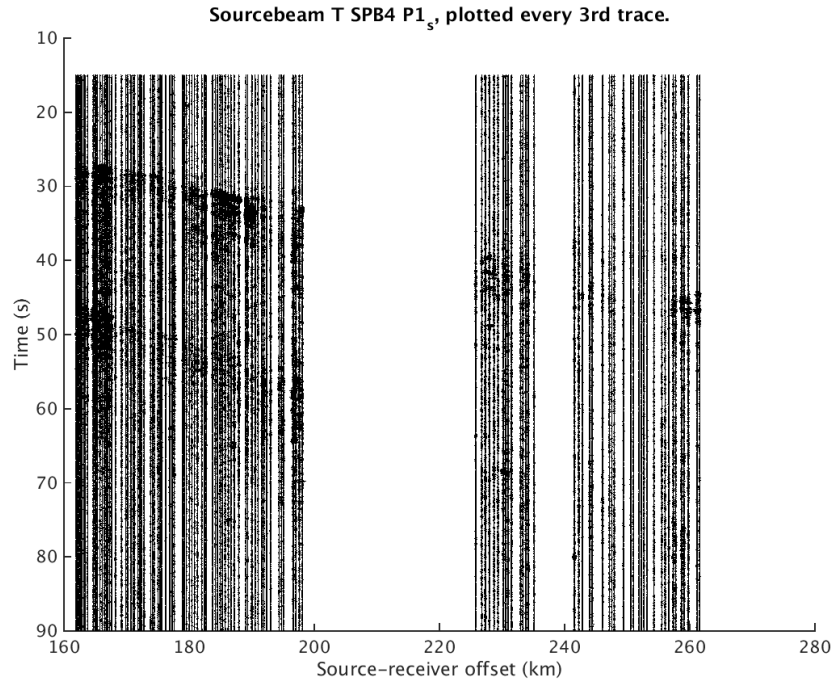

Figure A.117: Source-beam $P1_s$ SPB1 T, plotted every 3rd trace

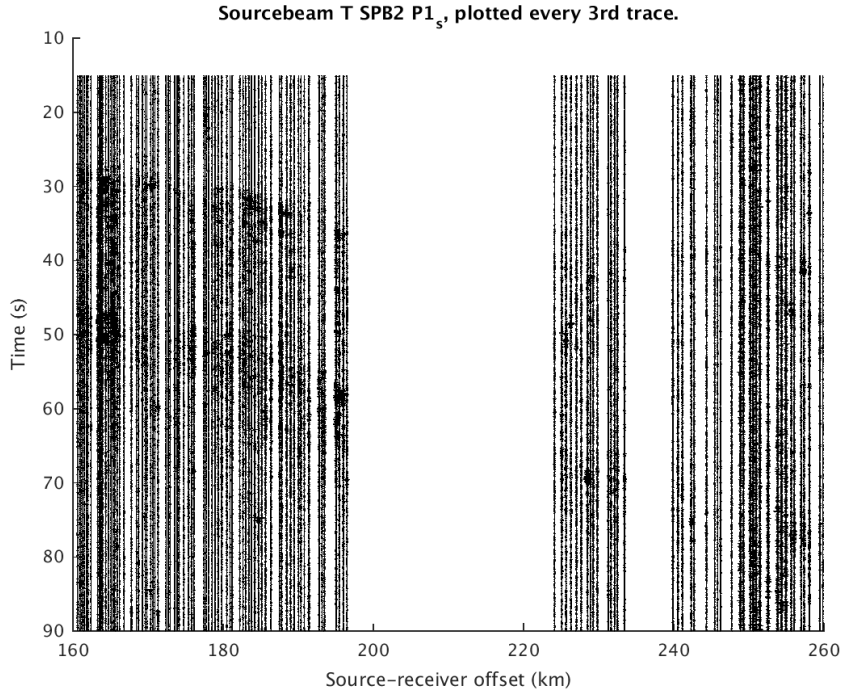

Figure A.118: Source-beam $P1_s$ SPB2 T, plotted every 3rd trace

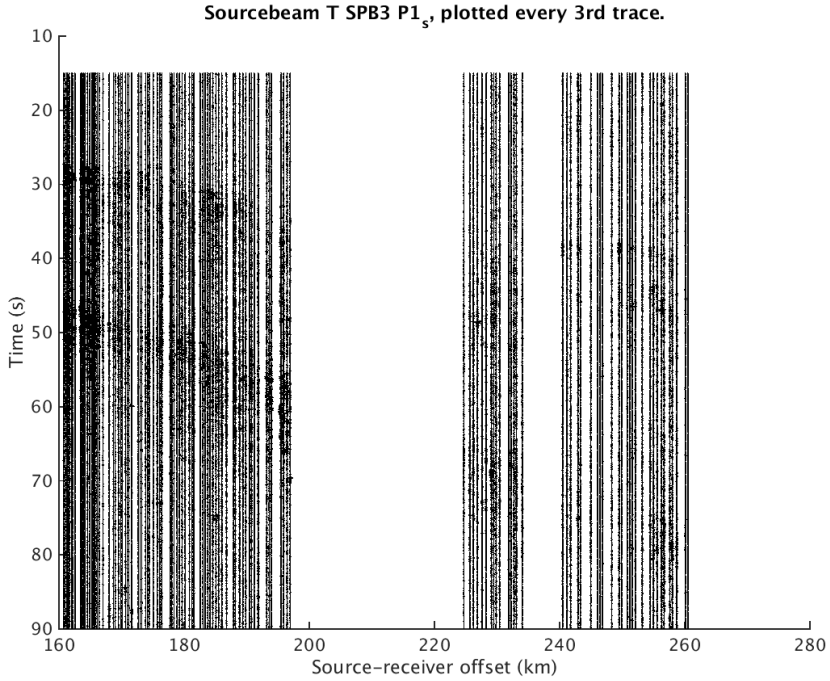

Figure A.119: Source-beam $P1_s$ SPB3 T, plotted every 3rd trace

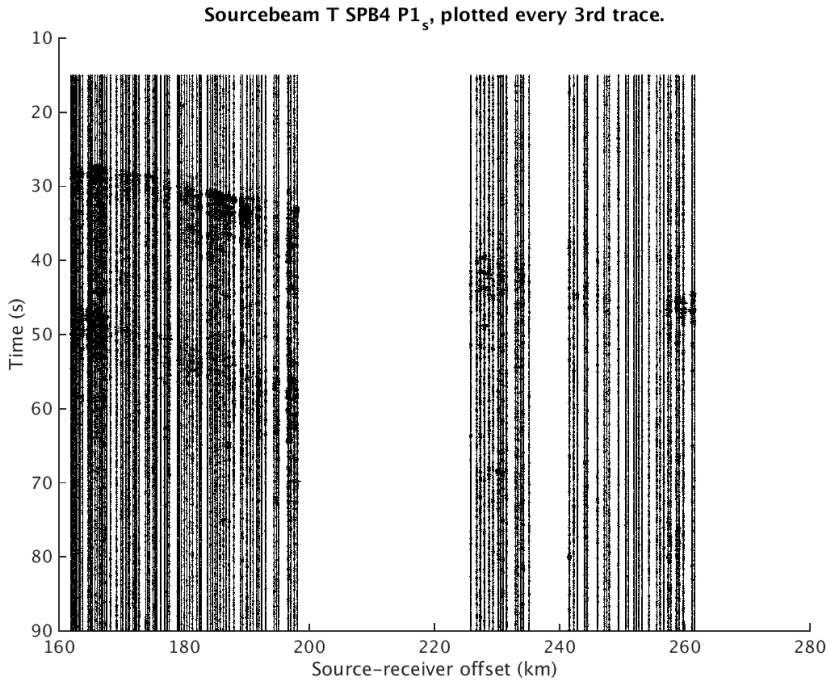

Figure A.120: Source-beam $P1_s$ SPB4 T, plotted every 3rd trace

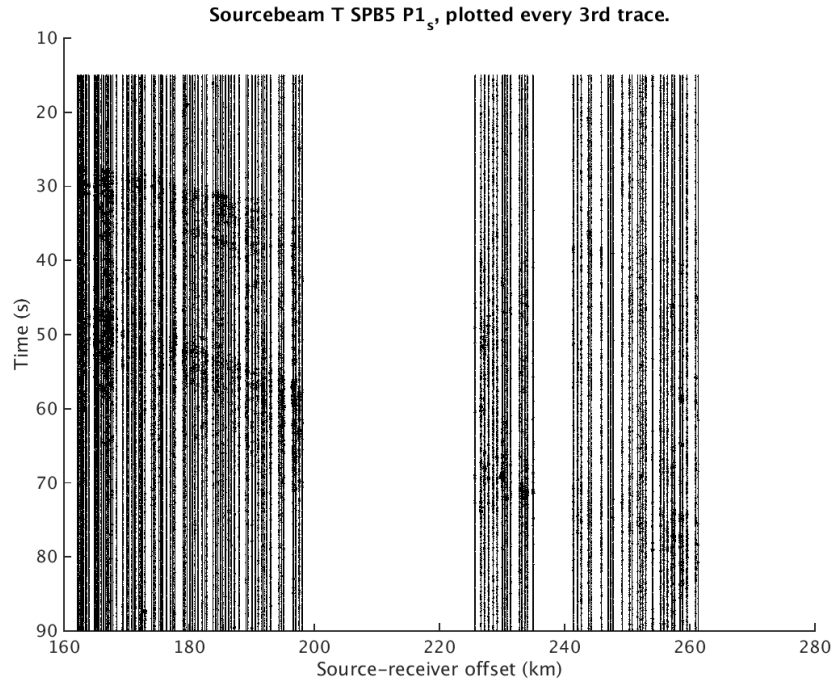

Figure A.121: Source-beam $P1_s$ SPB5 T, plotted every 3rd trace

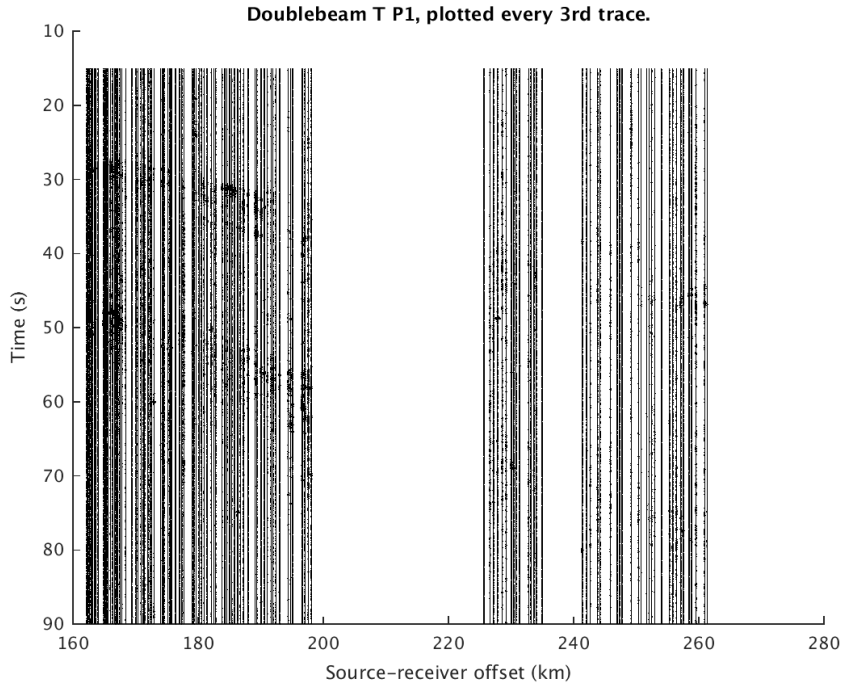

Figure A.122: Double-beam $P1_s$ T, plotted every 3rd trace

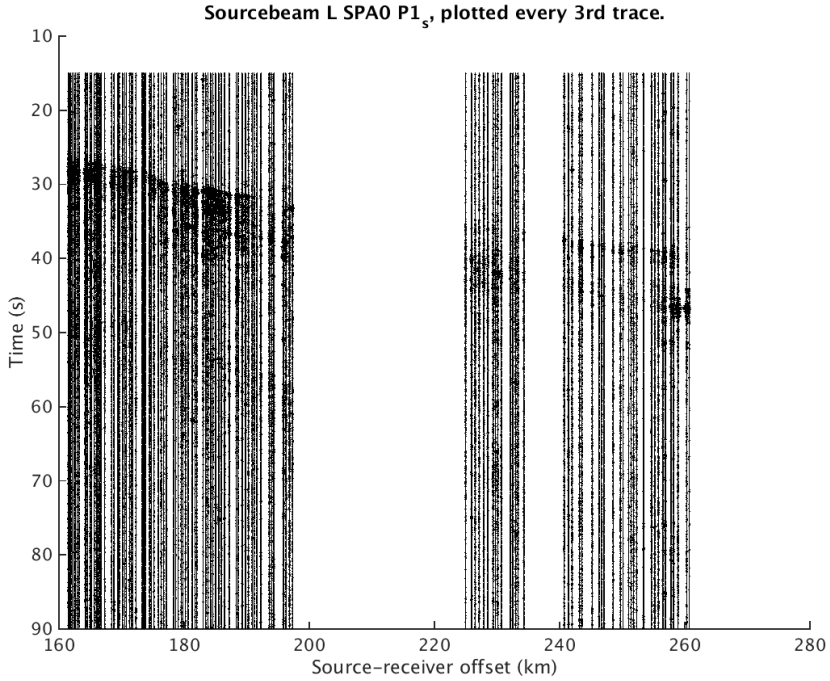

Figure A.123: Source-beam $P1_s$ SPA0 L, plotted every 3rd trace

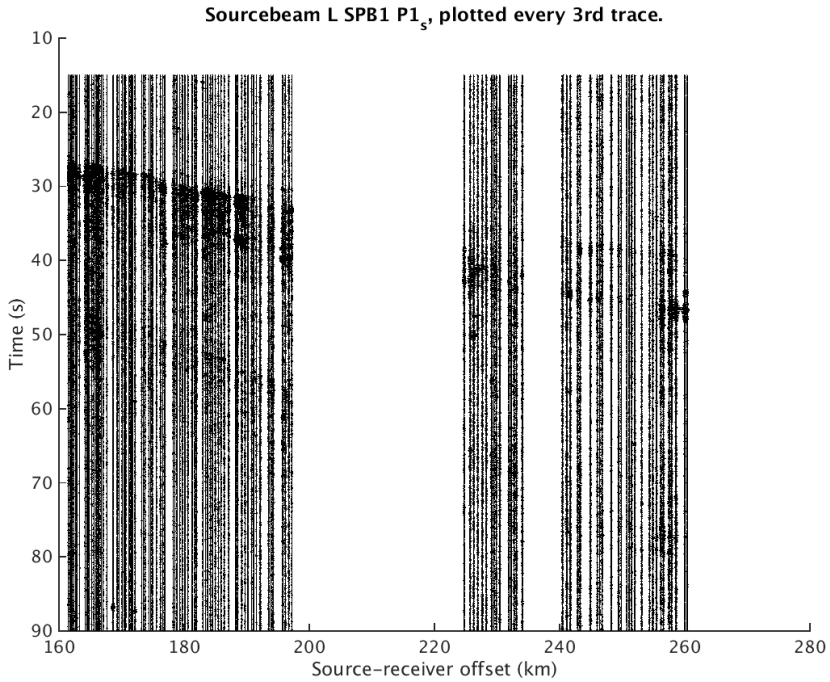

Figure A.124: Source-beam $P1_s$ SPB1 L, plotted every 3rd trace

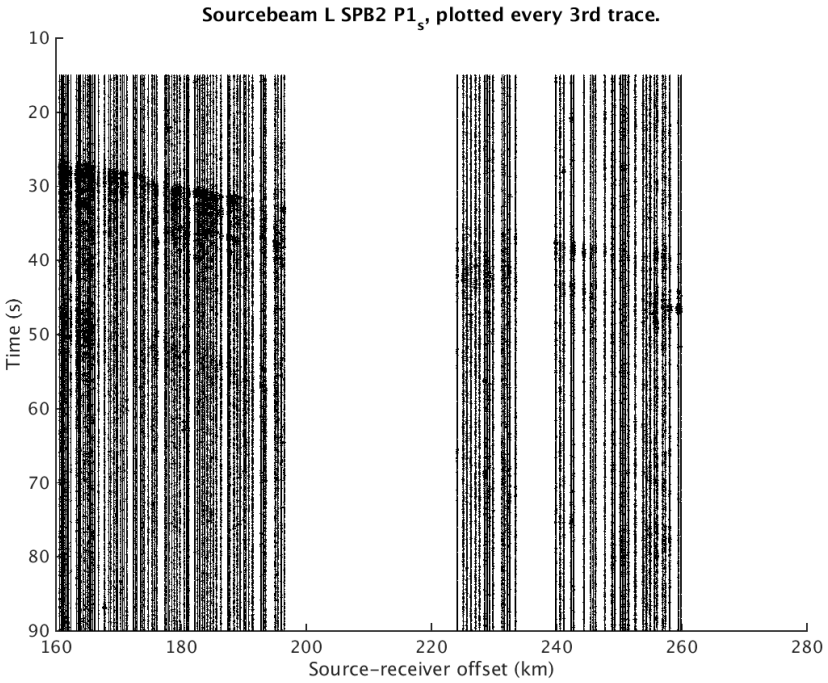

Figure A.125: Source-beam $P1_s$ SPB2 L, plotted every 3rd trace

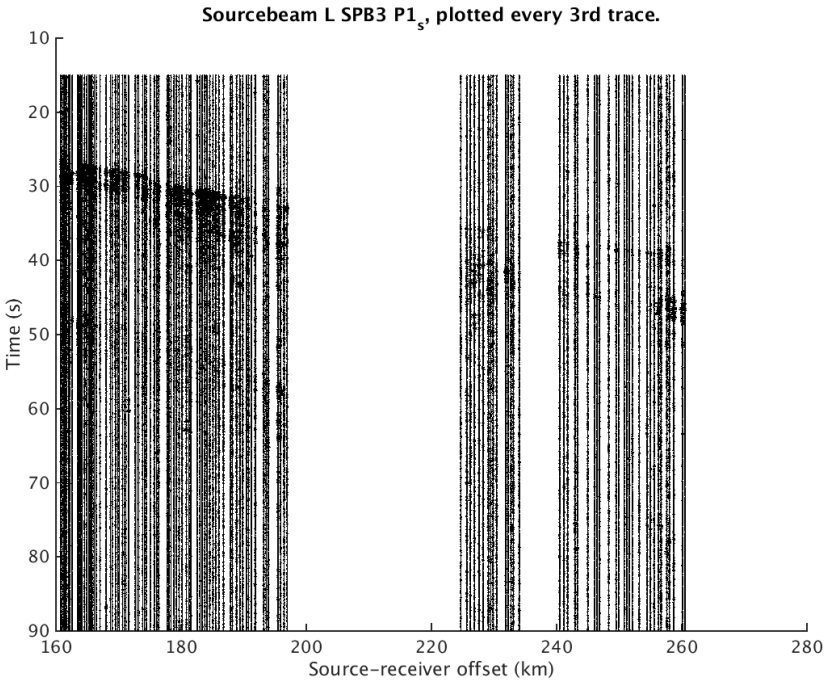

Figure A.126: Source-beam $P1_s$ SPB3 L, plotted every 3rd trace

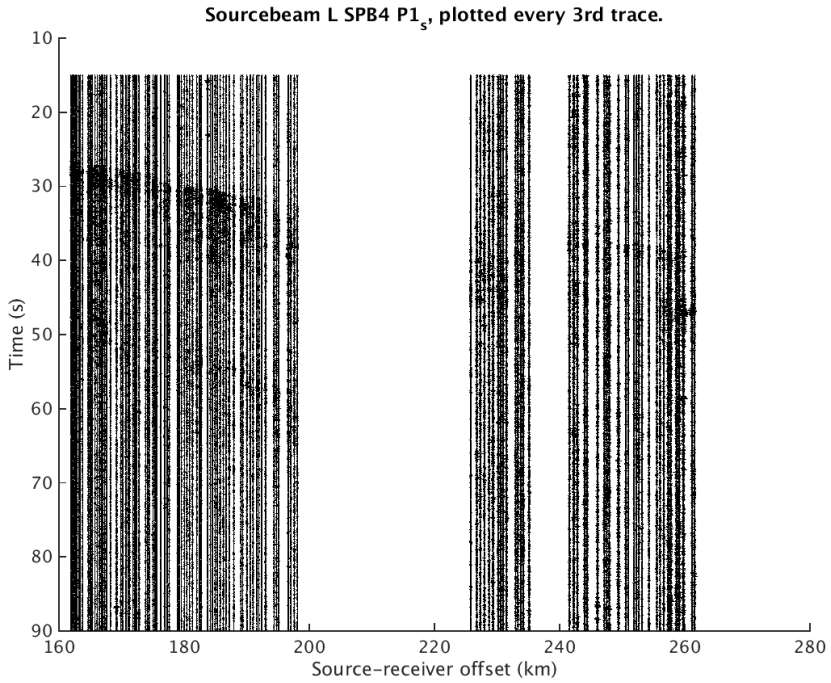

Figure A.127: Source-beam $P1_s$ SPB4 L, plotted every 3rd trace

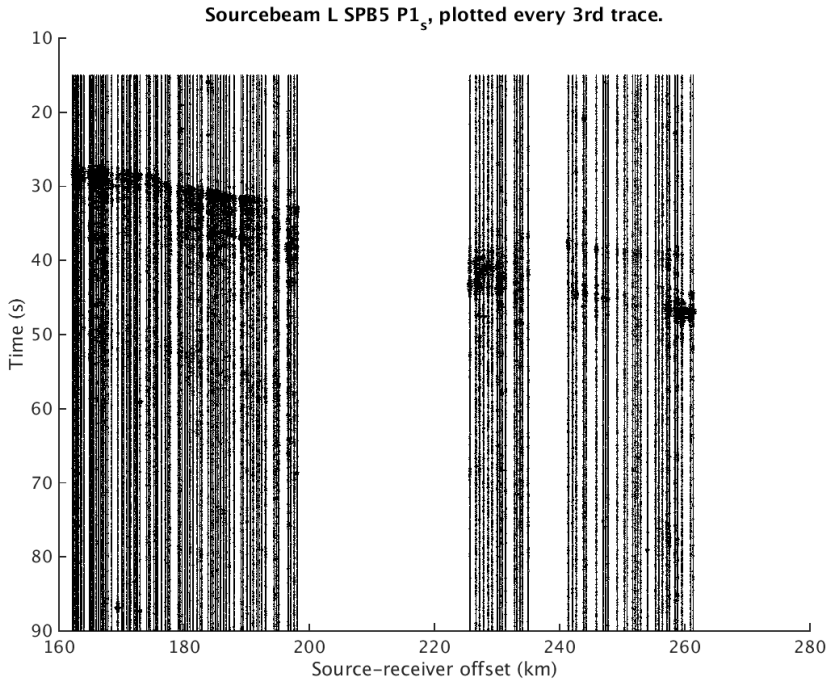

Figure A.128: Source-beam $P1_s$ SPB5 L, plotted every 3rd trace

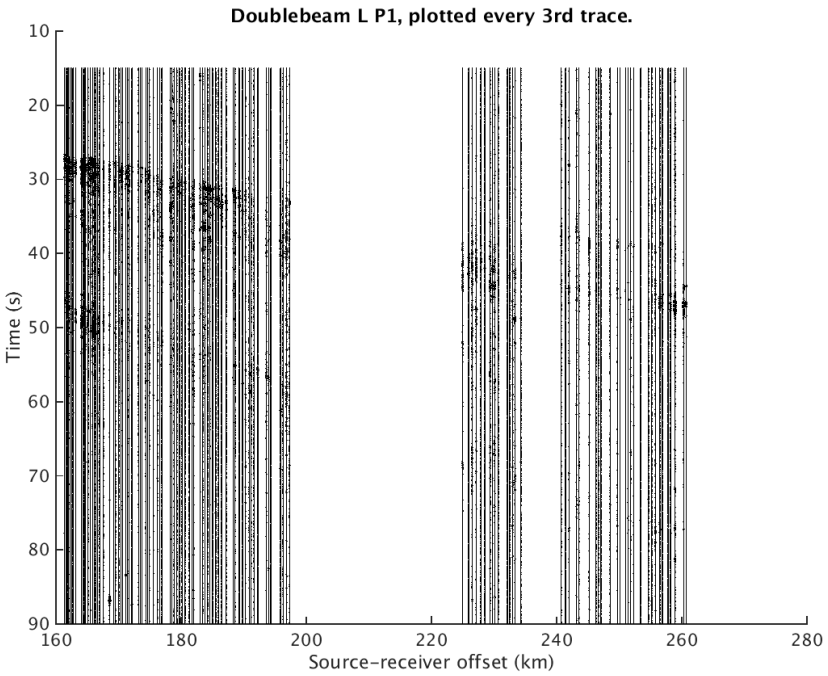

Figure A.129: Double-beam $P1_s$ L, plotted every 3rd trace

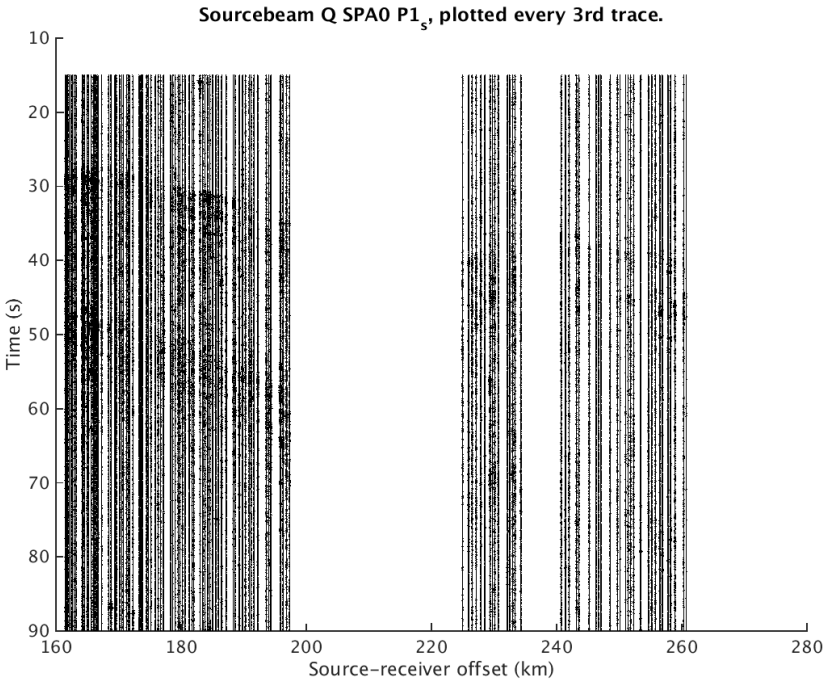

Figure A.130: Source-beam $P1_s$ SPA0 Q, plotted every 3rd trace

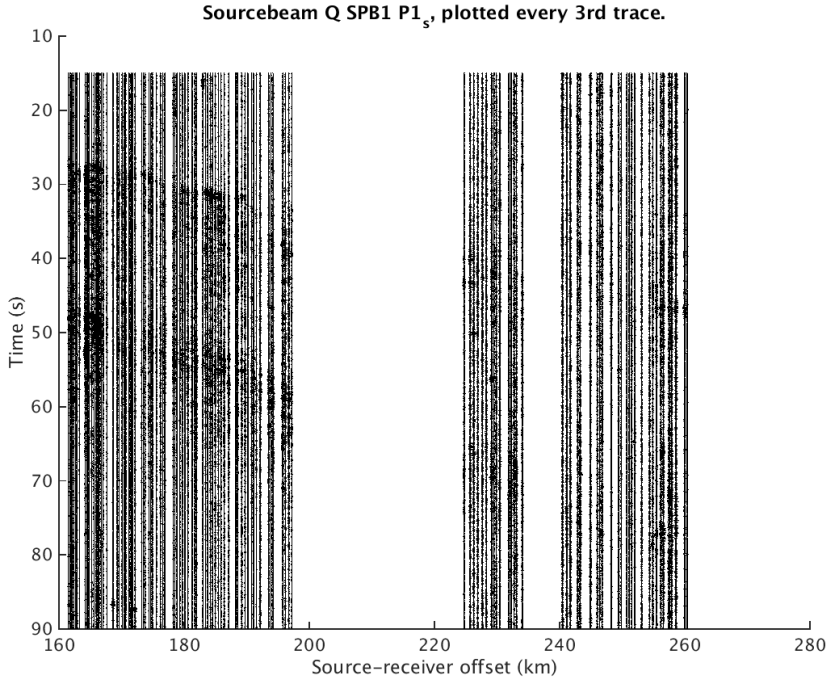

Figure A.131: Source-beam $P1_S$ SPB1 Q, plotted every 3rd trace

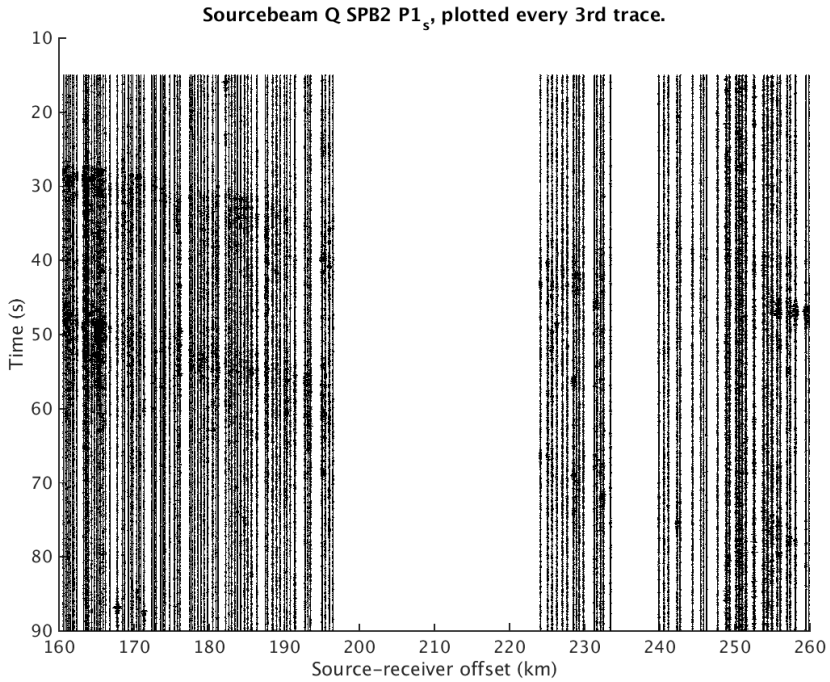

Figure A.132: Source-beam $P1_S$ SPB2 Q, plotted every 3rd trace

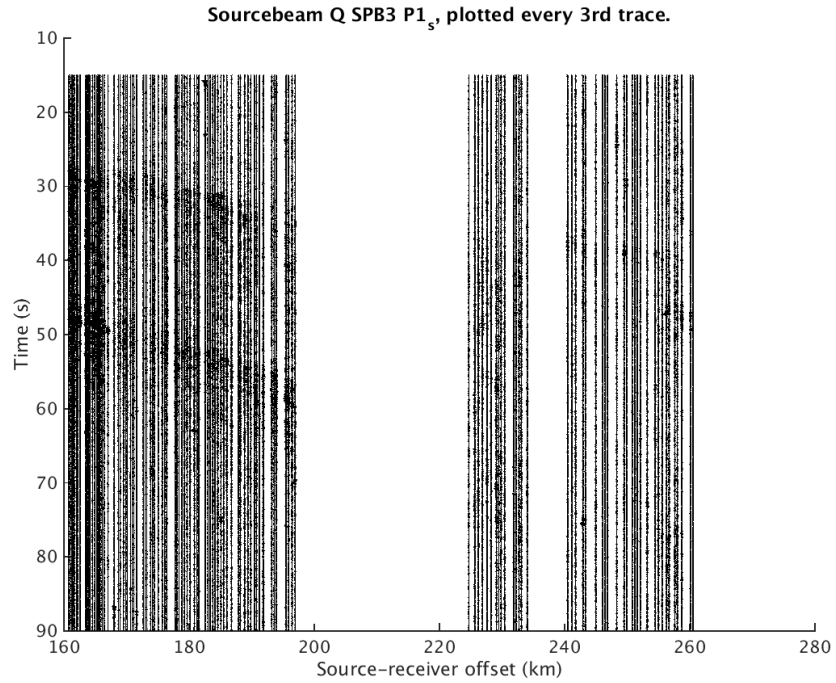

Figure A.133: Source-beam $P1_s$ SPB3 Q, plotted every 3rd trace

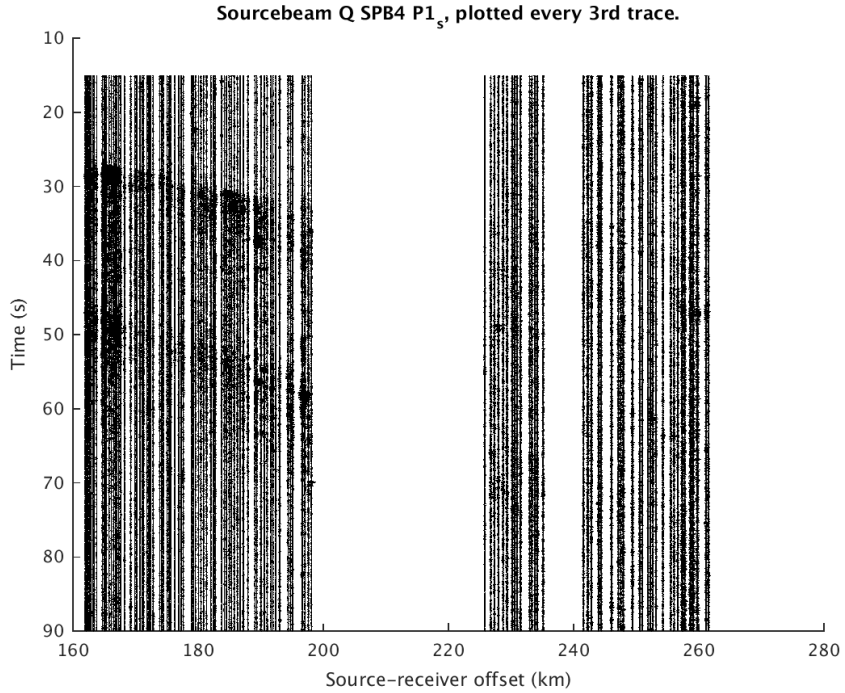

Figure A.134: Source-beam $P1_s$ SPB4 Q, plotted every 3rd trace

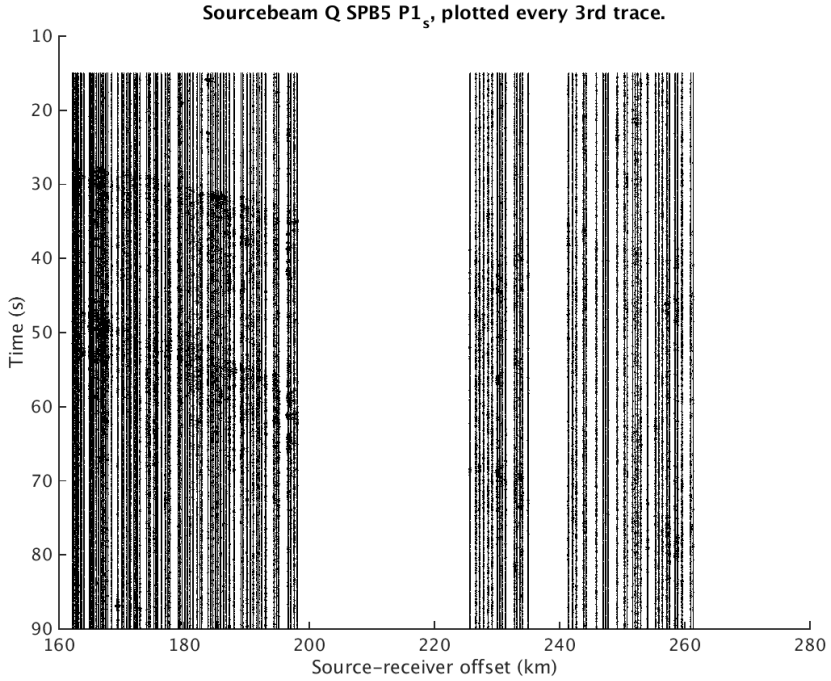

Figure A.135: Source-beam $P1_s$ SPB5 Q, plotted every 3rd trace

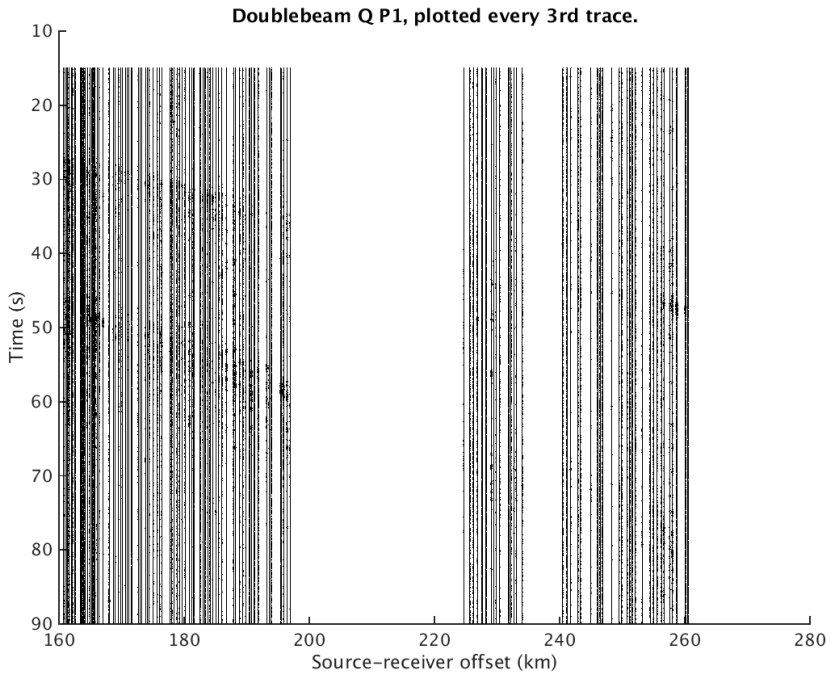

Figure A.136: Double-beam $P1_s$ Q, plotted every 3rd trace

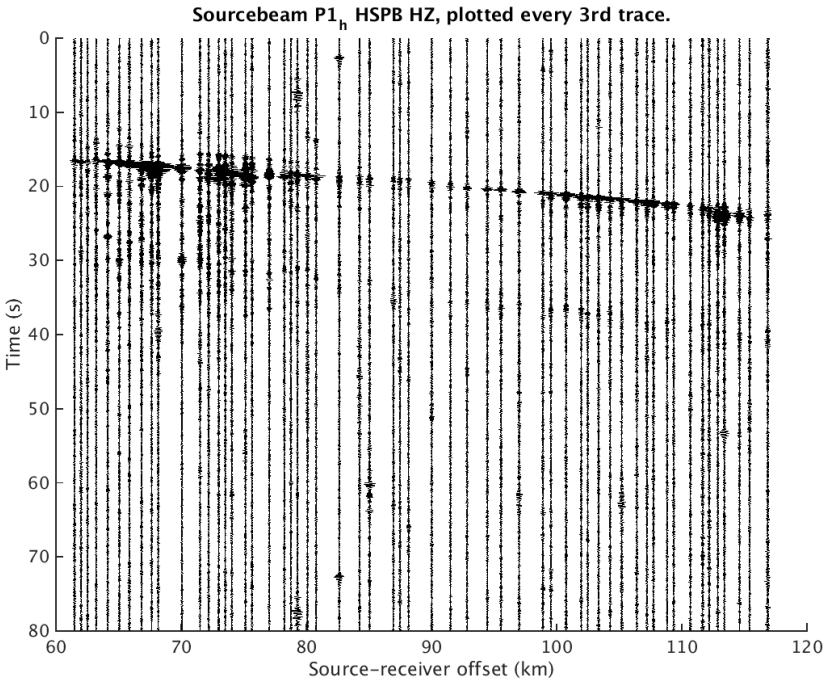

Figure A.137: Source-beam $P1_h$ HSPB HZ, plotted every 3rd trace

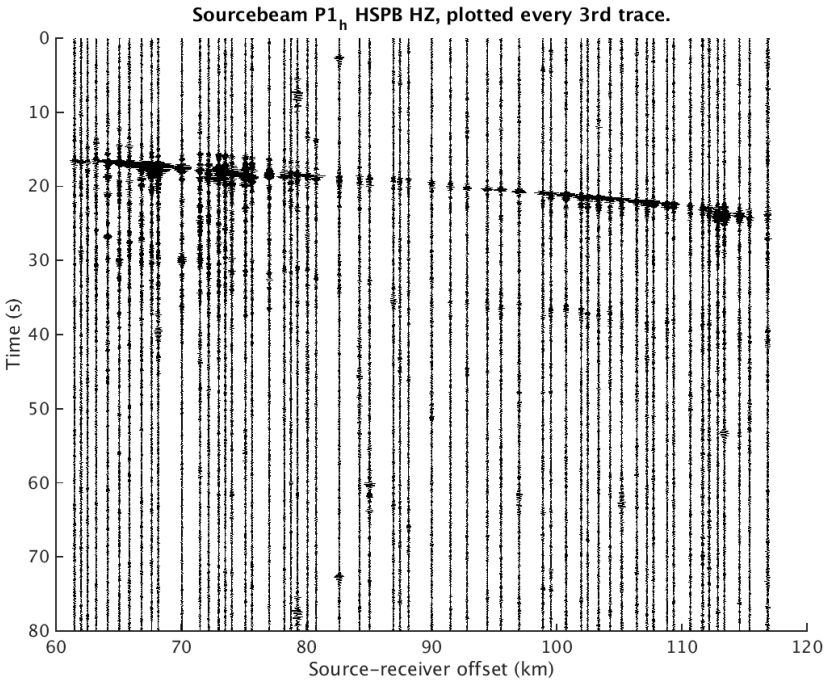

Figure A.138: Source-beam $P1_h$ HSPB HZ v_{app} = 4 km/s, plotted every 3rd trace

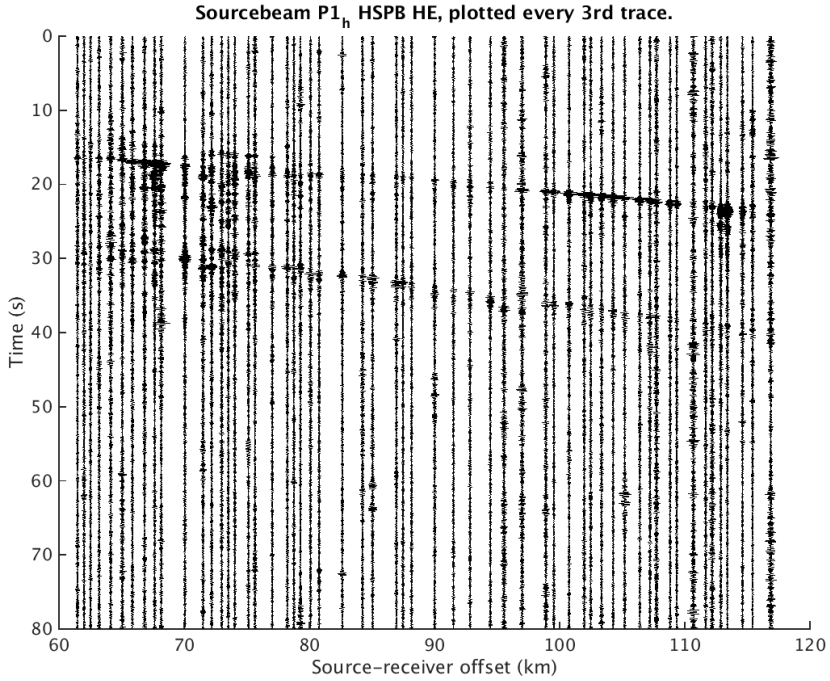

Figure A.139: Source-beam $P1_h$ HSPB HE, plotted every 3rd trace

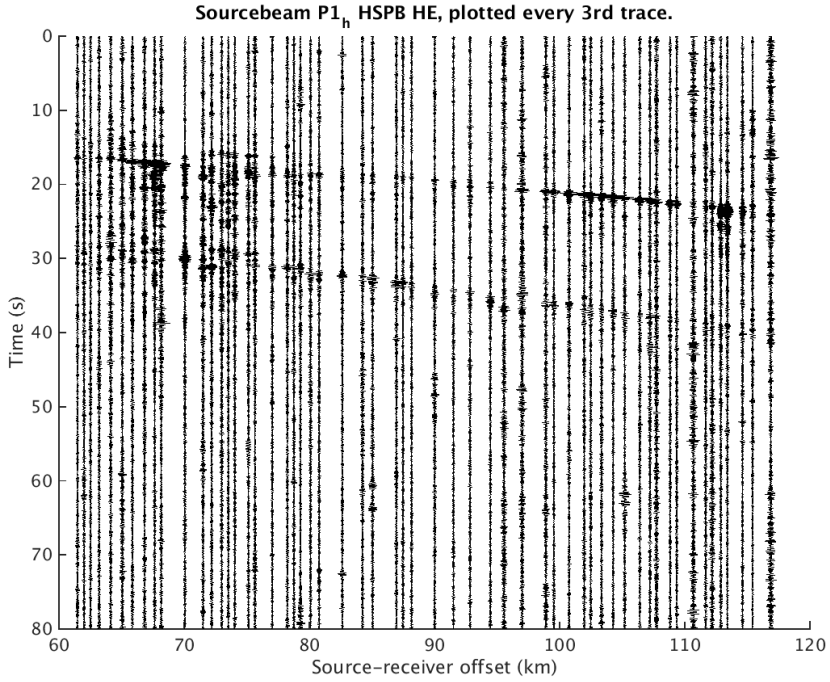

Figure A.140: Source-beam $P1_h$ HSPB HE v_{app} = 4 km/s, plotted every 3rd trace

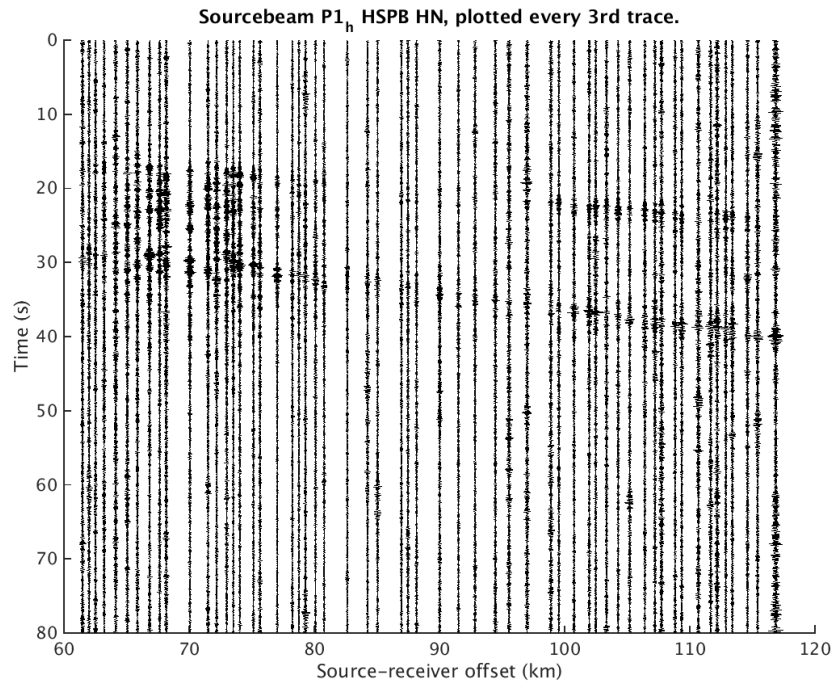

Figure A.141: Source-beam $P1_h$ HSPB HN, plotted every 3rd trace

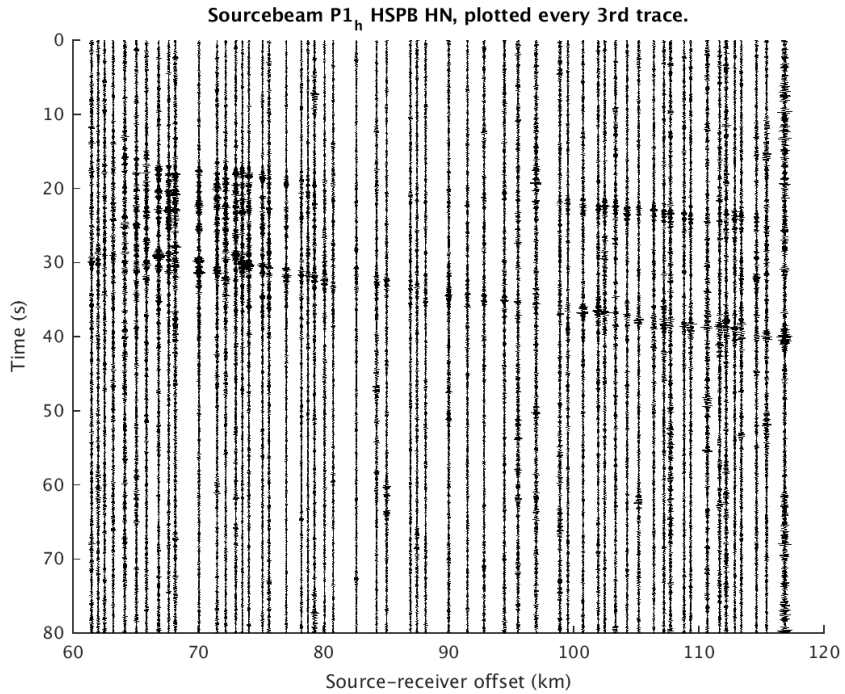

Figure A.142: Source-beam $P1_h$ HSPB HN v_{app} = 4 km/s, plotted every 3rd trace

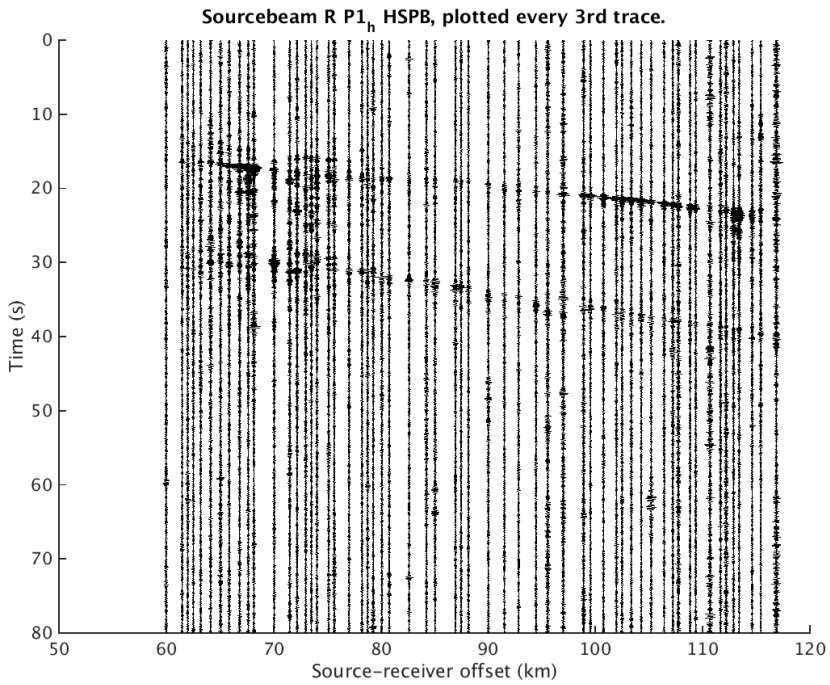

Figure A.143: Source-beam $P1_h$ HSPB R, plotted every 3rd trace

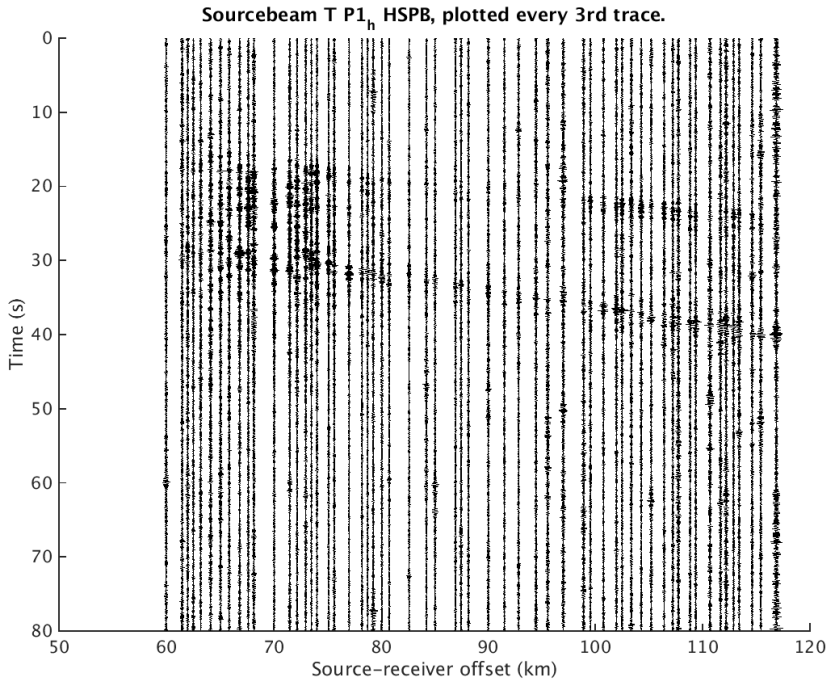

Figure A.144: Source-beam $P1_h$ HSPB T, plotted every 3rd trace

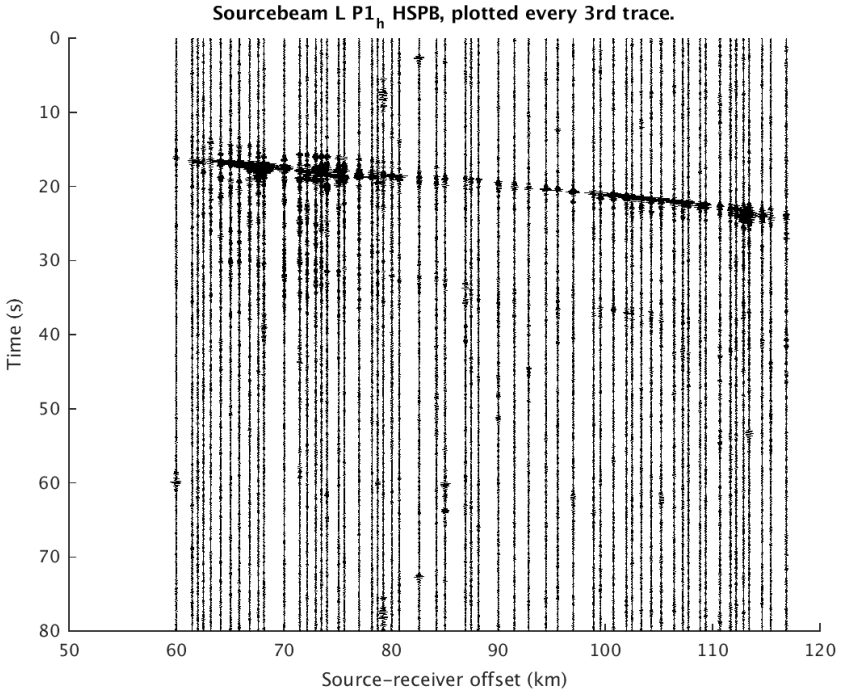

Figure A.145: Source-beam $P1_h$ HSPB L, plotted every 3rd trace

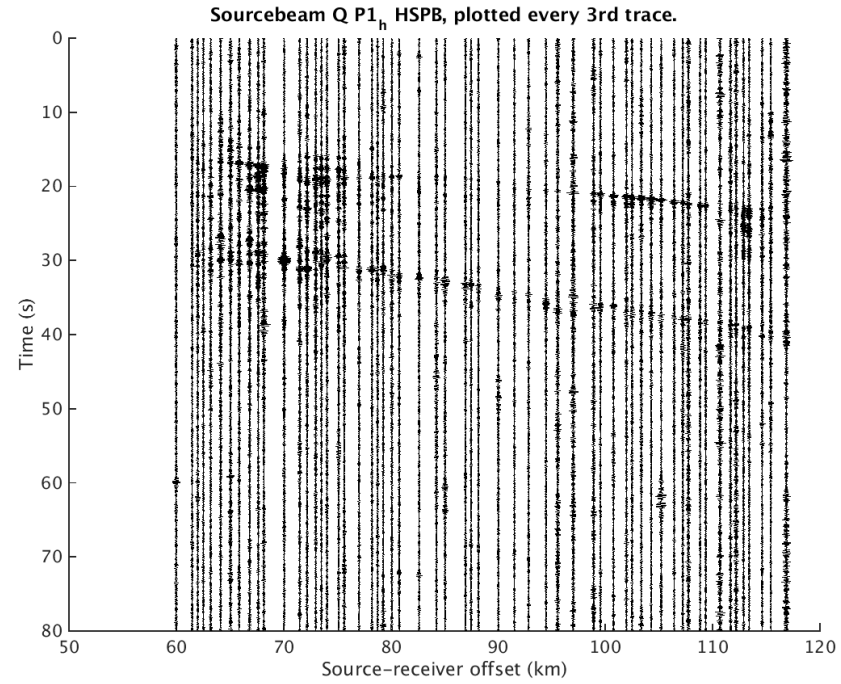

Figure A.146: Source-beam $P1_h$ HSPB Q, plotted every 3rd trace

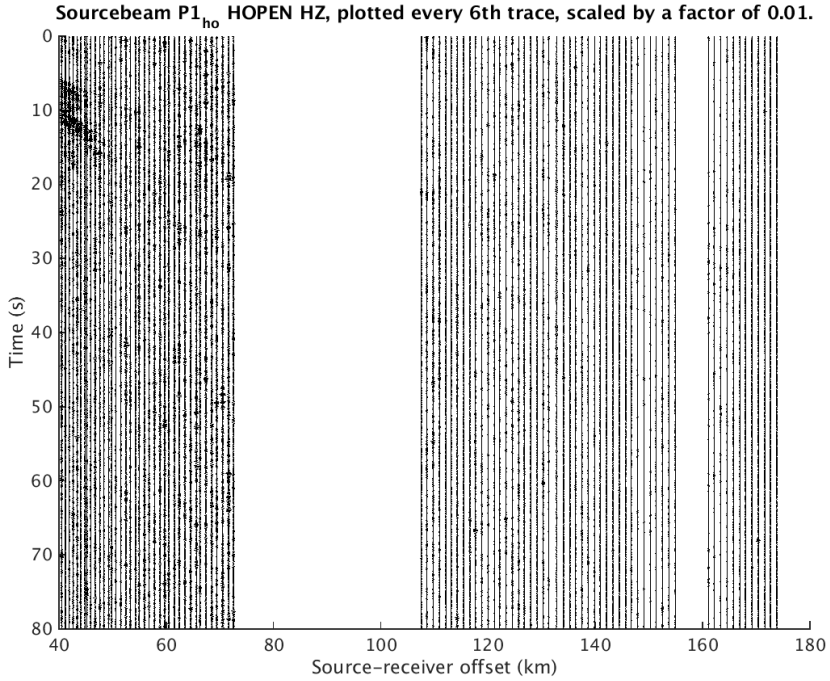

Figure A.147: Source-beam $P1_{ho}$ HOPEN HZ, plotted every 3rd trace

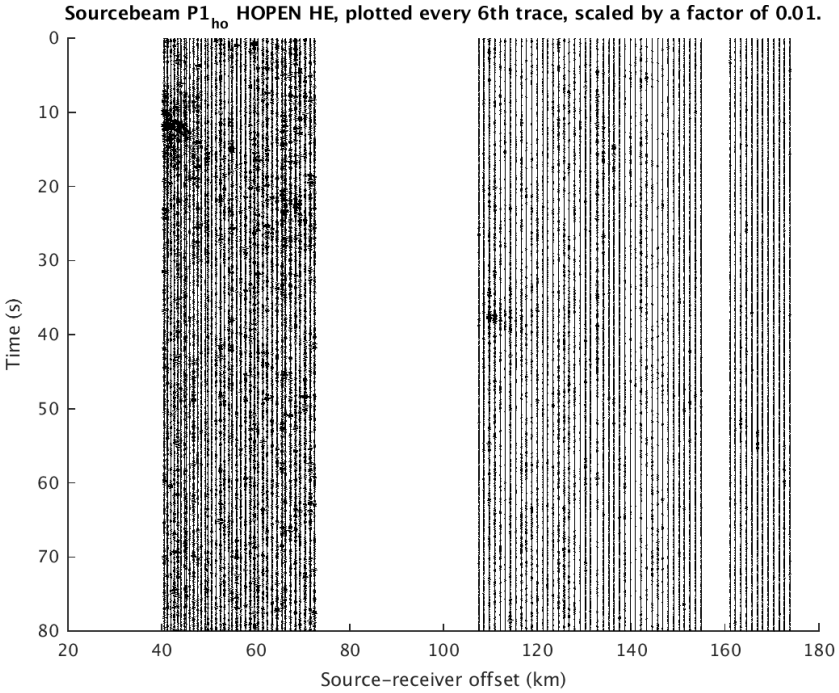

Figure A.148: Source-beam $P1_{ho}$ HOPEN HE, plotted every 3rd trace

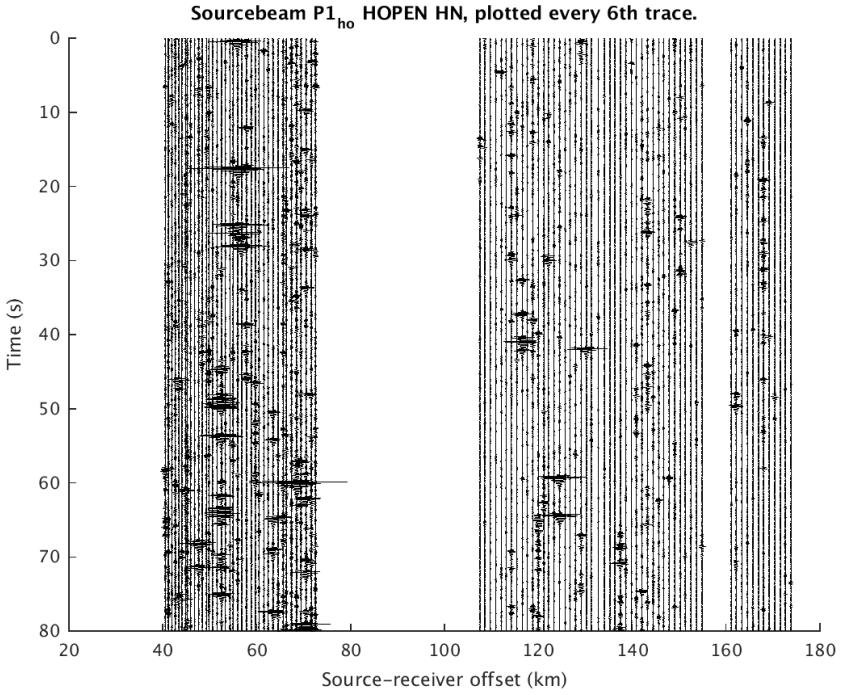

Figure A.149: Source-beam $P1_{ho}$ HOPEN HN, plotted every 3rd trace

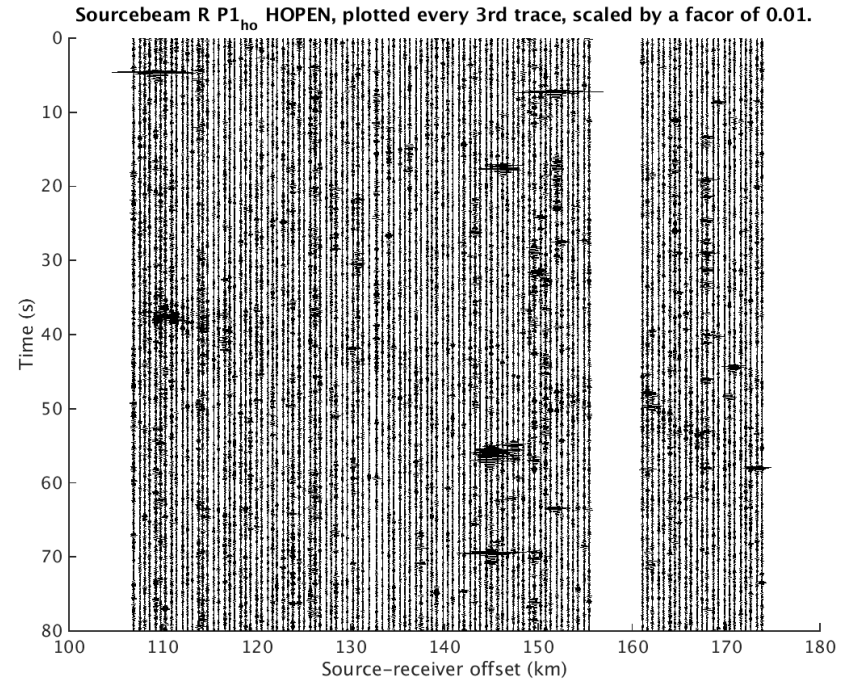

Figure A.150: Source-beam $P1_{ho}$ HOPEN R, plotted every 3rd trace

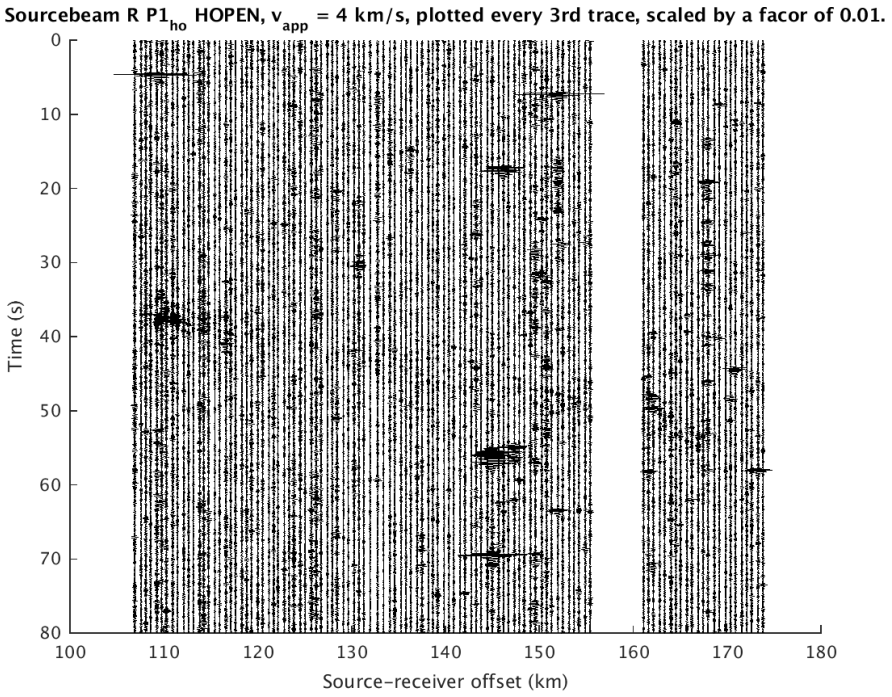

Figure A.151: Source-beam $P1_{ho}$ HOPEN R, apparent velocity = 4 km/s, plotted every 3rd trace

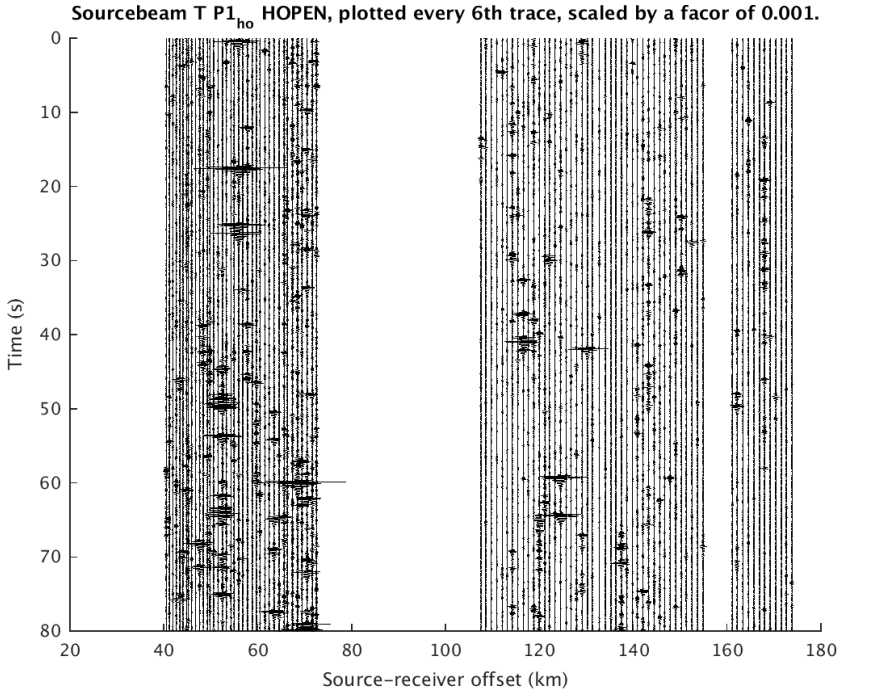

Figure A.152: Source-beam $P1_{ho}$ HOPEN T, plotted every 3rd trace

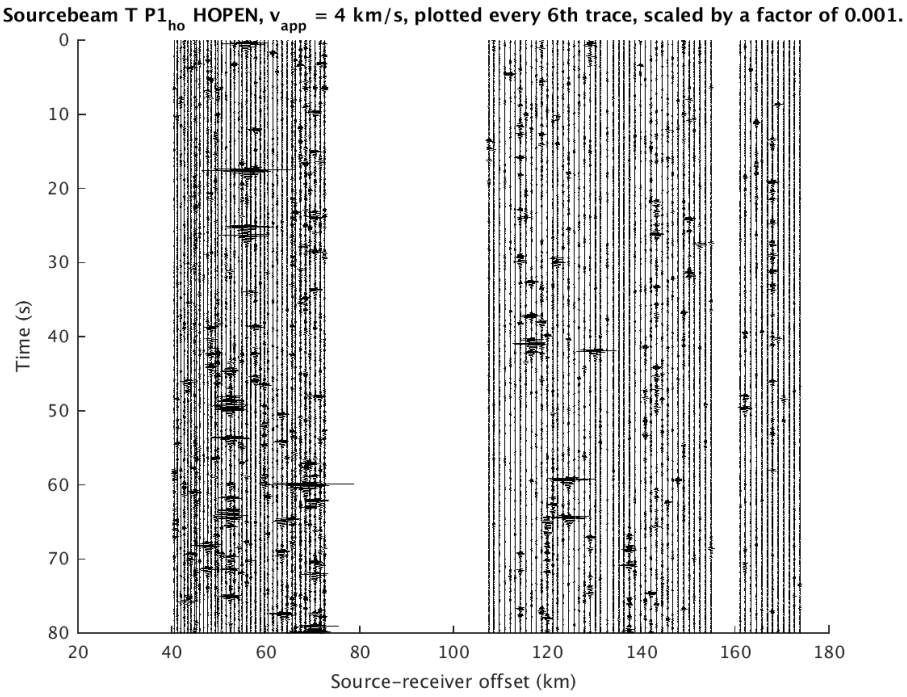

Figure A.153: Source-beam $P1_{ho}$ HOPEN T, apparent velocity = 4 km/s, plotted every 3rd trace

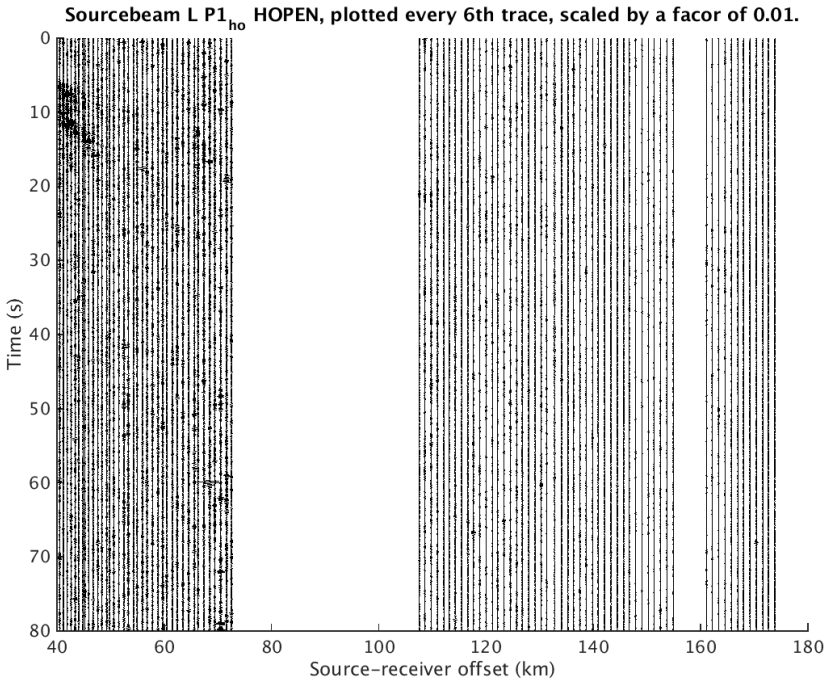

Figure A.154: Source-beam $P1_{ho}$ HOPEN L, plotted every 3rd trace

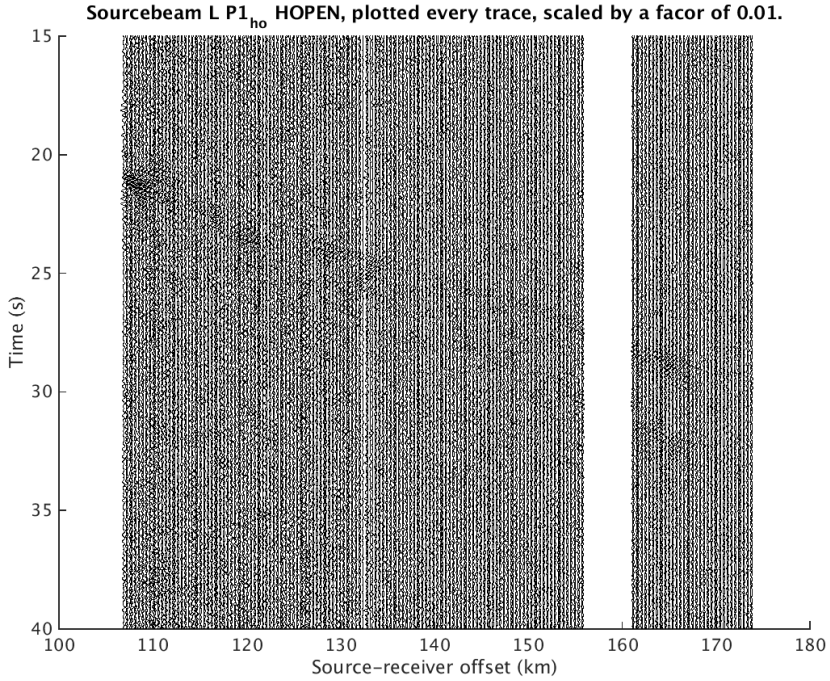

Figure A.155: Source-beam $P1_{ho}$ HOPEN L, scaled by a factor of 0.01 and plotted every trace

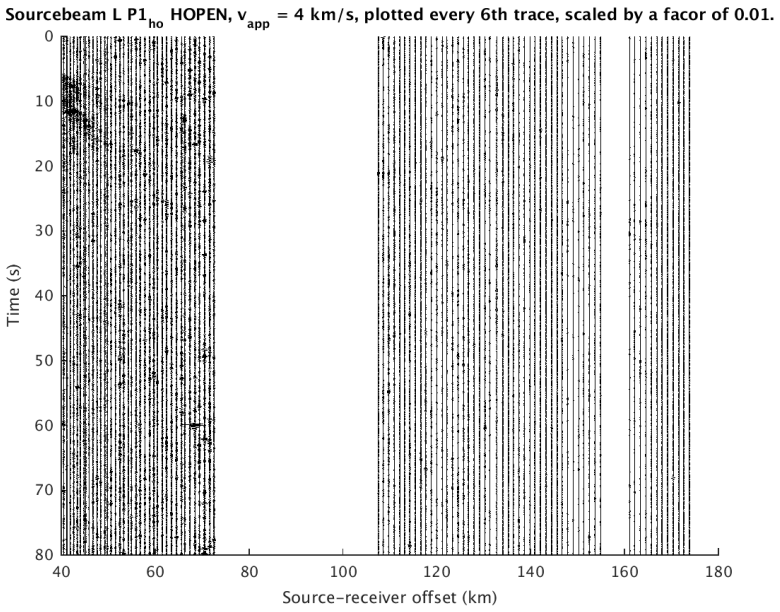

Figure A.156: Source-beam $P1_{ho}$ HOPEN L, apparent velocity = 4 km/s, plotted every 3rd trace

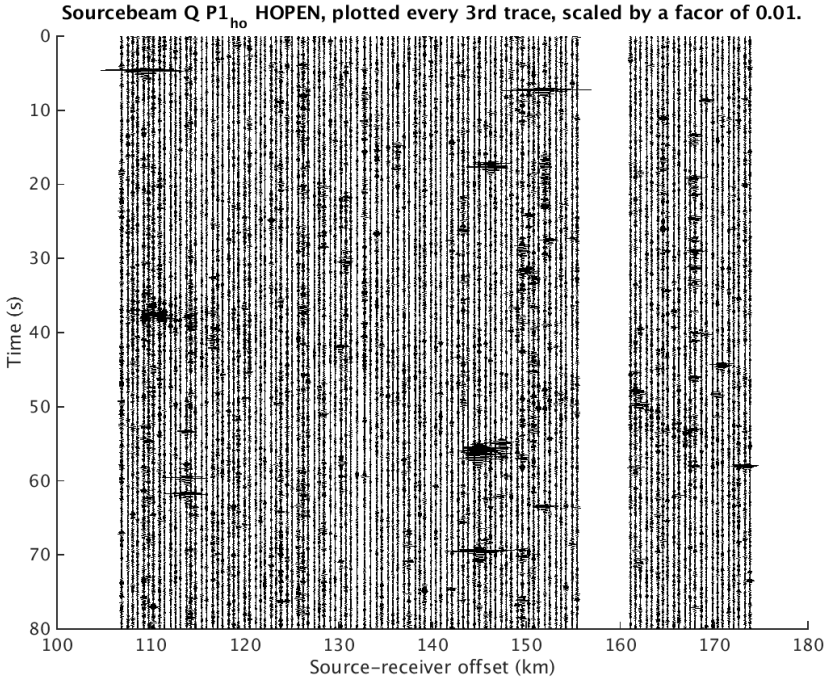

Figure A.157: Source-beam $P1_{ho}$ HOPEN Q, plotted every 3rd trace

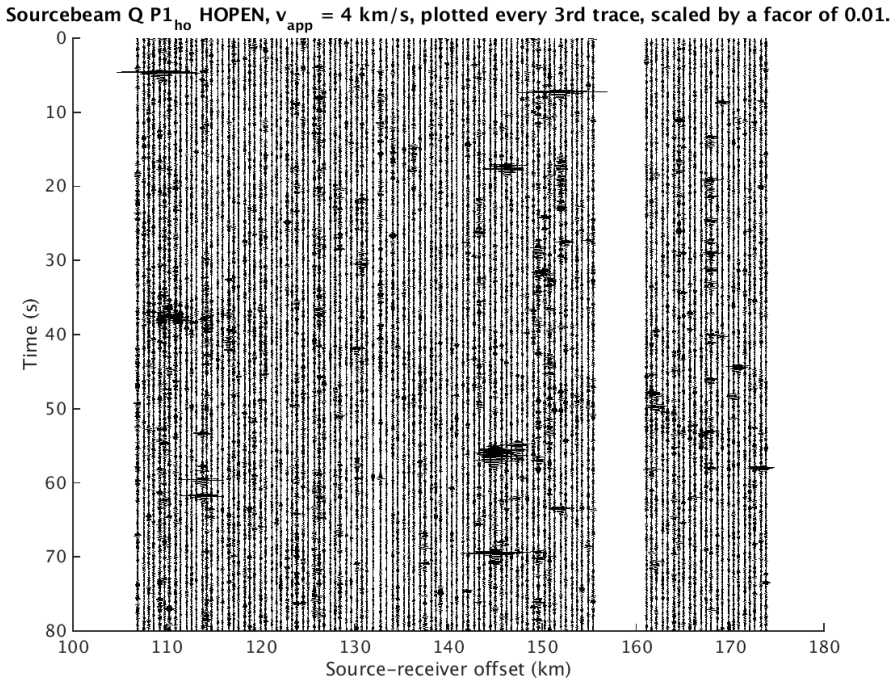

Figure A.158: Source-beam $P1_{ho}$ HOPEN Q, apparent velocity = 4 km/s, plotted every 3rd trace

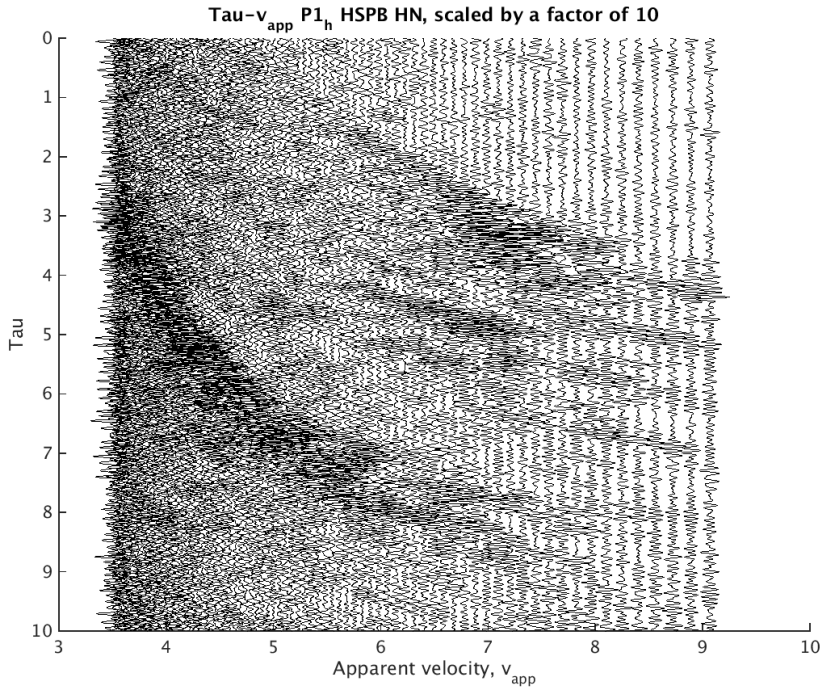

Figure A.159: $\tau - v_{app}$ seismogram, $P1_h$ HSPB HN, plotted every 3rd trace

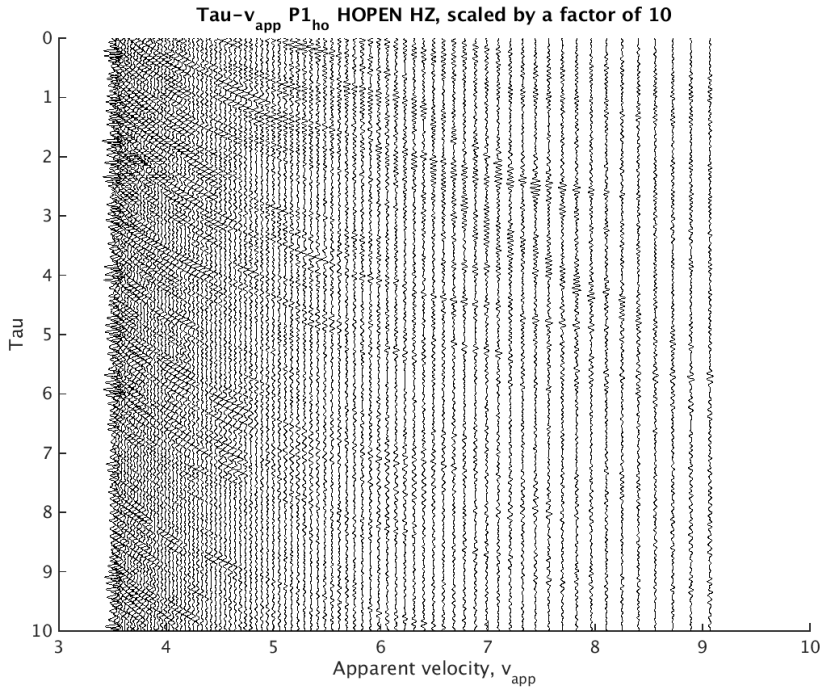

Figure A.160: $\tau - v_{app}$ seismogram, $P1_{ho}$ HOPEN HZ, plotted every 3rd trace, scaled by a factor of 10.

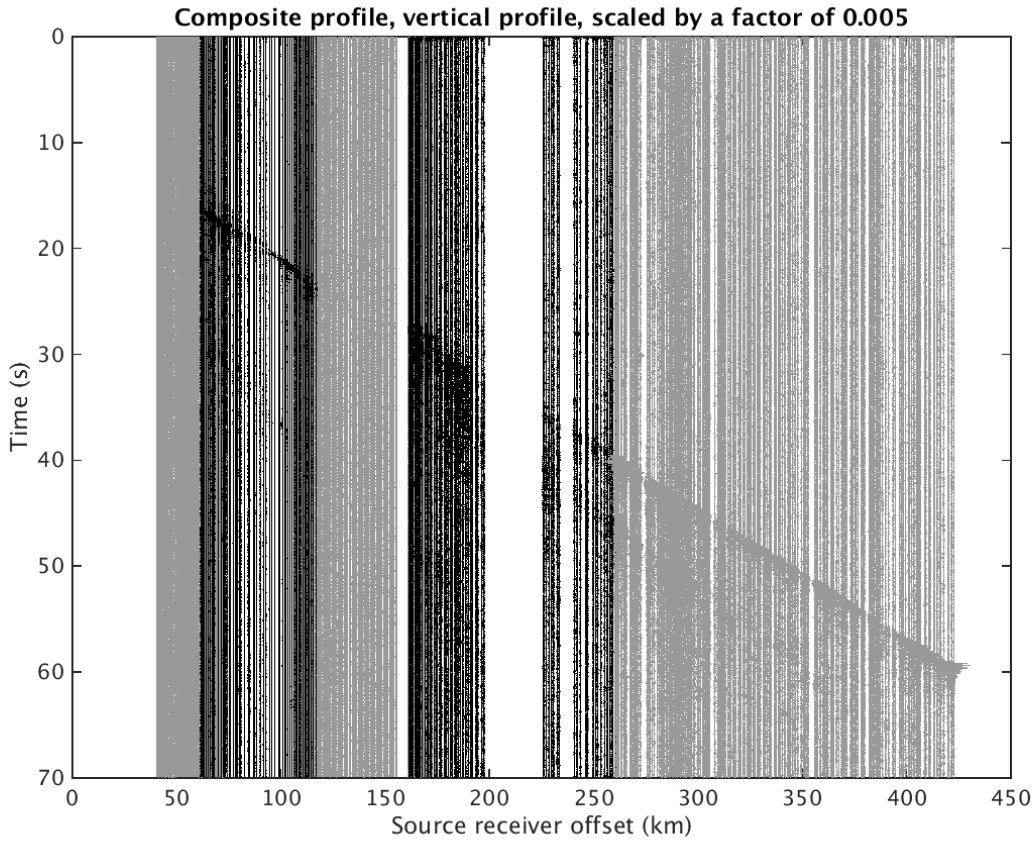

Figure A.161: Composite profile of the vertical component of $P1_{ho}$ $P1_h$ $P1_s$ and $P2$. $P1_{ho}$ has been scaled by a factor of 0.01 while $P1_h$, $P1_s$ and $P2$ has been scaled by a factor of 0.005. $P1_h$ and $P2$ have been plotted every third trace, while $P1_s$ and $P1_{ho}$ have been plotted every sixth trace. Light grey = HOPEN, black = HSPB, black = SPITS P1 and light grey = SPITS P2.

A.2 Forward modelling

A.2.1 Raypaths in Barents50

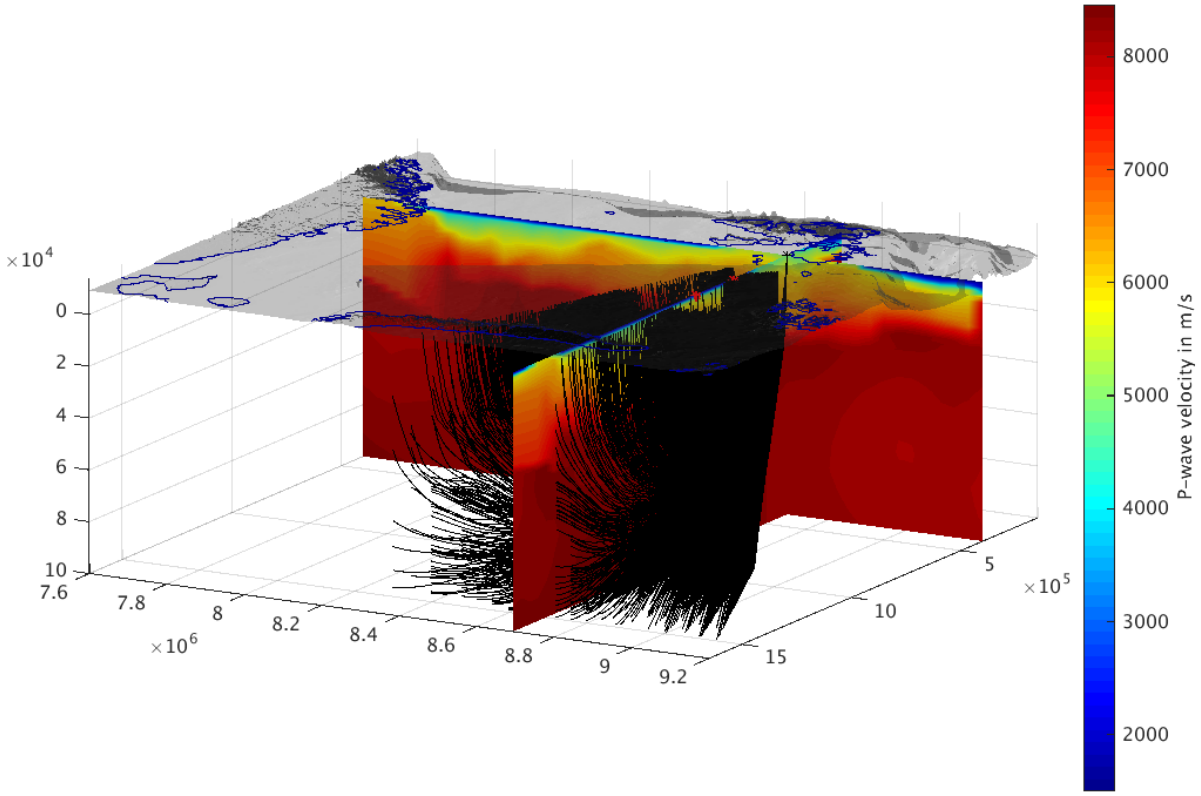

Figure A.162: Raypaths of P-waves from SPB3 towards *P*2 through the Barents50 3D model with Etopo bathymetry. Endpoints of *P*2 plotted as red crosses. View towards west south-west.

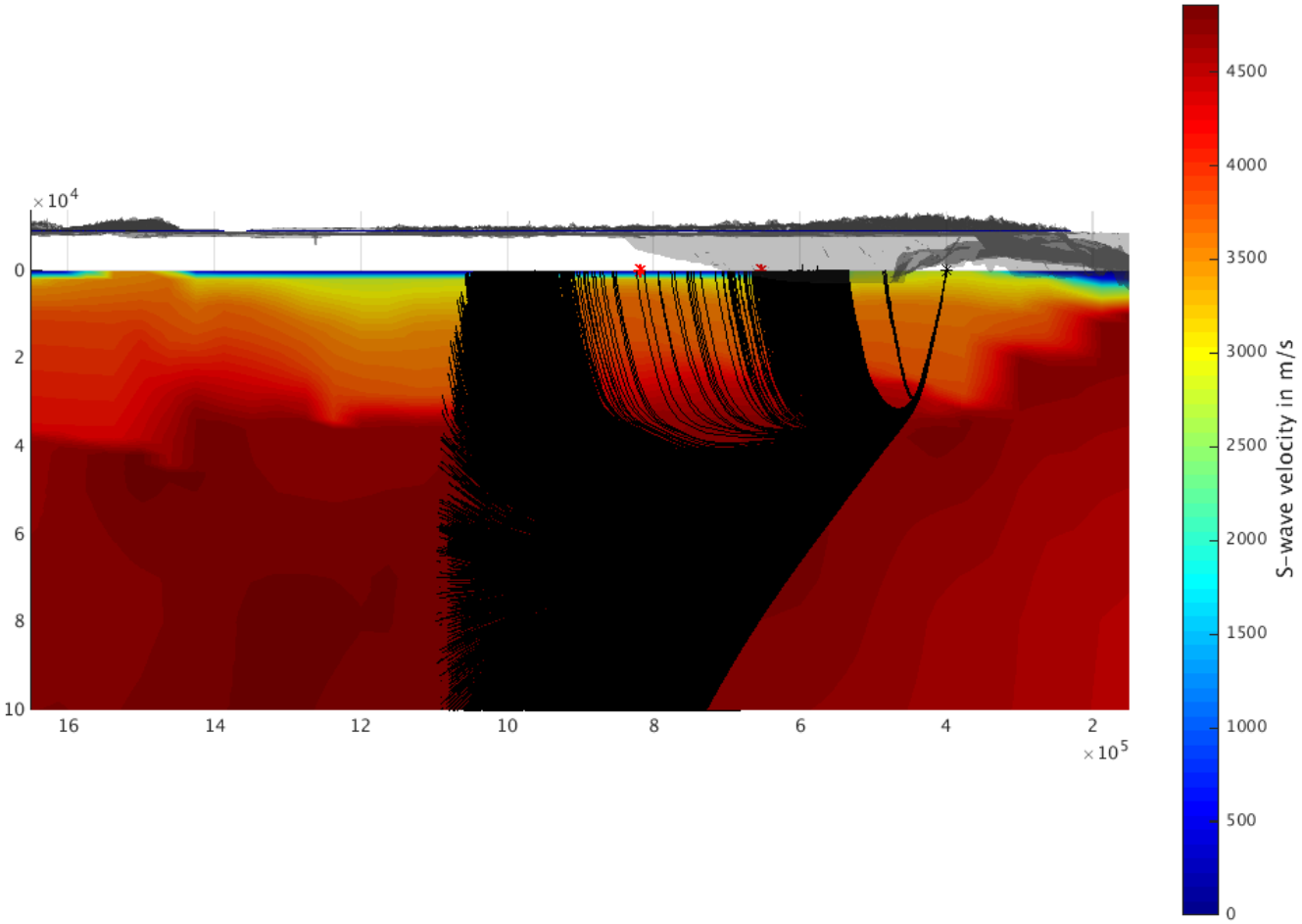

Figure A.163: Raypaths of S-waves from SPITS (SPB3) towards *P*2, plotted every 10th ray. Endpoints of *P*2 are red crosses. View towards north. The depth is in meter and the velocity is in meter per second.

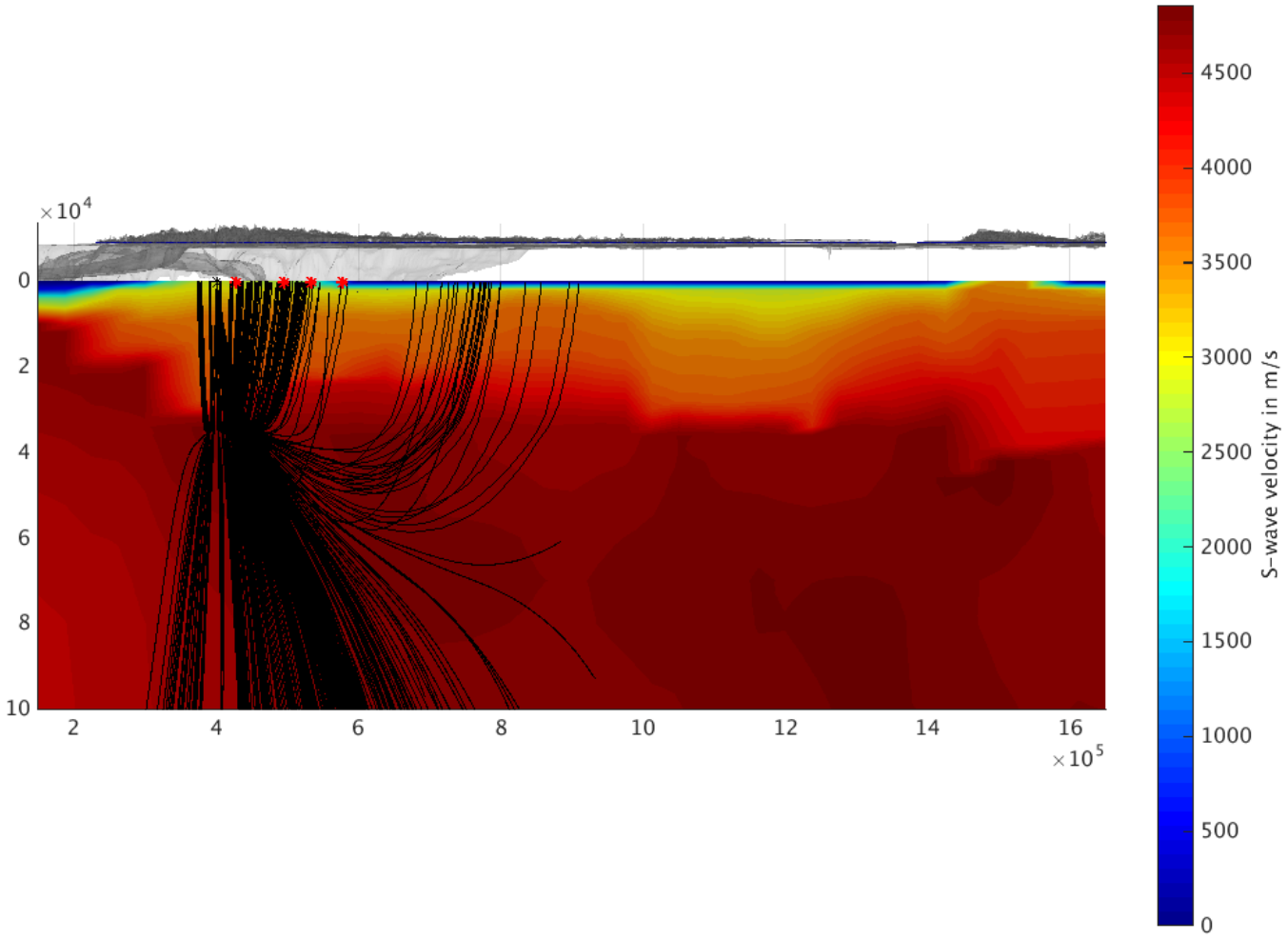

Figure A.164: Raypaths of P-waves from SPITS (SPA0) towards $P1_s$, plotted every 15th trace. Endpoints of the two sections of $P1_s$ plotted as small red crosses. View towards north. The depth is in meter and the velocity is in meter per second.

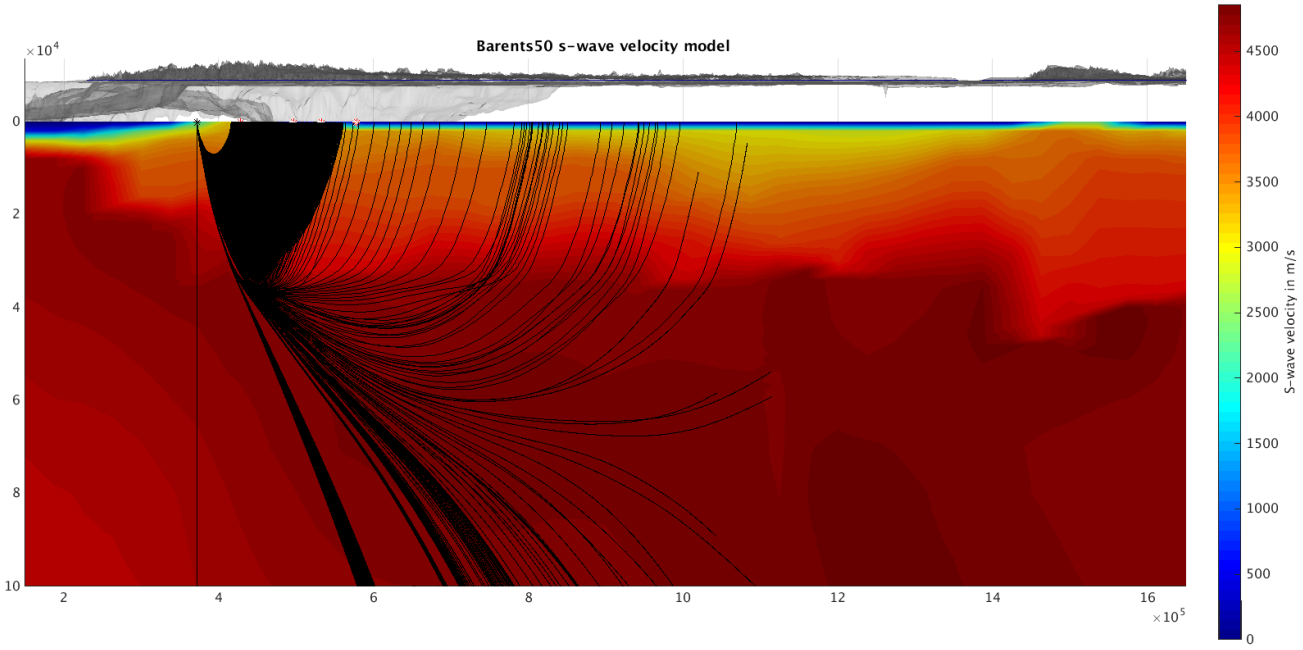

Figure A.165: Raypaths of S-waves from HSPB towards $P1_h$. Endpoints of the two sections of $P1_h$ plotted as small red crosses. View towards north. The depth is in meter and the velocity is in meter per second.

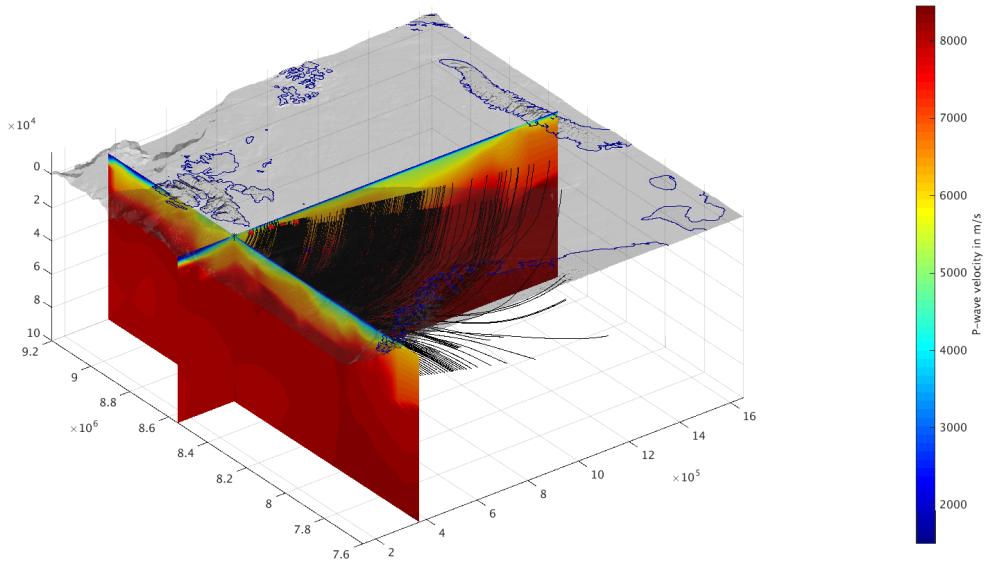

Figure A.166: Raypaths of P-waves from HSPB towards $P1_{ho}$ through the Barents50 3D model with Etopo bathymetry. Endpoints of the two sections of $P1_{ho}$ plotted as red crosses. View towards north-east.

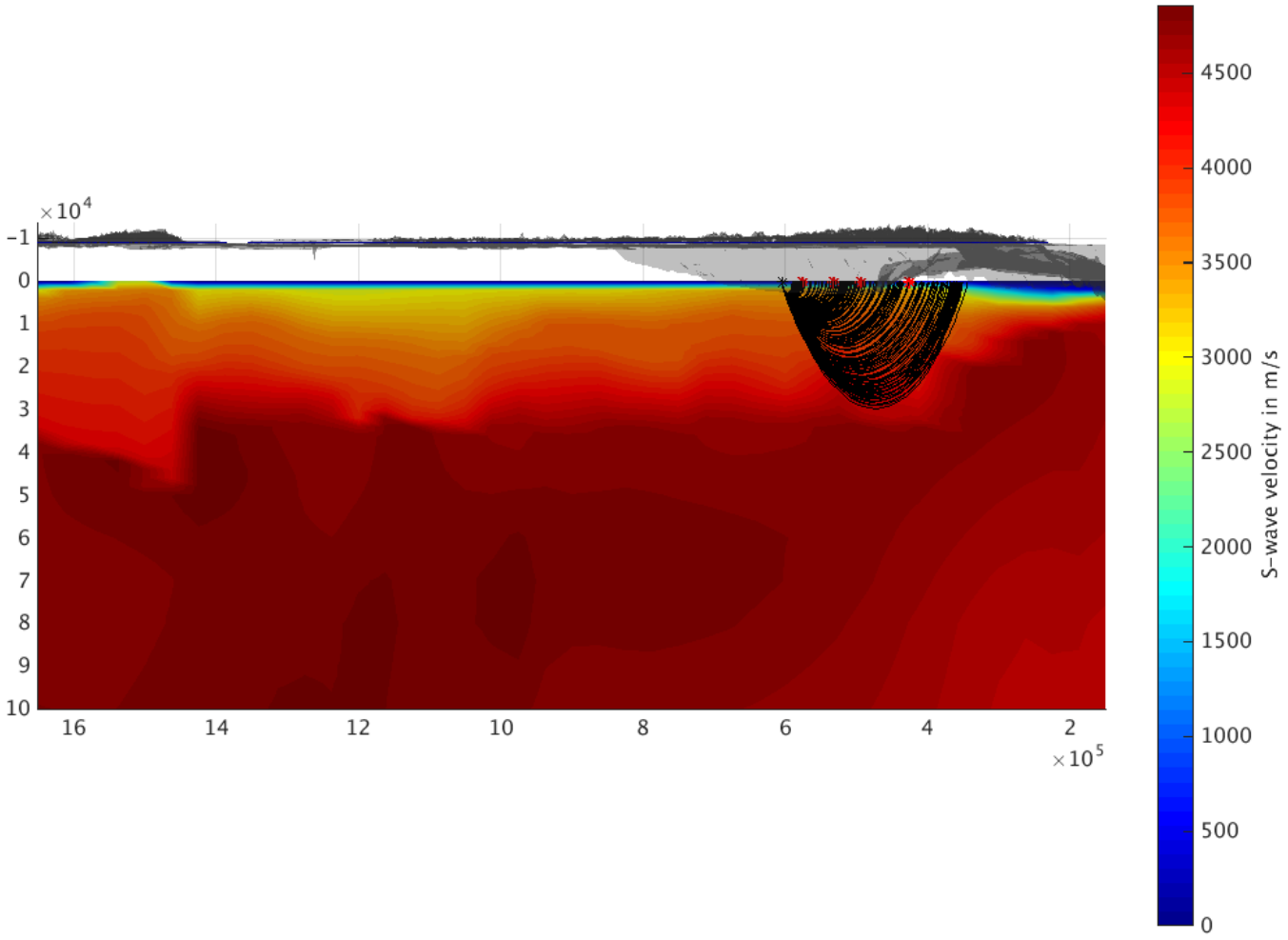

Figure A.167: Raypaths of S-waves from HOPEN towards $P1_{ho}$. Endpoints of the two sections of $P1_{ho}$ plotted as small red crosses, every 25th ray are plotted. View towards south. The depth is in meter and the velocity is in meter per second.

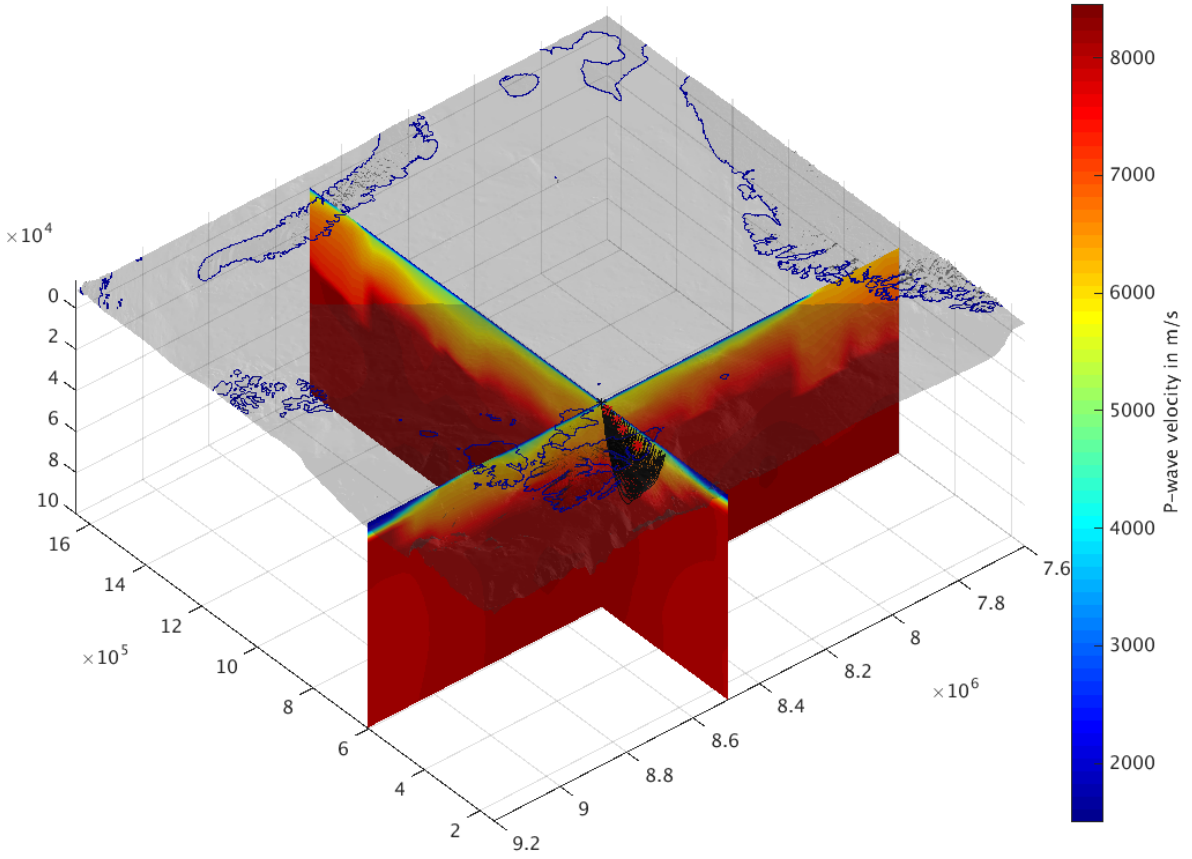

Figure A.168: Raypaths of P-waves from HOPEN towards $P1_{ho}$ through the Barents50 3D model with Etopo bathymetry. Endpoints of the two sections of $P1_{ho}$ plotted as red crosses. View south south-east.

A.2.2 Synthetic seismograms

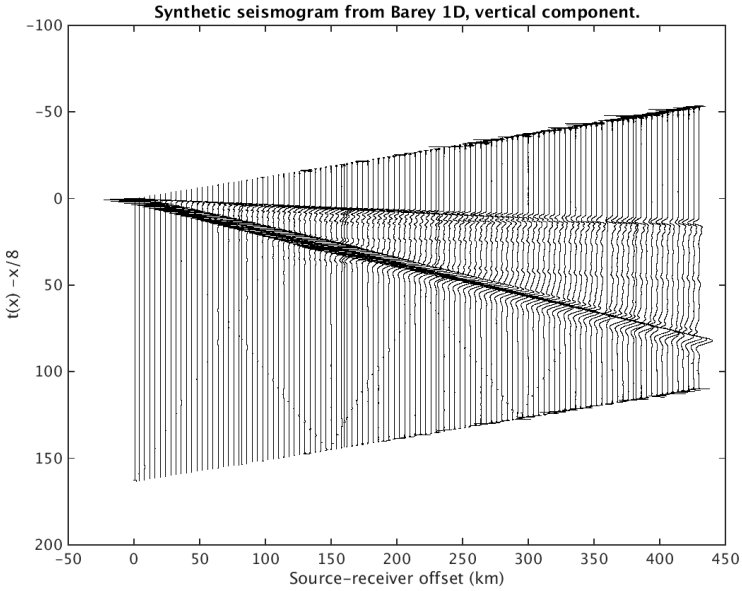

Figure A.169: Synthetic seismogram from the 1D model Barey in reduced time, vertical component.

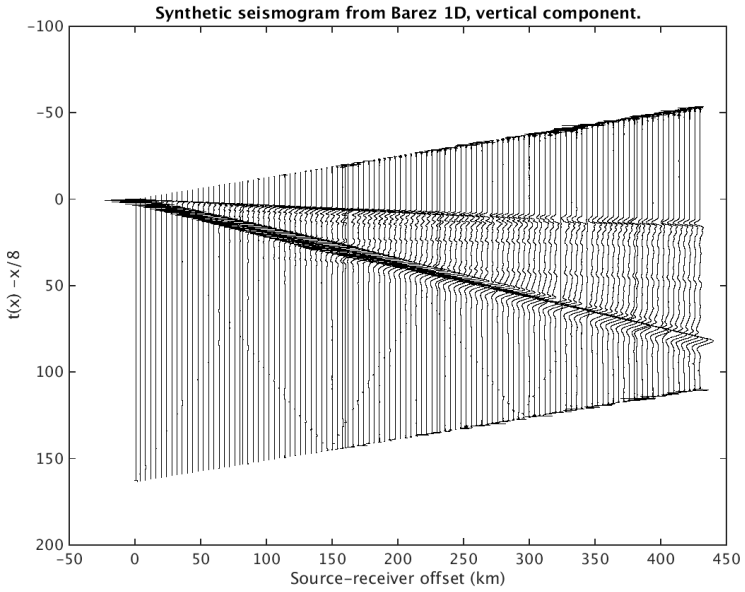

Figure A.170: Synthetic seismogram from the 1D model Barez in reduced time, vertical component.

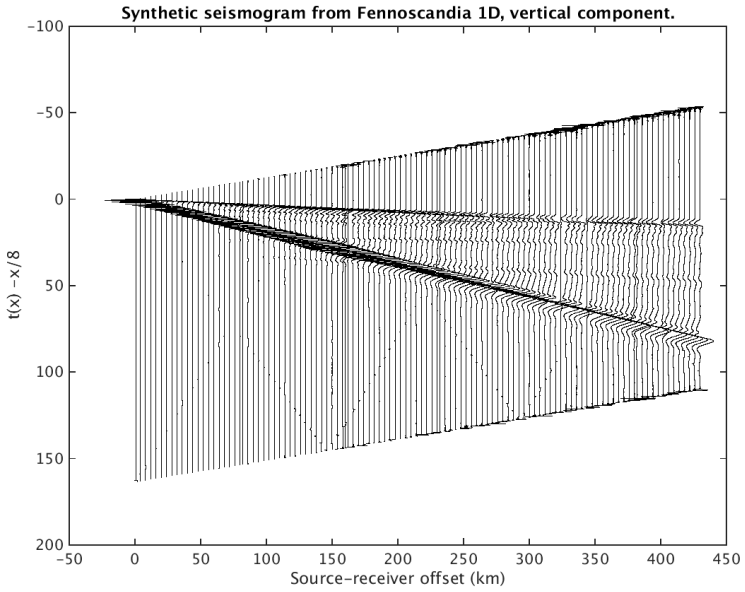

Figure A.171: Synthetic seismogram from the 1D model Fennoscandia in reduced time, vertical component.

A.3 Inversion

A.3.1 1D inverted velocity models

Table A.1: 1D velocity model Barents, from Kremenetskaya et al. (2001)

Depth (km)	P-wave velocity (km/s)	S-wave velocity (km/s)
0	6.20	3.580
16.0	6.20	3.580
16.0	6.70	3.870
40.0	6.70	3.870
40.0	8.10	4.60
55.0	8.10	4.60
55.0	8.23	4.68
210.0	8.23	4.68

Table A.2: 1D velocity model Barey, from Schweitzer and Kennett (2002)

Depth (km)	P-wave velocity (km/s)	S-wave velocity (km/s)
0	6.2000	3.5800
16.0	6.2000	3.5800
16.0	6.7000	3.8700
41.0	6.7000	3.8700
41.0	8.1000	4.5760
70.0	8.2250	4.6470
210.0	8.2600	4.6670

Table A.3: 1D velocity model Barez, from Schweitzer and Kennett (2002)

Depth (km)	P-wave velocity (km/s)	S-wave velocity (km/s)
0	6.2000	3.5800
16.0	6.2000	3.5800
16.0	6.7000	3.8700
41.0	6.7000	3.8700
41.0	8.1000	4.7090
70.0	8.2250	4.7820
210.0	8.2600	4.8020

Table A.4: 1D velocity model Fennoscandia, from Mykkeltveit and Ringdal (1981).

Depth (km)	P-wave velocity (km/s)	S-wave velocity (km/s)
0	6.20	3.580
16.0	6.20	3.580
16.0	6.70	3.868
40.0	6.70	3.868
40.0	8.15	4.705
95.0	8.15	4.705
95.0	8.25	4.763
210.0	8.30	4.792

Table A.5: 1D velocity model from inversion for $P2$. The S-wave data are values lying between the 1D models Barents, Barey, Barez, Fennoscandia and Barents50, while density comes from Barents50. The S-wave and density values are presented here since they are used in the frequency wavenumber integration.

Depth (km)	P-wave velocity (km/s)	S-wave velocity (km/s)	Density (gm/cc)
0.6217	4.3535	3.1622	2.5320
3.3453	4.8139	3.3035	2.5622
7.1216	5.2115	3.5828	2.7586
10.0307	5.5702	3.6444	2.8218
18.6565	6.2555	3.8784	2.9546
24.0231	6.3490	3.9026	2.9700
29.3360	6.5665	4.1638	3.2439
32.0458	8.0526	4.1837	3.2533
42.7598	8.1771	4.6220	3.2725
47.0714	8.2041	4.6281	3.2773
60.5979	8.2305	4.6320	3.2833

Table A.6: 1D velocity model from inversion for $P1_s$. The S-wave data are values lying between the 1D models Barents, Barey, Barez, Fennoscandia and Barents50, while density comes from Barents50. The S-wave and density values are presented here since they are used in the frequency wavenumber integration.

Depth (km)	P-wave velocity (km/s)	S-wave velocity (km/s)	Density (gm/cc)
0.3021	4.2625	3.1507	2.5270
6.1752	5.5614	3.5799	2.7566
12.2650	5.6922	3.8656	2.9426
19.0526	6.2922	3.9026	2.9656
22.0487	6.3478	3.9166	2.9786
27.3966	6.4478	4.0451	3.1882
30.8958	8.0629	4.1476	3.2381

Table A.7: 1D velocity model from inversion for $P1_h$. The density data comes from Barents50. The density values are presented here since they are used in the frequency wavenumber integration.

Depth (km)	P-wave velocity (km/s)	S-wave velocity (km/s)	Density (gm/cc)
0.3427	4.2669	3.1507	2.5270
7.8642	5.4370	3.5799	2.7566
16.7670	6.1400	3.8987	2.9756
18.9098	6.1864	3.9016	2.9786
20.1019	6.3149	3.9027	2.9788
23.9133	6.3511	3.9681	3.0895

Table A.8: 1D velocity model from inversion for $P1_{ho}$. The S-wave data are values lying between the 1D models Barents, Barey, Barez, Fennoscandia and Barents50, while density comes from Barents50. The S-wave and density values are presented here since they are used in the frequency wavenumber integration.

Depth (km)	P-wave velocity (km/s)	S-wave velocity (km/s)	Density (gm/cc)
0.2521	4.2548	3.1507	2.5270
3.8260	5.5904	3.9228	2.5507
10.8370	5.9024	3.7083	2.9276
17.5463	6.2342	3.8987	2.9756
26.1019	6.4349	4.0450	3.1882
29.8133	8.0311	4.0565	3.2002

A.3.2 Synthetic seismograms from inverted data

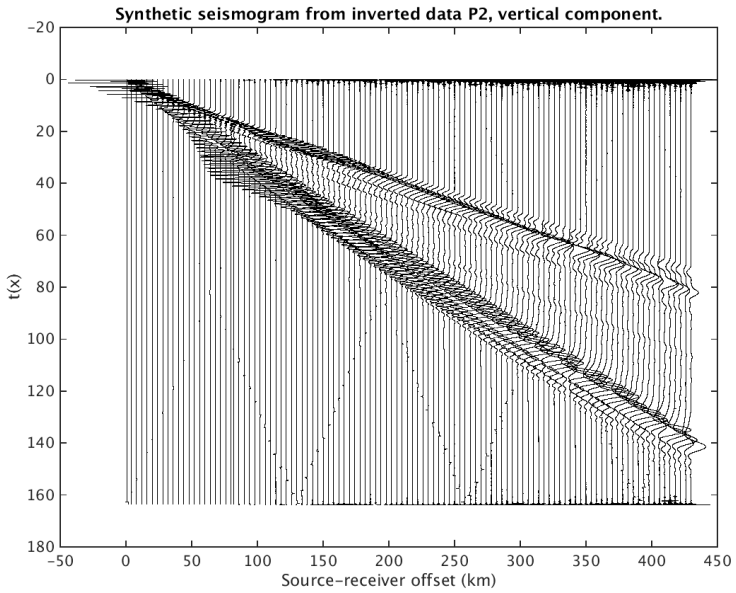

Figure A.172: Synthetic seismogram from the 1-D inverted velocity of *P*2.

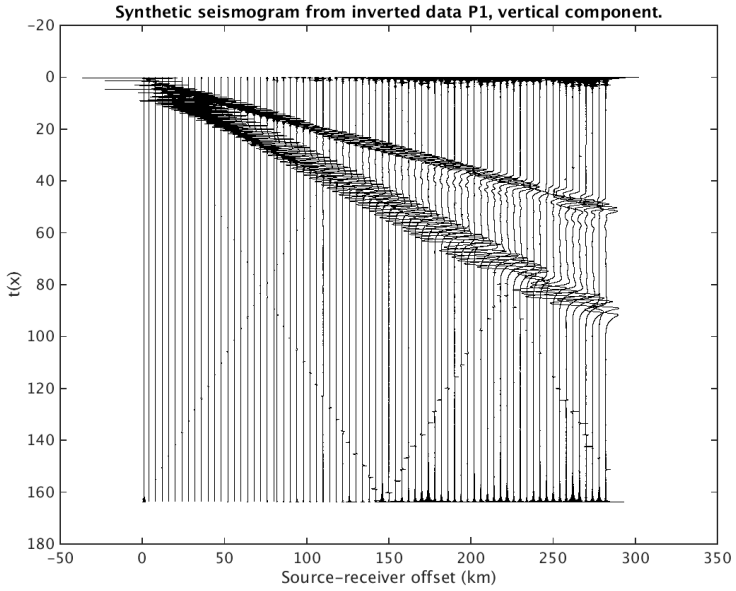

Figure A.173: Synthetic seismogram from the 1-D inverted velocity of $P1_s$.

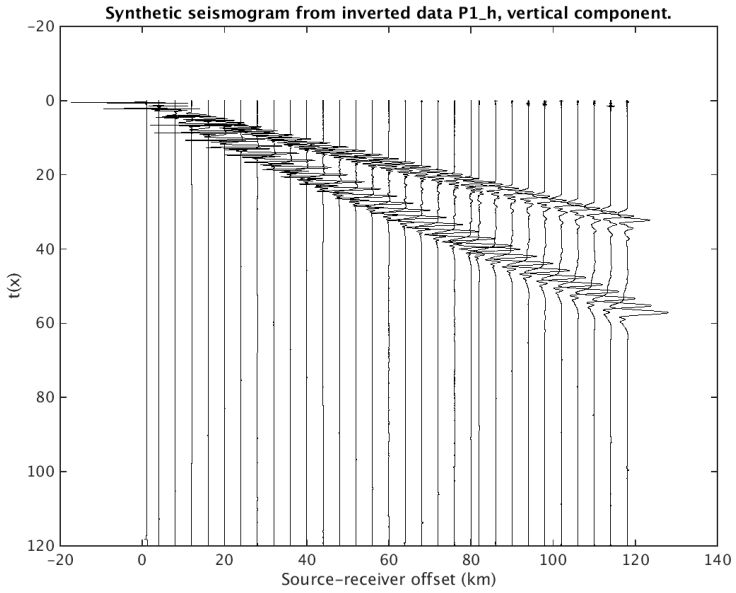

Figure A.174: Synthetic seismogram from the 1-D inverted velocity of $P1_h$.

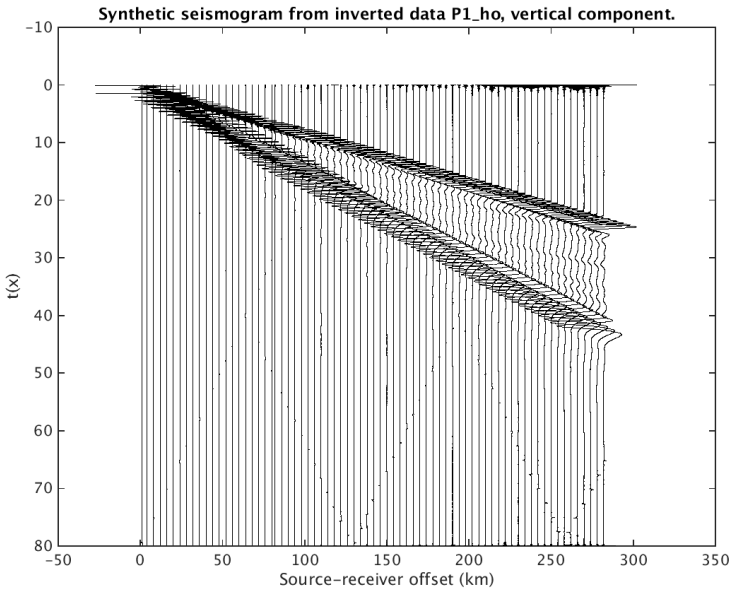

Figure A.175: Synthetic seismogram from the 1-D inverted velocity of $P1_{ho}$.